GROUNDWATER DYNAMICS AND THE SALINITY STRUCTURE IN SANDY BEACHES

Nick Cartwright, BSc

Division of Civil Engineering
University of Queensland
Australia

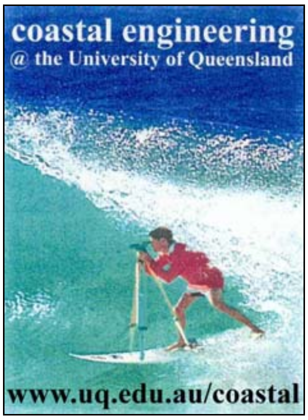

Thesis presented to the University of Queensland, Australia, in fulfilment
of the requirements for the degree of Doctor of Philosophy.

July, 2004

Abstract

Groundwater dynamics in beaches have been investigated through field and laboratory experiments. The observations have been used to test the ability of currently available mathematical and numerical models to adequately account for the influence of processes such as vertical flow and capillarity.

New 1D sand column experiments have been conducted to examine the influence of a truncated capillary fringe on periodic water table oscillations. As the fringe becomes increasingly truncated the aquifer storage term, the complex effective porosity $n_{\omega,}$ is substantially reduced in agreement with previous findings under steady flow conditions. The findings are a useful starting point for an investigation of the dynamics of the water table exit point in beaches where the water table lies just below the sand surface.

A simple 2D laboratory aquifer, influenced by finite-depth and capillarity effects, subject to simple harmonic periodic forcing has been used to investigate the dispersion of the water table waves. The performance of existing dispersion relation theories, accounting for both capillarity and finite-depth effects, deteriorates at higher oscillation frequencies suggesting that other, neglected processes have some influence. Horizontal flow in the capillary fringe is suggested as such a process.

The generation of higher harmonics due to a sloping beach face is also investigated in the laboratory. The observations reveal that the generation process is strongest near the sand surface, likely to be due to vertical flows into the aquifer being strongest near the sand surface. A 2DV numerical model is applied to the data and does well in predicting the nature of the generation process, qualitatively reproducing the variation in oscillation amplitude with depth in the inter-tidal zone.

Application of a modified Boussinesq equation to estimate aquifer recharge due to infiltration from wave runup is critically applied to field and laboratory measurements. Finite amounts of flux across the water table are seen at, and landward of, the runup limit where there is zero infiltration at the sand surface. This suggests that the capillary fringe and vertical flows in this region are significant and that application of the model be undertaken with care.

Field observations of the salinity structure and its response to ocean forcing reveal no response to tidal forcing but a significant response to a wave-induced pulse in groundwater levels. The infiltration of salty ocean water due to infiltration from wave runup is shown to reverse the traditional “salt-wedge” scenario in the surficial aquifer with a thin salty layer overlying the fresh water.

Statement of Sources

I, the undersigned, declare that the work presented in this thesis is, to the best of my knowledge and belief, original, except as acknowledged in the text, and that the material has not been submitted, either in whole or in part, for a degree at this or any other university.

Nick Cartwright

Acknowledgements

I would like to gratefully acknowledge the enthusiasm and guidance of my supervisor, A/Prof. Peter Nielsen. In particular, his willingness to get out into the field, the understanding of which is why we are here.

I extend my appreciation to Dr. Ling Li and Prof. Pierre Perrochet who have given me invaluable assistance and advice along the way. Thanks also go to Drs. Tom Baldock, David Lockington and Ian Turner for their helpful input and interesting discussions. Many thanks go to Graham Illidge for his invaluable advice and assistance with experimental design and construction.

A big ‘cheers’ goes to my fellow coastal engineering graduate students; Dave Callaghan, Ian Teakle and Matt Tomkins for their helpful and interesting discussions on all things science and some things not.

A very special thanks to my family for their support throughout my schooling career, and finally to Nina for her companionship and continual reality check.

This research was made possible through the financial support provided by an Australian Postgraduate Award, and a CRC for Sustainable Tourism Supplementary Scholarship. Additional research funding was provided as part of CRC for Sustainable Tourism project number 52001 and Australian Research Council project number DP0346461.

The wave and tide data used in this thesis has been kindly provided by Coastal Services, Environmental Protection Agency, Queensland, and the New South Wales Department of Public Works and Services', Manly Hydraulics Laboratory for New South Wales Department of Land and Water Conservation. The modelling package, Mike SHE/Mike 11, and training and support have been provided by the Danish Hydraulic Institute (Denmark and Australia).

Publications

The following publications have so far been produced as a result of the present research.

Journal Papers

Cartwright, N., L. Li and P. Nielsen, Response of the salt-freshwater interface to a wave-induced groundwater pulse: field observations and modelling, *Advances in Water Resources*, 27(3), 297-303, 2004.

Cartwright, N., P. Nielsen and S. L. Dunn, Water table waves in an unconfined aquifer: Experiments and modelling, *Water Resources Research*, *39*(12), 1330, 2003.

Cartwright, N., P. Nielsen and L. Li, Experimental observations of watertable waves in an unconfined aquifer with a sloping boundary. *Advances in Water Resources*, in press 2004.

Li, L., N. Cartwright, P. Nielsen and D. A. Lockington, Response of coastal groundwater table to offshore storms, *China Ocean Engineering*, in press 2004.

Conference Proceedings

Cartwright, N., L. Li and P. Nielsen, The influence of offshore storm waves on beach groundwater dynamics and salinity in a sandy ocean beach, *ICCE 2004 - The 29th Intl. Conf. on Coastal Engineering*, ASCE, Lisboa, Portugal, September 19-25, 2004. Accepted for presentation.

Cartwright, N., P. Nielsen and L. Li, Water table wave dispersion in sandy coastal aquifers, *ICHE 2004 - The 6th Intl. Conf. on Hydroscience and Engineering*, Brisbane, Australia, CD-ROM, May 30-June 3, 2004.

Cartwright, N. and P. Nielsen, Groundwater dynamics and salinity in sandy ocean beaches, *Proc. 2nd Intl. Conf. on Civil and Environmental Eng.*, Hiroshima, Japan, 107-115, October 23-25, 2003.

Cartwright, N., P. Nielsen, L. Li and D. Callaghan, Water table waves in unconfined aquifers: sloping boundary effects, *Proc. Coasts and Ports 2003, 16th Australasian Coastal and Ocean Engineering Conference*, Auckland, New Zealand, CD-ROM, September 25-28, 2003.

Cartwright, N. and P. Nielsen, Dynamics of the salt-freshwater mixing zone in ocean beaches, *Proc. 2nd Intl. Conf. on Salt Water Intrusion and Coastal Aquifers - Monitoring, Modeling and Management*, Merida, Mexico, CD-ROM, March, 2003.

Cartwright, N., P. Nielsen and O. Z. Jessen, Swash and near-shore water table dynamics, *Proc. 28th Intl. Conf. on Coastal Engineering*, ASCE, Cardiff, Wales, 1006-1015, July 9-12, 2002.

Cartwright, N. and P. Nielsen, Groundwater Dynamics and Salinity in Beaches., *Proc. Coasts and Ports 2001, 15th Australasian Coastal and Ocean Engineering Conference*, Gold Coast, Australia., 441-446, September 25-28, 2001.

Cartwright, N. and P. Nielsen, Groundwater Dynamics and Salinity in Coastal Barriers, *Proc. 1st Intl. Conf. on Salt Water Intrusion and Coastal Aquifers - Monitoring, Modeling and Management*, Essaouira, Morocco, CD-ROM., April 23-25, 2001.

Table of Contents

Chapter 5 – Water table wave dispersion: observations vs theory 42

Chapter 6 – Observations and modelling of vertical flow effects 64

Chapter 7 – Observations and modelling of sloping boundary effects 77

List of Figures

List of Tables

List of Symbols

Roman symbols

A	Forcing amplitude, m.
AHD	Australian height datum ($\approx MSL$)
A_o	Driving head amplitude, m.
$B_{\omega,j}$	First harmonic amplitude of the piezometric head at $(x,z) = (0,d)$ for the jth wave mode, m.
BM	Bench mark datum
C	TDS concentration of water sample, g/L.
$c(\psi)$	Capillary capacity ($= d\theta/d\psi$), m^{-1}.
C_{sea}	TDS concentration of sea water, g/L.
d	Mean aquifer depth, m.
D	Hydraulic diffusivity ($=Kd/n_e$), $m^2/[T]$.
d_{50}	Median sediment diameter, mm.
dt	Time step, [T].
dz	Vertical node spacing, m.
F	(Linear) frequency response function ($= \eta/\eta_o$)
g	Acceleration due to gravity, m/s^2.
h	Water table height, m.
H_ψ	Equivalent saturated height of the static capillary fringe, m.
h^*	Piezometric head, m.
h^*_j	Piezometric head of the jth wave mode, m.
h_c	Equivalent saturated height of the capillary fringe, m.
h_{max}	Maximum water table height, m.
h_o	Driving head height, m.
H_{rms}	Offshore, root mean square wave height ($\approx \sqrt{2}\, H_{sig}$), m.
H_{sig}	Significant wave height, m.
h_{SL}	Shoreline height, m.
h_{tide}	Tide height, m.
h_{tot}	Equivalent saturated height of the total moisture ($= h + h_c$), m.
$\overline{h^*_\infty}$	Asymptotic mean inland piezometric head, m.
HWM	High water mark
K	(Saturated) hydraulic conductivity, m/s.
k_j	Wave number for the jth wave mode, m^{-1}.
$k_{m\omega}$	Harmonic wave number ($= k_{m\omega,r} + ik_{m\omega,i}$), m^{-1}.
$k_{m\omega,i}$	Rate of (linear) increase in phase lag
$k_{m\omega,r}$	Amplitude decay rate, m^{-1}.
LWM	Low water mark
m	Harmonic component
m	*van Genuchten* [1980] moisture retention parameter ($= 1 - 1/\beta$)
MSL	Mean sea level
MWS	Mean water surface
n	Drainable porosity ($= \theta_s - \theta_r$), vol/vol.
n_ω	Complex effective porosity

p	Gauge pressure, Pa.
$R_{\omega,j}$	First harmonic amplitude of the *j*th wave mode, m.
RL	Runup limit
$R_{m\omega}$	Harmonic (Fourier) amplitude, m.
S	Storage coefficient
S_e	Effective saturation, vol/vol.
SL	Shoreline
S_s	Specific storage (= $\rho g(\alpha_m + n\beta_w)$), m^{-1}.
SWI	Salt-fresh water interface
SWS	Still water surface
t	Time, [T].
T	Oscillation period, [T].
T_p	Characteristic time scale of storm duration, [T].
Ui	Aquifer recharge rate/infiltration velocity, m/s.
w	Vertical velocity, m/s.
x	Horizontal (shore-normal) coordinate, m.
x_{SL}	Shore-normal shoreline location, m.
z	Vertical coordinate, m.
z_{sand}	Sand surface elevation, m.

Greek symbols

α	*van Genuchten* [1980] moisture retention parameter, m^{-1}.
α^d	*van Genuchten* moisture retention parameter for the *drying* curve, m^{-1}.
α_m	Compressibility of the aquifer matrix, Pa^{-1}.
α^w	*van Genuchten* moisture retention parameter for the *wetting* curve, m^{-1}.
β	*van Genuchten* [1980] moisture retention parameter
β_F	Beach face slope, radians.
β_w	Compressibility of water, Pa^{-1}.
ε	Beach slope perturbation parameter (= $kA\cot\beta_F$)
$\phi_{m\omega}$	Harmonic (Fourier) phase, radians.
η	Water level elevation, m.
η_o	Driving head elevation, m.
$\eta^{+`}$	water table overheight above *MSL*, m.
$\overline{\eta}$	Time-mean water level, m.
$\overline{\eta_\infty}$	Asymptotic inland water table over height, m.
ν_f	Viscosity of fresh water, m^2/sec.
ν_s	Viscosity of salt water, m^2/sec.
θ	Moisture content, vol/vol.
θ_r	Residual moisture content, vol/vol.
θ_s	Saturated moisture content, vol/vol.
ρ	Density of the fluid, kg/m^3.
ρ_f	Density of fresh water, kg/m^3.
ρ_s	Density of salt water, kg/m^3.
ω	Angular frequency, rad/[T].
ψ	Suction pressure head, m.
ζ	*van Genuchten* hysteresis ratio (= α^w/α^d)

Chapter 1 – Introduction

Coastal aquifers form an integral part of the water resources available for coastal cities, towns and communities around the world. Of these aquifers, beaches make up a significant portion of them, providing the interface between salty ocean water and fresh aquifer water. The details of the physical processes occurring in this zone of mass exchange (salt and nutrients) and mixing are the focus of this research.

This thesis examines the influence of oceanic oscillations (tides and waves) on the exchange processes occurring at the ocean-beach interface. The ocean-induced beach groundwater hydrodynamics will determine the temporal and spatial variation in the degree of saturation of a beach face which has been linked to sediment mobility on the beach face.

A significant proportion of this project involved the conduction of extensive field and laboratory experiments, compiling and adding to, a comprehensive database on beach groundwater dynamics and salinity. The database is used throughout the thesis to test currently available theories and models, the shortcomings of which assist in the identification of previously neglected processes, steering the direction of this research.

In Chapter 2, the reader is provided with an introduction to the beach groundwater environment via an overview of relevant terminology and definitions that will be used throughout. Field observations of beach groundwater dynamics are presented in Chapter 3, drawing the reader's attention to certain processes which are investigated further in later chapters.

In Chapter 4 the influence of the capillary fringe on an oscillating water table is discussed from experimental and modelling perspectives. Chapter 5 details observations of water table wave dispersion in the field and laboratory which are then used to test existing small amplitude dispersion relation theories. Experimental observations from a 2D sand flume with a vertical interface are used to discuss the influence of both vertical flow effects and capillarity on the propagation of water table waves in Chapter 6. In Chapter 7 the same flume is used to examine the influence of a sloping interface on the nature of water table waves including the generation of higher harmonic components and increased overheight relative to the vertical boundary case.

In Chapter 8 the additional mass flux into a coastal aquifer as result of infiltration from wave runup is investigated through field, laboratory and numerical experiments. The influence of the dynamic beach groundwater system on the salinity structure is then discussed in Chapter 9 based upon field observations. Finally, conclusions and directions for future research are outlined in Chapter 10.

Chapter 2 – The beach groundwater system: terminology and definitions

2.1 Introduction

This chapter will provide the reader with a general picture of the beach groundwater system and its forcing, the details of which are the focus of this thesis. Oceanic forcing is introduced first followed by a description of the beach aquifer. Observations of beach groundwater dynamics in the field are presented in Chapter 3.

A descriptive overview of the terminology and definitions used throughout this thesis is presented below.

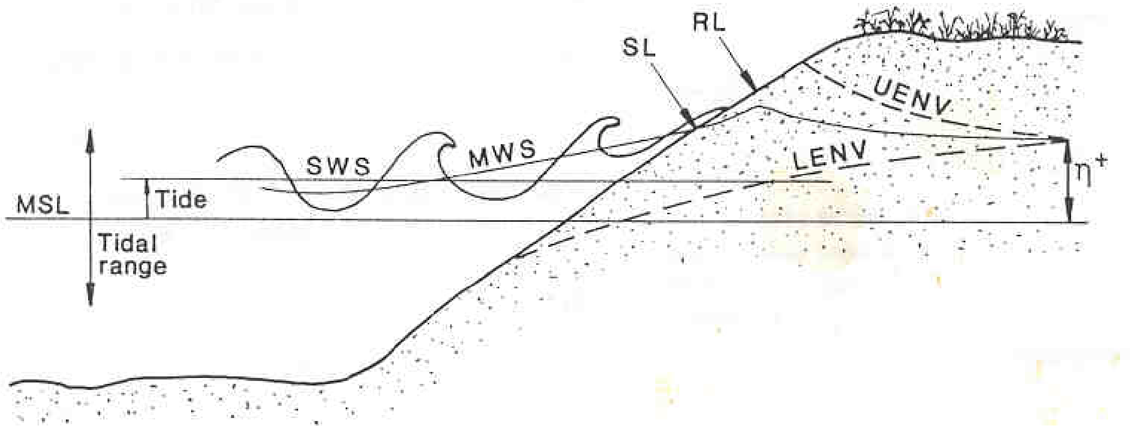

Figure 2.1: Schematic of the ocean forcing of coastal aquifers. *MSL* = *M*ean *S*ea *L*evel, *SWS* = *S*till *W*ater *S*urface, *MWS* = *M*ean *W*ater *S*urface, *SL* = *S*hore*L*ine, *RL* = *R*unup *L*imit. *LENV* and *UENV* are the lower and upper bounds of the water table oscillation envelope. η^+ = water table overheight above *MSL* generated by oceanic forcing. From *Nielsen* [1999a].

2.2 Oceanic forcing

Figure 2.1 schematically illustrates the nature of the oceanic forcing of coastal aquifers, which is made up of a combination of fluctuations occurring over a range of magnitudes and frequencies.

2.2.1 Tides

Ocean tides cause the still water surface (*SWS*) to oscillate about mean sea level (*MSL*) over a range of time scales. For the present study region (south-east Queensland and northern New South Wales, cf. Figure 3.1), the dominant tidal constituent is the semi-diurnal constituent (12.25hours) with significant a contribution from the diurnal constituent (24.5hours). A neap-to-spring variation (14days) is also present due to the interaction of various constituents. Figure 2.2 shows the observed tidal signal from the Tweed Offshore tide gauge (see Figure 3.1 for gauge location), which is dominated by the semi-diurnal constituent (spring tide amplitudes of the order 1m) with a slight diurnal oscillation (approximately 10 to 30cm).

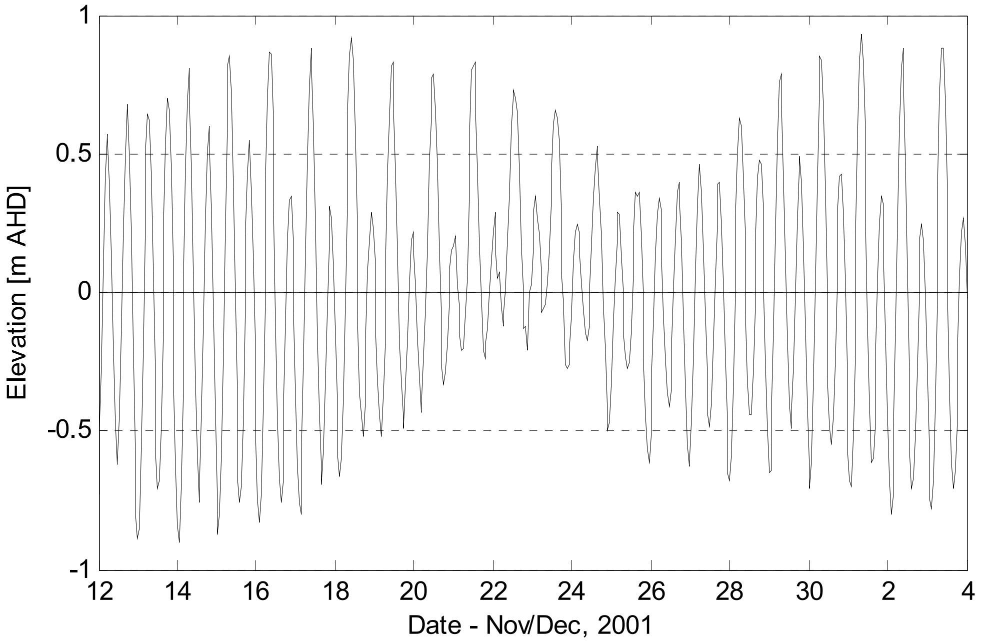

Figure 2.2: Typical tidal signal for northern New South Wales and south-east Queensland. Data collected from the Tweed Offshore tide gauge courtesy of the Manly Hydraulics Laboratory.

2.2.2 Waves

Superimposed upon the tide are wind driven waves and/or swell that vary in both magnitude and frequency in response to the prevailing weather patterns. Wind generated waves therefore influence beach groundwater dynamics in various ways. Those influences cannot be neglected, as this can severely limit the applicability of a given model.

2.2.2.1 Time averaged effect of waves

The time averaged effect of wave breaking in the surf zone is the generation of wave setup due to the decay of radiation stresses with decaying wave height [*Longuet-Higgins*, 1964] resulting in a non-horizontal mean water surface (see *MWS* in Figure 2.1). Using the radiation stress theory of *Longuet-Higgins* [1964] and linear wave theory, *Bowen et al.* [1968] obtained a solution that predicts the wave setup to grow linearly from the break point to the shoreline. However, contrary to this, field measurements of the mean water surface at numerous locations along the New South Wales coast [*Nielsen et al.*, 1988; *Hanslow and Nielsen*, 1993] indicate that the mean water surface is upwardly concave in nature as shown in Figure 2.3. A sharp increase in setup is seen just seaward of the shoreline, defined after *Nielsen et al.* [1988] as the intersection of the *MWS* with the beach face (cf. Figure 2.1).

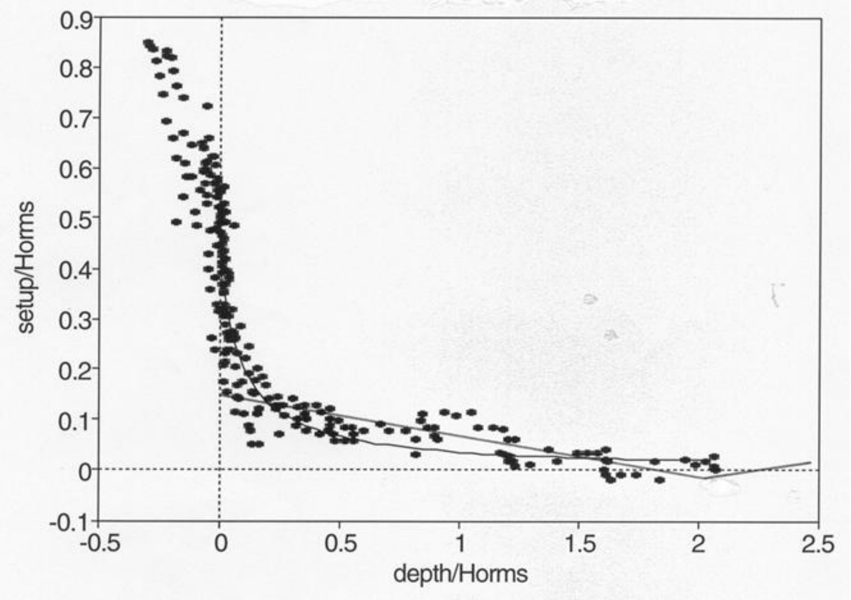

Figure 2.3: Setup profile in a natural surf zone. Measurements from South Beach, Brunswick Heads 22/6/1989 [from *Hanslow and Nielsen*, 1993].

From the data shown in Figure 2.3, *Hanslow and Nielsen* [1993] estimated that the shoreline setup (above the tidal level) to be approximately 40% of the offshore, root mean square wave height, an amount that cannot be neglected in environments where wave action is significant. *Turner et al.* [1997] demonstrated that if the time averaged wave effects (i.e. additional shoreline setup) were ignored, then their model of a northern NSW beach groundwater system overestimated groundwater discharge to the ocean by a factor of two.

Nielsen et al. [1988] also demonstrated the significance of time averaged wave effects with field data from a narrow sand isthmus. The water table overheight at the exposed ocean coast (wave and tide forcing) was observed to be substantially higher than at the sheltered coast (tidal forcing only). The consequence of this being that a steady groundwater flow towards the sheltered side exists, an important consideration in terms of groundwater contaminant transport to the sheltered waters [cf. *Nielsen*, 1999a].

2.2.2.2 Instantaneous wave effects

In more recent years, a research focus has been directed towards the high frequency response of beach groundwater to individual swash events [e.g. *Wadell*, 1976; *Wadell*, 1980; *Hegge and Masselink*, 1991; *Baldock and Holmes*, 1996; *Turner and Nielsen*, 1997]. The dynamic coupling of the swash zone and aquifer plays a crucial role in the transfer of mass and pressure across the beach face which in turn has implications for processes such as sediment mobility and salt water intrusion. The above studies measured pressure fluctuations within a few tens of centimetres from the sand surface and identified a near instantaneous response of the water table ($p = 0$) to overtopping swash events due to the presence of the capillary fringe (cf. section 2.3.2) above the water table.

2.3 The beach aquifer

2.3.1 Basic aquifer parameters

The water table, or phreatic surface, is defined as the surface along which the pressure is atmospheric, i.e. with a gauge pressure, $p = 0$. The movement of water within the porous medium is dependent upon two primary hydraulic parameters: (1) the storage coefficient, which for an unconfined aquifer with no capillary fringe is defined as the drainable porosity, n, and (2) the hydraulic conductivity, K.

2.3.2 The capillary fringe

Due to surface tension of the fluid and the (small) interstitial pore spaces, moisture will rise above the water table due to capillary action [e.g. *Fetter*, 1994]. This region above the water table is generally referred to as the partially saturated zone and the capillary fringe is defined as the equivalent region of saturated moisture content [e.g. *Silliman et al.*, 2002].

The capillary fringe plays an important role in the transfer of mass from the sand surface to the saturated zone as mentioned in section 2.2.2.2. It has been shown that the influence of the capillary fringe on periodic water table oscillations increases at higher frequencies [e.g. *Barry et al.*, 1996; *Li et al.*, 1997; *Nielsen and Turner*, 2000]. A detailed investigation into the effects of capillarity on an oscillating water table, including an overview of the complex effective porosity concept of *Nielsen and Perrochet* [2000a,b], is given in Chapter 4.

2.3.3 Water table waves

Oceanic oscillations will induce oscillations in the coastal water table, represented in Figure 2.1 by the oscillation envelope *UENV* and *LENV*. As the wave propagates landward its amplitude decays and a phase lag develops. The propagation of these oscillations will be influenced by a variety of processes such as vertical flow [e.g. *Dagan*, 1967; *Parlange et al*., 1984; *Nielsen et al.*, 1997] and capillarity [e.g. *Parlange and Brutsaert*, 1987; *Barry et al.*, 1996; *Li et al.*, 1997; *Li et al.*, 2000a]. Chapter 5 provides a detailed discussion of the comparison between observed water table wave dispersion and that predicted by existing theories.

The form of the water table wave generated in response to oceanic fluctuations will be influenced by the sloping beach face boundary condition [e.g. *Nielsen*, 1990; *Li et al.*, 2000b]. This will be discussed in Chapter 7.

2.3.4 The water table exit point

Another important factor influencing the boundary condition at the beach face is the formation of a seepage face. If the rate of fall of the ocean water level - the runup limit - is faster than the rate of drainage of the beach aquifer then it will become decoupled from the water table exit point and a seepage face will form. The exit point is observable in the field as the boundary between the seaward glassy, saturated sand surface and the landward, matted (dry) sand surface as shown in Figure 2.4.

Figure 2.4: The water table exit point and seepage face.

Chapter 3 – Beach groundwater dynamics: observations from the field

3.1 Introduction

As introduced in Chapter 2, the hydrodynamic climate at the interface between ocean and aquifer is complex, both in the nature of the oceanic forcing and in the nature of the boundary condition at the beach face. For science to understand, and replicate through modelling, the natural system, there is a need for ongoing field observations to help achieve this aim.

Groundwater dynamics in beaches have long been observed, for example, *Grant* [1948], *Emery and Foster* [1948], *Duncan* [1964], *Lanyon et al.* [1982], *Nielsen* [1990], *Kang et al.* [1994a]; *Turner et al.* [1997] and *Raubenheimer et al.* [1999]. In continuation of this previous work, the present study involved a field measurement campaign conducted at several locations in south-east Queensland and northern New South Wales as shown in Figure 3.1. The data collected from these experiments, in addition to existing databases for the region [cf. *Kang et al.*, 1994a; *Nielsen and Voisey*, 1998], is used to test current models and theory and to assist in obtaining additional insight into the physical processes occurring at the beach face.

This chapter provides an overview of the present field campaign including details of measurements and some general findings. The experimental data can be found in Appendix A.

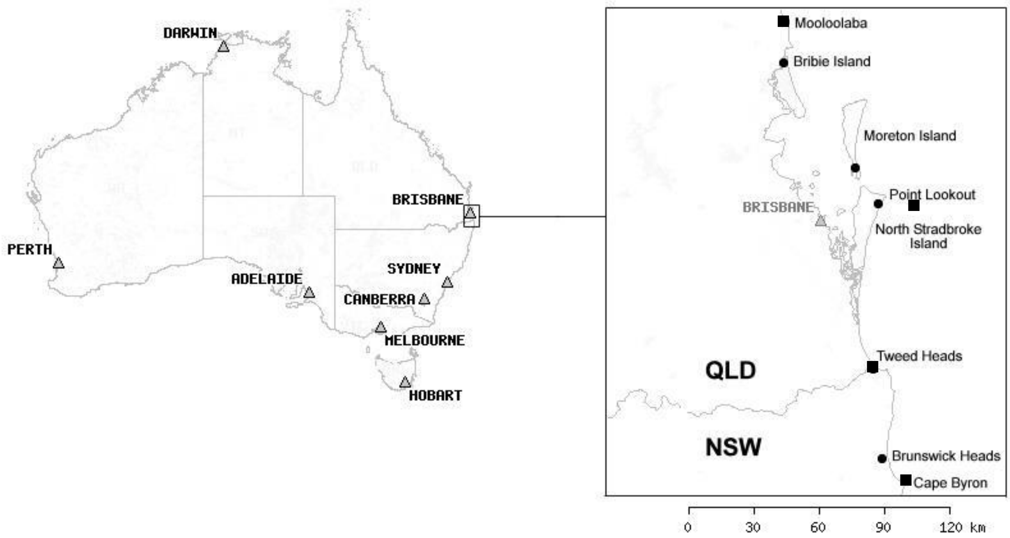

Figure 3.1: Location map of field sites (•) and nearby wave and tidal monitoring stations (■).

3.2 Field measurements

Figure 3.2 shows a typical field monitoring transect, running shore-normal from seaward of the low water mark to a point landward (out of view) where the tidal water table fluctuations become immeasurable. In the intertidal zone, clear, polycarbonate stilling wells with external measuring tape (see Figure 3.3) were used to measure the near-shore and swash zone mean water levels [cf. *Nielsen*, 1999b]. To eliminate oscillations in response to individual wave events, the stilling wells were damped with geo-textile filter cloth to a response time of the order of 100sec. Landward of the high water mark, piezometers screened at the base were installed by hand augering and subsurface piezometric heads monitored using a dip meter (see Figure 3.4).

Figure 3.2: Typical field transect (to the right) used to monitor an aquifers response to periodic, ocean forcing. Photo taken of an experiment conducted just south of Point Lookout on North Stradbroke in south-east Queensland.

Figure 3.3: Stilling well used to measure the near shore and swash zone mean water level.

Figure 3.4: Dip meter and piezometer used to monitor subsurface piezometric head levels.

The monitoring transects were installed around low tide, ensuring measurability during the entire monitoring period. Once installed, the well tops were surveyed in to a local bench mark which was, if available, surveyed in to a nearby survey point of known level relative to the Australian Height Datum (AHD is approximately mean sea level). If no AHD marker was available the most seaward stilling well was fitted to tidal observations from the nearest tide gauge (of known AHD). The beach face profile was also surveyed, and wave and tide data from the nearest regional monitoring station (cf. Figure 3.1) collected post-experiment from the appropriate controlling body.

3.3 General observations

Figure 3.5 shows observations of groundwater and near-shore water levels during a 24.5hour diurnal tidal period from Point Lookout on North Stradbroke Island. The dominant semi-diurnal fluctuations (cf. section 2.2.1) are clearly apparent. The effect of wave setup through the surf zone is also visible upon comparison of the tidal and shoreline elevation curves where the shoreline lies above the tide. The difference in elevation between the two is of the order predicted by *Hanslow and Nielsen*'s [1993] 'rule of thumb', $h_{SL} \approx h_{tide} + 0.4H_{rms}$.

3.3.1 Water table wave dispersion and ocean generated overheight

As shown in Figure 3.5, the water table wave is driven into the aquifer and its amplitude decays and a phase lag develops up until a point about 125m landward of the mean shoreline position where any aquifer response to the tide becomes immeasurable. At this point the overheight of the water table above mean sea level is of the order 1.2m. Such a significant amount should be considered in larger, catchment scale coastal aquifer models which tend to use mean sea level as its ocean boundary condition.

3.3.2 Non-linear filtering effect of the sloping boundary

Also illustrated in Figure 3.5 is the non-linear filtering effect of the sloping boundary [e.g. *Lanyon et al.*, 1982; *Nielsen*, 1990]. The temporal rise in groundwater levels is steeper than the fall due to the beach filling more easily than it can drain. This induces the generation of higher harmonics at the boundary, further complicating the beach groundwater boundary condition. The effect of the sloping boundary on the generation of water table waves is discussed in detail in Chapter 7.

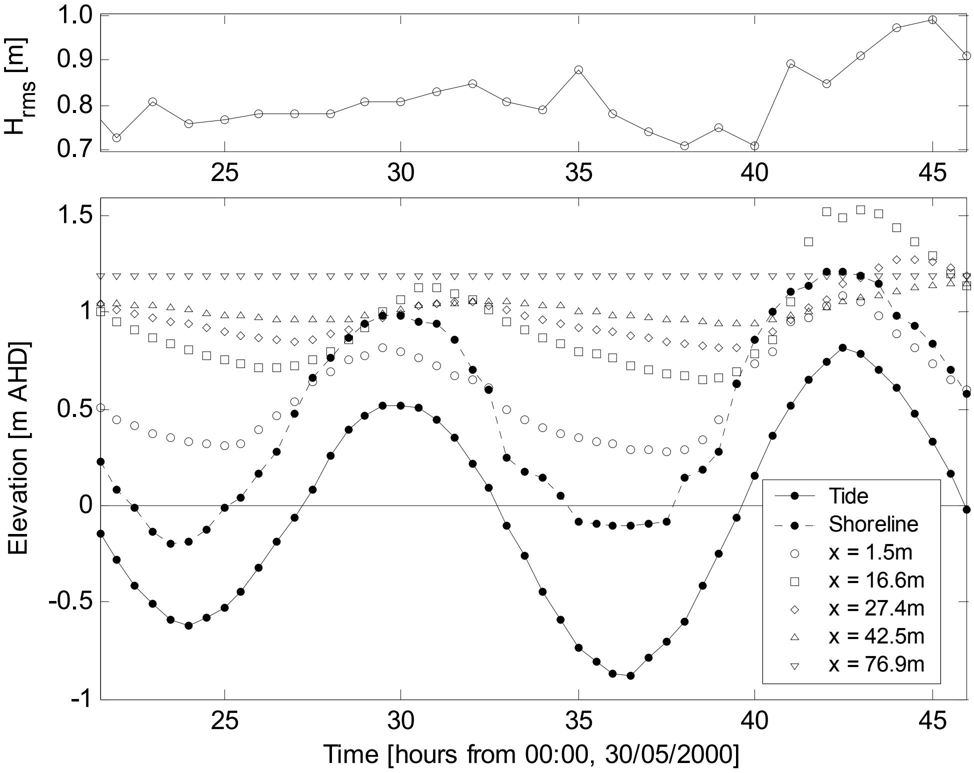

Figure 3.5: Time series of the root mean square wave height, H_{rms} (top panel), tide, shoreline and groundwater elevations. Observations from Point Lookout, North Stradbroke Island, May 2000. Indicated x coordinates are relative to the mean shoreline position. Tide and wave data courtesy of EPA Queensland.

3.3.3 Infiltration from wave runup

Another interesting observation in beaches subject to wave as well as tidal forcing is the "hump" in the water table profile observed on the rising tide [e.g. *Kang et al.*, 1994b]. Figure 3.6 shows the water table profile at quarter period intervals for the same dataset shown in Figure 3.5. The "hump" is clearly apparent for the rising tide phase as the wave action encroaches upon drier, partially saturated sand in the upper reaches of the intertidal zone. With the falling tide however, the hump disappears as the wave action moves seaward, acting on sand saturated from the previous high tide. This phenomenon of aquifer recharge due to infiltration from wave runup is investigated in detail in Chapter 8.

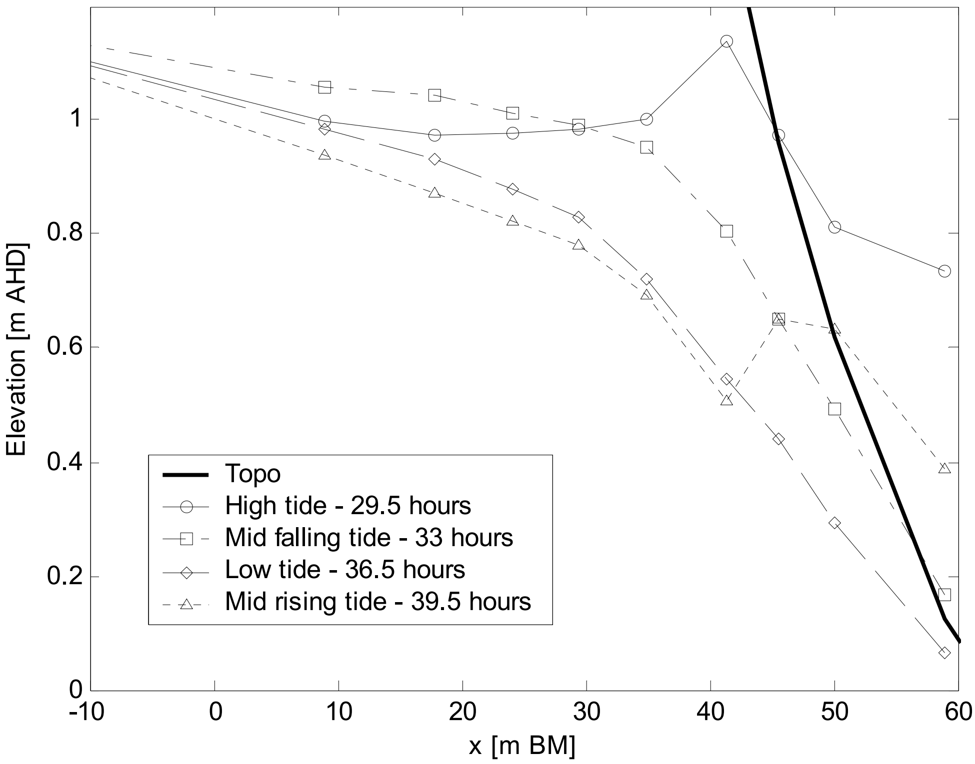

Figure 3.6: Evolution of groundwater level profile during a semi-diurnal tidal cycle. Observations from Point Lookout, North Stradbroke Island, May 2000.

3.3.4 Rainfall effects

Figure 3.7 depicts observations collected during a one in twenty-five year storm at Brunswick Heads (25-27th June, 2003). A short period of intense rainfall (panel (a)) was experienced, during which the wave height (panel (b)) steadily increased and continued to do so even after the rainfall had abated. Visual evidence of the influence of rainfall was seen during the low tide ($t \approx$ 26.5days) where, despite the low tide and corresponding low runup limit, the exit point remained near the upper reaches of the inter-tidal zone (panel (c)). This was due to the water table lying just below the sand surface and the moisture content above the water table being almost saturated to the sand surface due to capillary rise (cf. section 2.3.2). Therefore, the additional water required at the surface to bring the water table to the sand surface was small and was easily provided by the rainfall experienced. The process of moisture exchange in this scenario is discussed in detail in Chapter 4.

However, despite such strong evidence of the influence of rainfall in the inter-tidal zone, efforts to separate the rainfall influence on the inland groundwater levels proved difficult. *Vigneaux* [2003] performed detailed analysis and modelling of the data shown in Figure 3.7 and was unable to conclusively separate out the individual contribution of the rainfall. The large increase in wave height also provided a significant contribution to the observed groundwater signal and was cited by *Vigneaux* [2003] as a dominant complicating factor along with the uncertainty in aquifer parameters.

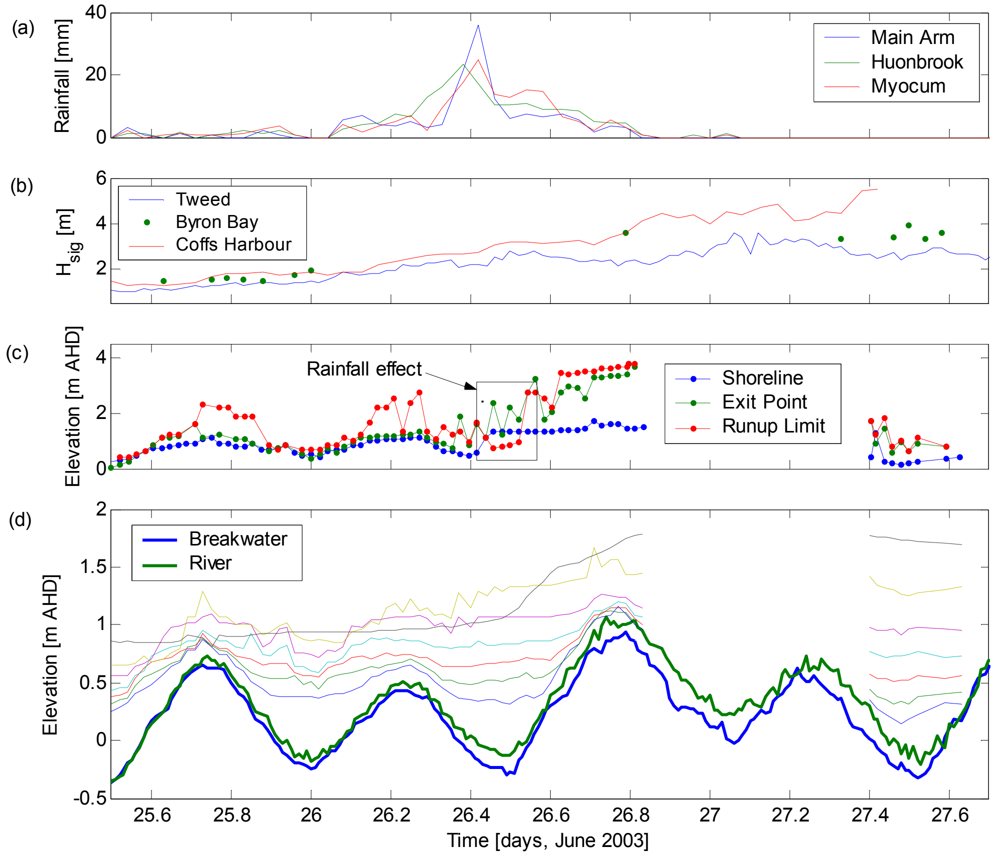

Figure 3.7: Field observations from Brunswick Heads - June 25 – 27, 2003.

3.4 Harmonic analysis

Throughout this thesis harmonic (Fourier) analysis [e.g. *Kreysig*, 1999] is used to extract amplitudes and phases from the observed water table fluctuations facilitating the comparison of observations with theory. The analysis is based on the decomposition of the observed, periodic signal into the trigonometric series,

$$\eta(x,t)=\overline{\eta}\left(x\right)+\sum_{m=1}^{\infty}R_m(x)\cos\left(m\omega t-\phi_m(x)\right) \tag{3.1}$$

where, $\eta(x,t)$ is the water level elevation, $\overline{\eta}\left(x\right)$ is the mean water level, $R_m(x)$ and $\phi_m(x)$ are the harmonic amplitudes and phases respectively, $\omega = 2\pi/T$ is the angular frequency with T the period, t denotes time, x the shore normal coordinate and m the harmonic component.

3.5 Acknowledgements

I would like to acknowledge the following people who assisted with the field experiments in the present study: Hokkie Blogg, Dave Callaghan, Zac Couper, Aaron Coutts-Smith, Michael Hughes, Graham Illidge, Brandon Kieseker, David Mitchell, Jesper Nielsen, Peter Nielsen, Wesley Nielsen, Julien Perrochet, Pierre Perrochet, Claudia Syhre, Stefan Szylkarski, Ian Teakle, Matt Tomkins, Koen van der Waal, Andy West, Nienke Wiersme and Nina Wittlings.

Chapter 4 – The influence of the capillary fringe on an oscillating water table

4.1 Introduction

Due to capillary rise in a porous medium there will be a certain amount of moisture present above the water table known as the capillary fringe (cf. Figure 4.1). By considering the force balance between the surface tension of the fluid and the weight of water in the capillary it can be shown that the height to which moisture will rise in the capillary tube at equilibrium is inversely related to the radius of the capillary tubes [e.g. *Hillel*, 1980]. That is, porous media with small pores (e.g. clays) will experience higher capillary rise above the water table than media with larger pores (e.g. gravels).

The capillary fringe will be represented here as an equivalent (static) saturated height, H_ψ, above the water table (cf. Figure 4.1) defined as,

$$H_\psi = \int_h^\infty \frac{\theta - \theta_r}{\theta_s - \theta_r} d\psi \tag{4.1}$$

with θ the moisture content, θ_s the saturated moisture content, θ_r is the residual moisture content, defined as the amount of water remaining when drained by gravity alone and ψ is the (suction) pressure head. This representation is considered reasonable for beach sands found in northern NSW and south-east Queensland whose moisture retention profiles are almost step curves (cf. Figure 4.5). Such a representation however, may have limited applicability for soils which have a gradual transition from saturated to residual moisture contents.

The presence of a capillary fringe will influence water table oscillations. Using the *Green and Ampt* [1911] 'capillary tube' approximation of the capillary fringe, *Parlange and Brutsaert* [1987] derived a capillary correction term for the Boussinesq groundwater flow equation. Using this modified Boussinesq equation, *Barry et al.* [1996] obtained an analytical solution for a periodic boundary condition and showed that the influence of the capillary fringe on water table oscillations increases with oscillation frequency.

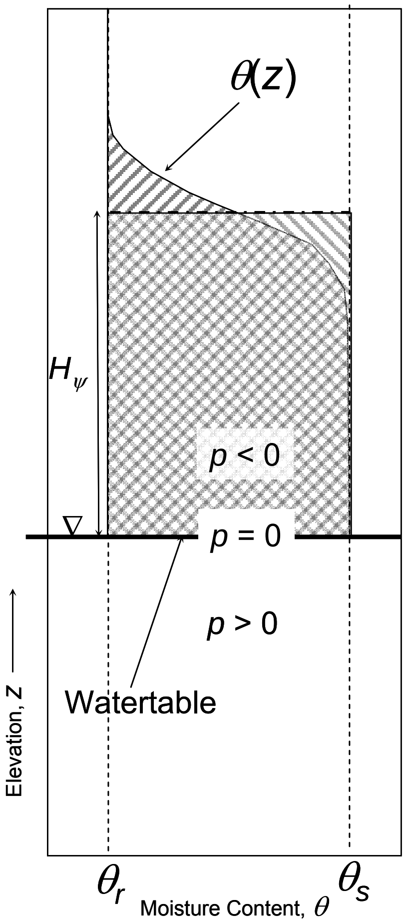

Figure 4.1: Schematic illustration of the moisture distribution above the water table.

Li et al. [1997] also used the *Green and Ampt* [1911] approximation of the capillary fringe to derive a modified kinematic boundary condition for their numerical boundary element model. They concluded that without the correction term their model was unable to reproduce the propagation of high frequency water table waves as observed in the field [e.g. *Wadell*, 1976; *Hegge and Masselink*, 1991; *Turner and Nielsen*, 1997].

Nielsen and Perrochet [2000a,b] tested the validity of the non-hysteretic *Green and Ampt* [1911] model against observations from a sand column subject to simple harmonic forcing at its base. The comparisons were shown to be poor although some improvement was achieved by allowing the hydraulic conductivity in the fringe to be smaller than in the saturated zone. *Nielsen and Perrochet* [2000a,b] suggested the use of a complex effective porosity, n_ω, to describe the dynamic relationship between the oscillating water table and capillary fringe. Additional sand column experiments by *Nielsen and Turner* [2000] over a wider range of oscillation frequencies further highlighted the inadequacies of the *Green and Ampt* [1911] approximation.

In this chapter, the experimental database of *Nielsen and Turner* [2000] is extended to further investigate the implications of a truncated capillary fringe (i.e. proximity to the sand surface) on the water table oscillations. Such an investigation is important for the water table dynamics beneath a sloping beach face where the water table lies close to the sand surface.

The concept of a complex effective porosity is described in section 4.2, followed by a review of the previous sand column experiments in section 4.3. Section 4.4 discusses the new "truncated fringe" experiments and their implications for natural systems. In section 4.5, a numerical model solving the well known *Richards'* equation [1931] is used to examine the effect of various soil moisture-pressure relationships on the results of simulations based on the sand column experiments.

4.2 The concept of a complex effective porosity, n_ω

Using the Dupuit-Forcheimer shallow aquifer assumption of hydrostatic pressure and considering only one dimension for simplicity, the unconfined groundwater flow equation can be derived based upon the principle of mass conservation and Darcy's law,

$$n\frac{\partial h_{tot}}{\partial t} = n\frac{\partial h}{\partial t} + n\frac{\partial h_c}{\partial t} = \frac{\partial}{\partial x}\left(hK\frac{\partial h}{\partial x} \right) \qquad (4.2)$$

where n is the drainable porosity, K is the (saturated) hydraulic conductivity, h is the water table height, $h_{tot} = h + h_c$ is the equivalent saturated height of the total moisture with h_c the equivalent saturated height of the capillary fringe.

In order to obtain an equation with only a single dependent variable, h, *Nielsen and Perrochet* [2000a,b] introduced the concept of a complex effective porosity, n_ω, defined as,

$$n_\omega \frac{\partial h}{\partial t} = n \frac{\partial h_{tot}}{\partial t} \tag{4.3}$$

which, upon substitution into (4.2), leads to the water table equation in the same form as the Boussinesq equation,

$$n_\omega \frac{\partial h}{\partial t} = \frac{\partial}{\partial x}\left(hK \frac{\partial h}{\partial x} \right) \tag{4.4}$$

where, in general,

$$n_\omega = n_\omega \left(n, K, H_\psi, \frac{\partial h}{\partial t}, \dots\dots\dots \right) \tag{4.5}$$

The data of *Nielsen and Turner* [2000] refined this relation for the case of simple harmonic oscillations to,

$$n_\omega = n_\omega \left(n, \frac{\omega H_\psi}{K}, z_{sand} - h_{\max} \right) \tag{4.6}$$

The reason that n_ω is complex in nature is that fluctuations in the total moisture, h_{tot}, are both damped and delayed relative to those in the water table, h (cf. Figure 4.2). The complex effective porosity mathematically accounts for the damping through its magnitude, $|n_\omega|$, and for the phase lag through its argument, $Arg\{n_\omega\}$.

4.2.1 The Green and Ampt [1911] capillary fringe model

The *Green and Ampt* [1911] approximation of the capillary fringe assumes that the capillary fringe is completely saturated with a fixed suction head, $-H_\psi$, at the top. Under these assumptions, the corresponding complex effective porosity will be [*Nielsen and Turner*, 2000],

$$n_\omega = \frac{n}{1 + i\dfrac{n\omega H_\psi}{K}} \tag{4.7}$$

where ω is the angular frequency and H_ψ is the equivalent, saturated capillary fringe height defined by (4.1). This equation can be obtained upon re-arrangement of the modified Boussinesq equation derived by *Parlange and Brutsaert* [1987] (their equation 8).

Examination of equation (4.7) shows that in the limit, $n\omega H_\psi/K \rightarrow 0$, the influence of the capillary fringe disappears, i.e. $n_\omega \rightarrow n$. This occurs, for example, when the forcing period is long and $\omega \rightarrow 0$ and/or when the sand is coarse and $H_\psi \rightarrow 0$. The complex effective porosity concept is therefore in general agreement with previous findings that the influence of the capillary fringe increases with increasing oscillation frequency [e.g. *Barry et al.*, 1996; *Li et al.*, 1997; *Li et al.*, 2000a].

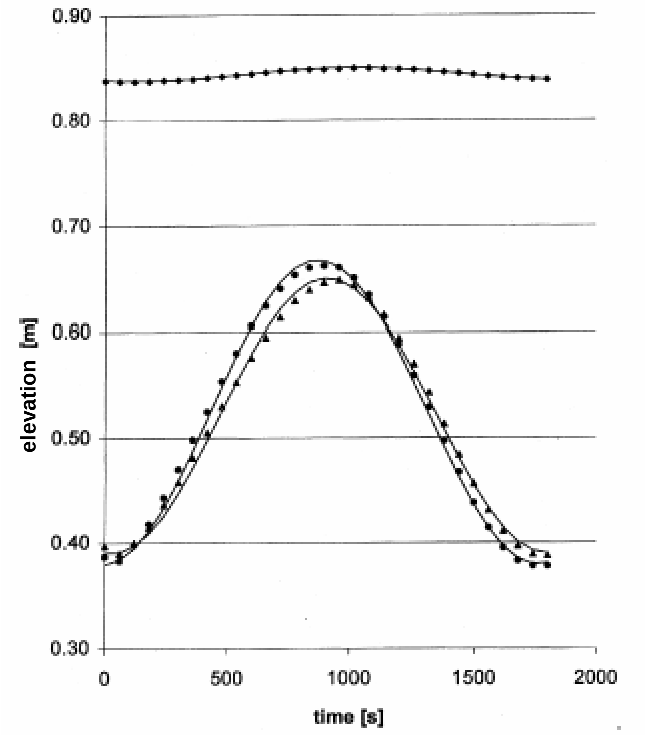

Figure 4.2: Measured variation of the piezometric head, $h^*(z,t)$ (▲), water table height, $h(t)$ (●), and the total moisture, $h_{tot}(t)$ (♦). T = 29min, d_{50} = 0.20mm. Symbols are the actual values, curves are the simple harmonic parts. From *Nielsen and Perrochet* [2000a,b], their Figure 4.

4.3 1D Sand column experiments

In this section the sand column experiments of *Nielsen and Perrochet* [2000a,b] and *Nielsen and Turner* [2000] are reviewed (a tabular summary of the data is given in Appendix B.1.) A description of the experimental procedure and analysis is provided along with results from new sand column experiments investigating the effect of a truncated capillary fringe on an oscillating water table.

Figure 4.3 depicts the sand column of dimensions 2m high with a 15cm square cross-sectional area. At the base is a clear water cell connected to an overflow reservoir which delivers simple harmonic head oscillations to the base of the column. The top of the column was loosely covered with plastic to minimise evaporation. The driving head in the clear water reservoir and the piezometric head at one of several possible locations in the (saturated) sand was monitored using pressure transducers connected to horizontal stainless steel piezometer tubes (OD 5mm) extending 65mm into the sand.

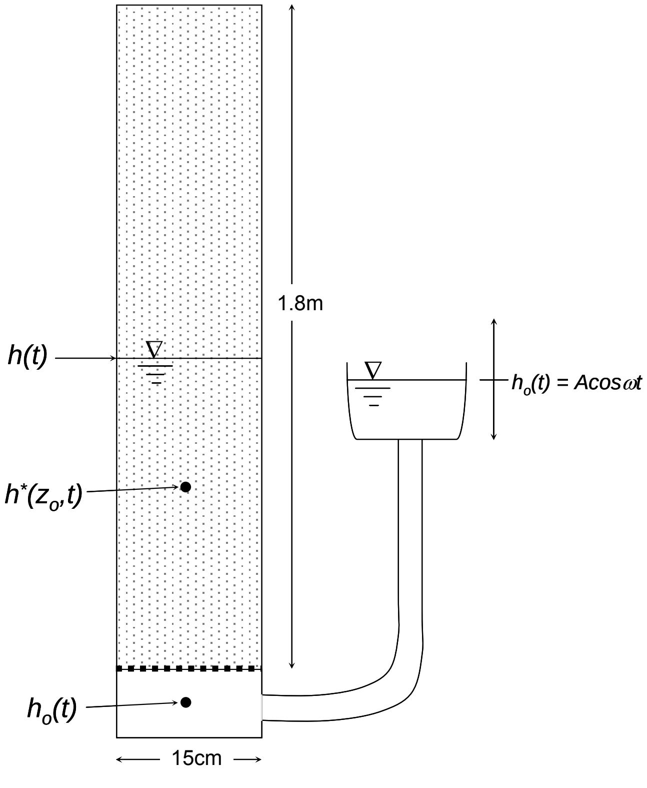

Figure 4.3: Schematic of the sand column.

4.3.1 Sediment characteristics

Nielsen and Turner [2000] present experimental effective porosities obtained for three different sediment types over the range of oscillation periods: 10sec < T < 7hours. The sediments used were: (a) d_{50} = 0.082mm glass beads; (b) d_{50} = 0.2mm locally mined quartz sand; (c) d_{50} = 0.78mm coarse sand. The sieve curves for each sediment type are shown in Figure 4.4 indicting the well-sorted nature of each. The first drying curve for each sediment type is shown in Figure 4.5 with all three having rapid transitions from saturated to residual moisture contents.

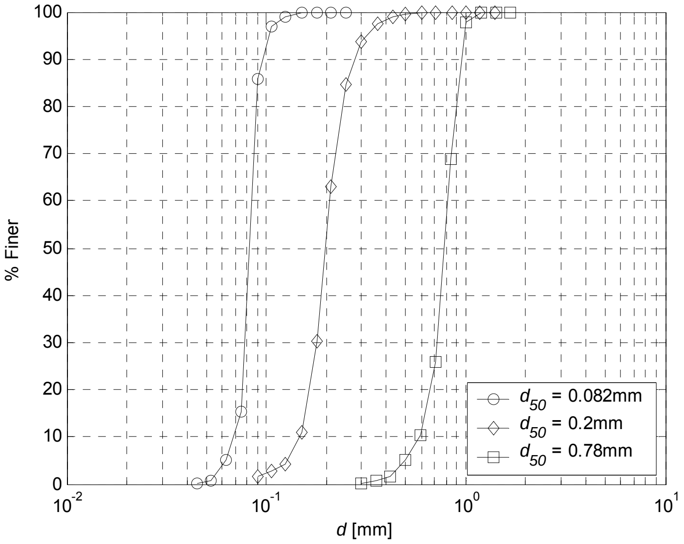

Figure 4.4: Sieve curves for the three sediments used in the sand column.

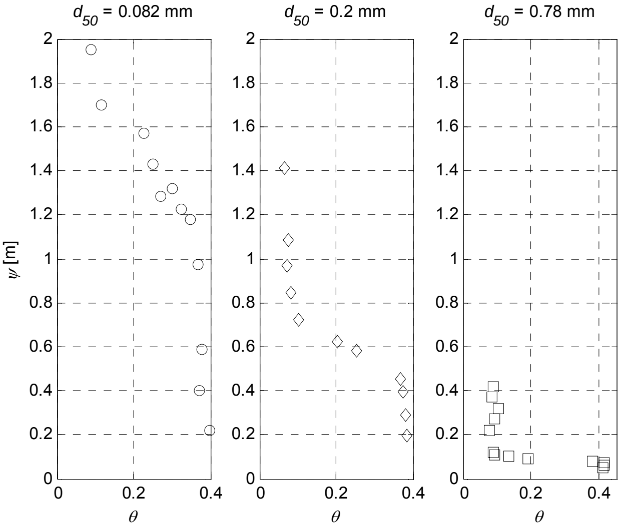

Figure 4.5: Moisture retention curves (first drying) for the three sediments used in the column experiments.

4.3.2 Determination of the water table elevation, $h(t)$

In the presence of vertical flows, and hence non-hydrostatic pressure conditions, direct measurement of the water table is not possible. *Nielsen and Perrochet* [2000a,b] derived the following expression to infer the water table elevation from observations of the clear water driving head and the piezometric head, $h^*(z_o,t)$, from a level z_o somewhere in the saturated zone (i.e. below the minimum driving head level),

$$h(t) = \frac{z_o h_o(t)}{z_o + h_o(t) - h^*(z_o,t)} \tag{4.8}$$

4.3.3 Experimental determination of the complex effective porosity, $n_\omega(\omega)$

Nielsen and Perrochet [2000a,b] describe the method of determining the complex effective porosity from experimental observations of the water table response to simple harmonic forcing. For reference, the procedure is outlined below.

Using continuity and Darcy's law, the flow equation for the sand column shown in Figure 4.3 is,

$$n\frac{\partial h_{tot}}{\partial t} = K\frac{h_o - h}{h} \tag{4.9}$$

Then by employing the definition of the complex effective porosity [cf. equation (4.3)], equation (4.9) can be written as,

$$n_\omega \frac{\partial h}{\partial t} = K\frac{h_o - h}{h} \tag{4.10}$$

Under the assumption of small amplitude oscillations ($A<<d$), equation (4.10) can be linearised to,

$$\frac{\partial \eta}{\partial t} = \frac{K}{n_\omega d}\left(\eta_o - \eta\right) \tag{4.11}$$

which, with a simple harmonic driving head, $\eta_o(t) = A\mathrm{e}^{i\omega t}$, has the solution,

$$\eta(t) = \frac{\eta_o(t)}{1 + i\omega\frac{n_\omega d}{K}} \tag{4.12}$$

i.e. the water table will have the frequency response function, $F(\omega)=\eta(t)/\eta_o(t)$,

$$F\left(\omega\right)=\frac{1}{1+i\omega\frac{n_\omega d}{K}} \tag{4.13}$$

which can be solved for n_ω based on the observed $F(\omega)$. That is,

$$\Re\left(n_\omega\right)=\frac{\sin\left(\phi_{wt}\right)}{\left|F\right|\omega d/K} \tag{4.14}$$

$$\Im\left(n_\omega\right)=\frac{1-\cos\left(\phi_{wt}\right)/\left|F\right|}{\omega d/K} \tag{4.15}$$

where ϕ_{wt} is the phase lag of the water table relative to the driving head, and $|F| = |\eta|/|\eta_o|$ is the magnitude of the water table response with $|\eta|$ and $|\eta_o|$ the amplitude of the water table and driving head respectively. The amplitudes and phases are extracted from the observed time series using harmonic analysis [cf. equation (3.1)].

4.3.4 Comparison of the *Green and Ampt* [1911] model with sand column data

Based on data from a limited range of frequencies (cf. triangles in Figure 4.6), *Nielsen and Perrochet* [2000a,b] concluded that the complex effective porosity was constant with a value,

$$n_\omega = 0.037 - 0.023i \tag{4.16}$$

However, additional experiments by *Nielsen and Turner* [2000] (see Appendix B.1) over a wider range of periods (10sec < T < 7hours) for three different sediment types (cf. Figure 4.4 and Figure 4.5) reveal a distinct frequency dependence of n_ω as shown in Figure 4.6. Based on these observations, *Nielsen and Turner* [2000] proposed the use of an empirical complex effective porosity model analogous to that corresponding to the *Green and Ampt* formulation [equation (4.7)]. The curve fit used in this thesis is given by,

$$n_\omega=\frac{n}{1+2.5\left(i\frac{n\omega H_\psi}{K}\right)^{2/3}} \tag{4.17}$$

The comparison between the *Green and* Ampt model [equation (4.7)] and the data [equation (4.17)] shown in Figure 4.6 highlight two main discrepancies:

1. The *Green and Ampt* [1911] model (— –) predicts $|n_\omega|$ to have an asymptotic slope of -1 whereas the data (——) indicate a slope of -⅔.
2. The asymptotic value of $Arg\{n_\omega\} \approx -\pi/2$ for the *Green and Ampt* model (— –) as opposed to $Arg\{n_\omega\} \approx -\pi/3$ according to the data (——).

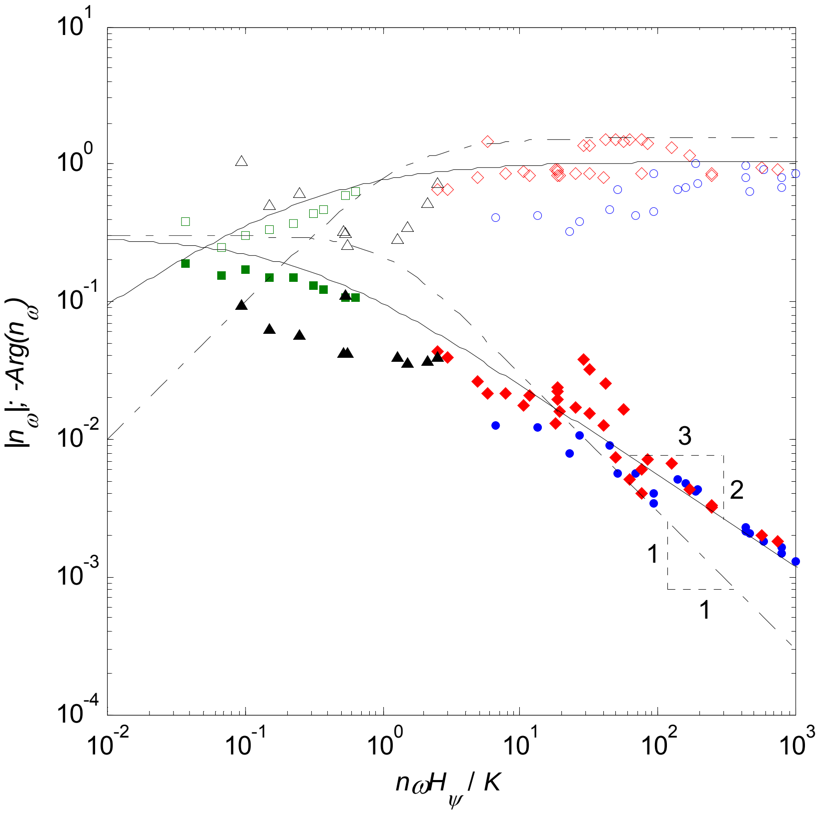

Figure 4.6: Effective porosities determined experimentally by *Nielsen and Turner* [2000] for three different sediments: d_{50} = 0.78mm sand (■, □), d_{50} = 0.2mm sand (♦,◊) and d_{50} = 0.082mm glass beads (•,○). Solid symbols denote $|n_\omega|$ and hollow symbols $-Arg\{n_\omega\}$. The symbols (▲,Δ) denote data from *Nielsen and Perrochet* [2000a,b] for d_{50} = 0.2mm sand. The curves represent the complex effective porosity corresponding to the *Green and Ampt* [1911] model, equation (4.7) (— –) and an analogous curve fit, equation (4.17) (——).

In other words, referring to the definition of n_ω, equation (4.3), as the high frequency limit ($n\omega H_\psi/K \to \infty$) is approached the *Green and Ampt* model tends to over-predict both the damping of the total moisture, $|n_\omega|$, and its phase lag, $Arg\{n_\omega\}$, relative to the corresponding water table quantities. This finding has implications for the propagation of water table waves which is discussed in Chapter 5.

The data shown in Figure 4.6 are limited to three sediment types all being well-sorted in nature (cf. Figure 4.4) with relatively sharp transitions from saturated to residual moisture (cf. Figure 4.5). Such sediment types are typical for the present study region and as such equation (4.17) can be applied with some confidence. Whether or not the application of the model to sediment types with markedly different characteristics (e.g. clays or silty loams which have a more gradual moisture retention curve) is an open question.

4.4 Implications of a truncated capillary fringe

In relation to the present study of beach groundwater, the presence of the capillary fringe will limit the exchange of water between the ocean and aquifer. In particular, for the case of flat beaches where the water table lies just below the sand surface, the sand can still be saturated to the sand surface due to capillary rise. Previous work has shown that if the water table is shallow, lying close to the surface of the porous medium, the amount of drainage occurring under a declining water table will be reduced relative to that experienced for a deep water table [e.g. *Duke*, 1972; *Gillham*, 1984; *Nachabe*, 2002].

In the situation where the water table lies near the surface, a disproportionate relationship exists between the moisture exchange and corresponding change in pressure as illustrated by Figure 4.7 [e.g. *Gillham*, 1984; *Nielsen et al.*, 1988]. The amount of water required to be added to the sand surface to cause the water table to rise to the sand surface is the order of a grain diameter (d_{50} < 1mm for beach sands) in comparison to the change in water table elevation (of the order of a capillary fringe height, $H_\psi \sim 0.5$m for the sands in the present study region). This phenomenon is sometimes referred to as the reverse Wieringermeer effect. This reduction in moisture exchange results in a significantly reduced complex effective porosity which upon inspection of equation (4.3) leads to the substantially reduced storage term,

$$n_\omega = n\frac{\partial h_{tot}}{\partial h} \approx n\frac{d_{50}}{H_\psi} \approx n\frac{0.001}{0.5} \approx 0.002n \qquad (4.18)$$

In this section the extent to which truncation of the capillary fringe limits moisture exchange under periodic forcing is examined via new sand column experiments and the complex effective porosity concept.

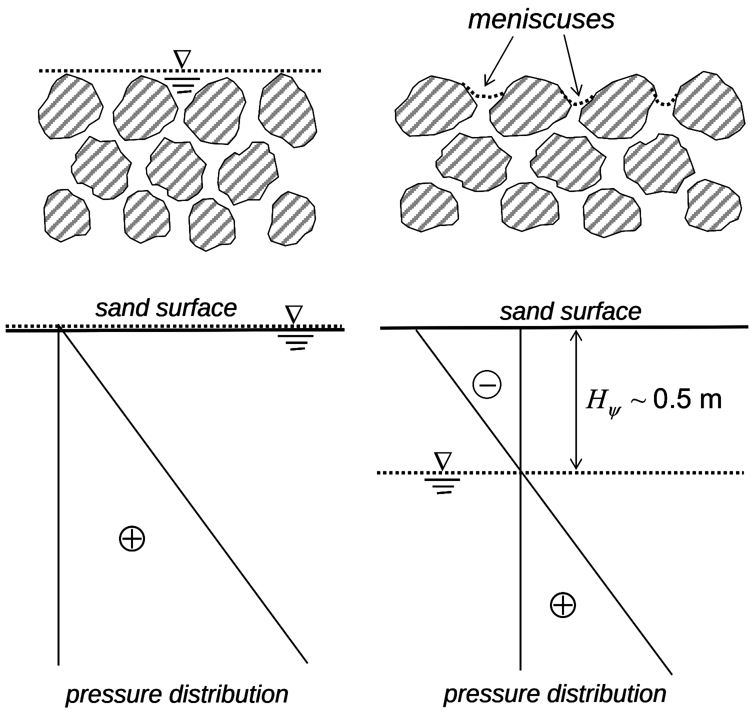

Figure 4.7: Schematic representation of the disproportionate relationship between the change in total moisture and change in pressure when the capillary fringe extends to the sand surface [after *Nielsen et al.*, 1988].

The sand column experiments were conducted with all forcing parameters held constant and the sand surface elevation, z_{sand}, lowered incrementally. For each elevation of the sand surface, the system was allowed to reach a state of steady oscillation and the frequency response function of the water table and complex effective porosity were calculated as described in sections 4.3.2 and 4.3.3. The experimental parameters and results are summarised in Appendix B.2.

Figure 4.8 shows the effect of different sand surface elevations on $|n_\omega|$, $-Arg\{n_\omega\}$, $|F|$ and $-Arg\{F\}$. Also plotted is the approximate static-equilibrium moisture distribution, $\theta(z)$, estimated from the first drying curve, $\theta(\psi)$, (cf. Figure 4.5 and equation (4.1)) by adding the suction head, ψ, to the mean driving head elevation, d.

While the sand surface is above the region of saturated moisture ($z_{sand} \geq$ 1.1m) there is no measurable effect of the sand surface on the water table oscillations. However, once the sand surface begins to truncate the tension saturated zone of the capillary fringe ($z_{sand} <$ 1.1m) there is a rapid decrease in $|n_\omega|$ and $-Arg\{n_\omega\}$ until a point where the sand surface equals the maximum driving head elevation ($z_{sand} = d + |\eta_o|$) and the magnitude of the frequency response almost reaches unity. This decrease in n_ω is clearly correlated with the rapid increase in $|F|$. That is, for a limited amount of moisture exchange (small n_ω) a disproportionately large change in pressure is observed (large $|F|$). This is consistent with previous observations that the specific yield decreases with proximity of the water table to the surface of the porous medium [e.g. *Childs,* 1969; *Duke*, 1972; *Nachabe,* 2002].

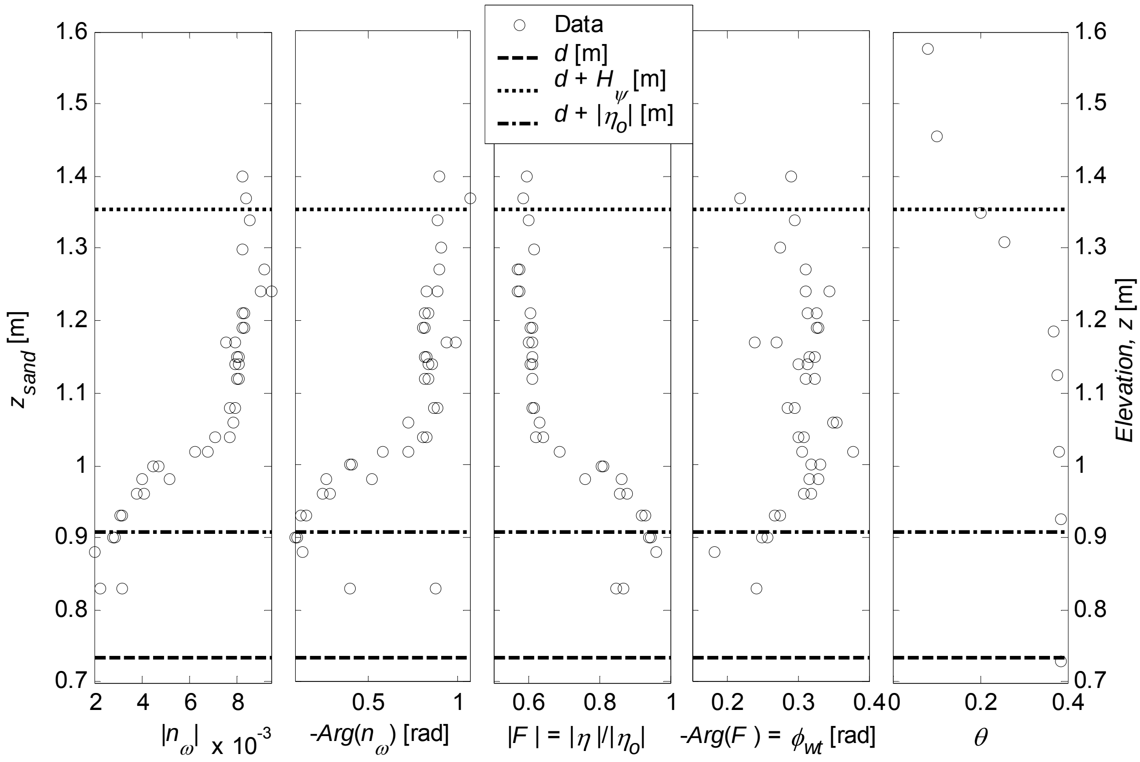

Figure 4.8: Influence of a truncated capillary fringe on: (a) $|n_\omega|$; (b) $-Arg\{n_\omega\}$; (c) $|F|$; (d) $-Arg\{F\}$. The equilibrium first drying curve where, $z = d + \psi$, is shown in panel (e). The horizontal lines in each plot represent the mean driving head level, d (dashed line), the maximum driving head elevation, $d + |\eta_o|$ (dash-dotted line) and the equivalent saturated height of the equilibrium total moisture, $d + H_\psi$ (dotted line).

The influence of a truncated capillary fringe on the propagation of water table waves is discussed further in section 5.5.3.

4.4.1 Meniscus effects – wetting and drying of the sand surface

For $z_{sand} < d + |\eta_o|$ in Figure 4.8, the data has limited meaning as clear water was observed above the sand surface for part of the oscillation period. In this case the parameters K and n_ω in the porous medium flow equation [equation (4.10)] both become equal to unity and the saturated thickness of the porous medium will be equal to the elevation of the sand surface. I.e. equation (4.10) becomes,

$$1.\frac{\partial h}{\partial t} = 1.\frac{h_o - h}{z_{sand}} \qquad (4.19)$$

These particular experiments however showed some interesting variations in the piezometric head observed in the saturated zone that are indicative of meniscus formation at the sand surface.

An example time series showing this is given in Figure 4.9 where the elevation of the driving head was above the sand surface for a significant part of the oscillation period. As a consequence the free surface, h, was observed by eye to also be above the sand surface for part of the oscillation period. Unfortunately the exact location of the free surface during this time was not recorded but its maximum elevation above the sand surface was no more than 1cm, i.e. of the order, $h_{max} - z_{sand} \approx 1$cm.

During falling water ($0 < t < 90$sec) the observed piezometric head falls steadily at a rate slower than the driving head level. At $t \approx 90$sec, there is a sharp drop in the observed piezometric head which is indicative of meniscus formation at the sand surface. In reference to Figure 4.7, meniscus formation only requires an amount of water of the order one grain diameter ($d_{50} \approx 1$mm) to be removed from the sand surface for a correspondingly large change in pressure.

Interestingly, the piezometric head only falls to a level equal to the driving head (less than a capillary fringe height) and then follows it with a virtually perfect response during rising water ($120 < t < 220$sec). This indicates that, during this time $|F| \approx 1$ which in turn indicates that n_ω is correspondingly very small (cf. Figure 4.8). At some time around $t >$ 230sec, clear water is again above the sand surface and the response of the piezometric head decreases.

The observed pressure dynamics are likely to play a significant role in the extent of moisture exchange in beaches and also on the dynamics of the water table exit point in beaches, an important pre-requisite in terms of quantifying sediment transport in the swash zone [e.g. *Elfrink and Baldock*, 2002]. The present observations provide a useful starting point for further investigation of the pressure dynamics in the beach face, clearly measurement of the clear water level would be an improvement on the present observations.

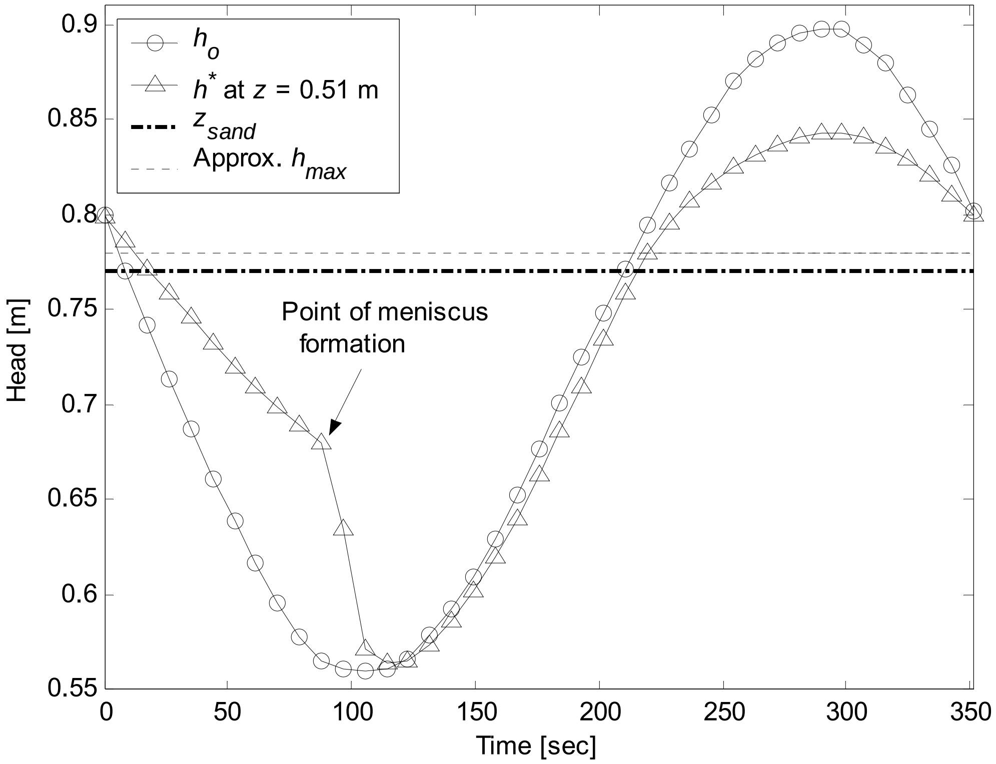

Figure 4.9: Observed time series from the sand column indicating the effect of meniscus formation at the sand surface.

4.5 1D Sand column - numerical modelling

4.5.1 Model description

In this section, existing $\theta = \theta(\psi)$ and $K = K(\psi)$ relationships are tested to see if they can match the experimental observations when substituted into the well known *Richards* equation [1931] for partially saturated flow,

$$c(\psi)\frac{\partial h^*}{\partial t} = \frac{\partial}{\partial z}\left(K(\psi)\frac{\partial h^*}{\partial z}\right) \tag{4.20}$$

where the piezometric head, $h^* = \psi + z$, is related to the moisture content, θ, by the capillary capacity,

$$c(\psi) = \frac{d\theta}{d\psi} \tag{4.21}$$

The *Richards* equation, (4.20), is solved here numerically using a 1D finite element model developed by *Perrochet* [2001, pers. comm][1]. Solution of the *Richards* equation requires prior knowledge of the soils moisture retention characteristics and is defined in the present model by the *van Genuchten* [1980] curve,

$$S_e = \frac{\theta - \theta_r}{\theta_s - \theta_r} = \left[\frac{1}{1 + (\alpha\psi)^\beta}\right]^m \tag{4.22}$$

where S_e is the effective saturation with α, β and $m = 1 - 1/\beta$ the empirical *van Genuchten* parameters. The corresponding *van Genuchten* function describing the partially saturated hydraulic conductivity, $K(\theta)$ is,

$$\frac{K(\theta)}{K_S} = \sqrt{S_e}\left\{1 - \left[1 - S_e^{1/m}\right]^m\right\}^2 \tag{4.23}$$

where K_s is the saturated hydraulic conductivity.

---

[1] 1D Finite element model and source code solving *Richard's* [1931] variably saturated flow equation was kindly provided by Professor Pierre Perrochet, University of Neuchatel, Switzerland [2001, pers. comm.]. The model employs a linear Crank-Nicolson-Galerkin scheme with matrix solution using a tri-diagonal algorithm.

Figure 4.10 shows the fit of equation (4.22) to the first drying curve for the three sediment types used in the sand column experiments of *Nielsen and Turner* [2000] (cf. section 4.3.1). The *van Genuchten* formulation is seen to adequately fit the measured profiles. The corresponding best fit *van Genuchten* parameters, α and β are summarised in Table 4.1.

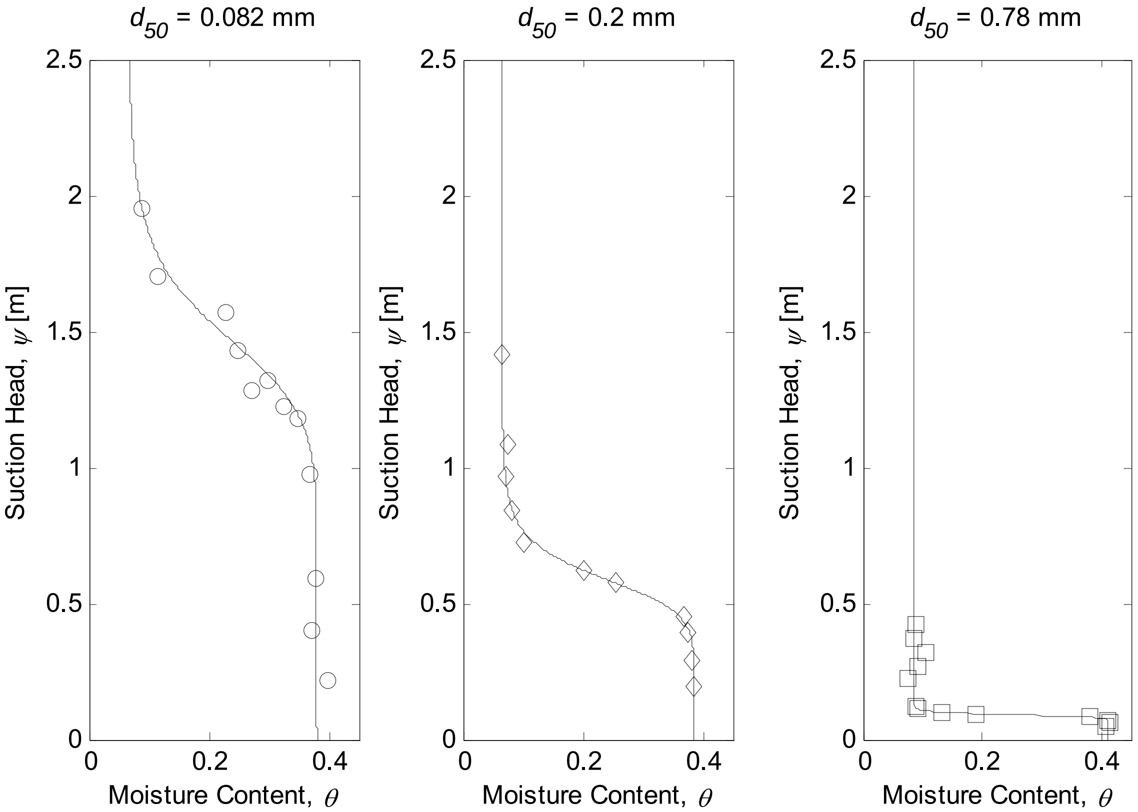

Figure 4.10: *van Genuchten* [1980] curve fits to the measured first drying curves for the three sediment types used in the column.

Table 4.1: Summary of best fit *van Genuchten* parameters for the first drying curve of each of the three sediment types used in the sand column, cf. Figure 4.10.

d_{50} [mm]	K_s [m/s]	θ_s [vol/vol]	θ_r [vol/vol]	α [1/m]	β [-]	H_ψ [m]
0.082	2.8×10^{-5}	0.38	0.065	0.68	10	1.52
0.2	4.7×10^{-4}	0.385	0.065	1.7	9	0.62
0.78	2.5×10^{-3}	0.413	0.085	11	20	0.092

To ensure numerical stability during the simulations the following spatial and temporal discretizations were employed: dz = 0.01m; dt = T/1000sec. A finer spatial resolutions was tested (dz = 0.005m) with little difference in results. At each period, the model was run until a state of steady oscillation was reached upon which the procedure described in sections 4.3.2 and 4.3.3 was followed to estimate n_ω.

4.5.2 Simulations using measured aquifer parameters

Figure 4.11 shows the results of numerical simulations based on the measured parameters for each sediment type (cf. Table 4.1). The forcing parameters were set at d = 0.57m and A = 0.17m.

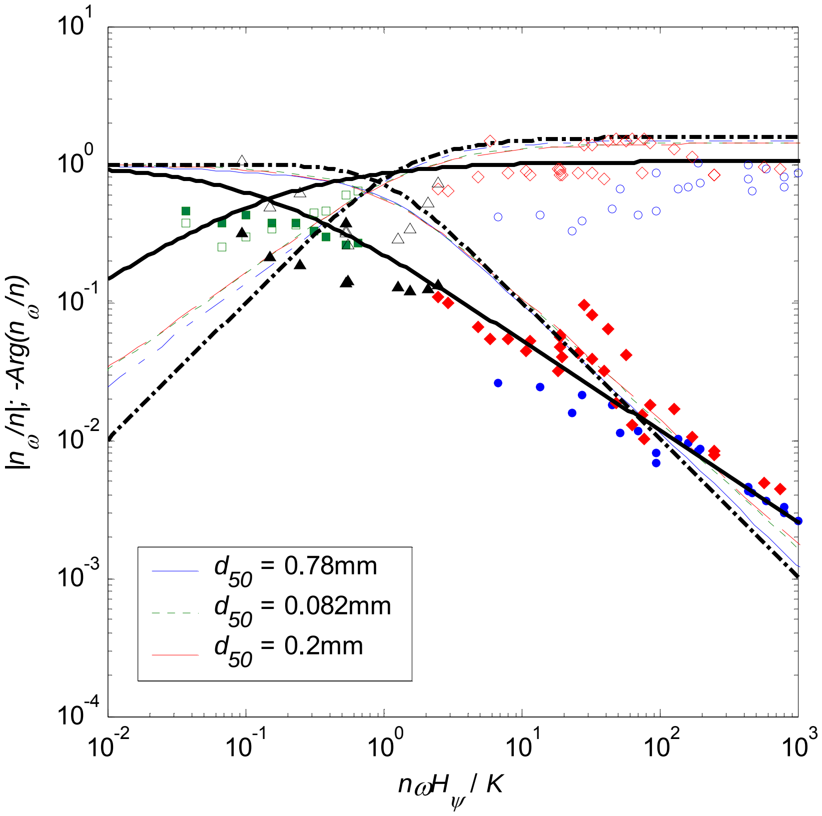

Figure 4.11: Comparison of simulated complex effective porosities against sand column observations. The solid lines and filled symbols depict the magnitude $|n_\omega/n|$ and the dash-dotted lines and open symbols depict the (negative) argument. Also shown are the theoretical *Green and Ampt* model (bold dash-dotted line) and the empirical model (bold solid line). The data symbols are as defined for Figure 4.6. Simulation parameters: d = 0.57m; A = 0.17m; all aquifer parameters as per Table 4.1.

Compared to the data, the simulations over-estimate both the asymptotic value of $-Arg\{n_\omega/n\}$ and the asymptotic slope of $|n_\omega/n|$. Interestingly, the non-hysteretic numerical simulations are close to the curves predicted by the non-hysteretic *Green and Ampt* model (bold dash-dotted lines), particularly with the asymptotic value of $-Arg\{n_\omega\}$. These findings support the suggestion of *Nielsen and Perrochet* [2000a,b] that the neglect of hysteresis in solving the *Richards* equation is the reason for its inability to replicate the column observations.

The d_{50} = 0.082mm and d_{50} = 0.2mm curves are virtually the same but the d_{50} = 0.78mm curve indicates some differences, particularly the divergence of the $|n_\omega/n|$ curve from the other curves in the high frequency limit, $n\omega H_\psi/K \to 0$. This will be shown in section 4.5.4 to be due to the difference in values of the *van Genuchten* β parameter (cf. Table 4.1).

4.5.3 Hysteretic simulations

In recent times the effects of hysteresis on periodic water table oscillations have been incorporated into models. *Lehman et al.* [1998] and *Stauffer and Kinzelbach* [2001] were both successful in reproducing their experimental observations by incorporation of hysteresis effects based on the model of *Mualem* [1984]. In both cases, the difference between their experiments and the experiments of *Nielsen and Perrochet* [2000a,b] and *Nielsen and Turner* [2000] was the non-simple harmonic forcing. *Lehman et al.* [1998] employed saw-toothed type forcing at the base and *Stauffer and Kinzelbach* [2001] employed almost simple harmonic forcing via a step motor controlled by a periodic program executed by pre-defined increments of h_o(t).

More recently, *Werner and Lockington* [2003] were able to reproduce the (simple harmonic) sand column observations of *Nielsen and Perrochet* [2000a,b] (d_{50} = 0.2mm) by including the hysteretic algorithms of *Parker and Lenhard* [1987]. A hysteresis ratio, $\zeta = \alpha^w/\alpha^d = 1.5$ provided the best agreement with the observed frequency response as shown in Figure 4.12. Also included in Figure 4.12 is the additional sand column data from *Nielsen and Turner* [2000] and the agreement of *Werner and Lockington's* [2003] hysteretic simulations at higher $n\omega d/K$ is still good.

In agreement with the results in Figure 4.11, the present non-hysteretic simulations (dash-dotted line) are unable to reproduce the observations. As discussed in section 4.5.2 the non-hysteretic simulations are quite close to the non-hysteretic *Green and Ampt* model (solid line).

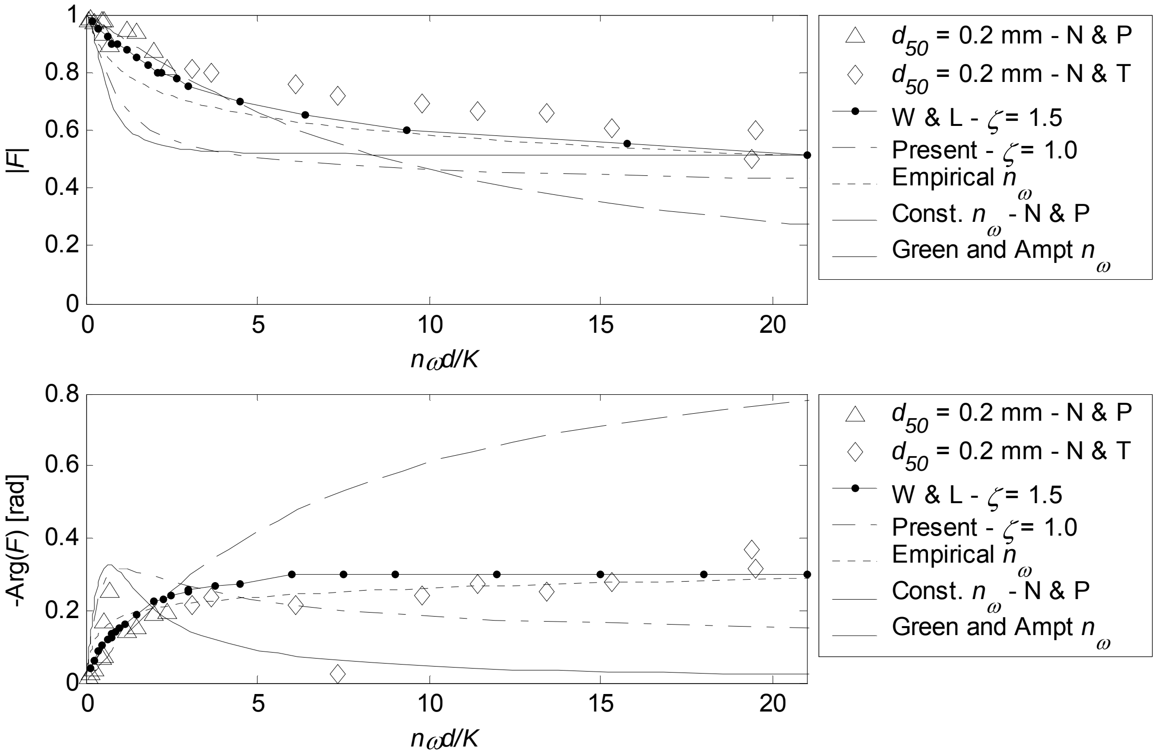

Figure 4.12: Comparison of sand column observations against the hysteretic (solid dot line) and non-hysteretic (dash-dotted line) [*Werner and Lockington*, 2003] *Richards'* equation simulations and three complex effective porosity models; n_ω constant (dashed line) [*Nielsen and Perrochet*, 2000a,b]; *Green and Ampt* n_ω (solid line) and the empirical n_ω (dotted line).

Werner and Lockington [2003] noted that the frequency response function calculated using equation (4.13) with the constant complex effective porosity obtained by *Nielsen and Perrochet* [2000a,b] (dashed line) [equation (4.16)] diverged from their hysteretic simulations (solid dot line) at higher dimensionless depths. The additional data of *Nielsen and Turner* [2000] however showed that the complex effective porosity to be a function of the oscillation frequency (cf. section 4.3.4 and Figure 4.6). The frequency response function calculated based on the empirical (hysteretic) complex effective porosity model [equation (4.17)] (dotted line) is seen to closely match the data and agrees well with the hysteretic simulations of *Werner and Lockington* [2003].

4.5.4 Influence of the van Genuchten parameters α and β on simulated n_ω

All of the modelling efforts mentioned above [*Lehman et al.*, 1998; *Stauffer and Kinzelbach*, 2001; *Werner and Lockington*, 2003] rely upon complex hysteresis algorithms to reproduce experimental observations. However, in the unpublished modelling work of *Perrochet* [2001, pers. comm.] it became apparent that numerical models based upon the *Richards* equation were able to reproduce the experimental observations with a single input moisture retention curve. The ability of the model to reproduce the sand column observations was seen to be dependent on the *van Genuchten* parameter β. In particular, the asymptotic slope of $|n_\omega/n|$ was able to be reproduced with a value of $\beta = 3$. This will be evidenced in the following section.

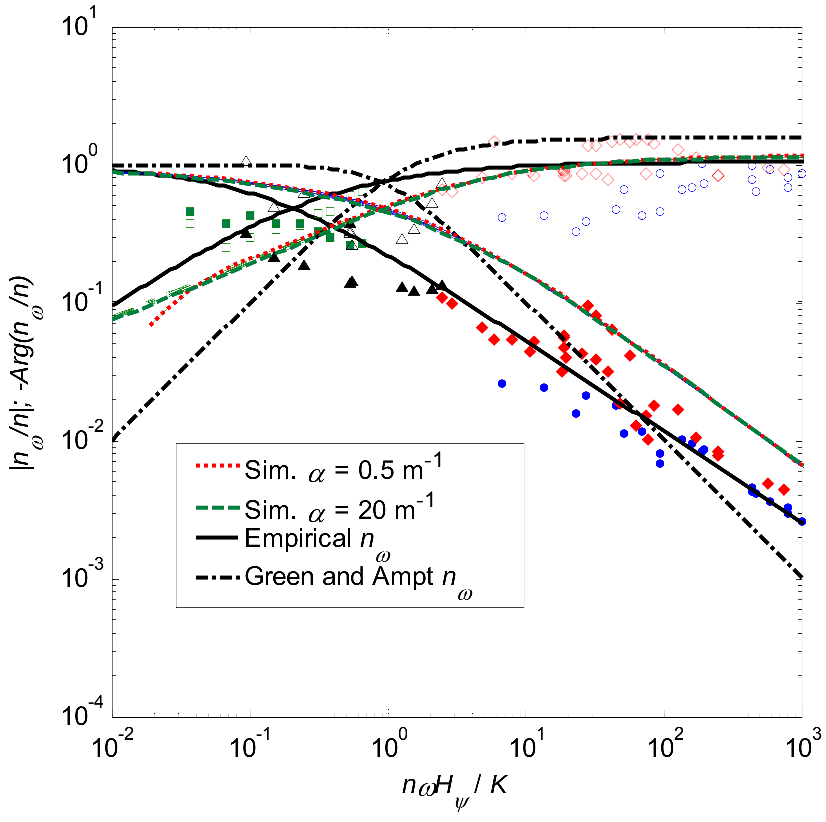

Figure 4.13: The influence of the *van Genuchten* parameter α on simulated $|n_\omega/n|$ (solid lines) and $-Arg\{n_\omega/n\}$ (dash dotted lines) for the range $\alpha = [0.5; 1; 2; 3; 4; 5; 6; 8; 10]$ m^{-1}. Parameters used: $d = 0.57$ m; $A = 0.17$ m; $\beta = 3$; $\theta_s = 0.385$; $\theta_r = 0.065$; $K_s = 4.7 \times 10^{-4}$ m/s.

Figure 4.13 and Figure 4.14 show respectively the variation of simulated complex effective porosities $n_\omega = n_\omega(n\omega H_\psi/K)$ for a range of the *van Genuchten* parameters, α and β. In Figure 4.13, the parameter α is seen to have no influence on the simulated n_ω whereas the parameter β has a significant influence as shown in Figure 4.14.

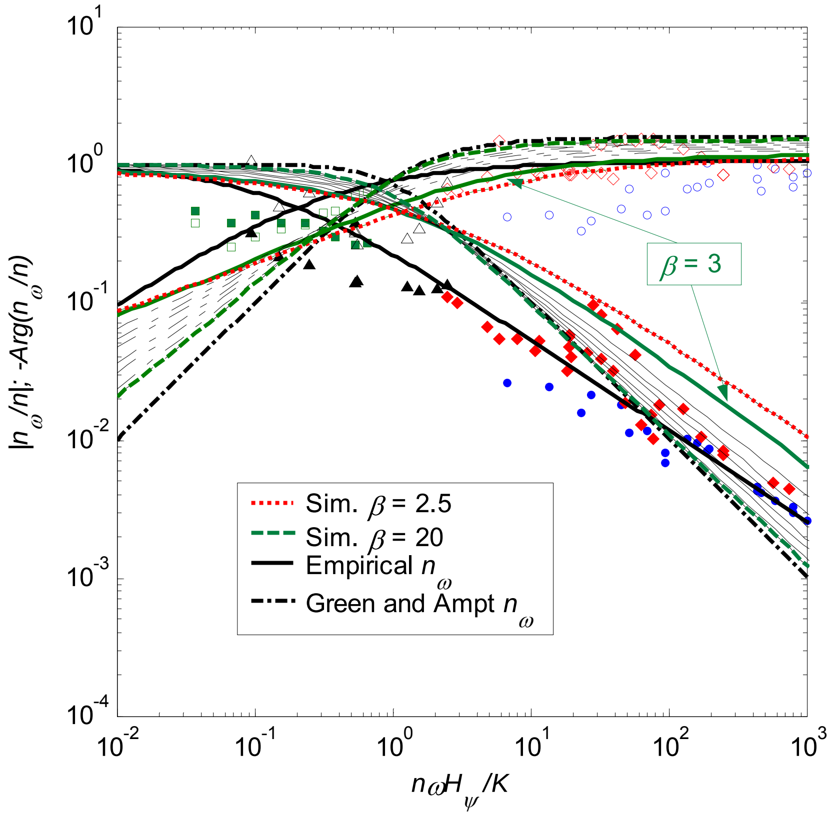

Figure 4.14: The influence of the *van Genuchten* parameter β on simulated $|n_\omega/n|$ (solid lines) and $-Arg\{n_\omega/n\}$ (dash dotted lines) for the range $\beta = [2.5; 3; 4; 6; 8; 10; 15; 20]$. Parameters used: $d = 0.57$m; $A = 0.17$m; $\alpha = 2.3\text{m}^{-1}$; $\theta_s = 0.385$; $\theta_r = 0.065$; $K_s = 0.00047$m/s.

The relationship between β and the asymptotic slope of the $|n_\omega/n|$ discovered by *Perrochet* [2001, pers. comm.] is clearly apparent in that the asymptotic slope $\approx 1/\beta - 1$. Therefore, the observed slope of $-⅔$ corresponding to the data requires $\beta = 3$. Similarly, for large β, the slope approaches the -1 slope corresponding to the *Green and Ampt* model, equation (4.7) (cf. dash-dotted line). The $\beta = 3$ curve is also seen to agree much better with the asymptotic value of $\pi/3$ for $-Arg\{n_\omega/n\}$.

Although matching the asymptotic slope of $|n_\omega/n|$, the $\beta = 3$ curve is shifted to the right of the data by a factor of five or so, therefore overestimating $|n_\omega/n|$. The reason(s) for this discrepancy is(are) not clear and requires further investigation.

This relationship between β and n_ω is potentially promising in that it appears that a single moisture retention curve could be used to simulate the dynamic response of the water table in a hysteretic, oscillating system. Compared to the complex hysteresis algorithms currently used to simulate the effect of hysteresis on a fluctuating water table [e.g. *Mualem*, 1984; *Parker and Leonard*, 1987; *Kool and Parker*, 1987], the use of a single moisture retention curve would greatly simplify numerical computations.

Despite such a curious finding, any physical interpretation of the result is to be undertaken with caution. The questions exist: How reasonable is the value of the *van Genuchten* parameter $\beta = 3$ in representing the moisture retention properties of the soil? Does there exist a representative curve with $\beta = 3$ which lies within the bounds of the hysteresis envelope (i.e. between the primary wetting and drying curves)?

In the absence of a measured first wetting curve for the present sediments, a hysteresis ratio, $\zeta = \alpha^w/\alpha^d = 2$, is adopted to calculate a wetting curve using equation (4.22). This value of ζ was suggested by *Kool and Parker* [1987] who measured the wetting and drying curves for eight different soils and found an average value of $\zeta \approx 2$ with a standard deviation of 0.46.

Figure 4.15 compares the measured first drying curve, calculated wetting curve and a "best fit" $\beta = 3$ curve for each of the three sediments. It is evident that much of the $\beta = 3$ curve lies within the bounds of the wetting-drying curve envelope and could therefore be taken to be reasonably representative of the porous medium. The question still remains though: Is there a physical reason why the $\beta = 3$ curve is able to capture dynamics of the hysteretic oscillations?

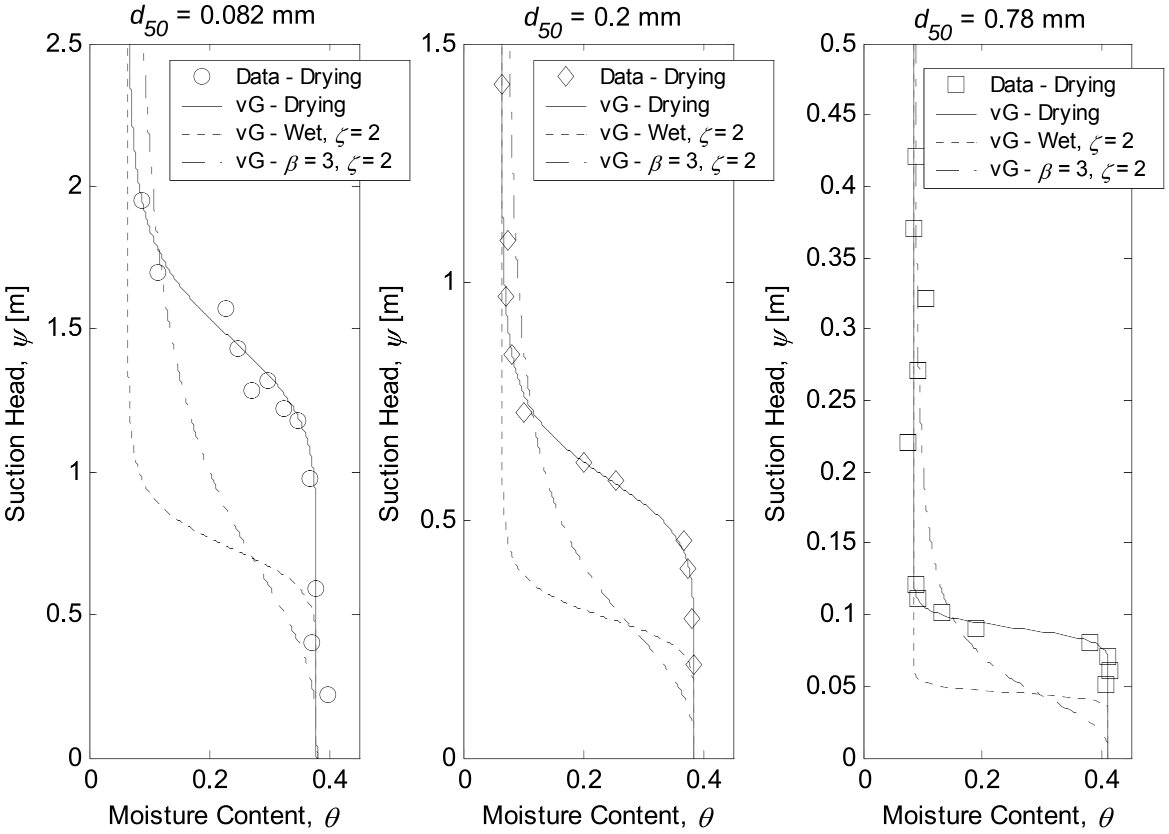

Figure 4.15: Moisture retention curves for all three sediment types. Symbols denote measured data and the lines represent the *van Genuchten* curves: the best fit to the measured first drying curve (solid line); the first wetting curve calculated with the hysteresis ratio, $\alpha^w/\alpha^d = 2$ (dashed line); the curve with $\beta = 3$ and $\alpha = 2\alpha^d$ (dash-dotted line).

4.6 Summary

In this chapter the concept of a complex effective porosity to account for the effects of capillarity on an oscillating water table [*Nielsen and Perrochet*, 2000a,b] has been described for use throughout this thesis. The additional sand column experiments of *Nielsen and Turner* [2000] have been summarised (cf. Figure 4.6), highlighting the significant discrepancies which exist between the data and the corresponding theoretical complex effective porosity model based on the widely used *Green and Ampt* [1911] approximation of the capillary fringe.

New sand column experiments have been presented which examine the influence of a truncated capillary fringe on water table oscillations. It has been shown that with an increasing degree of truncation the complex effective porosity is substantially decreased (cf. Figure 4.8). Based on the definition of the complex effective porosity [equation (4.3)] the decrease in n_ω corresponds to a decrease in amount of moisture exchange across the water table compared to that under a fully developed capillary fringe in agreement with previous findings of a reduced specific yield for shallow water tables [e.g. *Childs,* 1969; *Duke*, 1972; *Nachabe,* 2002]. This process has important implications for pressure fluctuations and the dynamics of the water table exit point on sloping beaches where the water table lies just below the sand surface.

Numerical simulation of the sand column observations has been conducted using a 1D finite element model [*Perrochet*, 2001 pers. comm.] which solves *Richards'* [1931] variably saturated flow equation. The non-hysteretic model was unable to reproduce the observations using the measured first drying curves (cf. Figure 4.11) in agreement with the findings of *Nielsen and Perrochet* [2000a,b]. Comparison of the hysteretic simulations of the sand column by *Werner and Lockington* [2003] with additional data has shown that consideration of hysteresis provides good agreement. This is further evidenced by the good agreement between the observed frequency response and that predicted by the hysteretic, empirical complex effective model of *Nielsen and Turner* [2000], equation (4.17).

The unpublished finding of *Perrochet* [2001, pers. comm.] that the column data is reasonably reproduced by using a value of β = 3 has been clearly evidenced and documented (cf. Figure 4.14). However, why such a relationship exists and how a single moisture retention curve is able to replicate a hysteretic system is left for future investigation.

Chapter 5 – Water table wave dispersion: observations vs theory

5.1 Introduction

The dispersion of water table waves in beaches will influence processes such as mixing of ocean and aquifer water and governs the degree of saturation of the beach aquifer as a function of time and space. These processes will, in turn, influence the quality of coastal groundwater resources and may affect the movement of sand at the beach face. Accurate prediction of the dispersive properties of water table waves is therefore a pre-requisite to accurate quantification of these other processes.

5.2 Estimation of the wave number from observations

The water table variation which results from periodic forcing at a boundary can be described by,

$$\eta(x,t) = \sum_{m=1}^{\infty} R_m\left(0\right) e^{-k_{m,r}x} \cos(m\omega t - k_{m,i}x) \tag{5.1}$$

where, $R_m(0)$ is the amplitude of the forcing at $x = 0$, $k_m = k_{m,r} + ik_{m,i}$ is the water table wave number with $k_{m,r}$ representing the amplitude decay rate and $k_{m,i}$ the rate of (linear) increase in phase lag and m denotes the harmonic component.

If the observed water table fluctuations behave in accordance with equation (5.1) then the water table wave number for each harmonic component can be estimated as follows.

According to (5.1), the amplitude of a single harmonic component of the observed water table wave at a distance, x, from the forcing is,

$$R_m(x) = R_m(0)e^{-k_{m,r}x} \tag{5.2}$$

and the phase by,

$$\phi_m(x) = -k_{m,i}x \tag{5.3}$$

The quantities, R_m and ϕ_m can be extracted from the data using harmonic analysis [cf. equation (3.1)] and equations (5.2) and (5.3) can be solved for $k_{m,r}x$ and $k_{m,i}x$ respectively, with the wave numbers estimated by least squares fitting to the following quantities,

$$k_{m,r}x = \ln\left(\frac{R_m(0)}{R_m(x)}\right) \tag{5.4}$$

$$k_{m,i}x = \phi_m(x) - \phi_m(0) \tag{5.5}$$

5.3 Wave numbers estimated from field observations

Wave numbers corresponding to the semi-diurnal period (T = 12.25hours) estimated from the present field campaign (cf. Appendix A) and from the data of *Kang et al.* [1994a] are summarised in Table 5.1 and plotted in Figure 5.1 along with the values obtained by *Nielsen* [1990], *Raubenheimer et al.* [1999] and *Vigneaux* [2003]. Also plotted is the dispersion relation curve predicted by the simplest theory corresponding to a shallow aquifer free of any capillary effects [e.g. *Todd*, 1964],

$$k_m d = \sqrt{i\frac{nm\omega d}{K}} \tag{5.6}$$

where n is the drainable porosity, ω is the angular frequency, d is the mean aquifer depth, K is the hydraulic conductivity and m is an integer value denoting the harmonic component.

The simple theory, equation (5.6), predicts $k_r = k_i$ which is clearly not the case for the field data which indicates $k_r > k_i$. This suggests that the surveyed aquifers are either: (a) shallow and influenced by capillarity [*Barry et al.*, 1996]; (b) of finite-depth (non-hydrostatic pressure) [*Parlange et al.*, 1984; *Nielsen et al.*, 1997]; or of finite-depth and influenced by capillarity [*Li et al.*, 2000a].

Table 5.1: Summary of wave numbers estimated from field observations at the semi-

diurnal tidal period, $T = 12.25$hours.

Date	***Location***	k_r [m^{-1}]	k_i [m^{-1}]	***Data source***
Apr - 89	Barrenjoey Beach, NSW Aust.	0.0930	0.0560	*Nielsen* [1990]
Sep - 91	Kings Beach, QLD Aust.	0.0529	0.0290	*Kang et al.*, [1994a]
Nov - 91	Eagers Beach, QLD Aust.	0.0462	0.0315	*Kang et al.*, [1994a]
Jun - 93	Brunswick Heads, NSW Aust.	0.0877	0.0473	*Kang et al.*, [1994a]
Nov - 93	Northern Bribie Island, QLD Aust.	0.0740	0.0523	*Kang et al.*, [1994a]
Sep - 96	Torrey Pines Beach, Calif. USA.	0.0770	0.0670	*Raubenheimer et al.* [1999]
May - 00	North Stradbroke Island, QLD Aust.	0.0592	0.0234	Present
Aug - 00	North Stradbroke Island, QLD Aust.	0.0462	0.0209	Present
Dec - 00	Southern Moreton Island, QLD Aust.	0.0317	0.0140	Present
Nov - 01	Brunswick Heads, NSW Aust.	0.0488	0.0155	Present
Feb - 02	Brunswick Heads, NSW Aust.	0.0728	0.0344	Present
Jun - 03	Brunswick Heads, NSW Aust.	0.0661	0.0356	*Vigneaux* [2003]

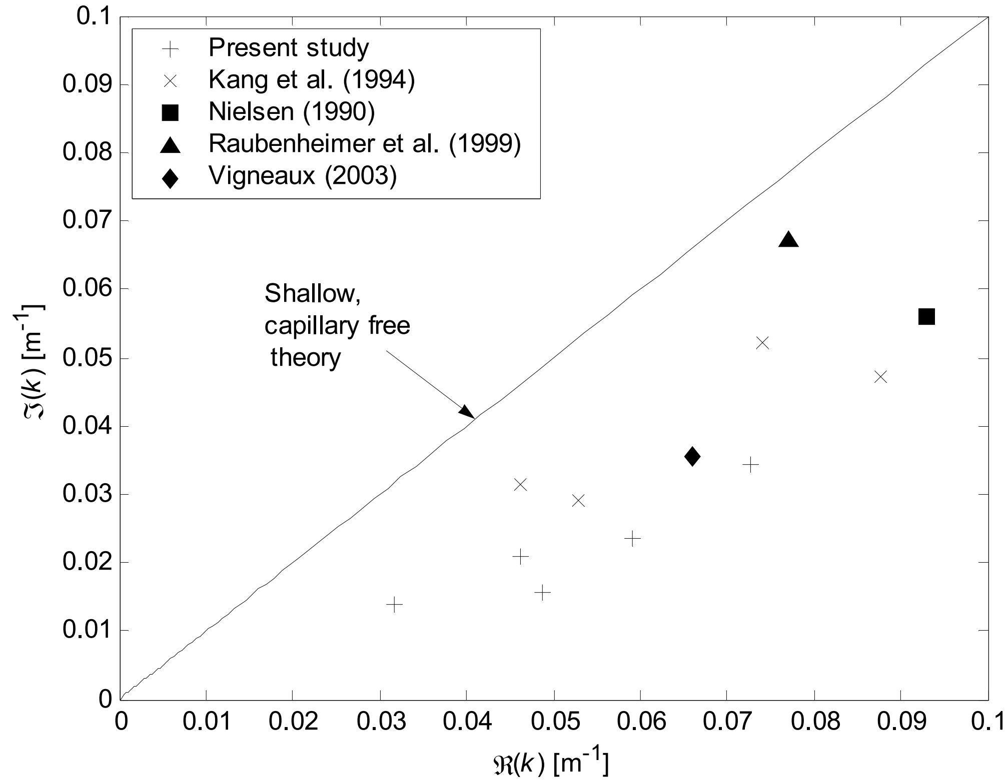

Figure 5.1: Wave numbers estimated from field observations of tidally forced water table waves ($T = 12.25$ hours) compared with that predicted by shallow, capillary-free aquifer theory [equation (5.6)].

5.3.1 Finite-depth aquifer free of capillary effects

Nielsen et al. [1997] relaxed the shallow aquifer assumption of hydrostatic pressure and derived the following infinite order, finite-depth dispersion relation,

$$k_m d \tan k_m d = i\frac{nm\omega d}{K} \tag{5.7}$$

Note that the shallow-aquifer dispersion relation [equation (5.6)] emerges from (5.7) when only the first term of the Taylor expansion for $\tan k_m d$ is used.

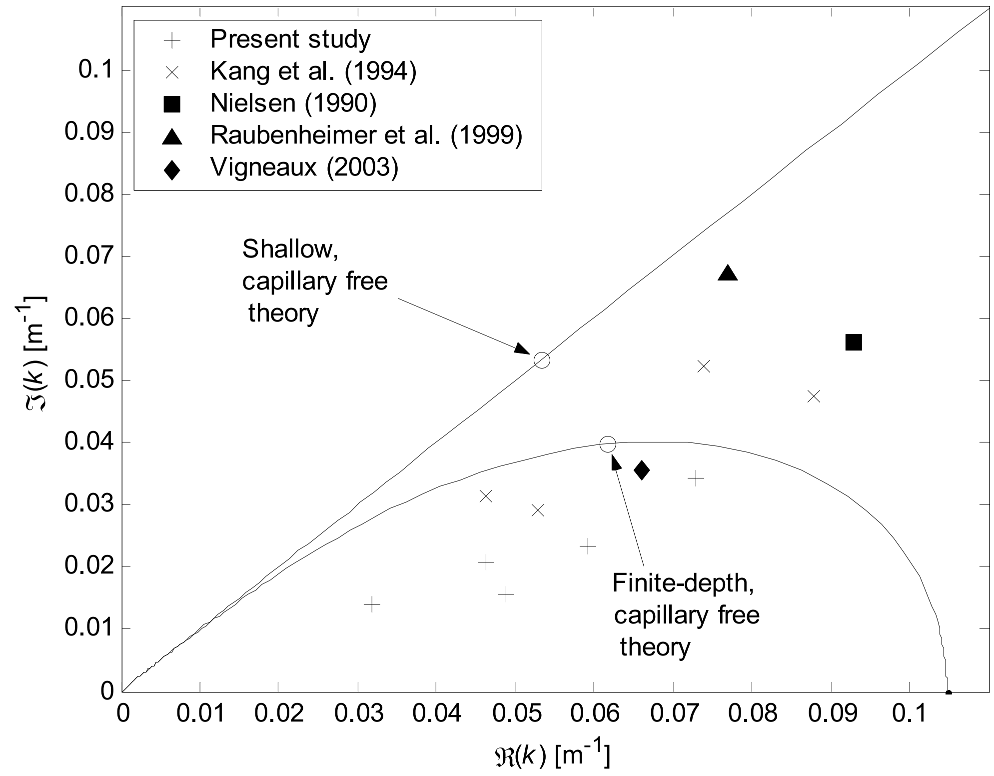

Figure 5.2: Comparison of field wave numbers with both shallow and finite-depth aquifer dispersion relations, equations (5.6) and (5.7) respectively. The symbols, ○, denote theoretical predictions based on the parameters: T = 12.25hours; n = 0.3; $K = 5 \times 10^{-4}$m/s; d = 15m.

Figure 5.2 shows the comparison of the shallow and finite-depth dispersion relation curves with the field values given in Table 5.1. Equation (5.7) is seen to greatly improve the agreement with the field data, predicting the observed relationship $k_r > k_i$. That is, in the presence of vertical flows the speed of propagation is faster than that predicted for a shallow aquifer. As the shallow aquifer limit ($n\omega d/K \rightarrow 0$) is approached the finite-depth theory predicts $k_r = k_i$ in agreement with the shallow aquifer theory.

5.3.2 Influence of the capillary fringe

The influence of the capillary fringe on an oscillating water table has been discussed in Chapter 4 in terms of the complex effective porosity concept of *Nielsen and Perrochet* [2000a,b]. In this section the influence of the capillary fringe on the dispersion of a propagating water table wave is discussed.

5.3.2.1 Shallow aquifer with a Green and Ampt capillary fringe

Barry et al. [1996] used the capillary correction term of *Parlange and Brutsaert* [1987], based upon the *Green and Ampt* [1911] approximation, to derive the following shallow aquifer with *Green and Ampt* capillary fringe dispersion relation,

$$\Re\left(k_m\right) = \sqrt{\frac{nm\omega}{2d}\left[\frac{1}{\sqrt{K^2 + \left(m\omega nH_\psi\right)^2}} + \frac{m\omega nH_\psi}{K^2 + \left(m\omega nH_\psi\right)^2}\right]} \qquad (5.8)$$

$$\Im\left(k_m\right) = \sqrt{\frac{nm\omega}{2d}\left[\frac{1}{\sqrt{K^2 + \left(m\omega nH_\psi\right)^2}} - \frac{m\omega nH_\psi}{K^2 + \left(m\omega nH_\psi\right)^2}\right]} \qquad (5.9)$$

Note that the same result can be obtained by inserting the complex effective porosity corresponding to the *Green and Ampt* [1911] approximation, equation (4.7), in for n in the shallow aquifer dispersion relation, equation (5.6). In the low frequency limit ($\omega \rightarrow 0$), and/or negligible fringe thickness ($H_\psi \rightarrow 0$), the influence of capillarity disappears and equation (5.8) is reduced to the real and imaginary parts of equation (5.6).

Figure 5.3 indicates that, at the tidal frequency (T = 12.25hours), the influence of the capillary fringe on water table waves is small in agreement with previous findings [*Barry et al.*, 1996; *Li et al.*, 1997]. Inspection of equations (5.8) and (5.9) indicates that the relative importance of the capillary fringe increases with forcing frequency. Observations from a sand flume aquifer subject to higher frequency forcing oscillations are used to test equations (5.8) and (5.9) more stringently in section 5.5.

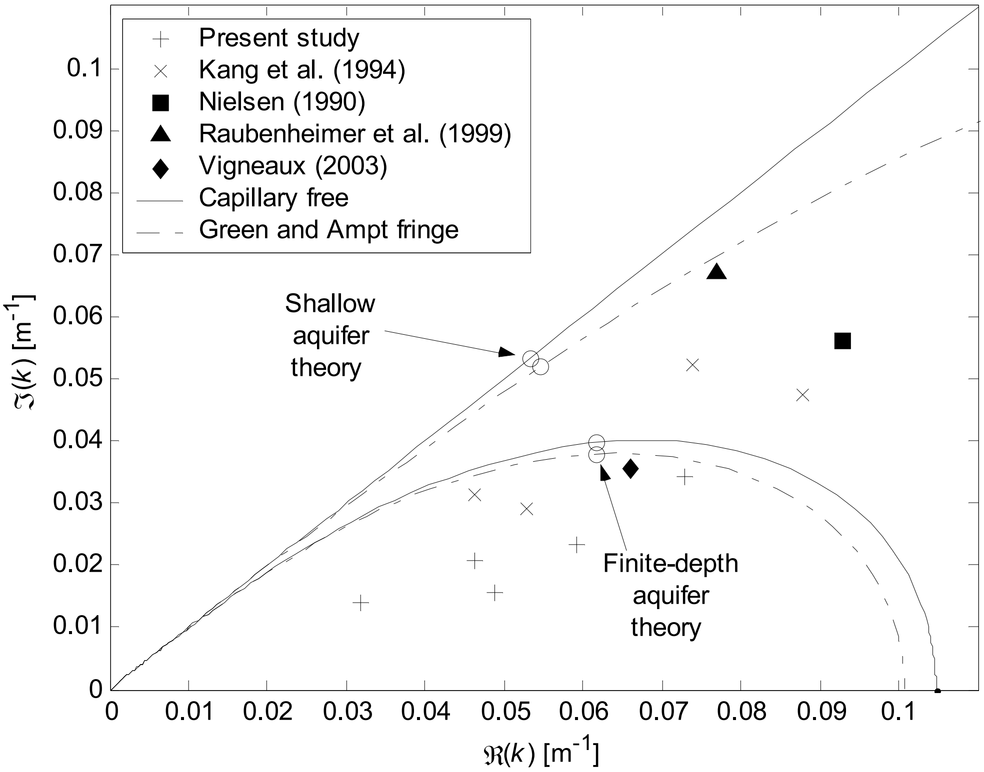

Figure 5.3: Field wave numbers in comparison with shallow and finite aquifer depth theories, with and without capillarity effects. The symbols, ○, denote theoretical predictions based on the parameters: $T = 12.25$hours; $n = 0.3$; $K = 5 \times 10^{-4}$m/s; $d = 15$m.

5.3.2.2 Finite-depth aquifer with a Green and Ampt capillary fringe

Using the *Green and Ampt* [1911] approximation for the capillary fringe, *Li et al.* [2000a] extended the work of *Nielsen et al.* [1997] and obtained the following dispersion relation including the effects of both finite aquifer depth and capillarity,

$$k_m d \tan k_m d = i \frac{nm\omega d}{K + im\omega n H_\psi} \tag{5.10}$$

Note that the same dispersion relation is obtained by inserting the complex effective porosity corresponding to the *Green and Ampt* [1911] approximation, equation (4.7), in for *n* in the finite aquifer depth dispersion relation, equation (5.7).

The comparison of equation (5.10) with the field observations is shown in Figure 5.3 where again the capillary fringe is seen to have little effect on the dispersion of the water table wave at the semi-diurnal tidal frequency.

As shown in Figure 5.1 through Figure 5.3, a great deal of scatter exists in the field observations. This is due to a combination of the complexity of the oceanic forcing and the uncertainty in aquifer geometry and parameter distribution. As a consequence of the large number of unknowns in the field, it is difficult to ascertain “what contributes to what?”. To eliminate some of these unknowns, laboratory experiments were conducted using a homogeneous sand flume aquifer of known geometry. These experiments are described in the following sections.

5.4 Sand flume description and methodology

Two types of experiments were conducted in the flume, the first with a vertical boundary and the second with a sloping boundary. In this chapter only the observed dispersion of the pressure wave is discussed. The vertical boundary experiment is revisited in Chapter 6 to verify the finite aquifer depth theory of *Nielsen et al.* [1997]. In Chapter 7, the sloping boundary experiment is used to examine in detail the generation of higher harmonics due to the sloping boundary.

5.4.1 The sand flume

The sand flume shown in Figure 5.4 and Figure 5.5 is 9m long by 1.5m high by 0.14m wide. At one end there is a simple harmonic periodic driving head and at the other end there is a no flow boundary. The driving head level is regulated by a variable height overflow delivering almost simple harmonic oscillations. The inland boundary condition is no flow.

Water pressure in the saturated zone was measured with piezometers extending 10cm into the sand. The piezometers are 5mm stainless steel tubes perforated with numerous 2.5mm diameter holes screened by stainless steel mesh with 0.1mm openings. Measurements were taken visually, by reading ID 8mm manometer tubes connected to the piezometers with a reading accuracy of ± 1mm.

Figure 5.4: The sand flume of dimensions 9m long by 1.5m high by 0.14m wide. The simple harmonic driving head is closest to camera and the far boundary condition is no flow.

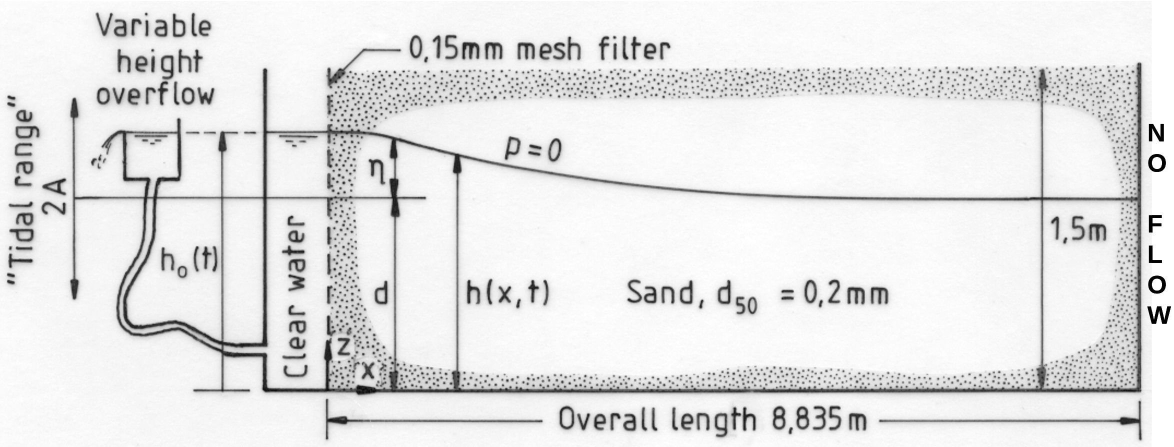

Figure 5.5: Experimental setup: the groundwater flow in a uniform aquifer of simple rectangular shape is driven by a simple harmonic driving head at $x = 0$. Capillary effects are significant and the aquifer is not shallow.

5.4.2 The sand

The sand used was locally mined quartz sand, the same as examined in detail by *Nielsen and Perrochet* [2000a,b]. It has a d_{50} = 0.2mm and d_{90}/d_{10} = 1.83. The sieve and moisture retention curves are given in Figure 4.4 and Figure 4.5 respectively.

For the vertical boundary experiment, the sand was packed by allowing the sand to settle through the water-filled flume thereby avoiding entrapment of air. The sand's hydraulic properties were taken to be those measured in the sand column experiments of *Nielsen and Perrochet* [2000a,b] as summarised in row 1 of Table 5.2. This value compares favourably with the value K = 0.00053m/s calculated using the empirical formulation of *Krumbein and Monk* [1942] based on the measured sediment characteristics (cf. Figure 4.4).

Table 5.2: Hydraulic parameters of the test sand: K = saturated hydraulic conductivity; θ_s and θ_r = saturated and residual moisture contents respectively; H_ψ = steady capillary fringe thickness.

Experiment	K [m/s]	θ_s [vol/vol]	θ_r [vol/vol]	H_ψ [m]
Vertical	4.70×10^{-4}	0.41	0.09	0.55
Sloping	1.32×10^{-4}	0.38	0.08	0.6

For the sloping boundary experiment a slightly different packing procedure was adopted. The sand was packed by allowing a layer (approximately 15cm thick) to settle through the water filled flume, each settled layer was then thoroughly mixed using a hose and the procedure repeated for each subsequent layer. This procedure ensured that: (a) no air was trapped in the sand and (b) any layering due to differing settling velocities was minimised.

The hydraulic conductivity was determined *in situ* using a slug test at numerous locations along the flume and then taking the average of several tests at each location. No systematic variation was found in the estimates of K along the flume. The average value for K over all locations measured was calculated to be 1.32×10^{-4}m/s with minimum and maximum values of 1.15×10^{-4}m/s and 1.49×10^{-4}m/s respectively. For comparison, *Robinson and Li*

[2004] estimated $K = 1.18 \times 10^{-4}$m/s based on measurements of the flow through the flume driven by a steady hydraulic gradient. The sand's hydraulic properties are summarised in Table 5.2. In both experiments, the flume was covered with loose plastic to minimise evaporation and the sand remained moist to the top.

5.4.3 The driving head

The driving head, $h_o(t)$, was virtually sinusoidal,

$$h_o(t) = d + A_o \cos \omega t = d + A_o \Re\left(e^{i\omega t}\right) \tag{5.11}$$

where d is the mean elevation, A_o is the amplitude and ω (=2π/T) is the angular frequency. The driving head parameters for all experiments are summarised in Table 5.3. The periods chosen fall in the range of infra-gravity and long waves observed in oceans.

Table 5.3: Summary of aquifer forcing parameters.

Boundary Type	*T* [s]	*R_ω* [m]	*$R_{2\omega}$* [m]	*d* [m]
Vertical	772	0.235	0.007	1.094
Sloping	348	0.203	0.004	1.009

For the range of parameters considered, the vertical accelerations are very small, with $\omega^2 A_o/g$ of the order 10^{-6}, and so the pressure in the clear water reservoir is taken to be hydrostatic. As an indication of the relative importance of capillarity to gravitational effects the following dimensionless number can be used, $N_{CAP} = n\omega H_\psi/K$ (i.e. the inverse of the "coastal" aquifer response number $N_{CAR} = K/n\omega H_\psi$ after *Li et al.* [1997]). For all of the present experiments is of the order 10^1 which indicates that capillary fringe effects will be important [cf. *Li et al.*, 1997]. For comparison, if forcing from a tide of period 12.25hours is considered (where capillary effects are considered to be small) with the same aquifer parameters N_{CAP} is of the order 10^{-1}.

5.5 Sand flume observations

In both experiments the pressure wave exhibited behaviour consistent with small-amplitude theory. That is the amplitude decayed exponentially and a phase lag developed linearly with distance *x* from the driving head [cf. equation (5.1)]. The corresponding experimental best fit wave numbers were estimated using the procedure described in section 5.2. The first harmonic wave numbers are summarised and compared with field values in Figure 5.6. Note that the wave numbers are plotted as the dimensionless depth *kd*. To enable the comparison, the field values have all been multiplied by the same assumed depth of $d = 15$m (except for the *Raubenheimer et al.* data where the measured value of $d = 4.7$m is used). For $d = 10$m and 20m, the field values are still comparable to the lab data.

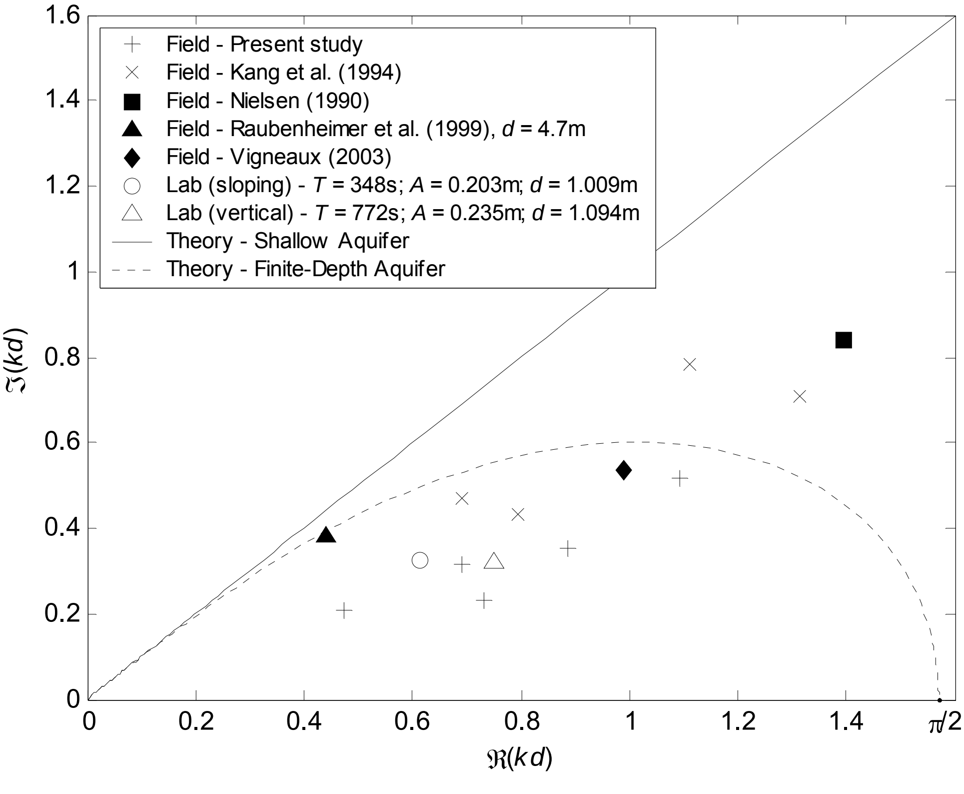

Figure 5.6: Comparison of dimensionless wave numbers, *kd*, with field observations.

5.5.1 Comparison with theoretical predictions

In this section the observations from the vertical boundary experiment (cf. Δ in Figure 5.6) are compared against the theories introduced in section 5.3. Observations from the sloping boundary experiment are used later in section 5.5.2 to discuss the dispersion of the higher harmonic waves generated as a result of the sloping boundary.

The best fit (dimensionless) wave number corresponding to the vertical boundary experiment is given by,

$$kd = 0.752 + 0.321i \tag{5.12}$$

This gives a ratio, $k_r/k_i \approx 2.3$ which is comparable to the field values given in Table 5.1 and with those found in the field by *Nielsen* [1990] and *Aseervatham* [1994]. The comparison of this value with that predicted by the theories described in section 5.3 are summarised in Table 5.4 and graphically in Figure 5.7.

Table 5.4: Comparison of the best fit experimental wave number, (5.12), with theoretical predictions. Parameters used are: $T = 772$sec; $d = 1.094$m; $n = 0.32$; $K = 0.00047$m/s; $H_\psi = 0.55$m.

Description	Equation	$k_{1\omega}d$
Experimental value (vertical boundary)	(5.12)	$0.752 + 0.321i$
Shallow, capillary-free theory	(5.6)	$1.741 + 1.741i$
Finite-depth, capillary-free theory	(5.7)	$1.526 + 0.257i$
Shallow with *Green and Ampt* fringe	(5.8)	$1.358 + 0.217i$
Finite-depth with *Green and Ampt* fringe	(5.10)	$1.063 + 0.097i$
Finite-depth with hysteretic fringe	(5.7) with (4.17)	$0.868 + 0.218i$

Relative to the shallow aquifer prediction [equation (5.6)], consideration of finite aquifer depth effects [equation (5.7)] is seen to greatly improve the comparison of the predicted rate of increase in phase, k_id, with the observed best fit value, (5.12). However, the amplitude decay rate, k_rd, is over-predicted by a factor of 2 suggesting that capillary effects are significant. A similar prediction is obtained from the theory corresponding to a shallow aquifer with a *Green and Ampt* capillary fringe, that is, a comparable k_id but a significant over-prediction of the decay rate, k_rd.

The finite-depth theory with a non-hysteretic *Green and Ampt* capillary fringe correction [equation (5.10)] is seen to improve the agreement with the decay rate somewhat but over-predicts the rate of increase in phase lag. Finally, consideration of hysteresis by inserting the empirical complex effective porosity model, equation (4.17), into the finite-depth dispersion relation, equation (5.7), is shown to provide the best agreement with the observed value, (5.12).

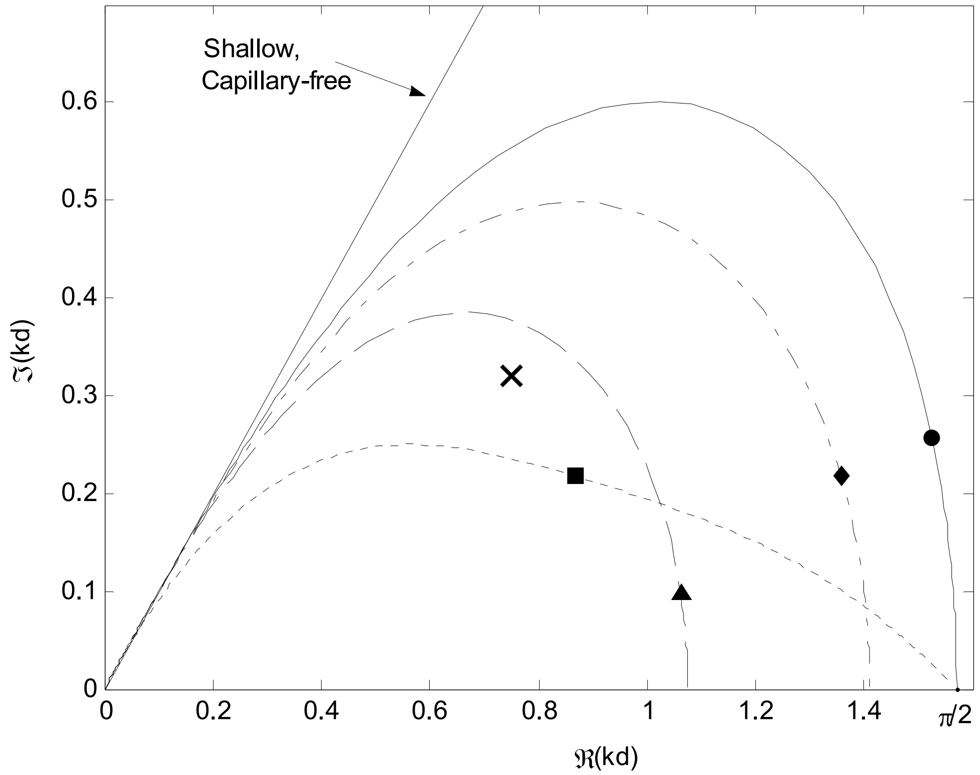

Figure 5.7: Comparison of the experimental wave number (5.12), (×), with those predicted by the finite-depth dispersion relation, equation (5.7), using a real valued porosity (•), and complex effective porosities as defined by (4.7), (▲), and (4.17), (■). The shallow aquifer, with *Green and Ampt* capillary fringe value defined by (5.8) is also shown (♦). The associated curves illustrate the wave dispersion properties for $0 < n\omega d/K < \infty$, for each of the above models. Parameters used are: $T = 772$sec; $d = 1.094$m; $n = 0.32$; $K = 0.00047$m/s; $H_\psi = 0.55$m.

The sensitivity of all models to the aquifer parameters K (□), n (○) and H_ψ (◊), is illustrated in Figure 5.8 where the following ranges of parameters were tested: $K = [2.35 \times 10^{-4}$m/s; 4.7×10^{-4}m/s; 9.4×10^{-4}m/s]; $n = [0.2; 0.32; 0.4]$; $H_\psi = [0.4$m; 0.55m; 0.7m]. The analysis shows that changes in K and n will shift the wave numbers along the same dispersion relation curve, whereas a change in H_ψ will shift the whole curve closer or further from the origin. Of all the models, the hysteretic empirical capillary fringe model (4.17) inserted into finite-depth dispersion relation (5.7), is seen to be the least sensitive as a consequence of the ⅔ power in the denominator of (4.17) as opposed to the power of 1 in the non-hysteretic *Green and Ampt* model (4.7).

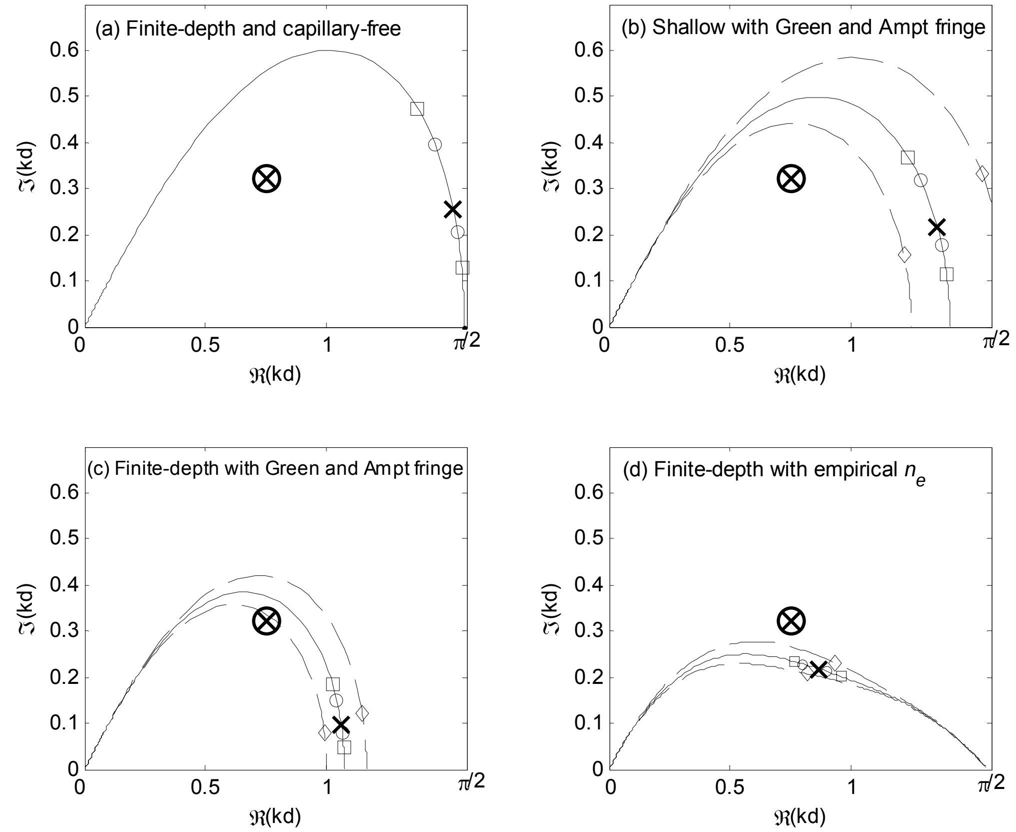

Figure 5.8: Sensitivity of theoretical dispersion relations to variations in the aquifer parameters, K (□), n (○) and H_ψ (◊). The points shown correspond to the range of parameters: $K = [2.35 \times 10^{-4}$m/s; 9.4×10^{-4}m/s]; $n = [0.2; 0.4]$; $H_\psi = [0.4$m; 0.7m]. ⊗ denotes the experimental value, (5.12), and × denotes the theoretical predictions based on the experimental parameters: $T = 772$sec; $d = 1.094$m; $n = 0.32$; $K = 4.7 \times 10^{-4}$m/s; $H_\psi = 0.55$m.

5.5.2 Dispersion of higher harmonic components

In the presence of a sloping boundary higher harmonics will be generated at the boundary due to the aquifer filling more easily than it can drain [e.g. *Lanyon et al.*, 1982]. In this section only the dispersion of these higher harmonic components in the interior is examined. The details of the generation process are discussed in Chapter 7.

The best fit wave numbers (first three harmonics) from the sloping flume experiment are summarised in Table 5.5. All of the estimated harmonic wave numbers indicate that $k_{m\omega,r} > k_{m\omega,i}$ in agreement with the field observations shown in Figure 5.1 and laboratory observations [e.g. *Nielsen et al.*, 1997; section 5.5].

Table 5.5: Comparison of wave numbers estimated from the sloping boundary flume data with theoretical predictions.

	Data (z = 0.8m)	Shallow, Capilary free	Finite-depth, Capillary free	Shallow with Green and Ampt fringe	Finite-depth with Green and Ampt fringe	Finite-depth with hysteretic fringe
Equation	-	(5.6)	(5.7)	(5.8)	(5.10)	(5.7) with (4.17)
$k_{1\omega,r}$ =	0.584	4.509	1.556	1.284	1.015	1.063
$k_{1\omega,i}$ =	0.343	4. 509	0.038	0.026	0.013	0.173
$k_{2\omega,r}$ =	0.779	6.377	1.557	1.285	1.015	1.137
$k_{2\omega,i}$ =	0.311	6.377	0.019	0.013	0.006	0.159
$k_{3\omega,r}$ =	0.781	7.810	1.557	1.285	1.015	1.177
$k_{3\omega,i}$ =	0.208	7.810	0.013	0.009	0.004	0.150

The comparison of the observed dispersion with theoretical predictions is summarised in Table 5.5. The shallow-aquifer, capillary-free theory [equation (5.6)] predicts that the dispersion of the higher harmonic components to be related to the primary harmonic by,

$$k_{m\omega} = \sqrt{m}k_{1\omega} \tag{5.13}$$

which is not evident in the data.

Figure 5.9 compares the data with the predictions if the finite-depth dispersion relation [equation (5.7)] both with and without consideration of the influence of the capillary fringe.

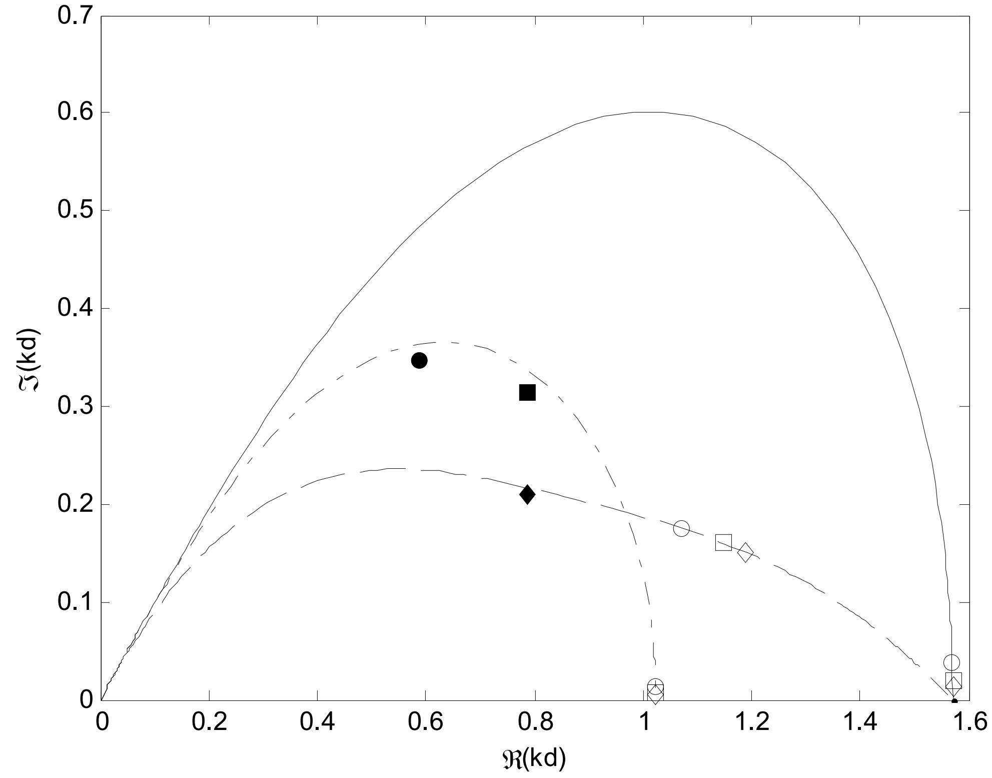

Figure 5.9: Comparison of best fit wave numbers (•,■,♦) for the first three harmonics respectively, (cf. Table 5.5, $z = 0.8$m), with those predicted by the finite-depth dispersion relation, (5.7). The curves shown are for the capillary free case using $n_\omega = n$ (—), and including capillary effects using n_ω by the *Green and Ampt* [1911] model, (4.7), (–· –), and the empirical formulation, (4.17), (–––). The open symbols (○,□,◊) associated with each curve denote the predicted wave numbers for the first, second and third harmonics respectively. Parameters used: $T = 348$sec, $d = 1.01$m, $H_\psi = 0.6$m, $K = 1.32 \times 10^{-4}$m/s; $n = 0.3$.

The neglect of any influence from the capillary fringe (solid line) causes a significant overestimation of the decay rate and each of the harmonic components are predicted to have the same decay rate. The rate of increase in phase lag is also overestimated relative to the data. The non-hysteretic *Green and Ampt* capillary fringe model (dash-dotted line) reduces the decay rate somewhat but again each of the harmonics are predicted to have the same decay rate and a near instantaneous ($k_i \rightarrow 0$) response to the driving head.

Consideration of a hysteretic capillary fringe through the empirical complex effective porosity model [equation (4.17)] sees a much improved comparison of the phasing but still a significant overestimation of the decay rate. The decay rate of the first two harmonics qualitatively matches that observed in the data. However, this model is unable to replicate the trend to $k_{3\omega}$. That is, in the data the decay rate of the second and third harmonics are more or less the same, whereas the model predicts $k_{3\omega} > k_{2\omega}$. It appears that the trend through all three of the harmonic components is best replicated by the curve corresponding to the *Green and Ampt* fringe model (dashed dotted line), however the model predictions (symbols on dash-dotted line) of the phase lag are very poor.

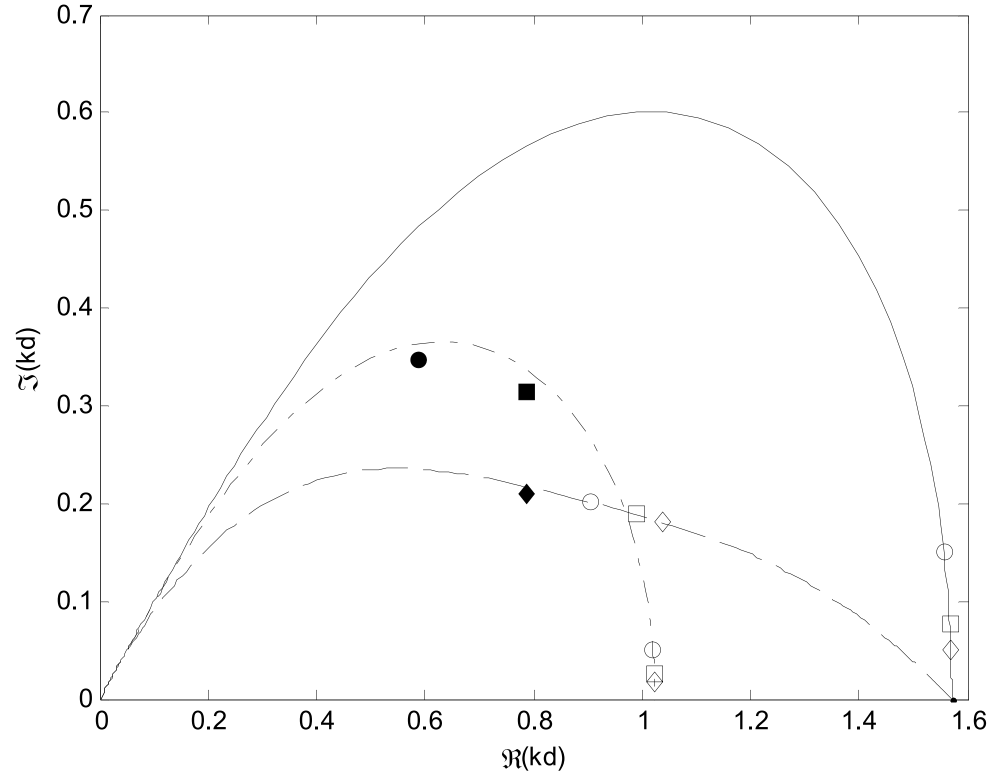

Figure 5.10: Comparison of the best fit wave numbers with theoretical predictions with a factor 4 increase in the measured hydraulic conductivity, $K = 5.28 \times 10^{-4}$m/s. All curves and symbols are as defined in Figure 5.9.

Figure 5.10 shows the comparison of theoretical with experimental wave numbers, with a factor 4 increase in K. An improved comparison results but discrepancies still persist. A fitting exercise with a free range of parameters was performed and the data was able to be matched (1ω and 2ω only) but with unrealistic parameter values, for example with a K value of an order of magnitude larger than the measured value.

The persistent discrepancies between data and theory suggest that additional process are occurring which haven't been taken in to account in the theories. In the following section the potential influence of a truncated capillary fringe on the dispersion of water table waves is discussed.

5.5.3 Potential influence of a truncated fringe on a propagating water table wave

As discussed in section 4.4, truncation of the capillary fringe will limit the moisture exchange across the water table which leads to a reduction in the complex effective porosity. This, in turn, will generally lead to smaller wave numbers [$k = k(n_\omega \omega d/K)$] which can be interpreted physically as a decrease in attenuation and increase in speed of the water table wave relative to the capillary-free case.

To examine if capillary fringe truncation influenced the sand flume results, the results of the sand column experiments described in section 4.4 are compared against the sand flume experiments via the experimental complex effective porosity. The complex effective porosity corresponding to the sand flume experiment was calculated by inserting the best fit wave number, $k_{1\omega}$ (cf. Table 5.5), into the finite-depth dispersion relation [equation (5.7)] and solving for $n = n_\omega$.

The comparison of the two is given in Figure 5.11 which plots n_ω as a function of the truncation factor,

$$TF = \frac{z_{sand} - h_{\max}}{H_\psi} \tag{5.14}$$

where h_{max} is the maximum water table elevation. For the sand flume experiments h_{max} is taken to be $d + A$ (i.e. the high water mark).

The fact that the flume effective porosity (×) lies below that found for the same degree of truncation in the sand column experiments suggests that truncation of the capillary fringe is not an important factor to the discrepancies observed and predicted wave numbers (cf. Figure 5.9). The estimated effective porosity from the flume required a truncation factor, *TF* ≈ 0.18 in the sand column, well below the value corresponding to the degree of truncation in the flume experiment, *TF* ≈ 0.48. Recall that there is limited meaning to the data shown for *TF* < 0 where clear water was observed above the sand surface for part of the oscillation period.

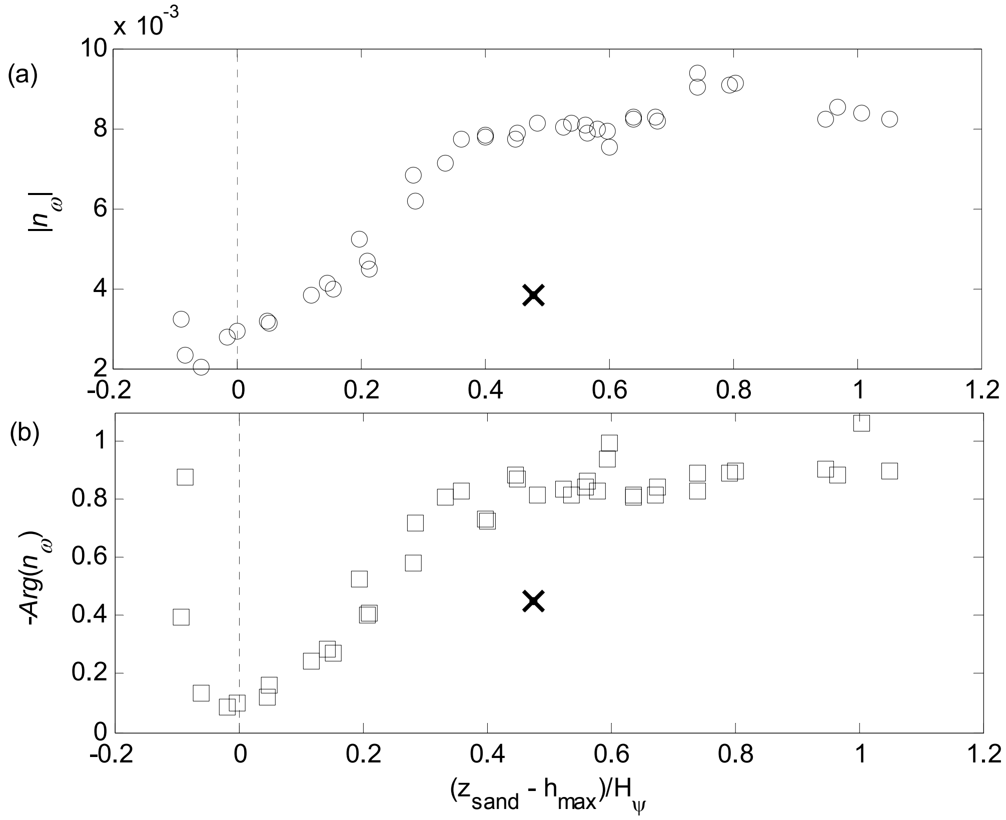

Figure 5.11: Results of sand column experiments to examine the effect of a truncated fringe on (a) the magnitude (○), and (b) negative argument (□), of estimated complex effective porosities. The crosses (×) denote the corresponding quantities for the sand flume (sloping boundary).

Due to the decay of the pressure wave as it propagates landward in the flume, *TF* will increase as h_{max} decreases, implying that any truncation effects will diminish into the interior of the flume. For the degree of truncation in the flume (*TF* ≈ 0.48), there is no observable effect on the estimated effective porosities for the same *TF* in the sand column experiments.

The influence of a truncated capillary fringe on the dispersion of the pressure wave is therefore deemed to be negligible for the present sand flume experiments. However, such a phenomenon is likely to be important for the interaction between wave runup and the water table in natural beaches, particularly for flat beaches where the water table lies very close to the sand surface.

5.6 Transferability of the complex effective porosity concept from 1D to 2D?

The empirical complex effective porosity model of *Nielsen and Turner* [2000], equation (4.17), is born from 1DV sand column experiments. The capillary correction term of *Parlange and Brutsaert* [1987], based upon the *Green and Ampt* [1911] approximation of the fringe, assumes that moisture exchange across the water table occurs only in the vertical and that there is no horizontal flow within the capillary fringe. Recently, *Silliman et al.* [2002] performed visualisation experiments using dye tracers in a laboratory sand flume forced by a steady hydraulic gradient and showed that horizontal flows were present in the capillary fringe. This, and the discrepancies described in the previous sections raises the question of "How transferable is the concept of a complex effective porosity from 1D to a 2D scenario?".

Table 5.6: Complex effective porosities estimated using the finite-depth dispersion relation, equation (5.7), and the best-fit wave numbers (first harmonic only) from the 2D sand flume experiments.

Experiment Description	n_ω	$\|n_\omega\|$	$Arg\{n_\omega\}$
Vertical boundary	$0.0345 - 0.0218i$	0.041	-0.57 (= 33°)
Sloping boundary	$0.0034 - 0.0013i$	0.004	-0.45 (= 26°)

To this end, the sand flume experiments described above in section 5.4 can be used to estimate a “2D” complex effective porosity by inserting the best fit wave numbers into the finite-depth dispersion relation, equation (5.7), and solving for n_ω (= n). The results are summarised in Table 5.6 and compared with those obtained from the 1D sand column experiments (cf. section 4.3) in Figure 5.12.

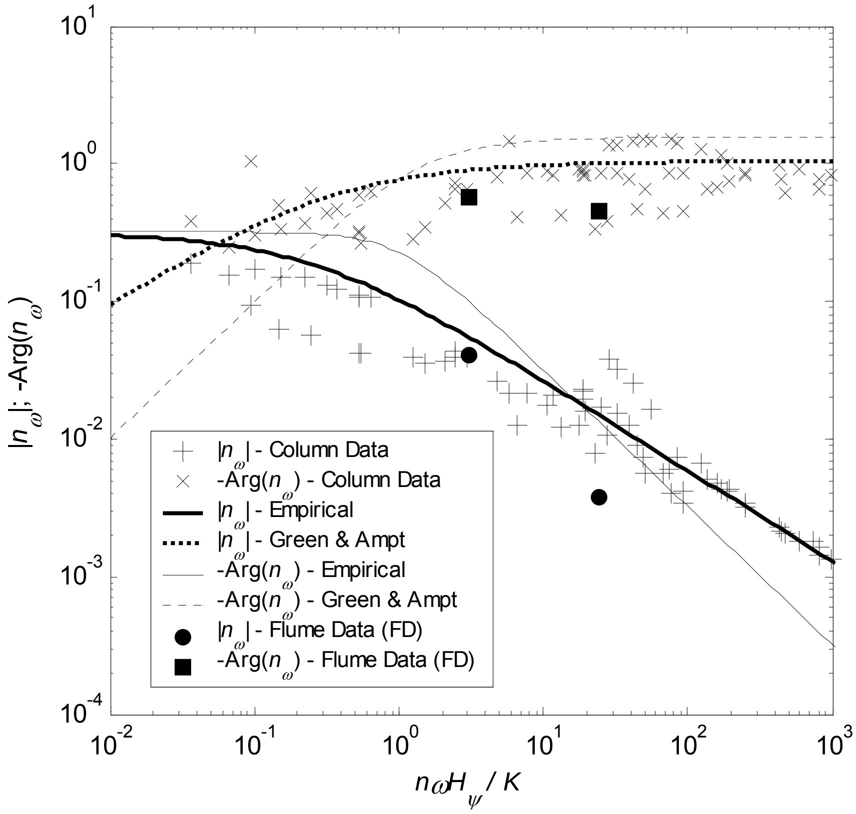

Figure 5.12: Comparison of “2D” complex effective porosities estimated from sand flume experiments with those estimated from 1D sand column experiments.

As shown in Figure 5.12 the “2D” complex effective porosities compare fairly well with the 1D sand column values. The biggest discrepancy occurring with $|n_\omega|$ for the higher frequency (sloping boundary) sand flume experiment whose $|n_\omega|$ lies well below the sand column data. For this particular experiment, large discrepancies were also found between the observed and theoretical predictions of the dispersion of the pressure wave as discussed in detail in section 5.5.2. The lower frequency (vertical boundary) sand flume experiment compares very well with the sand column data.

As a result of the discrepancies at the higher frequency leaves the question of the transferability of the complex effective porosity concept from 1D to 2D, an open one. To adequately address such a question, further experiments need to be conducted over a wide range of frequencies and in particular at higher frequencies. Such an investigation is left for future research.

5.7 Summary

Shallow aquifer water table wave dispersion theory has been shown to be inadequate in replicating, even qualitatively, observation from several field sites and in laboratory experiments. That is, all data show that the amplitude decay rate, k_r, is significantly larger than the rate of increase in phase lag, k_i, whereas the shallow aquifer theory predicts $k_r = k_i$. Consideration of vertical flow effects using the finite-depth dispersion relation theory of *Nielsen et al.* [1997] greatly improves the comparison with field data.

Sand flume experiments conducted at higher forcing frequencies further expose the limitations of the above theories due to the added influence of the capillary fringe. Consideration of the influence of the capillary fringe via the non-hysteretic *Green and Ampt* [1911] approximation in both the shallow [*Barry et al.*, 1996] and finite-depth [*Li et al.*, 2000a] aquifer theories provides some improvement but discrepancies persist. Consideration of a hysteretic capillary fringe via the empirical complex effective porosity concept [*Nielsen and Perrochet*, 2000a,b; *Nielsen and Turner*, 2000] further improves the comparison but discrepancies still persist, particularly with the higher frequency (sloping) sand flume experiment.

The persistent discrepancies suggest additional processes, not accounted for in current theory, are occurring, for example horizontal flow in the capillary fringe. The question of how transferable is the complex effective porosity concept from a 1D to a 2D propagating system remains open.

Chapter 6 – Observations and modelling of vertical flow effects

6.1 Introduction

The field data shown in Figure 5.1 indicates that the ground water dynamics in real world scenarios often deviate significantly from the simplest theories, i.e., those based on the Dupuit-Forchheimer assumptions for shallow aquifers, small amplitude oscillations and neglecting any influence from the partly saturated zone above the water table. Similar findings have been made from field observations by *Nielsen* [1990] and *Aseervatham* [1994] and also in the Hele-shaw cell experiments of *Nielsen et al.* [1997].

Nielsen et al. [1997] improved the theoretical predictions by relaxing the shallow aquifer assumption of a hydrostatic pressure distribution and derived a new, infinite order unconfined groundwater flow equation accounting for the effects of vertical flow. They obtained small-amplitude solutions to the new governing equation for a periodic boundary condition and showed them to compare well with their observations from a Hele-shaw cell. In this chapter, the finite-depth theory of *Nielsen et al*. [1997] is further verified against laboratory observations from a larger scale sand flume aquifer subject to periodic forcing and is influenced by capillarity.

The aquifer is of constant depth and packing with a simple harmonic driving head acting on a vertical interface as shown in Figure 5.5. Strong effects of finite aquifer depth and of the capillary fringe are present and enable evaluation of the theory of *Nielsen et al*. [1997]. The experimental setup and measurement procedure have been described previously in section 5.4.

6.2 Observations and Analysis

The observed time series of head oscillations from selected stations along the flume are shown in Figure 6.1 with the head variation at all stations essentially simple harmonic like the driving head.

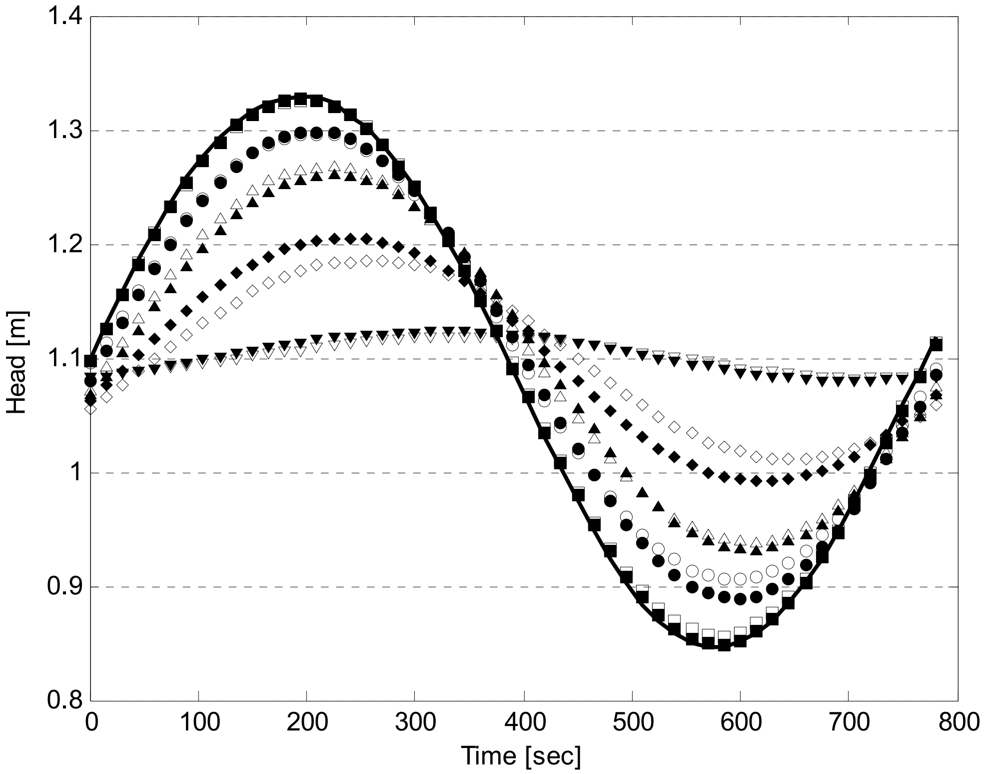

Figure 6.1: The driving head (—) and the piezometric head measured at $z = 0.1$m (solid symbols) and $z = 0.8$m (open symbols) at five selected stations along the flume: $x = 0.04$m (■,□), $x = 0.29$m (●,○), $x = 0.54$m (▲,Δ), $x = 1.34$m (♦,◊) and $x = 3.34$m (▼,∇).

Comparison of the behaviour near the base, $z = 0.1$m (solid symbols), with that closer to the water table, $z = 0.8$m (open symbols), reveals effects of finite aquifer depth. Closest to the interface at $x = 0.04$m (■,□), the head at both levels is very similar to that of the driving head, i.e. little damping has occurred and the head is more or less hydrostatic as in the clear water. The slight difference at low tide is believed to be due to seepage face formation. At $x = 0.29$m (●,○), the heads are hydrostatic except at low water where the head at $z = 0.8$m is above that at $z = 0.1$m. At $x = 0.54$m (▲,Δ), the oscillation amplitudes are similar but the mean at $z = 0.8$m is greater than at $z = 0.1$m (cf. section 6.2.1). At $x = 1.34$m (♦,◊), finite-depth behaviour becomes evident in that the oscillations near the bottom (solid symbols) have a greater amplitude and lead those near top (open symbols).

The latter is consistent with the finite-depth theory of *Nielsen et al.* [1997] who, by relaxing the hydrostatic pressure assumption, obtained the small-amplitude, expansion solution,

$$h_j^*(x,z,t) = B_j \operatorname{Re}\{e^{-k_j x}\frac{\cos k_j z}{\cos k_j d}e^{i\omega t}\} \tag{6.1}$$

where the subscript j = 1..∞, represents the wave mode and B_j is the amplitude of the piezometric head at $(x,z) = (0,d)$ for the jth wave mode. Equation (6.1) shows that the pressure distribution due to each mode is non-hydrostatic so a combination of modes is required to match the hydrostatic clear water boundary condition. The non-hydrostatic behaviour and higher wave mode boundary condition requirements are discussed in detail in sections 6.2.3 and 6.2.4 respectively.

Table 6.1: Time mean values ($\overline{h^*}$), and amplitudes ($R_{m\omega}$), and phases ($\phi_{m\omega}$) of the first 2 harmonics (angular frequencies ω and 2ω) of the piezometric head at different points in the flume.

x [m]	0	.035	.135	0.29	0.54	0.84	1.34	1.84	2.34	3.34	4.84	6.84	8.84
z [m]	-	0.10	0.10	0.10	0.10	0.10	0.10	0.10	0.10	0.10	0.10	0.10	0.10
$\overline{h^*}$ [m]	1.094	1.094	1.096	1.097	1.098	1.099	1.099	1.100	1.100	1.101	1.099	1.099	1.099
R_ω [m]	.235	.233	.223	.200	.165	.139	.106	.076	.047	.022	.009	.002	.001
ϕ_ω [rad]	0	.01	.05	.13	.25	.24	.37	.48	.69	1.07	1.47	2.00	2.34
$R_{2\omega}$ [m]	.007	.006	.007	.004	.003	.002	.001	-	-	-	-	-	-
$\phi_{2\omega}$ [rad]	0	.03	3.36	.76	.68	.74	.82	-	-	-	-	-	-
x [m]	-	.035	.135	0.29	0.54	0.84	1.34	1.84	2.34	3.34	4.84	6.84	8.84
z [m]	-	0.80	0.80	0.80	0.80	0.80	0.80	0.80	0.80	0.80	0.80	0.80	0.80
$\overline{h^*}$ [m]	-	1.096	1.099	1.101	1.102	1.101	1.100	1.100	1.101	1.099	1.099	1.099	1.099
R_ω [m]	-	.229	.210	.192	.163	.132	.088	.058	.039	.019	.008	.003	.001
ϕ_ω [rad]	-	.01	.05	.10	.22	.32	.53	.73	.94	1.23	1.62	2.28	2.31
$R_{2\omega}$ [m]	-	.005	.001	.002	.002	.001	.001	-	-	-	-	-	-
$\phi_{2\omega}$ [rad]	-	0.00	1.04	2.00	2.49	3.02	2.79	-	-	-	-	-	-

Table 6.1 summarises the results (time means, amplitudes and phases) of harmonic analysis conducted on observations from all piezometers. If the amplitude of the second harmonic $R_{2\omega}(x,z)$ was large enough (≥ 1mm), it too was extracted along with the corresponding phase $\phi_{2\omega}$.

6.2.1 Mean head values

The time-averaged head profiles $\overline{h^*(x,0.1m)}$ and $\overline{h^*(x,0.8m)}$ are shown in Figure 6.2. At both levels, the piezometric head is higher for $x \to \infty$ than at $x \to 0^+$. However, the common asymptotic value, $\overline{h_\infty^*}$, of approximately 1.099m is below the "Boussinesq" value of $\sqrt{d^2 + A_o^2/2} \approx 1.107$m derived by *Philip* [1973]. In other words, with a mean water level of d = 1.094m in the driving head reservoir, the measured inland over-height was only $\overline{\eta_\infty}$ = 0.005m compared to 0.013m given by *Philip's* [1973] shallow aquifer, capillary-free theory.

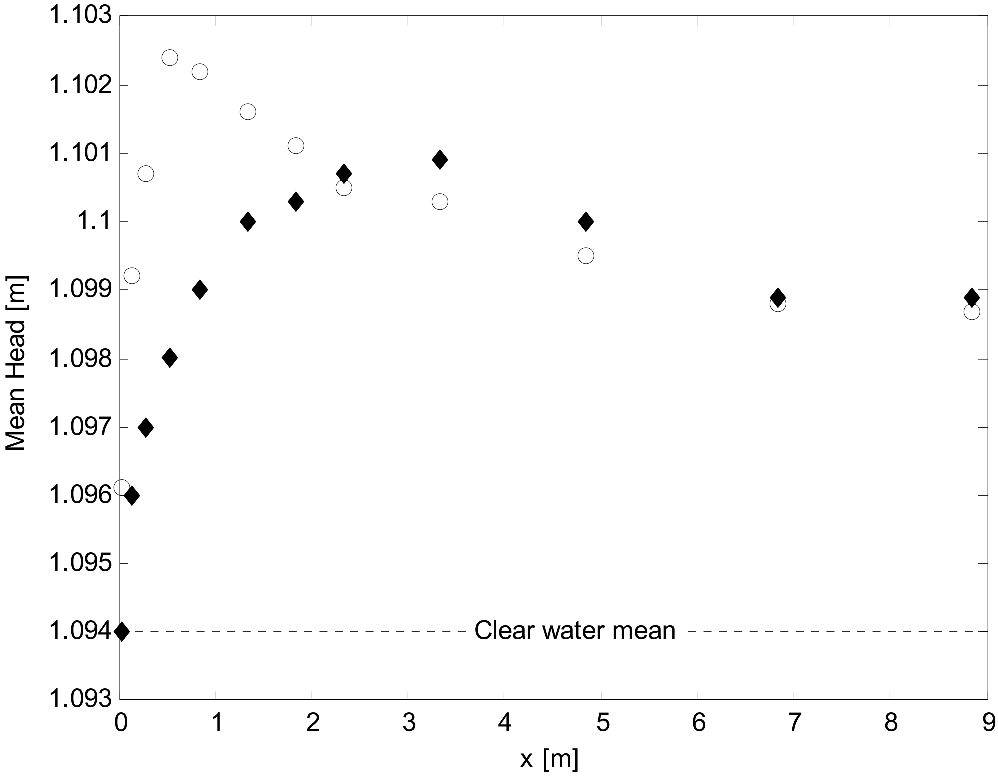

Figure 6.2: Measured time averaged piezometric heads close to the bottom $\overline{h^*(x,0.1m)}$ (♦) and close to the water table $\overline{h^*(x,0.8m)}$ (○). The mean driving head level is also shown (----).

This difference is interesting, because *Philip's* [1973] shallow aquifer result was shown by *Knight* [1981] to be valid even if the aquifer is not shallow. The differences are therefore believed to be due to capillary effects in the form of flow above the water table or suction on the vertical faces. Recently, *Siliman et al.* [2002] demonstrated that horizontal as well vertical flows were present in the capillary fringe and this may play a role. Also, meniscus suction on the vertical face of the aquifer at $x = 0$ may well be different from that at the inland boundary. If there was no such imbalance, the simple requirement of balance between the total porewater pressure forces at $x = 0$ and at $x = 8.84$m (where the oscillation has died out),

$$\overline{\int_{z=0}^{sandsurface} p(0,z,t).dz} = \overline{\int_{z=0}^{sandsurface} p(8.84,z,t).dz} \tag{6.2}$$

would lead to *Philip's* [1973] result, i.e., $\overline{h(8.84m)} = \sqrt{d^2 + A_o^2/2} \approx 1.107$m.

Since the flume was covered with loose plastic and the sand remained moist at the top, evaporation is not believed to have been significant.

Conditions are hydrostatic in the clear water reservoir and below the water table at the landward end, and hence $\overline{h^*}$ does not depend on z at these boundaries. However, in the range $0 < x < 4$m, it is evident that the conditions are not hydrostatic as the mean piezometric head is different at the two levels, with values at the top being greater than at the bottom. The pressure in the driving head reservoir at $x = 0$ is hydrostatic but inside the sand, deviations from hydrostatic conditions develop very rapidly to a peak difference of 4 mm between $x = 0.25$m and $x = 0.5$m. The fact that both $\overline{h^*(x,0.1m)}$ and $\overline{h^*(x,0.8m)}$ show local maxima instead of increasing monotonically with x is not covered by any theory known to the writer. *Dunn et al.* [in prep.] present a detailed investigation of the observed time-averaged head levels including an analytical solution to describe the resultant circulation.

6.2.2 Oscillation amplitudes and phases

The dispersive properties of the observed pressure wave have been discussed previously in section 5.5.

6.2.3 Non-hydrostatic behaviour

At the interface with the clear water reservoir, at $x = 0$, conditions must be hydrostatic. Hence, oscillation amplitudes and phase shifts are observed to be practically identical at the top and at the bottom of the aquifer for $x = 0.04$m, cf. Figure 6.1 and Table 6.1. However, both oscillation amplitudes and phases display clear non-hydrostatic features in the interior. That is, for $x > 1$m, the oscillation amplitudes R_ω and $R_{2\omega}$ are larger at the bottom than at the top (cf. Table 6.1). This is in qualitative agreement with the small amplitude, finite-depth theory of *Nielsen et al.* [1997], as expressed by equation (6.1). The theory predicts different ratios, $R_{\omega,j}(x,0.1\text{m})/\ R_{\omega,j}(x,0.8\text{m})$, for the different modes at each frequency and the overall behaviour corresponds to a linear combination of several modes. However, the primary mode dominates for $x > 1$m because the higher modes decay very rapidly due to their much larger k_r values, see Table 6.2.

Table 6.2: Wave numbers in terms of the dimensionless depths $k_{\omega,j}d$ ($d = 1.094$m) and head coefficients for $z = 0$ ($A_{\omega,j}$) and at $z = d$ ($B_{\omega,j}$) based on the $k_{\omega,1}d$ equal to the overall best fit value (5.12) and the small amplitude theory of *Nielsen et al.* [1997].

j	$k_{\omega,j}d$	$A_{\omega,j}$	$B_{\omega,j}$
1	.752 +.321i	1.079 +.078i	.846 -.181i
2	3.283 +.190i	-.094 -.100i	.098 +.098i
3	6.351 +.102i	.022 +.031i	.022 +.031i
4	9.469 +.069i	-.010 -.014i	.010 +.014i
5	12.600 +.052i	.005 +.008i	.005 +.008i
6	15.734 +.042i	-.003 -.005i	.003 +.005i
7	18.872 +.035i	.002 +.004i	.002 +.004i
8	22.010 +.030i	-.002 -.003i	.002 +.003i
	Sum:	.999 -.001i	.989 -.018i

The primary mode with wave number $k_{\omega,1}$ taken as the overall best fit value, corresponding to (5.12), gives the head amplitude ratio $R_\omega(x,0.1\text{m})/\ R_\omega(x,0.8\text{m})$,

$$\frac{\cos\left(k_{\omega,1}\times 0.1m\right)}{\cos\left(k_{\omega,1}\times 0.8m\right)}=1.117+0.155i=1.13e^{0.14i} \tag{6.3}$$

i.e., a magnitude ratio of 1.13 and a phase lead of the head at z = 0.1m by 0.14radians.

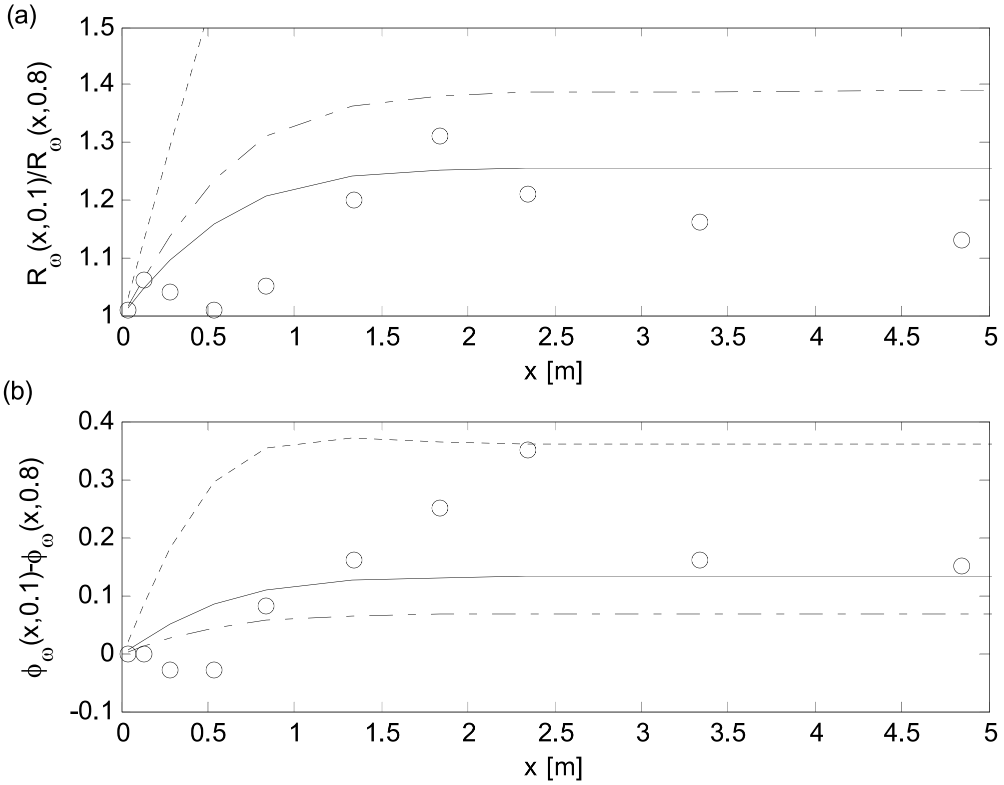

Figure 6.3: Comparison of measured (○) amplitude ratios, (a), and phase leads, (b), with those obtained by equation (6.1). Theoretical wave numbers were calculated using the dispersion relation (5.7) with a real valued porosity (---), and the complex effective porosities by (4.7) (– – –) and (4.17) (—). Parameters used are: T = 772sec; d = 1.094m; n = 0.32; K = 0.00047m/s; H_ψ = 0.55m.

The data, which contains contributions from all modes, show considerable variation as seen for x < 1m in Figure 6.3. However, for x > 1m where the higher modes are insignificant, there is reasonable agreement. Thus the non-hydrostatic behaviour displayed landward of the decay of the higher modes is in agreement with small amplitude theory. Also comforting is the much improved agreement upon inclusion of capillarity effects via both the non-hysteretic *Green and Ampt* and hysteretic empirical complex effective porosity models, equations (4.7), (– - –), and (4.17), (—), respectively.

6.2.4 Multiple mode content due to the hydrostatic boundary condition at x = 0

The pressure distribution in the clear water reservoir at $x = 0$ is hydrostatic. However, the individual water table wave modes all have a non-hydrostatic pressure distribution given by (6.1) which corresponds to,

$$h^*_{\omega,j}(x,z,t) = h^*_{\omega,j}(x,0,t)\cos k_{\omega,j} z \tag{6.4}$$

where $k_{\omega,j}$ with $j = 1,2,\ldots\infty$, are the infinitely many roots of the finite-depth dispersion relation (5.7). This means that an expansion solution, i.e., a combination of modes, is needed in order to match a hydrostatic boundary condition such as,

$$h^*(0,z,t) = d + A_o \cos\omega t = d + \mathrm{Re}\{A_o e^{i\omega t}\} \qquad , \qquad 0 < z < d \tag{6.5}$$

Following the notation of *Nielsen et al.* [1997], the piezometric head is written as an expansion of the form,

$$h^*(x,z,t) = d + \mathrm{Re}\left\{A_o e^{i\omega t} \sum_{j=1}^{\infty} A_{\omega,j} e^{-k_{\omega,j}x} \cos k_{\omega,j} z\right\} \tag{6.6}$$

which for $x = 0$ becomes,

$$h^*(0,z,t) = d + \mathrm{Re}\left\{A_o e^{i\omega t} \sum_{j=1}^{\infty} A_{\omega,j} \cos k_{\omega,j} z\right\} \tag{6.7}$$

which means that the head coefficients, $A_{\omega j}$, for the different modes are determined from,

$$1 = \sum_{j=1}^{\infty} A_{\omega,j} \cos k_{\omega,j} z \qquad \text{for} \qquad 0 < z < d \tag{6.8}$$

The values corresponding to the present experiment for $A_{\omega j}$, which gives the mode contribution at $(x,z) = (0,0)$, along with the coefficient $B_{\omega j} = A_{\omega j}\cos k_{\omega j} d$, which gives the mode contribution at $(x,z) = (0,d)$, are given in Table 6.2. The alternating behaviour of $A_{\omega j}$ is typical, see Table 1 of *Nielsen et al.* [1997], and is seen to converge quite rapidly with respect to the head at the bottom, $B_{\omega j}$. Hence the convergence of the expansion is slower near the water table than at the bottom.

The way in which the successive approximations, including more and more modes in (6.6) - (6.8), approach the constant (hydrostatic) head over the range $0 < z < d$ at $x = 0$, is illustrated by Figure 6.4 with the parameter values for the present experiment, corresponding to the coefficients $A_{\omega j}$ and $B_{\omega j}$ in Table 6.2. The convergence of (6.8) is much faster at $z = 0$ than at $z = d$. The expansion solution (6.8), being part of a small amplitude solution, exact only for $A_o/d \rightarrow 0$, has limited meaning above $z = d$.

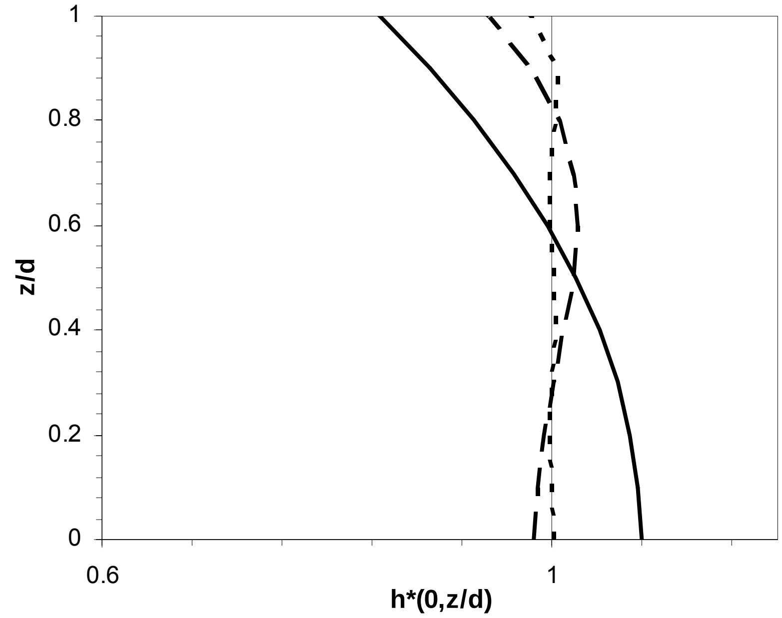

Figure 6.4: Dimensionless head amplitude at $x = 0$, $h^*(0, z/d)$, given by equation (6.8) including the primary mode only (——), the first two modes (— — —) and the first five modes (-----).

The solution, (6.1), solves, in part, the problem of matching the hydrostatic clear water reservoir with the non-hydrostatic pressure field of each mode in the interior as outlined by *Dagan* [1967]. This is achieved by matching the hydrostatic boundary condition with a suitable combination of non-hydrostatic modes at $x= 0$. However, the small amplitude expansion, (6.1), is only applicable over the range $0 < z < d$ and therefore neglects the water pressure between $z = d$ and the water surface at maximum driving head level. It also neglects any meniscus suction above $z = d$ at minimum driving head level. The modelling of these aspects requires a finite amplitude formulation of the boundary condition and consideration of capillary suction at the vertical interface, including seepage face dynamics. To the knowledge of the writer, such a boundary condition is so far not available in a form suited for analytical solution. Hopefully, the experimental findings of the present study can assist in the process of achieving this.

Capillary suction and a possible seepage face will complicate the boundary condition at $x = 0$ in the way qualitatively outlined in Figure 6.5.

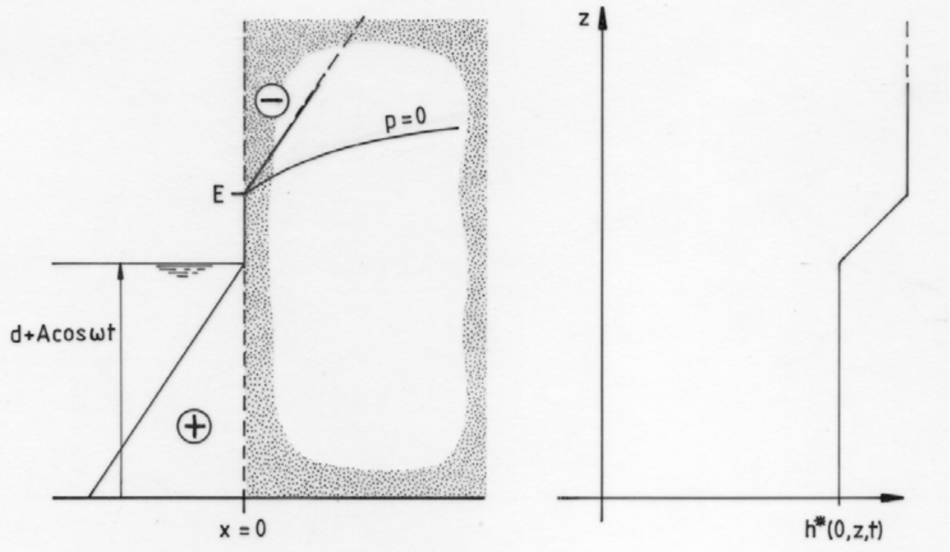

Figure 6.5: At low water a seepage face may form between the driver level and the moving exit point E, along which, the pressure is atmospheric. Hence $h^* = p/\rho g + z$ will increase linearly between the surface and E. Above E, the pore pressure may again be hydrostatic and h^* constant up to a height comparable with H_ψ above E. The appearance of a seepage face is seen to increase the time-mean head at $x = 0$ and hence throughout. The variation of the seepage face height through the forcing cycle might be expected to drive higher harmonic components of h^* in the aquifer. However, in this study such higher harmonics were found to be insignificant.

The fact that the complete small amplitude solution contains many modes, each decaying with x at different rates, suggests that the overall decay of the head oscillations is not necessarily exponential and that the overall phase shift may not necessarily grow linearly with x. This is illustrated in Figure 6.6 which shows the first three metres only and the phase of the driving head has been subtracted from the local phase angles. The multiple-mode theory near the bottom, (solid lines), show a slight downward convex trend while closer to the top, (dashed lines), an upward convex behaviour is seen. As in Figure 6.3, the comparison in the transitional, multiple-mode zone, $0 < x < 1$m, is not so good.

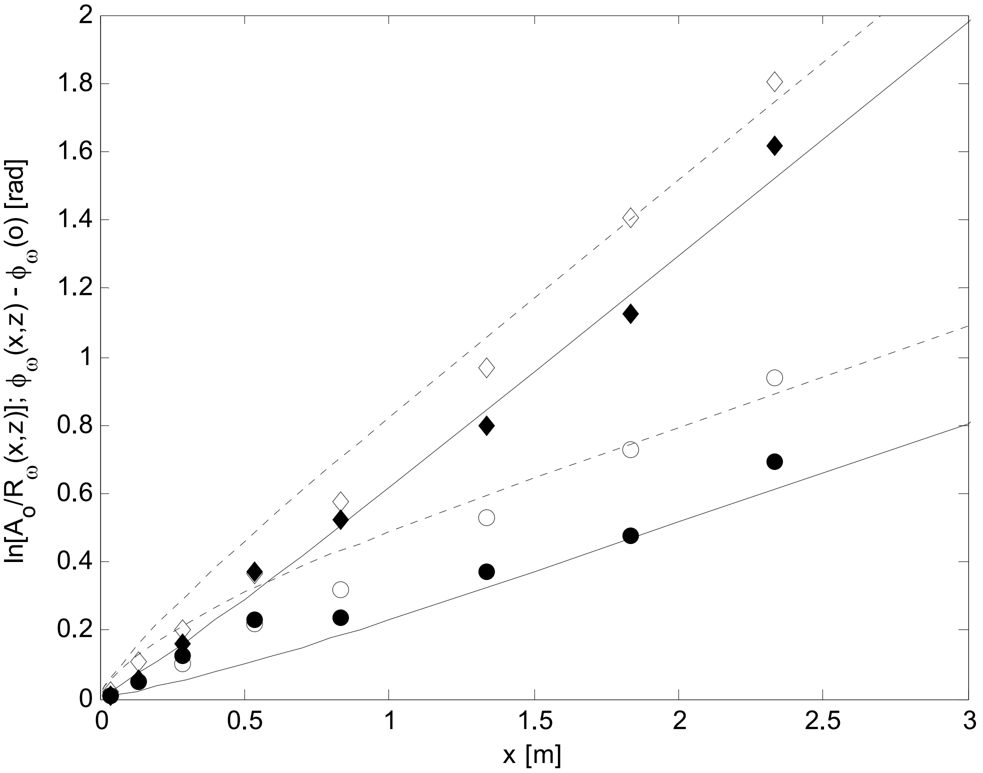

Figure 6.6: Details of the h^* oscillation decay measured by $\ln[A_o/R_\omega(x,z)]$ and phase lags, $\phi_\omega(x,z)$ - $\phi_\omega(0)$, over the first 3 metres of the flume. Symbols shown represent; phase lag at z = 0.1m (•) and at z = 0.8m (o); $\ln[A_o/R_\omega(x,z)]$ at z = 0.1m (♦) and at z = 0.8m (◊). For each symbol, the nearest line shows the same quantity according to the small amplitude expansion, (6.6).

By definition, the lines and the symbols in Figure 6.6 all come together at the origin. The lines then diverge and become parallel for x > 1m indicating that only the primary mode remains. The asymptotic distance between the upper lines corresponds to the amplitude ratio $R_{\omega,1}(x,0.1\text{m})/R_{\omega,1}(x,0.8\text{m})$ = 1.13 calculated from (6.3). The asymptotic distance between the lower lines corresponds to the phase lead of 0.14radians (7.9°) by $h^*_{\omega,1}(x,0.1\text{m})$ ahead of $h^*_{\omega,1}(x,0.8\text{m})$.

The differences between each set of symbols and the corresponding line in Figure 6.6 are, of course, partly due to measurement scatter. However, the differences may also indicate “theoretical” differences, i.e., the differences that would exist between perfect measurements and the expansion solution (6.6) which is derived from a simplified boundary condition as discussed in connection with Figure 6.4 and Figure 6.5.

6.2.5 Higher harmonics due to non-linearity in the interior

If a seepage face forms during part of the forcing cycle (cf. Figure 6.5), the $h^*(0,z,t)$ variation at points above $z = d$ will not necessarily be simple harmonic. Hence, the seepage face will probably generate higher harmonic components of $h^*(x,z,t)$ near $x = 0$. It is also conceivable that other non-linear phenomena could generate higher harmonics. However, the second harmonics measured in the experiment were everywhere equal to or smaller than that in the driving head reservoir (cf. Table 6.1 with $R_{2\omega}(0)$ = 7mm). In other words, the measured second harmonics do not indicate that seepage face formation or any other phenomenon generated significant second harmonic oscillations at $x = 0$.

A number of investigators: *Steggewentz* [1933], *Dagan* [1967] and *Parlange et al.* [1984] have investigated the generation of higher harmonics in the interior due to non-linearity of the field equation. They carried out the analysis for shallow aquifers with no capillary effects and found that due to the non-linearity of the Boussinesq equation a simple harmonic wave at frequency ω and wave number k will generate two waves at frequency 2ω, one that decays as $\exp(-\sqrt{2}\,k_r x)$ and one that decays as $\exp(-2k_r x)$. These two, 2ω-modes cancel each other at $x = 0$ but yield a maximum amplitude of approximately $0.179A_o^2/d$ for $kx \approx 0.6$ which, for the experiment, corresponds to a maximum amplitude of 5mm between $x = 0.5$m and $x = 1$m. The experimental data show essentially a monotonic decay of $R_{2\omega}$ from the driving head value of 7mm at $x = 0$. Hence, the generation of second harmonics by non-linearity in the interior seems to have been weakened by the presence of a capillary fringe in the experiment. All in all, the present finite amplitude ($A_o/d \approx 0.22$) experiments show no evidence of significant second harmonics being generated at the interface or in the interior.

6.3 Summary

Applied in a quasi-predictive manner (i.e. using the experimental wave number, (5.12), as input), the small amplitude theory of *Nielsen et al.* [1997], (6.1), appropriately accounts for the observed finite-depth effects of greater amplitude and phase lead at the base [cf. Figure 6.3]. The h^* oscillations far from the driving head reservoir (x > 1m) have greater amplitude near the bottom than near the water table $|h^*(x,0.1\text{m},t)|/|h^*(x,0.8\text{m},t)| \approx 1.13$ and the oscillations at the bottom lead those close to the water table by about 0.14radians. This is in agreement with the finite-depth, small amplitude theory of *Nielsen et al.* [1997] as described by (6.1).

The transition from the multiple mode hydrostatic behaviour near the driving head reservoir ($x \to 0^+$) to the asymptotic single mode behaviour for x > 1m is qualitatively modelled by small amplitude theory. However, the observed differences in the details of this transition (Figure 6.6), between the small amplitude solution and the measurements, are probably more than measurement scatter. It is expected that upwards from the present value ($A_o/d = 0.22$) a more detailed finite amplitude formulation of the boundary condition is warranted.

The mean water table height is higher for $x \to \infty$ than for $x \to 0^+$ in qualitative agreement with the shallow aquifer theories of *Philip* [1973] and *Parlange et al.* [1984]. However, the rise in mean head levels is not monotonic as predicted by these theories, a maximum occurs at about x = 1m (cf. Figure 6.2). The asymptotic inland over-height is only about 1/3 of the shallow, capillary free aquifer value. This reduction may not be entirely due to non-shallowness. Differences in the time-averaged capillary suction patterns at the two ends of the aquifer may also play a role. The time-mean piezometric head $\overline{h^*(x,z)}$ is significantly non-hydrostatic in the range 0.04m < x < 2.5m with larger values at the top indicating steady downward flow through the upper part of the aquifer.

Non-linear effects were surprisingly small in the experiments with no evidence of second harmonics being generated either by the finite amplitude ($A_o/d = 0.22$) boundary condition or by non-linearity in the interior.

Chapter 7 – Observations and modelling of sloping boundary effects

7.1 Introduction

In natural systems, the boundary between an aquifer and an oscillating clear water body will generally be non-vertical. A prime example is a sloping beach face subjected to a complex combination of tidal and wave forcing. *Lanyon et al.*, [1982] present field observations which clearly illustrate the temporal skewing of the water table oscillations due to the non-linear filtering effect of the sloping boundary. This is explained simply by the sloping beach filling more easily than it can drain under gravity leading to a steeper rise than decline in water levels.

From a mathematical perspective, the main implication of the sloping boundary illustrated in Figure 7.1 is that the periodic boundary condition is no longer applied at a fixed x-coordinate, as is the case if the boundary were vertical. The boundary condition is now applied at the moving x-coordinate of the shoreline i.e.,

$$h\left(x_{SL}\left(t\right),t\right)=d+A\cos\omega t \tag{7.1}$$

where,

$$x_{SL}\left(t\right)=A\cos\omega t\cot\beta_F \tag{7.2}$$

with β_F the slope of the beach face.

Nielsen [1990] first addressed this problem by applying a step-wise perturbation approach to solving the linearised Boussinesq equation,

$$\frac{\partial h}{\partial t}=\frac{Kd}{n}\frac{\partial^2 h}{\partial x^2} \tag{7.3}$$

where *h* is the water table elevation; *K* is the hydraulic conductivity; *d* is the mean aquifer thickness; *n* is the drainable porosity; and *x* and *t* represent the shore-normal coordinate and time, respectively.

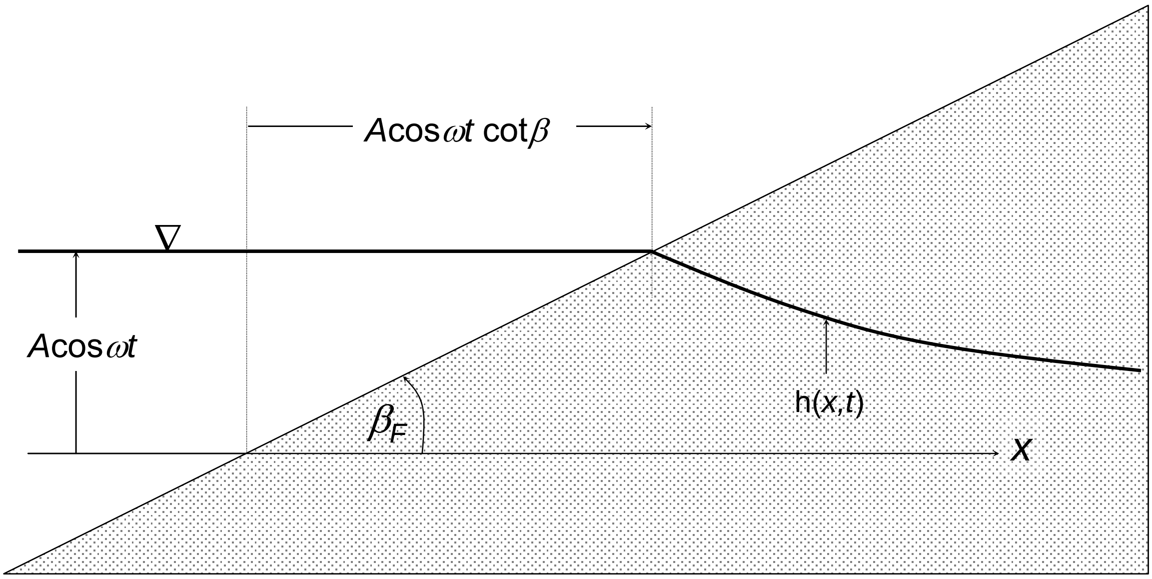

Figure 7.1: Schematic of the moving shoreline boundary condition.

Setting the perturbation beach slope parameter,

$$\varepsilon = kA\cot\beta_F \tag{7.4}$$

Nielsen [1990] used successive approximations to the boundary condition and obtained the following solution,

$$\begin{aligned} h_{Nielsen}(x,t) &= d + Ae^{-kx}\cos(\omega t - kx) \\ &+ \varepsilon A\left[\frac{1}{2} + \frac{\sqrt{2}}{2}e^{-\sqrt{2}\,kx}\cos(2\omega t + \frac{\pi}{4} - \sqrt{2}\,kx)\right] \\ &+ \varepsilon^2 A\left(\frac{1}{4} - \frac{\sqrt{2}}{2}\right)\left[e^{-kx}\sin(\omega t - kx) + e^{-\sqrt{3}\,kx}\sin(3\omega t - \sqrt{3}\,kx)\right] + \mathrm{O}\left(\varepsilon^3\right) \end{aligned} \tag{7.5}$$

This solution describes the effect of the sloping boundary, including the generation of higher harmonics due to the non-linear filtering effect of the sloping interface. The solution also demonstrated that the presence of a sloping boundary induces a water table overheight above mean sea level greater than that induced by non-linearity in the interior [cf. *Philip*, 1973; *Knight*, 1981; *Parlange et al.*, 1984]. Further mathematical refinement of the problem has been conducted in recent times [e.g. *Li et al.*, 2000b; *Teo et al.*, 2003] the results of which are described later in section 7.5.

Despite the theoretical advancements, only a few investigators have addressed the problem from a physical perspective and of those most of them have conducted field experiments [e.g. *Lanyon et al.*, 1982; *Nielsen*, 1990; *Raubenheimer et al.*, 1999] where it is difficult to ascertain exactly what causes what. In this chapter, the sand flume described in section 5.4 is used to eliminate some of the complicating factors found in field experiments (e.g. unknown aquifer geometry and complex forcing conditions). The experimental observations are discussed in section 7.3 in terms of process identification and reveal some new insights into the details of the generation of higher harmonics at the boundary (section 7.4). In sections 7.5 and 7.6 the data is used to test existing analytical and numerical models respectively.

7.2 Experimental setup and procedure

The experimental setup and procedure has been described in detail in section 5.4. Figure 7.2 shows the same sand flume configuration but with a linear sloping boundary. The reader is referred to Table 5.2 and Table 5.3 for the aquifer and forcing parameters respectively.

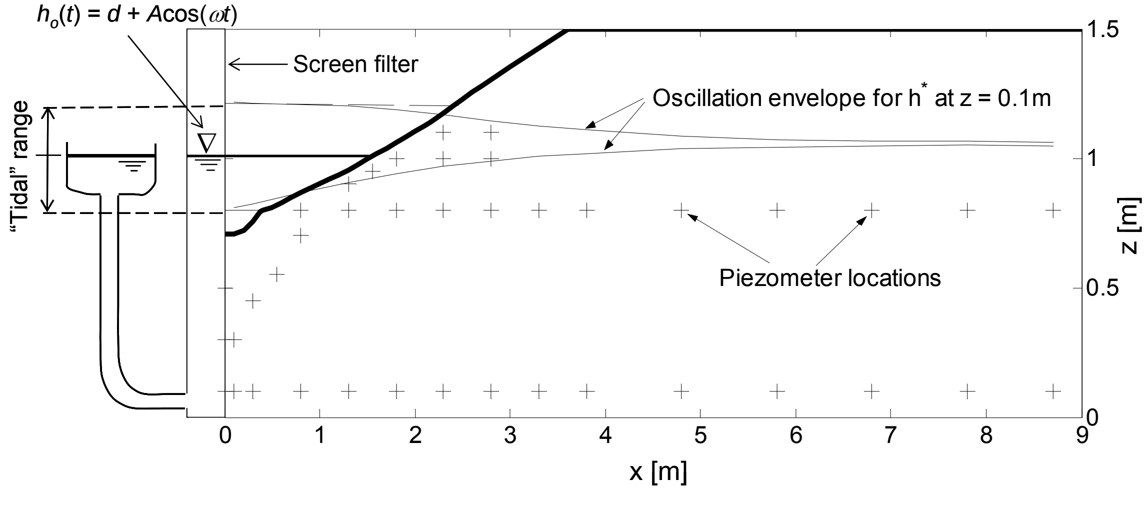

Figure 7.2: Experimental flume setup. The simple harmonic driving head parameters were: T = 348sec; d = 1.01m; A = 0.204m. The boundary slope, β_F = 0.205radians (= 11.7°) and the coordinates, (x, z), of the high, and low water marks were (0.4m, 0.8m) and (2.46m, 1.21m) respectively, and (1.57m, 1.01m) for the mean clear water level.

7.2.1 The sloping boundary

The choice of slope for the boundary was determined such that it remained stable for the given forcing frequency. An initial estimate of a linear profile was set manually and then the flume was left running for a couple of days and the profile monitored until it became stable. The resulting linear part of the stable profile was then set for the whole boundary and again the flume was left running for a couple of days to ensure the slope remained stable. The beach slope was determined by least squares fitting of a straight line to the surveyed profile between the high and low water marks, yielding β_F = 0.205radians (or 11.7°) with a high regression coefficient value, R^2=0.995. The coordinates, (x, z), of the low and high water marks were (0.47m, 0.81m) and (2.45m, 1.21m) respectively, and (1.57m, 1.01m) for the mean clear water level.

7.3 Results and discussion

A comparison of observed head levels measured near the base (z = 0.1m, solid symbols) with those measured near the water table (z = 0.8m, open symbols) at several locations along the flume is shown in Figure 7.3.

Two particular features in the observations stand out and are consistent with observations from the field [e.g. *Lanyon et al.*, 1982; *Nielsen*, 1990]. Firstly, at all locations the non-linear filtering effect of the sloping boundary is clearly apparent with a steep rise as the beach fills and a more gradual decline as it drains, thereby generating higher harmonics at the boundary. Secondly, evidence of seepage face formation is seen when the heads in the active forcing zone, $0.4 < x < 2.46$m (squares and circles), become decoupled from the driving head and remain near the level of the sand surface, again contributing to the generation and nature of higher harmonics. Accurate measurement of the exit point proved difficult because of non-uniformity across the width of the flume due to the presence of rivulets within the seepage face. Hence the "effective elevation" (effective with respect to the water table dynamics) of the exit point was estimated based on head level measurements near the sand surface (see ---- in Figure 7.3).

Another point of interest is the non-hydrostatic pressure in the vicinity of the boundary. In the active forcing zone (squares and circles) the upper piezometers (open symbols) have larger amplitudes and tend to lead the fluctuations near the base (solid symbols) on the rising tide. Around the low water mark, during the presence of a seepage face, the pressure briefly approaches hydrostatic conditions before the shoreline passes over the piezometers. Just landward of the high water mark, at x = 2.85m (▲,Δ), similar trends are seen but the deviations from hydrostatic pressure are substantially reduced. During low water, more or less hydrostatic conditions prevail.

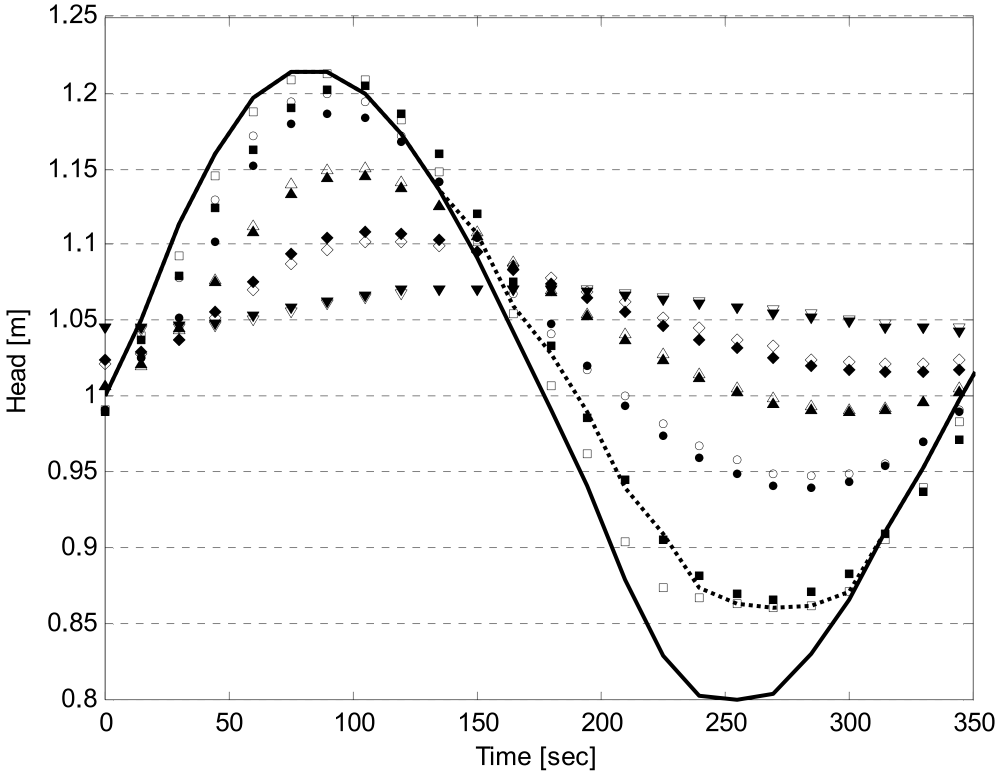

Figure 7.3: Observed driving head (—) and piezometric head levels measured at z = 0.1m (solid symbols) and z = 0.8m (open symbols) at five selected stations along the flume: x = 0.85m (■,□), x = 1.85m (•,○), x = 2.85m (▲,Δ), x = 3.85m (♦,◊), x = 5.85m (▼,∇). (----) denotes the approximate exit point elevation.

In the interior, at x = 3.85m (♦,◊) and x = 5.85m (▼,∇), the trend is reversed, with measurements near the base (♦,▼) exhibiting both a greater amplitude and a phase lead of that at the top (◊,∇). This is indicative of vertical flow effects in a finite-depth aquifer, consistent with the theory of *Nielsen et al.* [1997] which has been verified against experiments in the same sand flume with a vertical boundary in Chapter 6.

It is also interesting to note that the exit point started to rise shortly before the passing of the shoreline. This has been seen previously in the field by *Turner* [1993] and in the numerical experiments of *Li et al*. [1997] and is a discussion point between *Li et al.* [1999b] and *Nielsen* [1999c]. A more detailed discussion of the phenomenon is given in section 7.6.2.4 in association with numerical modelling of the present data.

The time-means, amplitudes and phases were extracted from the data by harmonic analysis and are presented in Table 7.1 where values for the first three harmonics are provided.

7.3.1 Amplitudes and phases

The extracted amplitudes for the first three harmonics are shown in Figure 7.4. Plotted on a log scale, an exponential decay in the interior (landward of the high water mark) is seen to be in agreement with small amplitude theory,

$$h(x,t) = d + Ae^{-k_r x}\cos(\omega t - k_i x) \tag{7.6}$$

where A is the (simple harmonic) driving head amplitude and $k = k_r + ik_i$ is the water table wave number with k_r representing the amplitude decay rate and k_i the rate of increase in phase lag. This is despite the fact that, for the current experimental parameters, $A/d \approx 0.2$, which suggests that the experiment is nearing the upper limit of the validity of the small amplitude assumption.

The non-linear filtering effect of the sloping boundary is clearly illustrated by the generation of the second and third harmonic components in the active forcing zone, 0.4m < x < 2.46m. The second harmonic has its maximum amplitude slightly landward of the mid point of the forcing zone at both piezometer elevations. The third harmonic shows an initial decay from the 3ω signal in the driving head, followed by an increase before reaching a maximum near the high water mark. More details of the generation of higher harmonics in the forcing zone are given in section 7.4.

Table 7.1: Results of harmonic analysis on observed head levels: $\overline{h^*}$ is the mean; $R_{m\omega}$ is the amplitude; $\phi_{m\omega}$ is the phase; the subscript $m\omega$ denotes the harmonic component.

x [m]	z [m]	$\overline{h^*}$ [m]	R_ω [m]	ϕ_ω [rad]	$R_{2\omega}$ [m]	$\phi_{2\omega}$ [rad]	$R_{3\omega}$ [m]	$\phi_{3\omega}$ [rad]
0	0	1.010	0.203	1.55	0.005	-1.37	0.009	-2.55
0.1	0.1	1.012	0.199	1.60	0.004	-1.52	0.009	-2.44
0.3	0.1	1.013	0.191	1.63	0.006	-2.12	0.008	-2.33
0.8	0.1	1.024	0.169	1.74	0.008	-2.68	0.001	-2.97
1.3	0.1	1.033	0.144	1.83	0.017	-2.80	0.003	-1.95
1.8	0.1	1.043	0.120	1.83	0.021	-3.01	0.006	-1.74
2.3	0.1	1.050	0.096	1.91	0.018	-2.99	0.004	-1.84
2.8	0.1	1.053	0.076	2.03	0.015	-2.90	0.004	-1.78
3.3	0.1	1.055	0.058	2.14	0.012	-2.80	0.003	-1.62
3.8	0.1	1.055	0.045	2.27	0.009	-2.69	0.002	-1.54
4.8	0.1	1.057	0.024	2.58	0.004	-2.51	0.001	-1.47
5.8	0.1	1.057	0.014	2.90	0.001	-2.27	0.001	-0.37
6.8	0.1	1.057	0.009	-3.00	0.001	-1.92	0.000	-0.21
7.8	0.1	1.056	0.005	-2.61	0.001	-1.40	0.000	1.05
8.7	0.1	1.057	0.003	-1.64	0.001	-0.73	0.000	2.78
0.8	0.8	1.020	0.180	1.64	0.014	-2.96	0.004	2.60
1.3	0.8	1.036	0.147	1.72	0.025	3.14	0.002	2.86
1.8	0.8	1.049	0.123	1.78	0.027	3.04	0.005	-2.20
2.3	0.8	1.055	0.100	1.91	0.023	-3.09	0.006	-2.00
2.8	0.8	1.055	0.077	2.04	0.017	-2.93	0.005	-1.75
3.3	0.8	1.055	0.057	2.18	0.012	-2.83	0.003	-1.78
3.8	0.8	1.056	0.040	2.38	0.007	-2.60	0.002	-1.50
4.8	0.8	1.057	0.022	2.69	0.003	-2.45	0.001	-1.47
5.8	0.8	1.057	0.013	3.05	0.002	-1.95	0.000	-1.20
7.8	0.8	1.056	0.005	-2.61	0.001	-1.40	0.000	1.05
8.7	0.8	1.058	0.003	-1.79	0.000	-0.76	0.000	1.30
0.1	0.3	1.010	0.201	1.61	0.004	-1.45	0.008	-2.44
0.3	0.45	1.013	0.194	1.64	0.005	-1.90	0.008	-2.40
0.55	0.55	1.016	0.187	1.66	0.008	-2.32	0.006	-2.38
0.8	0.7	1.022	0.177	1.65	0.013	-2.88	0.003	3.13
1.3	0.9	1.038	0.149	1.68	0.028	3.01	0.002	2.11
1.55	0.95	1.048	0.137	1.70	0.031	2.91	0.003	-2.45
1.8	1.0	1.054	0.126	1.75	0.031	2.87	0.006	-2.47
2.3	1.0	1.056	0.102	1.89	0.026	-3.14	0.009	-2.05
2.3	1.1	1.059	0.106	1.90	0.030	3.12	0.011	-1.98
2.8	1.0	1.055	0.077	2.05	0.018	-2.94	0.006	-1.80
2.8	1.1	1.053	0.078	2.06	0.016	-2.82	0.007	-1.97

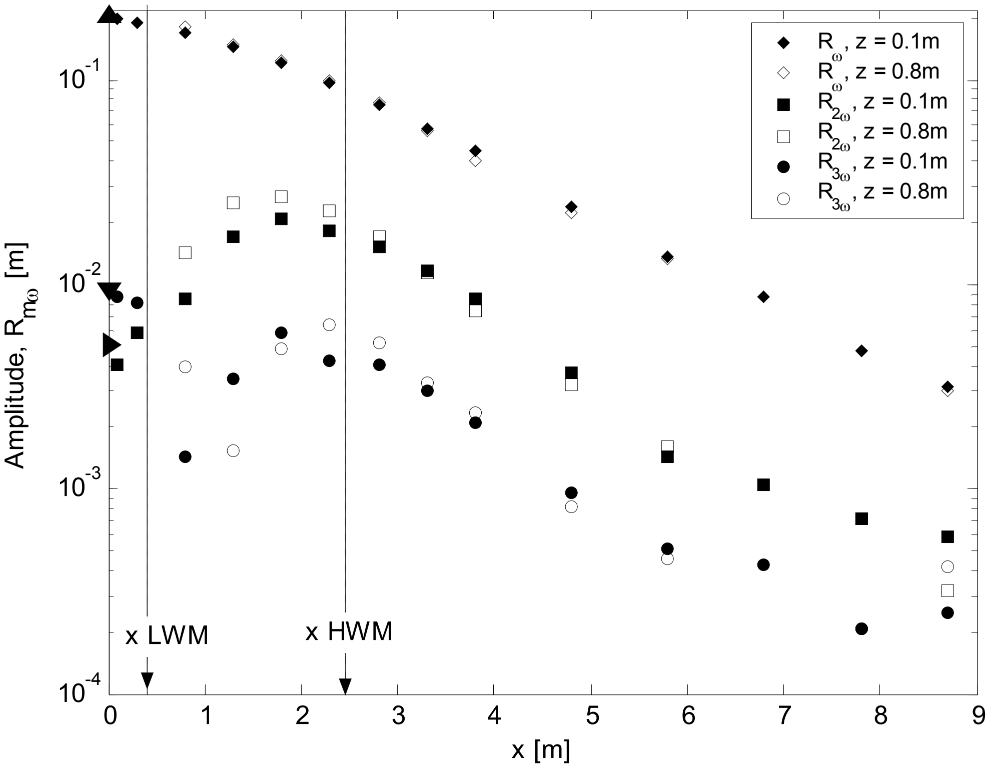

Figure 7.4: Amplitudes extracted from the observed head level oscillations at z = 0.1m (♦,■) and z = 0.8m (◊,□), for the first (♦,◊), second (■,□) and third (•,○) harmonics. The corresponding values for the driving head are also indicated (▲,►,▼).

Figure 7.5 shows the along flume profile of extracted phases for the first three harmonics at z = 0.1m and z = 0.8m. A more or less linear increase in phase is observed landward of the high water mark, again in agreement with the small amplitude theory described by equation (7.6). An interesting feature occurs in the active forcing zone where the higher harmonics are generated. The phase of the second harmonic exactly mirrors the behaviour of its amplitude (see Figure 7.4), decreasing during the generation process, with a minimum value again, occurring slightly landward of the mid point of the forcing zone. Significant scatter is seen with the third harmonic in the forcing zone, relative to the first and second harmonics. However, the third harmonic appears to have a minimum value just landward of the low water mark before rising rapidly to a value which remains more or less constant in the landward half of the forcing zone.

The dispersive properties of all harmonic components in the interior have been discussed previously in section 5.5.2.

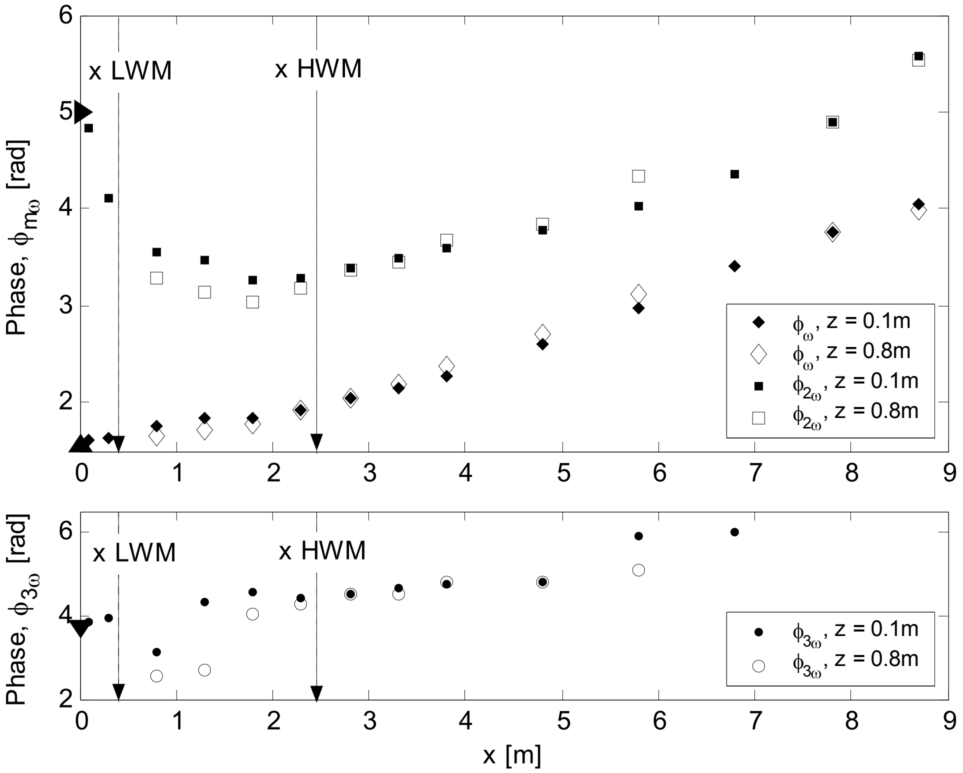

Figure 7.5: Phases extracted from the observed head level oscillations at $z = 0.1$m (♦,■) and $z = 0.8$m (◊,□), for the first (♦,◊), second (■,□) and third (•,○) harmonics. The corresponding values for the driving head are also indicated (▲,►,▼).

7.3.2 Time mean head levels

Figure 7.6 shows the time mean of the observed head levels near the bottom ($z = 0.1$m, ♦) and near the water table ($z = 0.8$m, □). In the active forcing zone and just landward of the high water mark the mean head at $z = 0.8$m is greater than that at $z = 0.1$m indicating that a steady downward flow exists in this part of aquifer in agreement with the experiments described in Chapter 6.

The observed asymptotic (furthest landward) overheight above the mean driving head level is,

$$\overline{\eta_{\infty}} = \overline{h^{*}(8.7,0.8)} - \overline{h^{*}(0)} = 0.047m \tag{7.7}$$

The perturbation theory of *Nielsen* [1990] predicts the water table overheight above the mean driving head level to be,

$$\overline{\eta_\infty} = \frac{1}{2}kA^2\cot\beta = \frac{A}{2}\left(\frac{A\cot\beta}{L}\right) \tag{7.8}$$

where the wave number, *k*, is the inverse of the length scale, *L*, of the pressure wave. Physically, the term in the brackets is the ratio of the amplitude of the horizontal shoreline excursion to the water table wavelength. Taking the wave number *k* to be the average of the best fit wave numbers, $k_{1\omega,r}$ and $k_{1\omega,i}$, at z = 0.8m (cf. Table 5.5) yields $k = 0.464$ which, when substituted into (7.8), yields the observed overheight, (7.7) to the nearest millimetre.

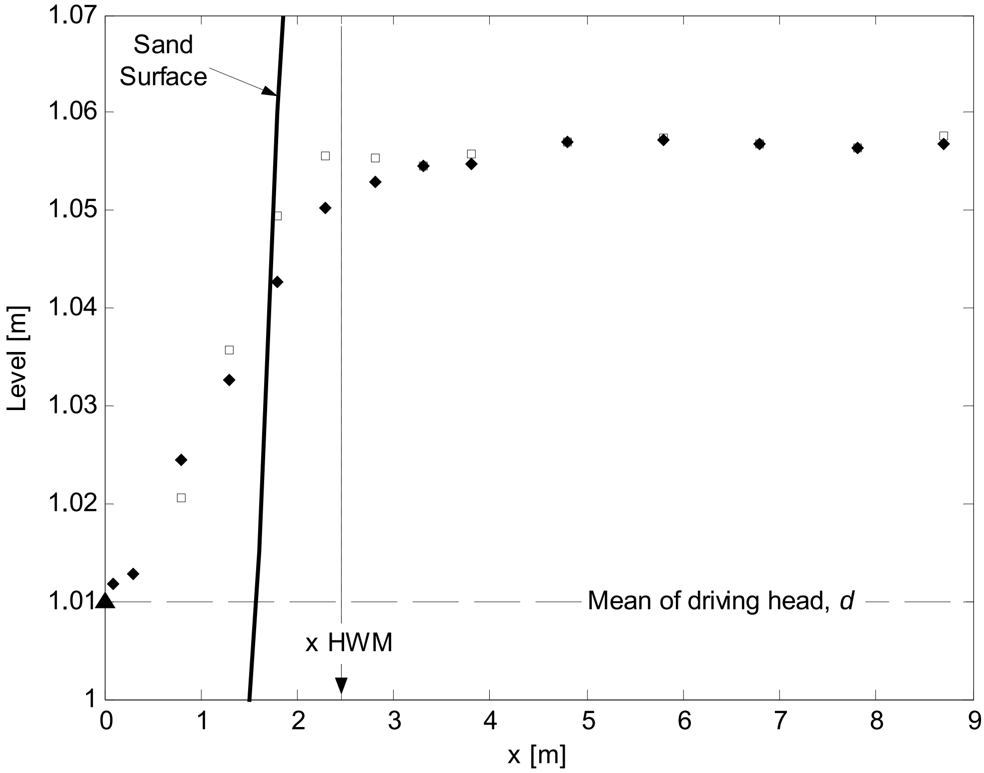

Figure 7.6: Mean piezometric head, $\overline{h^*}$, at z = 0.1m (♦) and z = 0.8m (□).

7.4 Generation of higher harmonics

In this section, detailed observations of $h^*(x,z,t)$ in the vicinity of the active forcing zone are presented and discussed.

7.4.1 Near the sand surface

Figure 7.7 shows the along slope amplitude and phase profiles extracted from observed head level time series at piezometers within a couple of centimeters of the sand surface.

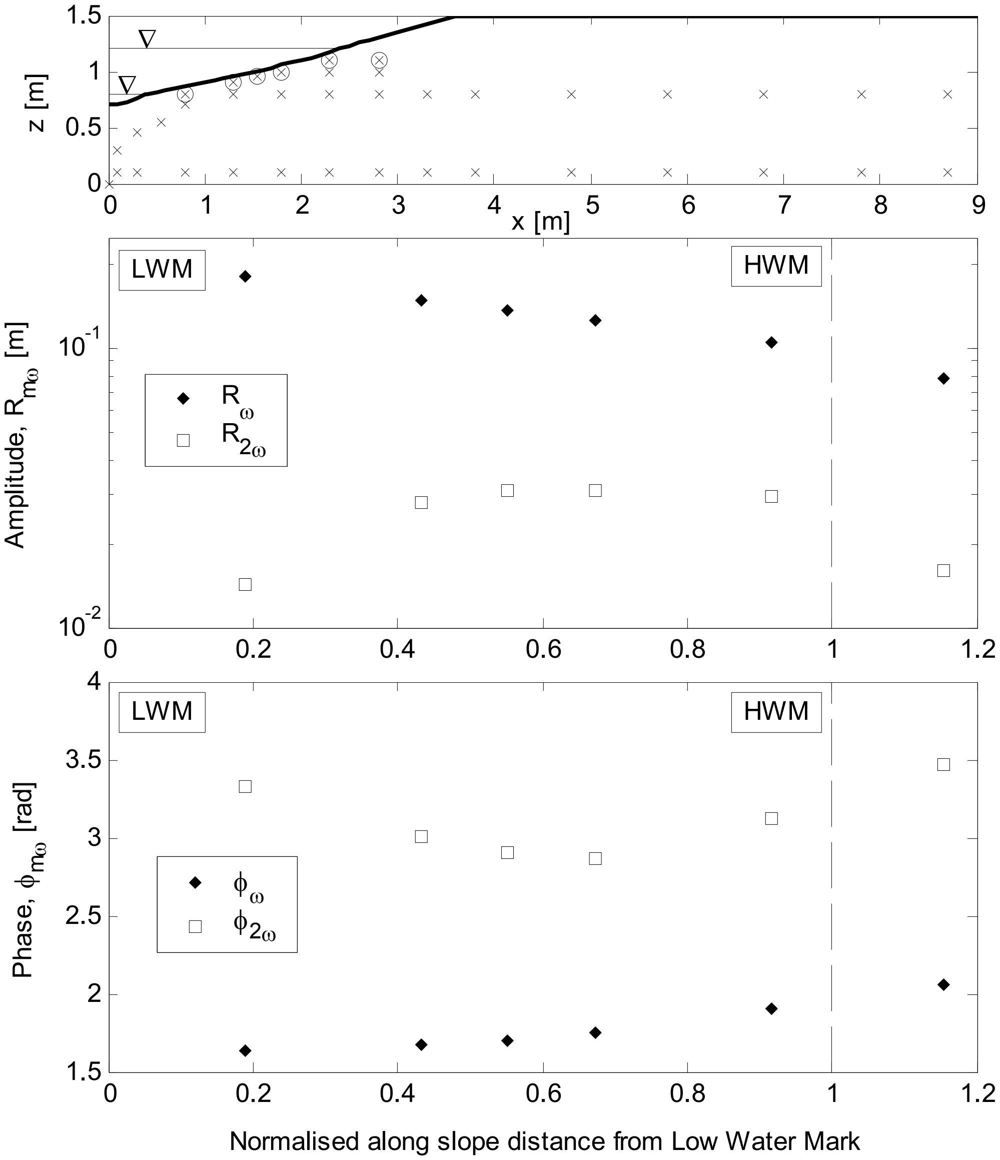

Figure 7.7: (a) Locations of piezometers (⊗), (b) along slope amplitude and (c) along slope phase profiles for the first (♦) and second (□) harmonics. *LWM* and *HWM* indicate low and high water marks respectively.

Similar trends to those observed in Figure 7.4 and Figure 7.5 are seen with a peak in $R_{2\omega}$ just landward of the mid point of the active forcing zone. This trend is mirrored by the phases which show a minimum in $\phi_{2\omega}$ at the same location. The numerical modelling discussed later in section 7.6 shows that the location of the maxima/minima is dependent upon the extent of seepage face formation.

7.4.2 Variation of amplitudes and phases with depth

Figure 7.8 shows variation of the amplitude with depth, normalised by the corresponding amplitude contained in the driving head, $R_{m\omega}(0)$, in the vicinity of the sloping boundary.

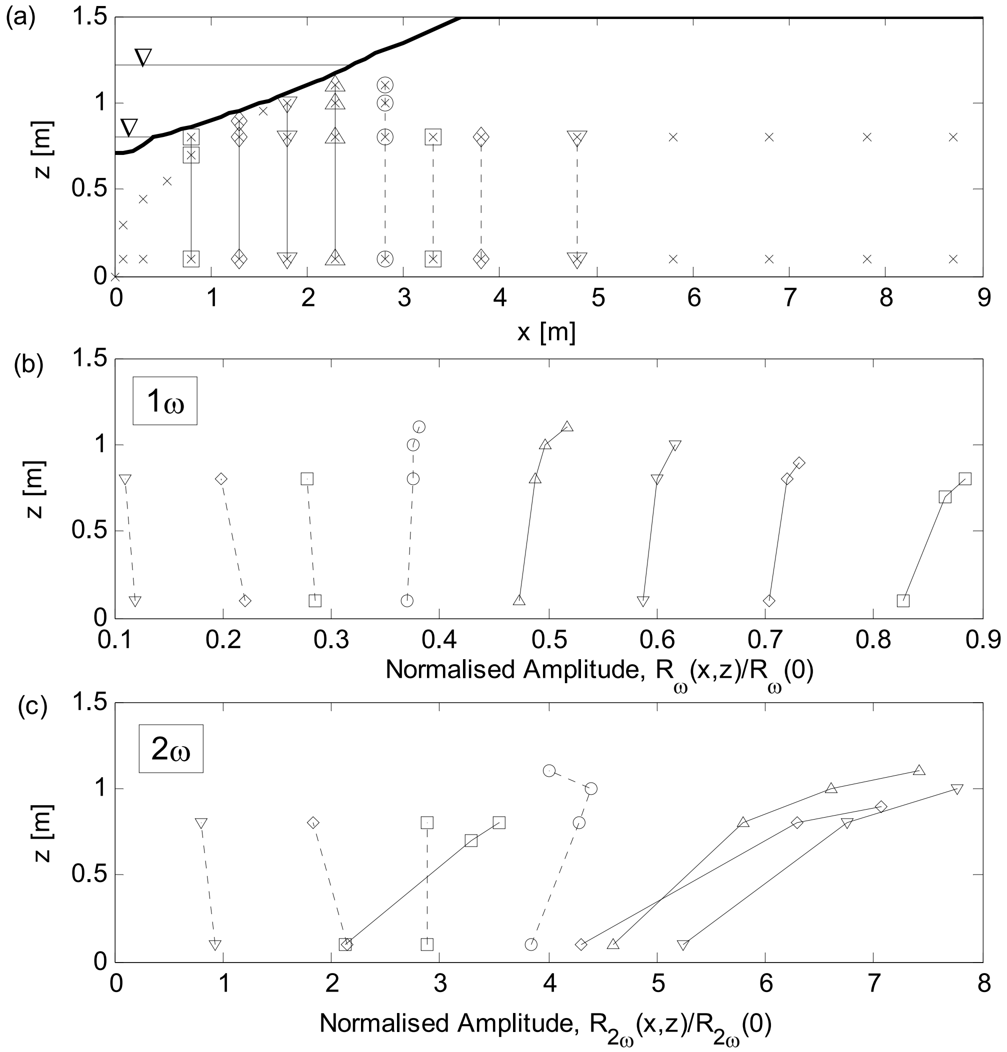

Figure 7.8: Depth profiles of amplitudes, $R_{m\omega}(x,z)$, normalised against that contained in the driving head, $R_{m\omega}(0)$, for the first, (b), and second, (c), harmonics. Panel (a) provides the profile locations in the flume; note the corresponding symbol/line type combinations in all three panels.

The first harmonic profiles show a monotonic decay and also illustrate the transition to finite-depth aquifer behaviour. In the forcing zone the amplitudes are greatest near the sand surface as the driving head oscillations experienced at the sand surface are damped with depth. Landward of the high water mark however, the trend is reversed and a larger amplitude is observed at the base in agreement with the finite aquifer depth theory of *Nielsen et al*. [1997].

The second harmonic profiles reveal some additional insight into the generation of higher harmonics at the boundary, in particular the strong generation observed near the sand surface relative to that near the bottom. This indicates that the non-linear filtering effect of the sloping boundary is much stronger in the upper part of the aquifer. This is intuitively explained by the fact that flow into the aquifer across the slope will be strongest at the sand surface relative to that experienced deeper in the aquifer. Flow out of the aquifer by seepage is likely to be fairly similar at varying depths, leading to a stronger non-linearity near the sand surface.

Similar trends are seen in the variation of phase with depth as shown in Figure 7.9. The first harmonic increases monotonically with distance from the driving head with the lag strongest near the bottom in the forcing zone. Landward of the high water mark the fluctuations at the bottom lead those at the top, additional evidence of finite aquifer depth behaviour [cf. *Nielsen et al*., 1997]. The second harmonic profiles again reveal much a stronger generation signal near the sand surface than at the bottom.

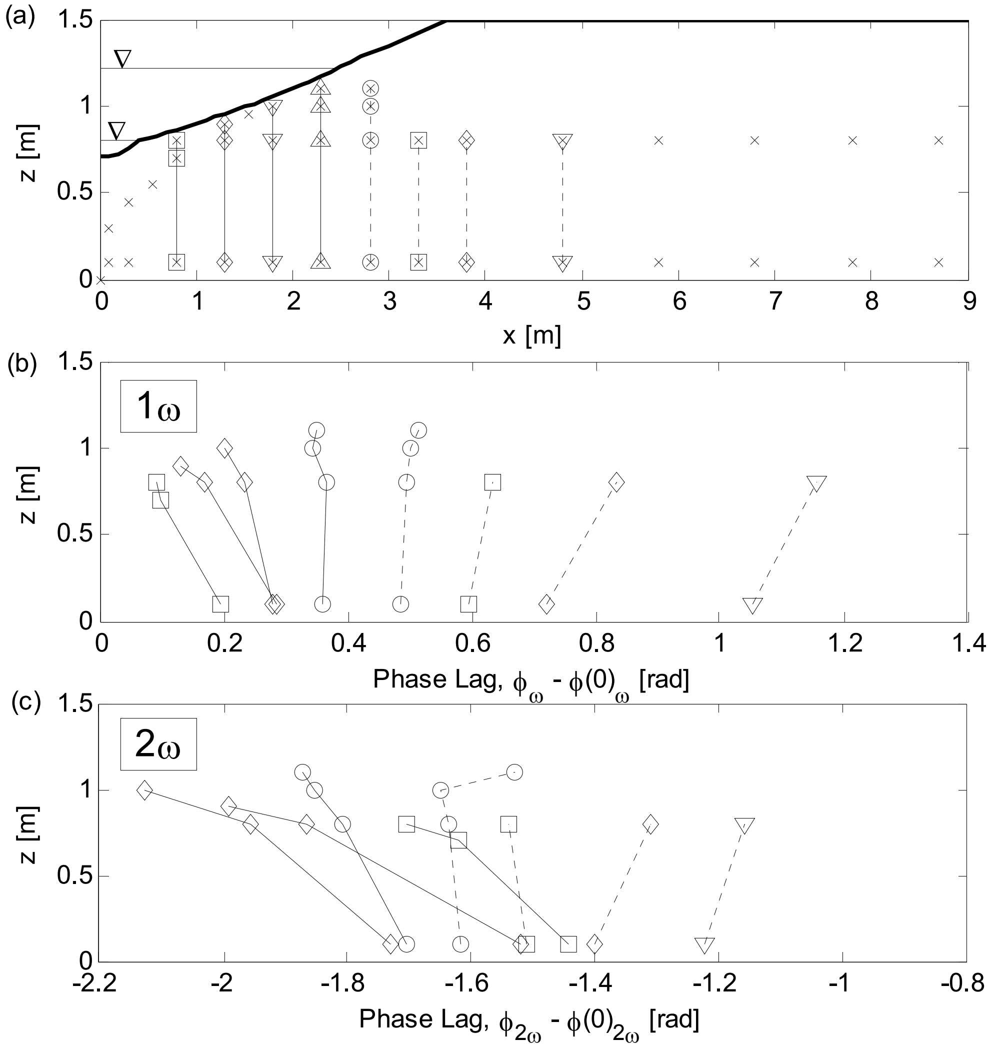

Figure 7.9: Depth profiles of phase lags, $\phi_{m\omega}(x,z) - \phi_{m\omega}(0)$ for the first, (b), and second, (c), harmonics. Panel (a) provides the profile locations in the flume; note the corresponding symbol/line type combinations in all three panels.

7.5 Analytical modelling

The sloping boundary experiments described above are used in this section to test existing small-amplitude perturbation solutions to the groundwater flow equation.

7.5.1 Existing models

Nielsen [1990] was the first to address the sloping boundary problem by solving the linearised Boussinesq equation (equation (7.3)) using a perturbation approach. The solution (equation (7.5)) has been described previously in section 7.1. Since then, other investigators have addressed the problem using slightly different approaches but all based upon the perturbation type solution. For reference, these additional perturbation solutions are summarised in this section.

While *Nielsen's* [1990] small-amplitude perturbation solution matched the periodic boundary condition only approximately, *Li et al.* [2000b] chose to match the boundary condition exactly and used successive approximations to the Boussinesq equation in the interior. To obtained an exact match of the boundary condition *Li et al.*, [2000b] mapped the moving boundary problem to a fixed boundary problem by the introduction of the variable,

$$z = x - x_{SL}(t) \tag{7.9}$$

thereby transforming the linearised Boussinesq equation, (7.3), to,

$$\frac{\partial h}{\partial t} = \frac{Kd}{n_e}\frac{\partial^2 h}{\partial z^2} + \frac{dx_{SL}(t)}{dt}\frac{\partial h}{\partial z} \tag{7.10}$$

Employing the beach slope parameter defined by (7.4), *Li et al.* [2000b] obtained the solution,

$$\begin{aligned} h_{Li}(x,t) \;=\; & d + Ae^{-kz}\cos(\omega t - kz) \\ & + \frac{\varepsilon A}{2}\left\{ \begin{array}{l} 1 + \sqrt{2}e^{-\sqrt{2}kz}\cos\left(2\omega t - \sqrt{2}\,kz + \dfrac{\pi}{4}\right) - \\ \sqrt{2}e^{-kz}\left[\cos\left(2\omega t - kz + \dfrac{\pi}{4}\right) + \cos\left(kz - \dfrac{\pi}{4}\right)\right] \end{array} \right\} + \mathrm{O}\left(\varepsilon^2\right) \end{aligned} \tag{7.11}$$

Li et al. [2000b] then obtained a solution for the bi-chromatic boundary condition,

$$h\left(x_{SL}(t),t\right) = d + A_1\cos\omega t + A_2\cos\left(\omega t - \delta\right) \tag{7.12}$$

and used it to investigate water table fluctuations induced by the neap to spring tidal cycle. The resulting solution compared well with the field observations of *Raubenheimer et al.* [1999].

All of the solutions above rely on a fixed, single-valued length scale $L = 1/k$, to account for both the amplitude decay rate and phase speed. However, as has been shown in Chapter 5, the respective length scale for the rate of decay ($1/k_r$) and for the phase speed ($1/k_i$) are unequal due to capillary effects [*Barry et al.*, 1996], vertical flow effects [*Nielsen et al.*, 1997], or both [*Li et al.*, 2000a; *Nielsen and Turner*, 2000].

Callaghan [2002, pers. comm.] addressed this in the perturbation approach by obtaining a general solution to the linearised Boussinesq equation, (7.3), where the wave number, *k*, is no longer required to have equal real and imaginary parts. Following the same successive approximations to the boundary condition approach as *Nielsen* [1990] with the boundary condition, (7.1), *Callaghan* [2002, pers. comm.] obtained the solution,

$$\begin{aligned}
h_{Call}(x,t) &= d + Ae^{-k_{1\omega,r}x}\cos\left(\omega t - k_{1\omega,i}x\right) \\
&+ A^2\cot\beta_F\left[\frac{k_{1\omega,r}}{2} + \frac{\left|k_{1\omega}\right|}{2}e^{-k_{2\omega,r}x}\cos\left(2\omega t + Arg\left\{k_{1\omega}\right\} - k_{2\omega,i}x\right)\right] \\
&+ \frac{A^3\cot^2\beta_F}{4}\begin{bmatrix}
\left\{-k_{1\omega,i}k_{2\omega,r} - k_{1\omega,r}k_{2\omega,i} + k_{1\omega,r}k_{1\omega,i}\right\}e^{-k_{1\omega,r}x}\sin\left(\omega t - k_{1\omega,i}x\right) + \\
\left\{\frac{3}{2}k_{1\omega,i}^2 - \frac{3}{2}k_{1\omega,r}^2 + k_{1\omega,r}k_{2\omega,r} + k_{1\omega,i}k_{2\omega,i}\right\}e^{-k_{1\omega,r}x}\cos\left(\omega t - k_{1\omega,i}x\right) + \\
\left\{-k_{1\omega,i}k_{2\omega,r} - k_{1\omega,r}k_{2\omega,i} + k_{1\omega,r}k_{1\omega,i}\right\}e^{-k_{3\omega,r}x}\sin\left(3\omega t - k_{3\omega,i}x\right) + \\
\left\{\frac{1}{2}k_{1\omega,i}^2 - \frac{1}{2}k_{1\omega,r}^2 + k_{1\omega,r}k_{2\omega,r} - k_{1\omega,i}k_{2\omega,i}\right\}e^{-k_{3\omega,r}x}\cos\left(3\omega t - k_{3\omega,i}x\right)
\end{bmatrix} \\
&+ H.O.T.
\end{aligned} \tag{7.13}$$

where the wave number, $k_{m\omega} = k_{m\omega,r} + ik_{m\omega,i}$ and the subscripts $m\omega$ (m = 1..3) denote the harmonic component and *r* and *i* denote the real and imaginary parts respectively.

The work of *Li et al.* [2000b] was extended to higher orders by *Teo et al.* [2003] obtaining the following solution, in non-dimensional form,

$$
\begin{aligned}
H_{Teo}\left(X_1,T_1\right) &= \alpha e^{-X_1}\cos\left(\theta_1\right) \\
&+\alpha^2\left[\frac{1}{4}\left(1-e^{-2X_1}\right)+\frac{1}{2}e^{-\sqrt{2}X_1}\cos\left(\theta_2\right)-\frac{1}{2}e^{-2X_1}\cos\left(2\theta_1\right)\right] \\
&+\frac{1}{\sqrt{2}}\cot\left(\beta_F\right)\varepsilon_s\alpha^2\begin{bmatrix}\dfrac{1}{\sqrt{2}}-e^{-X_1}\cos\left(X_1-\dfrac{\pi}{4}\right) \\ +e^{-\sqrt{2}X_1}\cos\left(\theta_2+\dfrac{\pi}{4}\right)-e^{-X_1}\cos\left(\theta_3+\dfrac{\pi}{4}\right)\end{bmatrix} \\
&-\frac{\sqrt{2}}{3}\varepsilon_s^2\alpha X_1 e^{-X_1}\cos\left(\theta_1-\frac{\pi}{4}\right) \\
&+\frac{1}{3}\varepsilon_s^2\alpha^2\begin{bmatrix}-1+\left(1+\dfrac{X_1}{2}\right)e^{-2X_1}-2X_1e^{-\sqrt{2}X_1}\cos\left(\theta_2-\dfrac{\pi}{4}\right) \\ +e^{-\sqrt{2}X_1}\sin(\theta_2)+\sqrt{2}X_1e^{-2X_1}\cos\left(2\theta_1-\dfrac{\pi}{4}\right)-e^{-2X_1}\sin(2\theta_1)\end{bmatrix}
\end{aligned}
\tag{7.14}
$$

where $\alpha = A/d$, $\varepsilon_s = kd$, $X = kx$, $T = \omega t$, $H = h/d$, $X_1 = X - X_o(T)$, $X_o(T) = kA\cot(\beta_F)\cos(T)$, $\theta_1 = T_1 - X_1$, $\theta_2 = 2T_1 - \sqrt{2}X_1$, $\theta_3 = 2T_1 - X_1$.

7.5.2 Model application

Section 5.5.2 discussed the inability of current small-amplitude dispersion theory to predict the observed wave numbers despite considering both finite-depth and capillarity effects. All of the solutions described above are therefore applied here in a 'quasi-predictive' manner only. That is, the required input wave numbers used are those obtained from the data (for z = 0.8m, cf. Table 5.5).

Except for *Callaghan's* [2002, pers. comm.] solution, (7.13), all the solutions above require is a single, real valued input length scale ($L = 1/k$). As the data indicate that $k_r \neq k_i$ (cf. Table 5.5) the input wave number for these solutions is set as the average of the real and imaginary parts of the first harmonic at z = 0.8m. That is, from $k_{1\omega,(z=0.8)} = 0.584 + 0.343i$, $k = 0.464$.

For all the above solutions, the solution only holds for $x > x_{SL}$. For $x \le x_{SL}$, the pressure is assumed to be hydrostatic and equal to the driving head, i.e.,

$$
\begin{aligned}
\eta(x,t) &= \eta_{solution}(x,t), && \textit{for} \quad x > x_{SL}(t) \\
\eta(x,t) &= A\cos\omega t, && \textit{for} \quad x \le x_{SL}(t)
\end{aligned}
\tag{7.15}
$$

The origin of the fixed coordinate system was set as the mid point of the forcing zone i.e. $x_0 = 1.44$ m.

7.5.3 Comparison with sand flume observations

7.5.3.1 Amplitudes

Figure 7.10 shows the comparison of observed amplitudes with those from all solutions.

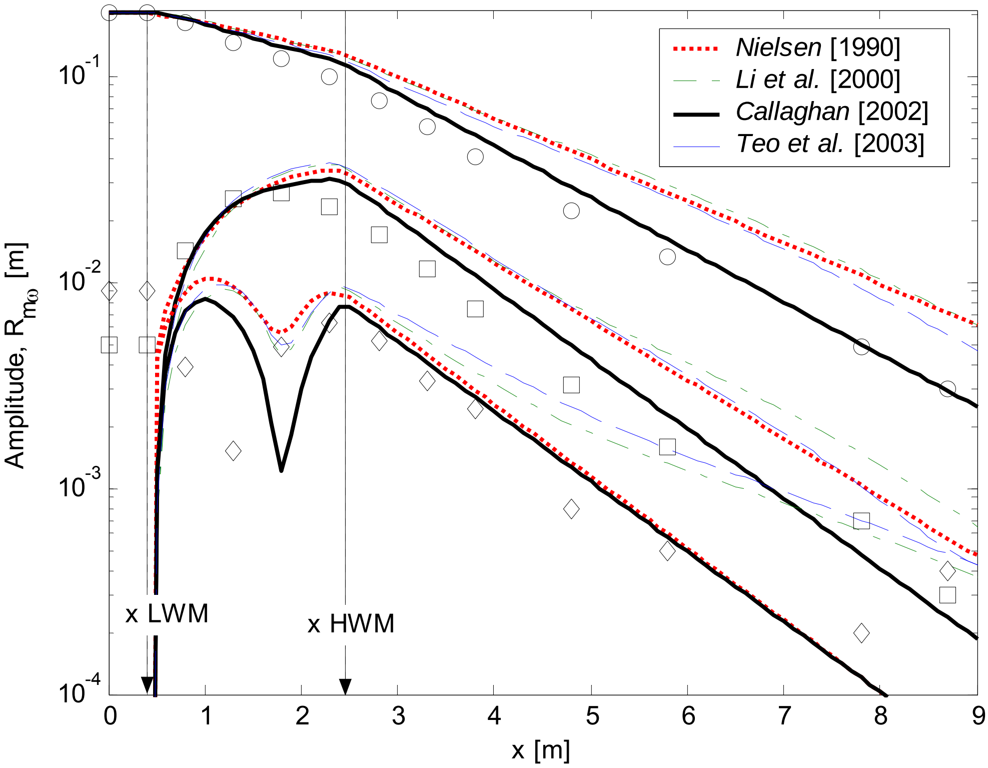

Figure 7.10: Comparison of observed amplitude profiles with that extracted from the analytical solutions.

All of the solutions under predict the decay rate of the first harmonic (○) in the forcing zone as a direct result of their neglect of seepage face formation. I.e. with the groundwater level being always coupled to the shoreline a larger amplitude results than if the exit point becomes decoupled from the shoreline as was the case in the experiments.

In the interior, the solution with separate decay and phase length scales, (7.13), provides much better agreement with the data as it utilises the experimental decay rate, $k_{1\omega,r}$, as input as opposed to the average of the real and imaginary parts, $k_{1\omega,r}$ and $k_{1\omega,i}$ used by the other solutions. Also in the interior, the influence of the higher order terms in solutions (7.11) and (7.14) are seen as deviations from a purely exponential decay, i.e. deviations from a straight line in the log-linear plot. This influence becomes more apparent in the higher harmonic profiles, in particular for the third harmonic (◊), where substantial curvature is clearly evident.

Each of the solutions illustrate the generation of higher harmonics in the forcing zone that is in reasonable agreement with the data. However small differences are present which reveal some insight into the processes occurring at the boundary. In the case of the second harmonic (□), each of the solutions predict a maximum amplitude at the high water mark whereas the maximum in the data occurs near the mid point of the forcing zone. The difference here will be shown in section 7.6 to be due to the presence of a seepage face in the experiment that is neglected in all of the solutions. It may well be argued that the differences seen between the solutions and the data in this regard is only small, however, in the field where the extent of seepage faces is substantially greater, neglect of their presence is likely to be detrimental to the solutions ability to accurately predict the generation of higher harmonics.

In the case of the third harmonic (◊), the dual length scale solution, (7.13), provides much better agreement with the observed amplitude profile as it utilises the observed dispersive properties of the higher harmonic components. The other solutions however use a single length scale and rely upon the interaction between higher order terms. However, all solutions do reasonably well at reproducing the observed profile in that an initial increase in amplitude decays to a minimum near the mid point of the forcing zone before reaching a maximum at the high water mark. Similar differences to those observed in relation to the second harmonic (□) are seen in that the solutions depict a minimum closer to the high water mark than is observed in the data, again due to the neglection of the seepage face.

7.5.3.2 Phases

Figure 7.11 compares the analytical phase lag profiles for the first (○), second (□) and third (◊) harmonics with the corresponding observed profile.

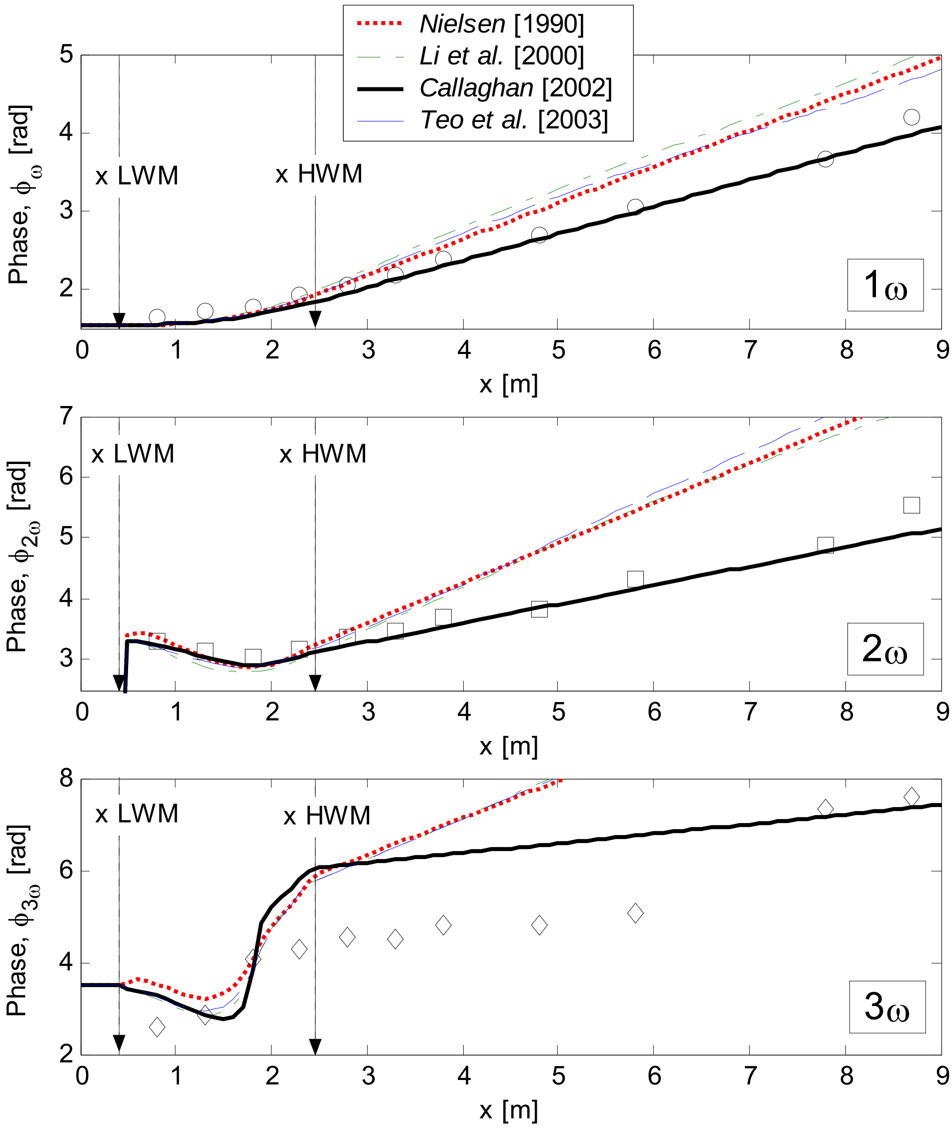

Figure 7.11: Comparison of observed phase profiles with that extracted from the analytical solutions.

The limiting dependence of equations (7.5), (7.11) and (7.14) on a single, real valued length scale $L = 1/k$ is clearly visible with all three under predicting the phase speed in the interior. The dual scale solution, (7.13), which uses the observed length scales for each harmonic, does very well at reproducing the development of the phase lag in both harmonics. Each of the solutions however, do reasonably well in reproducing the generation of the second harmonic in the forcing zone. Evidence of the higher order terms contained in solutions (7.11) and (7.14) is again seen as deviations from the straight line predicted by small amplitude theory. The influence of these terms on the phase lag profile is significantly smaller relative to that seen in the amplitude profile, Figure 7.10.

The reader is reminded that each of the solutions above have been applied in a 'quasi-predictive' manner only. This is due to large discrepancies between the observed dispersion of the pressure wave and that predicted by small-amplitude dispersion theory corresponding to the solutions (cf. section 5.5.2). As such, further analytical development of the dynamic coastal aquifer system requires further investigation of the physical processes occurring, in particular in relation to the effect of a capillary fringe above the water table.

7.6 Numerical modelling

7.6.1 Model description

In order to investigate further the role of the sloping boundary on the generation of higher harmonics in the forcing zone, a 2D vertical numerical model was built using the Mike SHE/Mike 11 simulation package [*Jessen*, 1998]. The model solves the non-linear Boussinesq equation,

$$S\frac{\partial h^*}{\partial t}=\frac{\partial}{\partial x}\left(K\frac{\partial h^*}{\partial x}\right)+\frac{\partial}{\partial z}\left(K\frac{\partial h^*}{\partial z}\right) \tag{7.16}$$

where $h^* = z + P/\rho g$ is the piezometric head, K is the saturated hydraulic conductivity, S is a storage term, t is time and x and z are the horizontal and vertical coordinates respectively. Figure 7.12 shows the setup profile of the 5 layered, 2DV model.

In the layered model applied here, the storage term in the uppermost computational layer (containing the water table) is given by the effective porosity, n_ω. All the lower layers, which are always saturated, are treated as confined layers and the storage term is given by the specific storage, $S_s = \rho g(\alpha_m + n\beta_w)$, where ρ is the density of the fluid, g is the acceleration due to gravity, α_m is the compressibility of the aquifer matrix and β_w is the compressibility of the fluid.

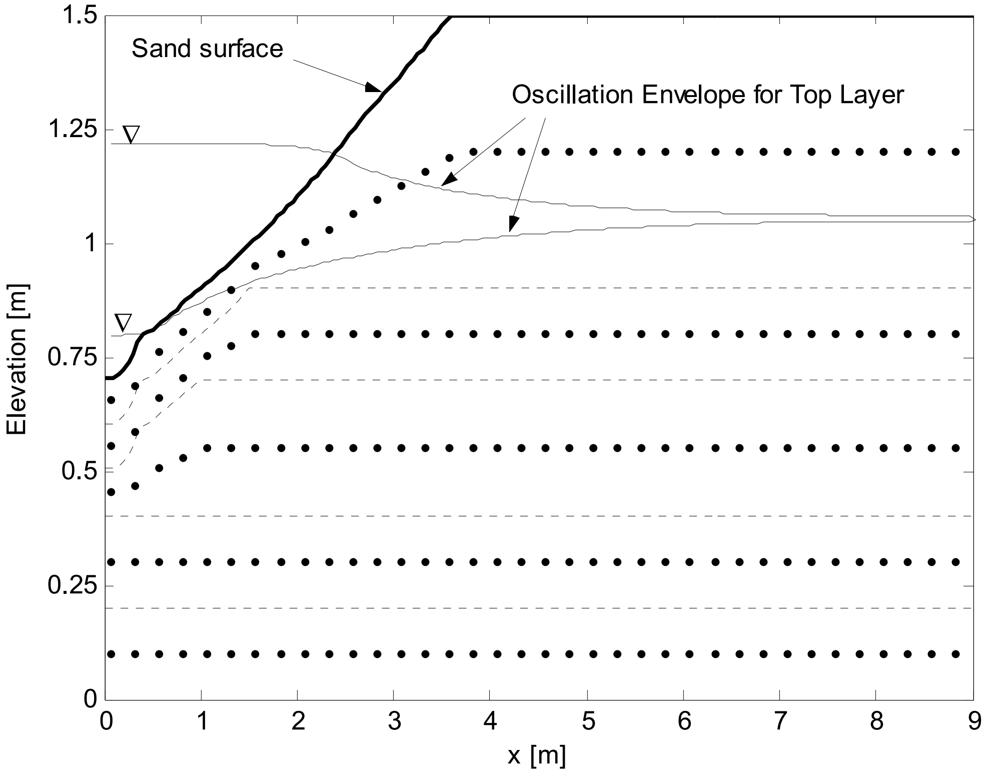

Figure 7.12: Setup of layered 2DV numerical model. (---) denotes the computational layer boundaries and (•) denotes the computational nodes (note that only every fifth node in the horizontal is shown for clarity).

7.6.1.1 Consideration of the influence of capillarity

The influence of the capillary fringe on the water table fluctuations is addressed in this application of the model by setting the effective porosity in the top layer equal to $|n_\omega|$, where $n_\omega = 0.0034 - 0.0013i$, is the best fit, complex effective porosity as estimated from the flume data in section 5.6 (cf. Table 5.6). The limitation of this approach (using $|n_\omega|$ rather than the complex form) is that it neglects the phase difference between fluctuations of the water table and the total moisture. This will be illustrated later upon examination of the predicted phase profile. The storage terms used in the model are summarised in Table 7.2, all other aquifer parameters used are as summarised in Table 5.2.

Table 7.2: Storage terms used in the numerical model.

$\lvert n_\omega \rvert$	S_s
0.0035	7.0×10^{-5}
[-]	$[m^{-1}]$

7.6.1.2 Implementation of the periodic boundary condition

The simulation package permits the dynamic coupling of the groundwater flow module with a surface, river module. This particular model configuration was first applied by *Jessen* [1998] in a numerical investigation of the effect of beach drainage on the pressure and flow field. The river module is used to represent the clear water forcing and is coupled with the groundwater flow module thereby allowing seepage between the two water bodies. The time series in the river module was generated using the experimental parameters summarised in Table 5.3. As in the experimental setup, the inland boundary and aquifer base were set as zero flow boundary conditions.

7.6.2 Comparison with experimental observations

7.6.2.1 Amplitudes

The comparison of the observed and predicted amplitude profiles is shown in Figure 7.13. In the interior, the model accurately predicts the amplitude decay rate for each of the first three harmonics, except for the third harmonic in the landward half of the aquifer. The model also predicts the observed influence of wave reflection from the landward, no flow boundary. This is seen as the curvature in the profiles near the no flow boundary.

The allowance of seepage face formation in the numerical model is seen to substantially improve the prediction of the generation of higher harmonics. The model predicts both the magnitude and the location of the maximum second harmonic amplitude (□). The comparison of the observed and simulated profiles for the third harmonic (◊) is not as good but, relative to the performance of the analytical models which neglect the seepage face, the agreement is improved.

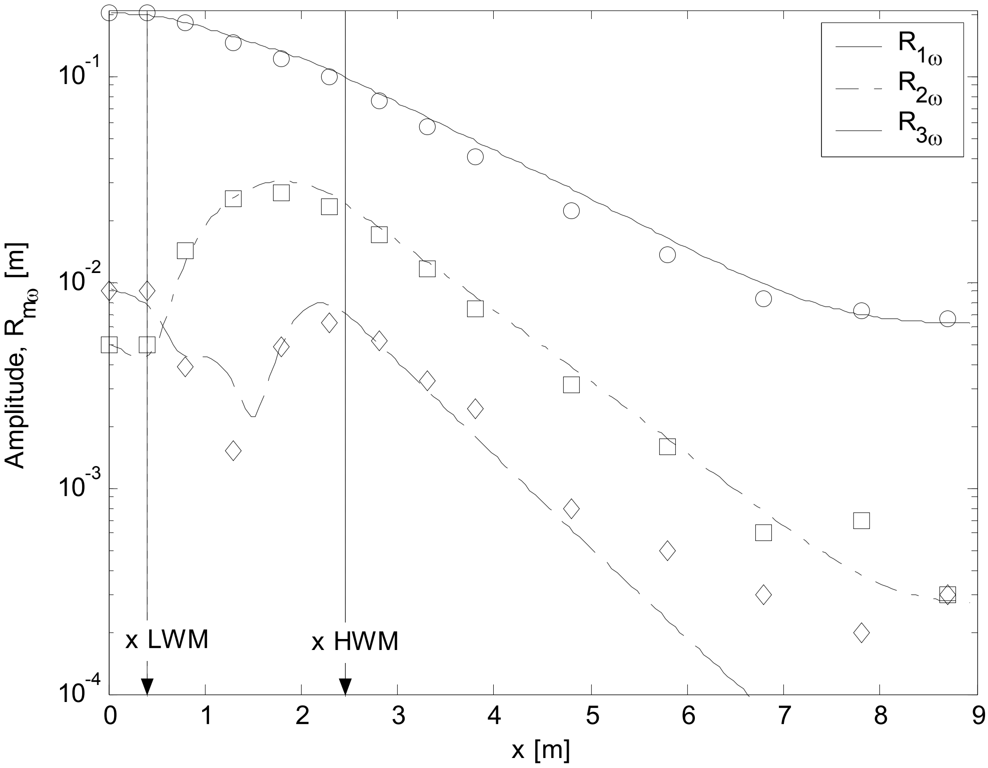

Figure 7.13: Comparison of the observed amplitude profile for the first (○), second (□) and third (◊) harmonics with that predicted by the 2DV numerical model.

7.6.2.2 Phases

The comparison of observed and simulated phase profiles is shown in Figure 7.14. It is seen that the model tends to over predict the rate of increase in phase lag for all three harmonics. This is a direct consequence of using $|n_{\omega}|$ as a means to account for the effect of capillarity (cf. section 7.6.1.1). The challenge still remains to account for time lags between the total moisture and water table height in the numerical solution of equation (7.16). A *Green and Ampt* [1911] capillary fringe (cf. section 4.2.1) can be accounted for by an extra $\frac{\partial}{\partial t}\frac{\partial^2}{\partial x^2}$ term in the Boussinesq equation as discussed by *Barry et al.* [1996] but a model which agrees with the sand column data (cf. section 4.3) requires a ⅔ order derivative as suggested by *Nielsen and Turner* [2000]. The other, more traditional approach would be to implement a 2DV numerical simulation of the unsaturated flow equation. This however, is left for future investigation.

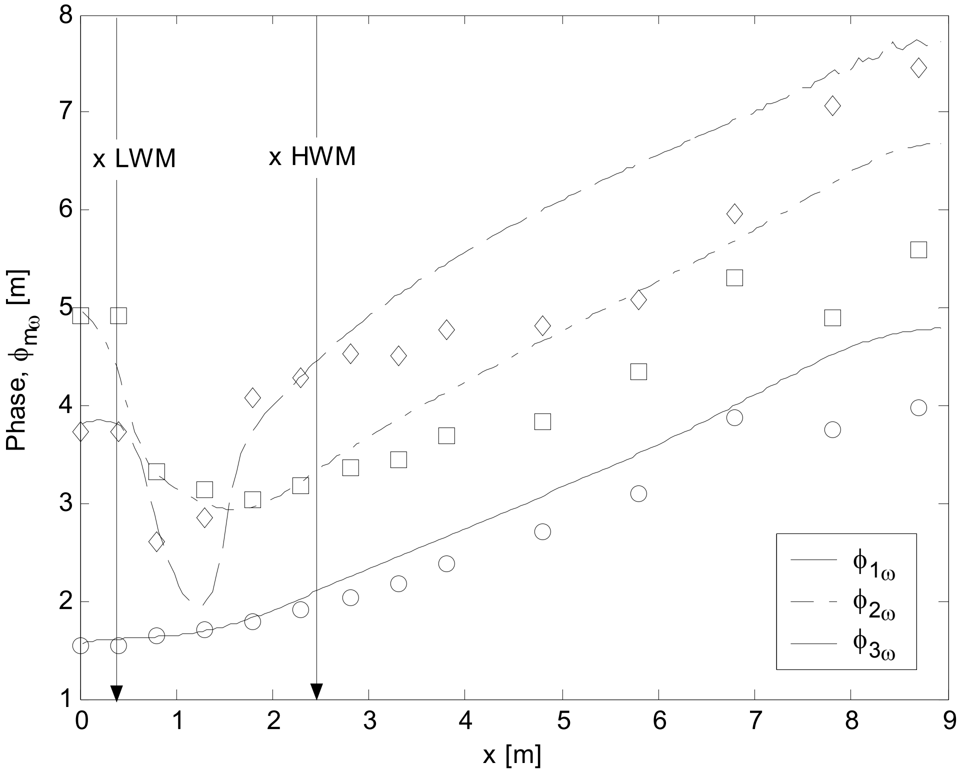

Figure 7.14: Comparison of the observed phase profile for the first (○), second (□) and third (◊) harmonics with that predicted by the 2DV numerical model.

7.6.2.3 Vertical distribution of harmonic components

An advantage of the 2DV numerical model is that it enables a closer inspection of the vertical, as well as horizontal, pressure distribution in the aquifer. In this section the observed depth profiles of both normalised amplitudes and phase lags (cf. Figure 7.8 and Figure 7.9) are compared with those predicted by the model.

Figure 7.15 and Figure 7.16 show the observed and simulated, normalised amplitude depth profiles respectively. Despite a slight over prediction of the first harmonic amplitude at all levels, the model predicts the two dominant features in the observed profile; (1) a damping of the amplitude with depth in the forcing zone and (2) the transition to finite aquifer depth behaviour in the interior, i.e. larger fluctuation amplitudes at the base than near the water table [cf. *Nielsen et al.*, 1997].

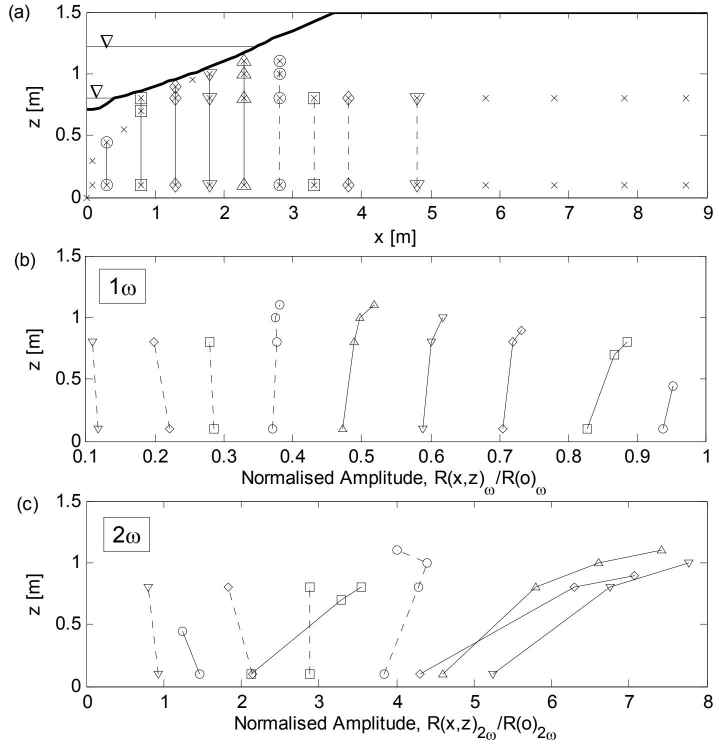

Figure 7.15: Observed amplitude depth profiles.

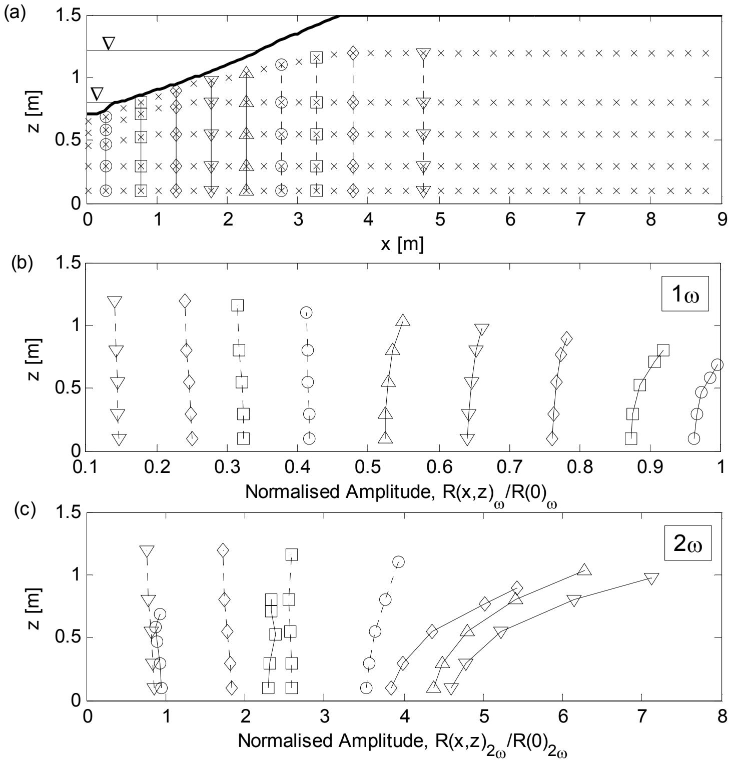

Figure 7.16: Simulated amplitude depth profiles.

The model also accurately reproduces the generation of the second harmonic component in the forcing zone. In particular, it does remarkably well at predicting the difference in the intensity of the generation process, with the generation in the upper parts of the aquifer as much as a factor 2.5 greater that in the lower parts of the aquifer as is the case in the observed profile.

Figure 7.17 and Figure 7.18 compares the observed with the simulated variation in phase lag with depth profiles. Consistent with the horizontal phase profiles shown in Figure 7.14, the model over predicts the observed phase lag profile at all levels. In the forcing zone the model predicts a near zero phase difference between the top and bottom of the aquifer in contrast with the observed profile which indicates the phase near the sand surface to lead that at the base. The comparison improves into the interior with the model predicting the transition to finite aquifer depth behaviour, i.e. the phase at the base leads that at the top [cf.*Nielsen et al*., 1997]. However, the model over predicts this finite-depth phase lead by a factor 2 on that which is observed in the sand flume. This is likely to be due to the use of the $|n_\omega|$ storage term in the model as discussed in sections 7.6.1.1 and 7.6.2.2.

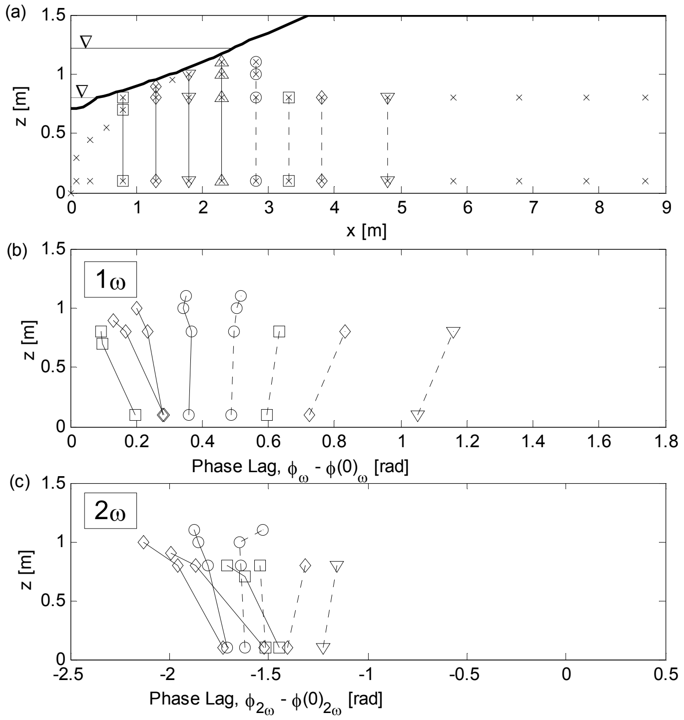

Figure 7.17: Observed phase depth profiles.

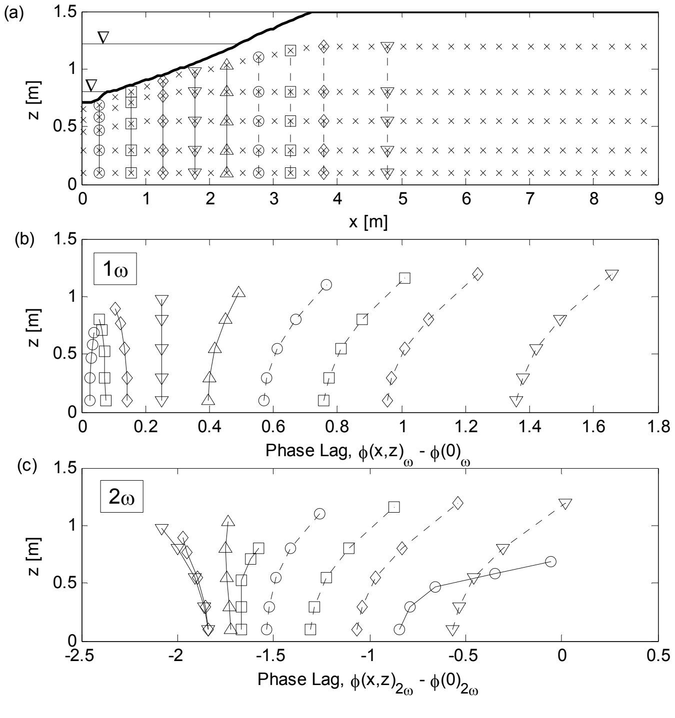

Figure 7.18: Simulated phase depth profiles.

7.6.2.4 Water table exit point dynamics

Unlike the analytical models described in section 7.5, the coupling of the numerical model's surface water and sub-surface modules allows the water table exit point to become decoupled from the driving head. The predicted water table exit point, determined by post-processing of the predicted water table profile, compares well against the observed exit point in Figure 7.19.

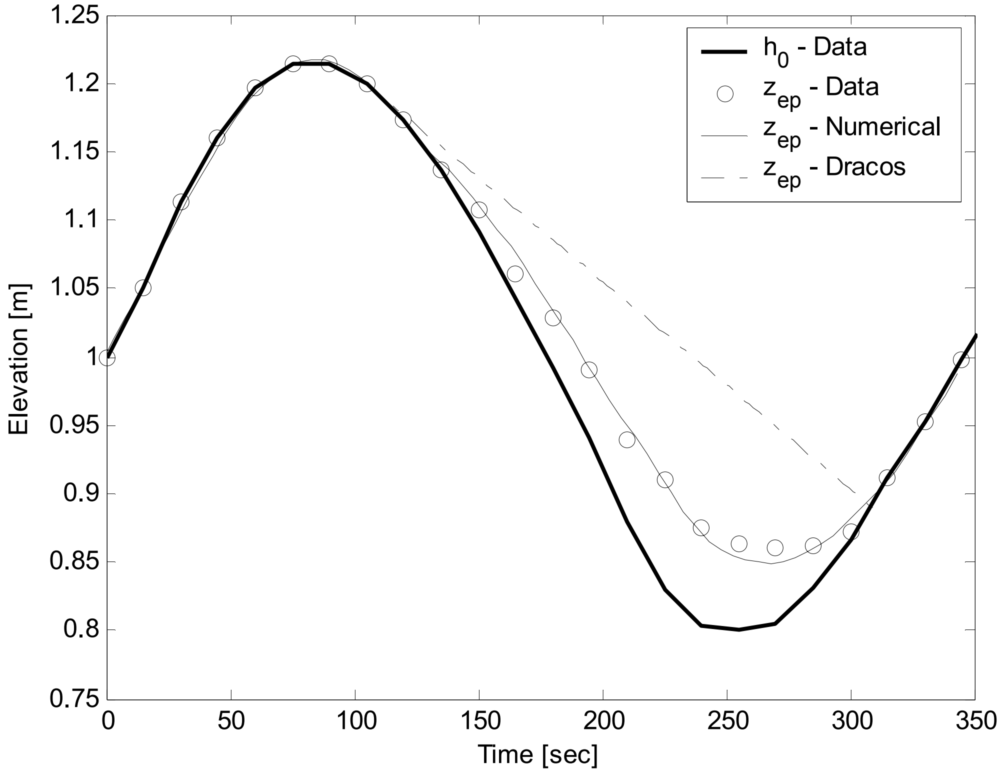

Figure 7.19: Comparison of observed and simulated water table exit point.

Also captured by the model is the curious early rise of the exit point prior to being overtopped by the shoreline as seen in field observations of *Turner* [1993] and the numerical simulations by *Li et al.* [1997]. *Turner* [1993] noted the phenomenon was only subtle in his data and cited over-topping from the first swash lens over the slightly convex inter-tidal profile as the cause. The phenomenon in the present data is also only subtle but as there were no waves in the present experiments, some other process(es) must be contributing to the early rise of the exit point.

In a comment on the findings of *Li et al.* [1997], *Nielsen* [1999c] couldn't see a reason for the simulated early rise of the exit point to which *Li et al.* [1999b] replied by citing the nature of the governing Laplace equation as the reason such that "any changes of a boundary condition will immediately cause the solution to behave differently". The present experiments have only qualitatively verified the model predictions as the simulated early rise of the exit point is much more pronounced than that seen in the data (cf. Figure 7.19). A definitive physical explanation of the phenomenon is so far unavailable. To further investigate the cause of the early rise in the exit point, a range of experiments in the sand flume are suggested, varying the oscillation amplitude and frequency and the beach face slope.

Atherton et al. [2001] observed in the field that the water table tended to rise whilst the wave runup limit was still >15m seaward of the monitoring location. They interpreted the observation as "the water table rising through the capillary fringe as the seaward boundary condition for ground water flow out of the beach changed". No direct observation of the location of the exit point was presented.

Also plotted in Figure 7.19 is the exit point predicted by the SEEP model of *Turner* [1993] based on the theory of *Dracos* [1963]. Briefly, the theory considers only the forces acting on a particle of water at the sand surface resulting in the following expression for the terminal (vertical) velocity of the exit point,

$$v_{ep} = -\frac{K}{n}\sin^2\beta \tag{7.17}$$

The time of decoupling occurs when $v_{ep} < v_{tide}$ and the exit point then falls according to equation (7.17).

The performance of the *Dracos* [1963] theory is seen to be quite poor with its neglect of the sub-surface pressure distribution the likely reason. Note that, as in the numerical simulation, the storage term, n, is taken to be the experimental $|n_\omega|$ as given in Table 7.2. Accurate prediction of the dynamics of the exit point clearly requires knowledge of the pressure distribution and hence flow net near the boundary. The real-world scenario in beaches will be further complicated by the influence of waves and their interaction with the sub-surface as discussed in relation to the reverse Wieringermeer effect in section 4.1.

7.7 Summary

The influence of a sloping as opposed to a vertical interface between a simple harmonic, clear water reservoir and a homogeneous laboratory aquifer has been investigated by detailed measurement and analysis of the piezometric head, $h^*(x,z,t)$.

The non-linear filtering effect of the sloping boundary is clearly evident with the maximum second harmonic amplitude occurring near the mid point of the forcing (intertidal) zone. The trend is mirrored in the phase profile with the second harmonic phase having a minimum at the same location. Depth profiles of both amplitudes and phases indicate this effect to be strongest near the sand surface, clearly related to the relative strength of vertical flows in this part of the aquifer.

The observed water table overheight is shown to be accurately reproduced by the small-amplitude perturbation theory of *Nielsen* [1990].

Of four analytical models compared against the data, the dual length scale solution (7.13) performs the best in the comparison of both phases and amplitudes for the first three harmonics. The remaining three solutions, which all rely on a single length scale to account for both the amplitude decay and development of the phase lag, are unable to reproduce either the amplitude or the phase profile. If the observed amplitude decay rate, $k_{r,1\omega}$, was used then the solutions would provide a reasonable agreement with the observed amplitude profile but much worse against the phase profile.

Application of a 2DV numerical model to the data provides a good comparison with many aspects of the data. In particular the generation of the higher harmonic components, both in comparison with amplitude and phase depth profiles and with the observed profiles in the inter-tidal zone. The good performance in the latter being due to the fact that the numerical models allows for the formation of a seepage face, a process that is ignored in all the analytical models. The simulated dynamics of the water table exit point compare well with the data, including the rise of the exit point prior to over-topping by the tide. The causes of the early rise remain an open question.

Chapter 8 – Aquifer recharge due to infiltration from wave runup

8.1 Introduction

Beaches located in a region of significant near-shore wave activity, will be subject to an additional flux of ocean water across the sand surface into the aquifer due to infiltration from wave runup on the beach face. This additional mass flux of salt water contributes to the nature and extent of the intrusion of salt water into freshwater aquifers which will affect interstitial chemical and biological processes. The extent of this infiltration is also of interest to swash zone sediment transport researchers who have indicated that infiltration-exfiltration across the beach face affects sediment mobility [e.g. *Turner and Nielsen*, 1997; *Elfrink and Baldock*, 2002].

Accurate quantification of swash-zone infiltration distributions therefore has wide ranging implications and applications across many disciplines. In this chapter, the use of a modified Boussinesq equation [*Nielsen et al.*, 1988] to estimate time-averaged recharge distributions from measured head level profiles in the swash zone is critically assessed using both field and laboratory observations.

8.2 Theory

8.2.1 Recharge distributions: the modified Boussinesq equation

Figure 8.1 illustrates the concept of a wave runup infiltration distribution, time averaged over several swash events. The active infiltration zone, or the region of water flow across the sand surface due to wave runup, is defined at its limits by the runup limit and the shoreline, the intersection of the mean water surface and the beach face. Intuitively, time-averaged infiltration distributions for a beach face are going to be a function of both supply (i.e. the wave runup distribution over that period), and the ability of the sand to take in water as defined by its permeability and moisture content.

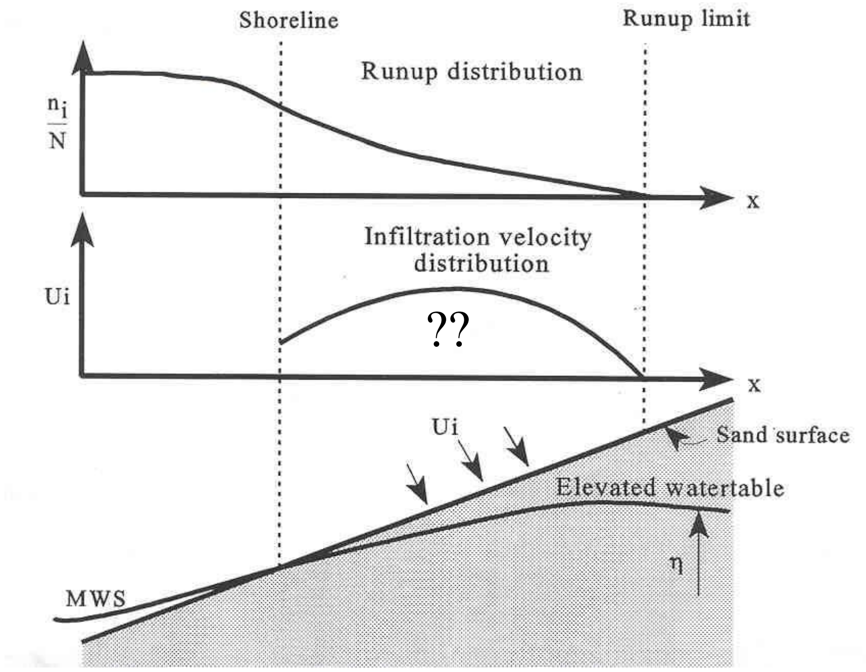

Figure 8.1: Schematic showing the zone of infiltration due to wave runup, from *Kang* [1995].

The present work critically assesses the use of the modified Boussinesq equation (8.1), first proposed by *Nielsen et al.* [1988], to infer a time-averaged infiltration rate, *Ui*, from observed head profiles.

$$n\frac{\partial h}{\partial t} = K\left[\frac{\partial}{\partial x}\left(h\frac{\partial h}{\partial x}\right)\right] + Ui(x,t) \tag{8.1}$$

This equation has been used in linearised form to examine the contribution of infiltration on the asymptotic inland water table overheight [*Turner*, 1989; *Kang et al.*, 1994b; *Kang*, 1995] and to also look at the influence of infiltration-exfiltration on sediment transport in the swash zone [*Turner and Masselink*, 1998].

It is noted that the graphical definition of *Ui* given in Figure 8.1 is not strictly correct, in fact *Ui*, is an additional flux term, or recharge rate, across the water table, not the sand surface as depicted in Figure 8.1. In the following it will be shown in this chapter that the presumption that *Ui* is representative of an infiltration rate across the sand surface may not necessarily be valid.

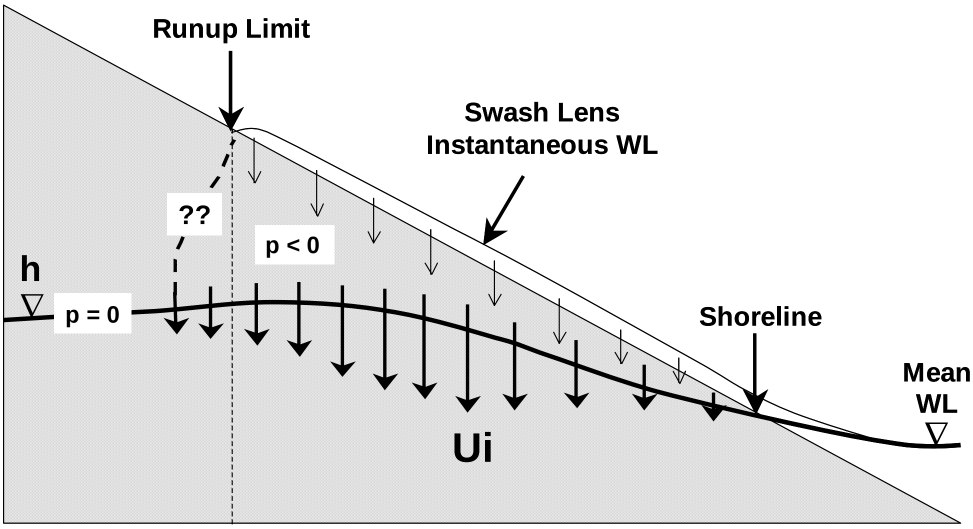

Figure 8.2: Definition of the Boussinesq "infiltration/recharge" flux term, *Ui*.

Ui(*x,t*) can be calculated from equation (8.1) using finite difference, local approximations of the derivatives,

$$\left[\frac{\partial h}{\partial t}\right]_i^n \rightarrow \frac{h_i^{n+1} - h_i^{n-1}}{2\Delta t} \tag{8.2}$$

$$\left[\frac{\partial}{\partial x}\left(h\frac{\partial h}{\partial x}\right)\right]_i^n \rightarrow \frac{h^{2n}_{i-1} - 2h^{2n}_{i} + h^{2n}_{i+1}}{2\Delta x^2} \tag{8.3}$$

with the subscripts, *i,* denoting time and the superscript, *n,* denoting space respectively. The normalised recharge rate is then calculated using,

$$\frac{Ui}{K} \approx \frac{n}{K}\frac{h_i^{n+1} - h_i^{n-1}}{2\Delta t} - \frac{h^{2n}_{i-1} - 2h^{2n}_{i} + h^{2n}_{i+1}}{2\Delta x^2} \tag{8.4}$$

Estimation of the partial derivatives using the finite difference technique when applied to actual data can result in significant scatter, particularly for the case of the second order spatial derivative [equation (8.3)] for relatively flat head level profiles. Significant reduction in scatter was achieved in the present analysis by expanding the local approximation, finite difference technique to include additional points, for example, *i+/- 2, i+/- 3*, centred on the point of interest.

The Boussinesq equation, (8.1), is derived from the fundamental principles of continuity and Darcy's law for saturated flow, neglecting both partially saturated flow and vertical flow effects. It is noted that in reality, the infiltration of wave runup will include some component of partially saturated or tension saturated flow. Vertical flow effects will also influence observed head levels but are overlooked when using the 1D equation (8.1).

8.2.2 Wave runup distributions

The ultimate control on aquifer recharge in the swash zone is the magnitude and duration of wave runup events, i.e. the time and amount of water available. In a time averaged sense, this can be best represented in the form of a wave runup distribution, i.e. in a given sampling period how many waves transgress a certain shore normal location.

8.3 Field experiment

A field experiment was undertaken at Brunswick Heads in northern New South Wales to examine the variation in time averaged, wave runup infiltration during a tidal cycle and to relate this to the wave runup distribution.

8.3.1 Experimental setup

Figure 8.3 shows the experimental setup consisting of a shore normal transect of stilling wells (cf. section 3.2) installed from seaward of the low water mark to some distance beyond the high water mark. Well spacings through the active intertidal zone were around 3m to ensure sufficient spatial resolution to infer a recharge distribution reasonably accurately. The wells were monitored every 10 minutes over a single, semi-diurnal tidal period (12.5hours). The data is given in Appendix A.5.

The observed high tide and low tide water table levels are shown in Figure 8.4 where the high tide 'hump' in the water table profile due to wave runup infiltration is clearly visible. Digital video was used to monitor wave runup for half hour periods every second half hour throughout the tidal period. Wave runup transgression statistics were then extracted later using the stilling wells and sand surface elevations as reference points.

Figure 8.3: Experimental transect at Brunswick Heads, February 18 2002.

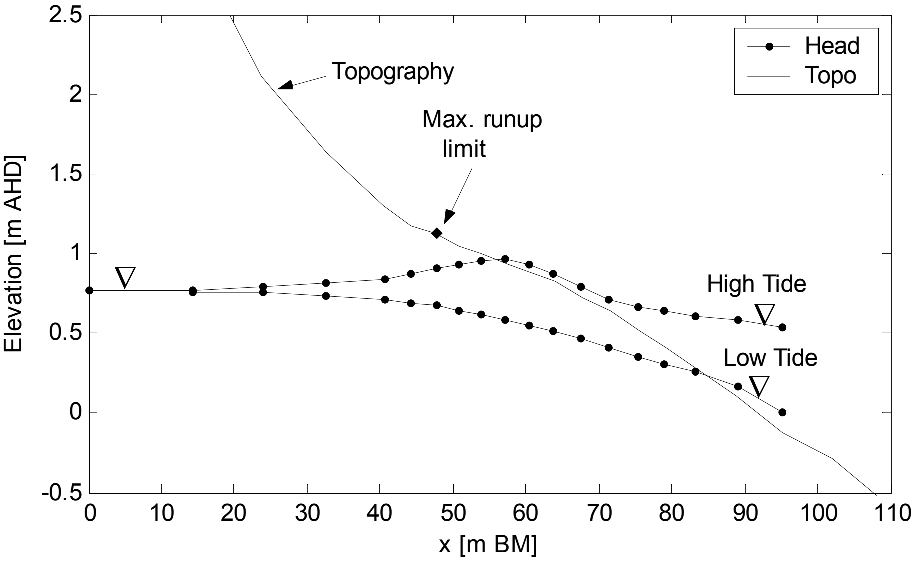

Figure 8.4: Profile of experimental conditions, showing high and low tide water table profiles with the points on the curves indicating measurement locations. Also indicated is the maximum wave runup limit observed during the monitoring period.

Figure 8.5 shows the oceanic forcing climate and the observed hydraulic response at the beach face. The amplitude of the dominant, first harmonic (T_ω = 12.25hours) in the tide was 0.45m and the offshore wave climate was fairly steady with a mean H_{rms} of 0.87m (+/- 0.02m) and mean period, T_W, of 8.8sec (+/- 0.4sec). The mean tidal elevation was 0.11m AHD compared to the mean shoreline elevation (the intersection of the mean water surface with the beach face, cf. section 2.2.2.1) of 0.52m AHD.

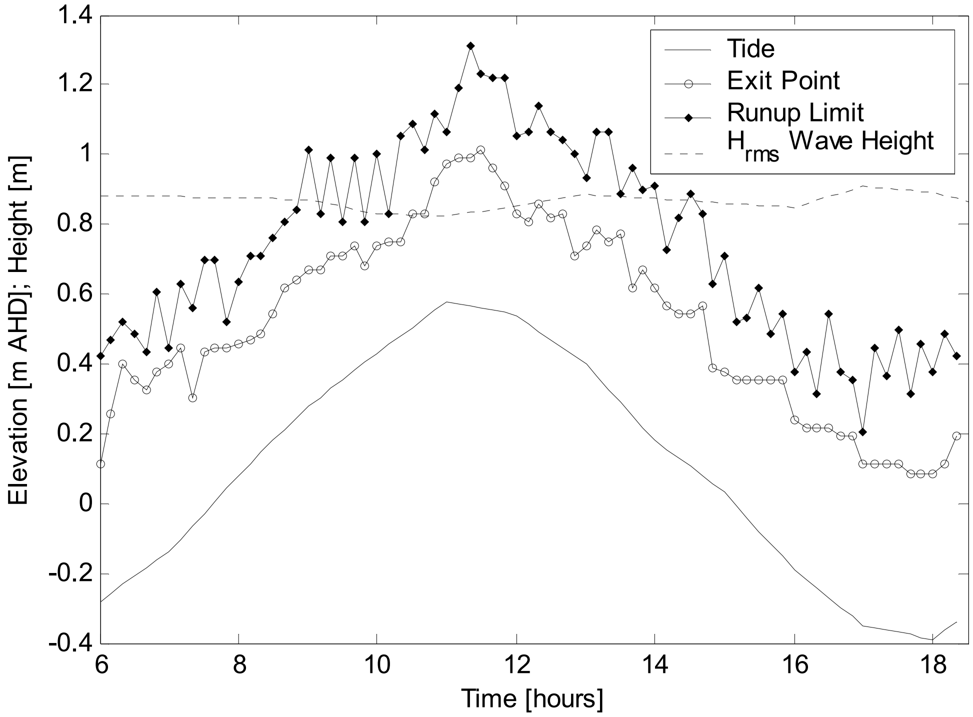

Figure 8.5: Observed tide (—), runup limit (♦), exit point (o) and offshore root mean square wave height, H_{rms}, (---) during the experiment.

8.3.2 Parameter estimation

The estimation of *Ui* is sensitive to the choice of aquifer parameters *K* the hydraulic conductivity, *n* the drainable porosity and (for the small amplitude equation) *d* the mean aquifer depth. In the field these parameters are not easily determined particularly the aquifer depth if deep drilling is unavailable. Previous researchers [*Turner*, 1989; *Kang et al.*, 1994b; *Kang*, 1995; *Turner and Masselink*, 1998] have assumed that landward of the high water mark, *Ui* = 0, and thus solved the linearised form of equation (8.1) for the hydraulic diffusivity, *Kd/n,* using the finite difference scheme,

$$\frac{Kd}{n} \approx \frac{\dfrac{h_i^{n+1} - h_i^{n-1}}{2\Delta t}}{\dfrac{h^{2n}_{i-1} - 2h^{2n}_{i} + h^{2n}_{i+1}}{2\Delta x^2}} \tag{8.5}$$

However, this method was found to be inappropriate for the present data as, with time, the spatial derivative occasionally passed through zero, sending the ratio, *Kd/n*, to infinity. At other times, *Kd/n* was not constant in time making a median value being hard to accurately define.

The method adopted for the present study utilised the infinite order, finite-depth dispersion relation of *Nielsen et al.* [1997], cf. equation (5.7). In section 5.3 this theory was shown to reasonably account for observations of water table wave dispersion at the semi-diurnal tidal period. The hydraulic conductivity, *K*, was determined using constant head permeability tests in the laboratory. Any influence of the capillary fringe on the dispersive properties of the water table wave was accounted for using the empirical complex effective porosity, n_ω, formulation of *Nielsen and Turner* [2000], equation (4.17). The aquifer depth, *d*, was then estimated using equation (5.7) with *d* as the fitting parameter to the experimental wave number, $k = k_r + ik_i$ determined using the procedure described in section 5.2.

Table 8.1: Parameters used in estimation of aquifer depth, *d*, using the dispersion relation, equation (5.7).

n	H_ψ	ω	K	n_ω	k_{Theory}	k_{Data}	d
0.35	0.50	1.4×10^{-4}	3.5×10^{-4}	$0.219 - 0.096i$	$0.075 + 0.034i$	$0.076 + 0.033i$	11.8
[ ]	[m]	[rad/s]	[m/s]	[ ]	[m^{-1}]	[m^{-1}]	[m]

8.3.3 Results and discussion

Figure 8.6 through Figure 8.8 show the evolution of the following quantities throughout the semi-diurnal tidal cycle: (1) Wave runup distribution; (2) Recharge distribution, *Ui/K*; (3) Head level profile, $h(x, t)$ and (4) Time series of the tide level and H_{rms} denoting tidal stage.

During the rising tide (07:00 to 11:00) *Ui/K* is positive (aquifer recharge/infiltration) in agreement with previous findings (e.g. *Kang*, 1995; *Turner and Masselink*, 1998). This is due to the swash zone wave action gradually encroaching upon the drier, more loosely packed sand in the upper reaches of the intertidal zone. On the falling tide (12:00 to 17:00) *Ui/K* becomes negative (aquifer discharge/exfiltration) as the swash zone recedes back over the (now) saturated lower reaches of the intertidal zone.

However, some peculiarities exist in the model output, the most notable being a maximum in/exfiltration at the runup limit and a finite amount of in/exfiltration being seen landward of this point. Landward of the runup limit there is no supply of water at the sand surface so the apparent in/exfiltration landward of this point raises some doubts in the application of the modified (1D) Boussinesq equation to this situation.

The equation (8.1) neglects any vertical flows which may well influence, even in the time-averaged sense, the pressure distribution and hence in/exfiltration in this region. Also the consideration of the influence of the capillary fringe through the complex effective porosity (cf. section 4.2) potentially has some limitations as discussed in section 5.6. That is, the complex effective porosity (born from 1DV experiments) and other theoretical considerations of capillarity effects (e.g. *Parlange and Brutsaert*, 1987) assume that flow within the fringe occurs solely in the vertical. The inferred observation that a finite amount of flux across the water table is occurring landward of the runup limit begins to suggest that there may indeed be a certain amount of horizontal flow in the fringe. Investigation of horizontal pressure gradients and hence flows in the capillary fringe is recommended for future research.

Despite the peculiarities in the present application of the model, it does produce findings that one would intuitively expect. During the rising tide infiltration occurs which increases in magnitude until a maximum is reached just after mid tide (10:00). Just after high tide (12:00) the flux changes direction and exfiltration begins reaching a maximum at mid falling tide (15:00). Around low tide the flux is at its smallest.

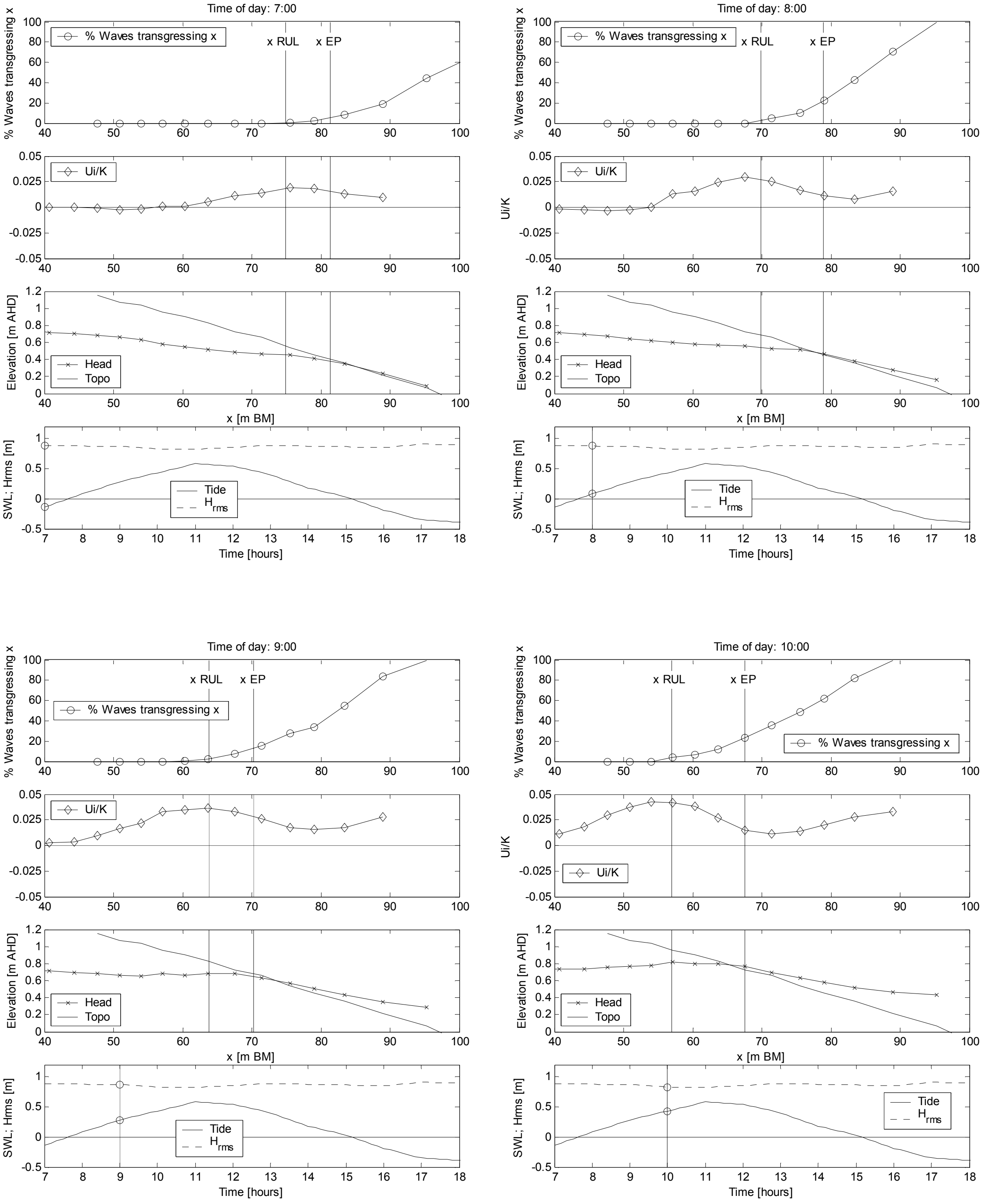

Figure 8.6: Evolution of recharge distributions, 07:00 to 10:00. In each quadrant, the four panels depict (from the top): (1) Wave runup distribution; (2) Recharge distribution, $Ui(x)/K$; (3) Head level profile, $h(x, t)$ and (4) Time series of the tide level and H_{rms} denoting tidal stage.

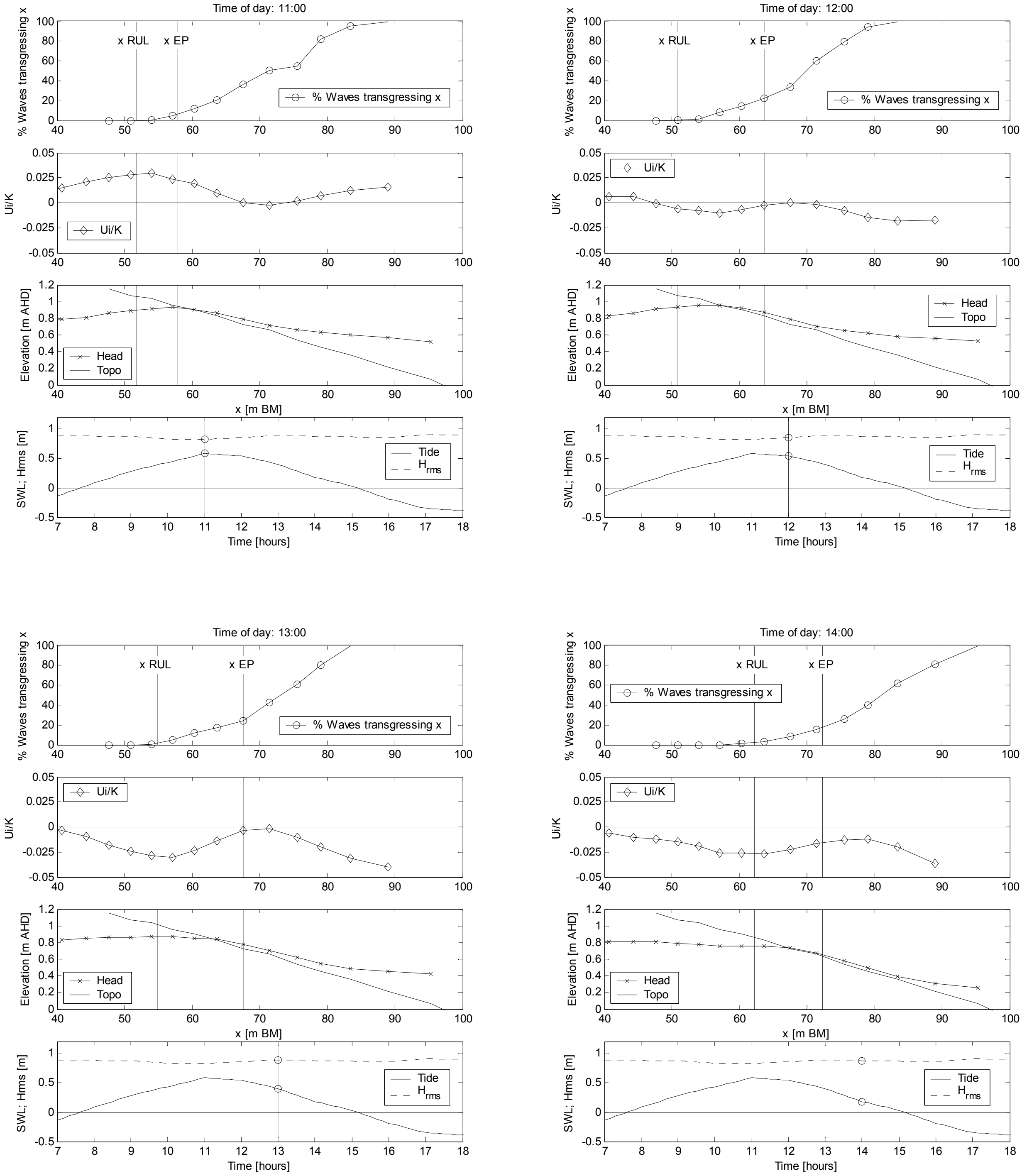

Figure 8.7: Evolution of recharge distributions, 11:00 to 14:00. In each quadrant, the four panels depict (from the top): (1) Wave runup distribution; (2) Recharge distribution, $Ui(x)/K$; (3) Head level profile, $h(x, t)$ and (4) Time series of the tide level and H_{rms} denoting tidal stage.

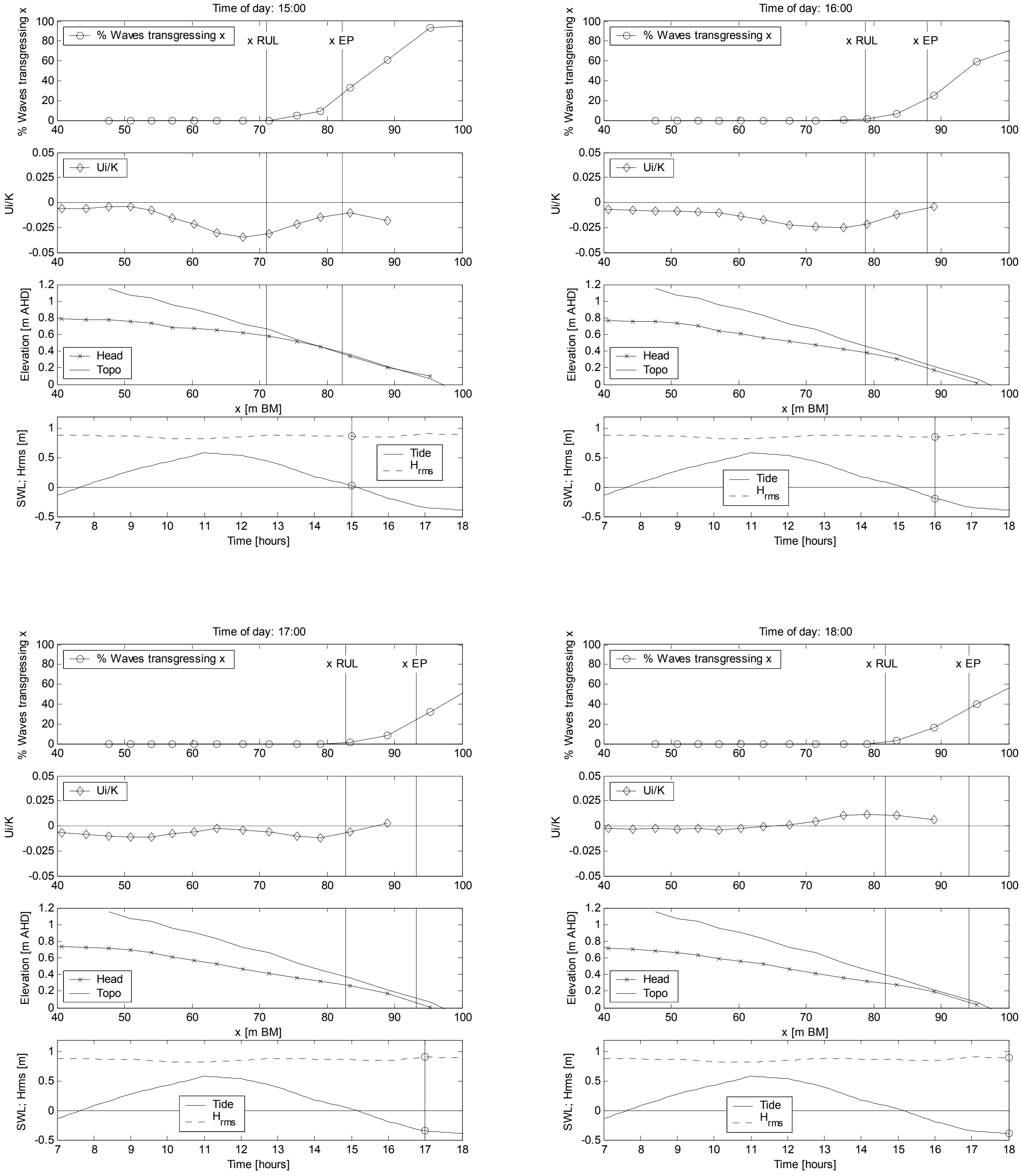

Figure 8.8: Evolution of recharge distributions, 15:00 to 18:00. In each quadrant, the four panels depict (from the top): (1) Wave runup distribution; (2) Recharge distribution, $Ui(x)/K$; (3) Head level profile, $h(x, t)$ and (4) Time series of the tide level and H_{rms} denoting tidal stage.

8.4 Laboratory experiments

Due to the oddities found when applying the modified Boussinesq equation to field data an experiment was run in the laboratory under regular wave forcing in the absence of a tide.

8.4.1 Experimental setup and procedure

The wave flume used was 80cm wide, all experimental parameters are summarised in Table 8.2. The waves were run for two days prior to the experiment to ensure that a quasi-steady beach profile was reached.

Table 8.2: Summary of beach and forcing parameters for laboratory experiments.

BEACH				FORCING			
d_{50}	d_{90}/d_{10}	β_F	K	z_{RUL}	SWL	H	T
0.78	1.60	0.19	0.0025	689	443	170	2.5
[mm]	[-]	[rad]	[m/s]	[mm]	[mm]	[mm]	[s]

d_{50} is the median grain size, d_{90}/d_{10} the grading coefficient, β_F the beach face slope, K the hydraulic conductivity, z_{RUL} the elevation of the runup limit, SWL the still water level, H the wave height and T the wave period.

Piezometric head levels were measured using bottom-mounted manometer tubes connected to an external manometer board at varying shore-normal locations along the centreline of the beach. Starting with a static head level at $h^*(x) = SWL$, the waves were run until a steady hydraulic state was reached. The evolution of the piezometric head profile from its initial condition was monitored using digital still images of the manometer board at time intervals varying from 10 seconds initially to 15 minutes as the accretion rate of the head levels slowed.

Recorded head levels were corrected for the response time of individual manometers by the linear differential equation,

$$h_{CORRECTED}(x,t) = h_{OBS}(x,t) + \mathrm{T}\frac{dh_{OBS}}{dt} \qquad (8.6)$$

with h_{OBS} the observed head levels and T the response time of the individual manometer tube as determined in situ.

8.4.2 Results and Discussion

Figure 8.9 shows the observed evolution of the head profiles, clearly depicting spatial maxima within the active infiltration zone for $t < 10$min. This is also observed in the field during the rising tide [cf. *Kang et al.*, 1994b; section 3.3.3] as the swash zone encounters the “dry” region of the intertidal zone where infiltration is enhanced. Initially the head levels rise rapidly before slowing and a steady state being reached after about 2.5hours. The upwardly concave mean water surface in the inner surf zone as a result of wave breaking is also seen.

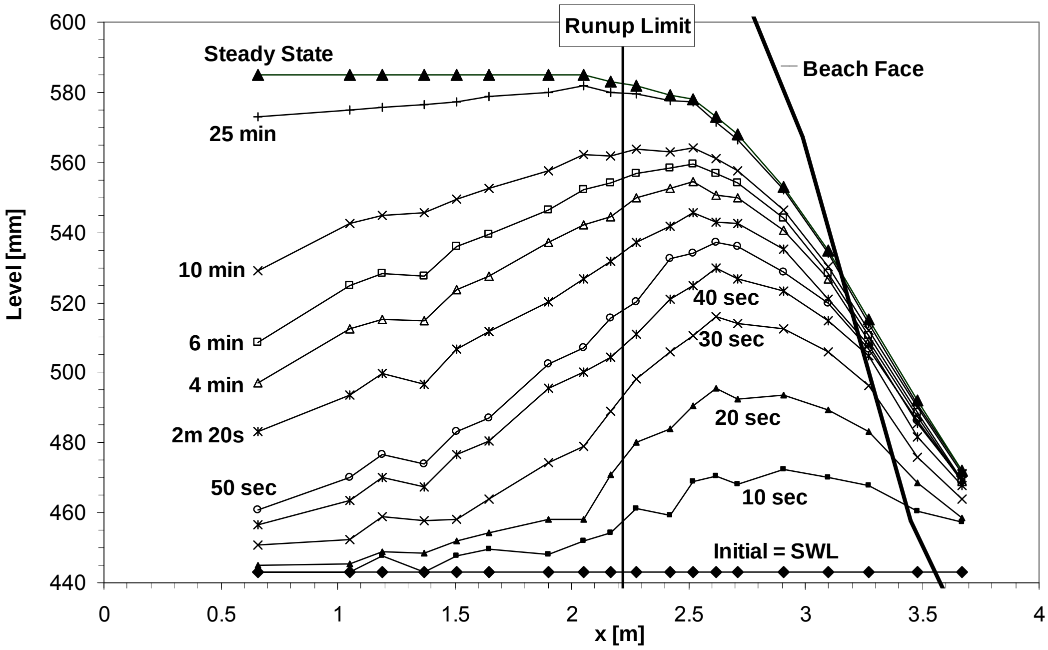

Figure 8.9: Evolution of $h^*(x,z=0,t)$ from the initial still water level (♦) to steady state (▲).

Inferred infiltration distributions are presented in Figure 8.10 with the X_n axis normalized to be 0 at the shoreline and 1 at the runup limit using,

$$X_n = \frac{x - x_{SL}(t)}{x_{SL}(t) - x_{RUL}} \tag{8.7}$$

where x = shore-normal coordinate of the manometer, x_{SL} = shoreline coordinate and x_{RUL} = runup limit coordinate.

Qualitatively, the peak magnitudes of *Ui/K* are initially 0.47 and then rapidly drop off to a steady state value of 0.14, which is in good agreement with the steady state values obtained by *Kang* [1995]. The larger values for the initial transient distributions are due to the initially "dry" beach and resultant rapid rise in head levels (i.e. large $\partial h/\partial t$). These values drop off rapidly in the first few minutes as the beach fills and $\partial h/\partial t$ approaches 0. There is also a shift in the position of the peak *Ui/K* value with time due to the changing balance between the supply (swash lens thickness) and reception (beach saturation) at a given shore-normal location. Initially, peak values are at $X_n \approx 0.67$ then gradually shift to a steady state location of $X_n \approx 0.46$ again in agreement with the findings of *Kang* [1995].

However, the peculiarity described in section 8.3.3 in relation to the field experiments is also present in the laboratory results. That is, a finite amount of infiltration occurring at the runup limit in the transient distributions.

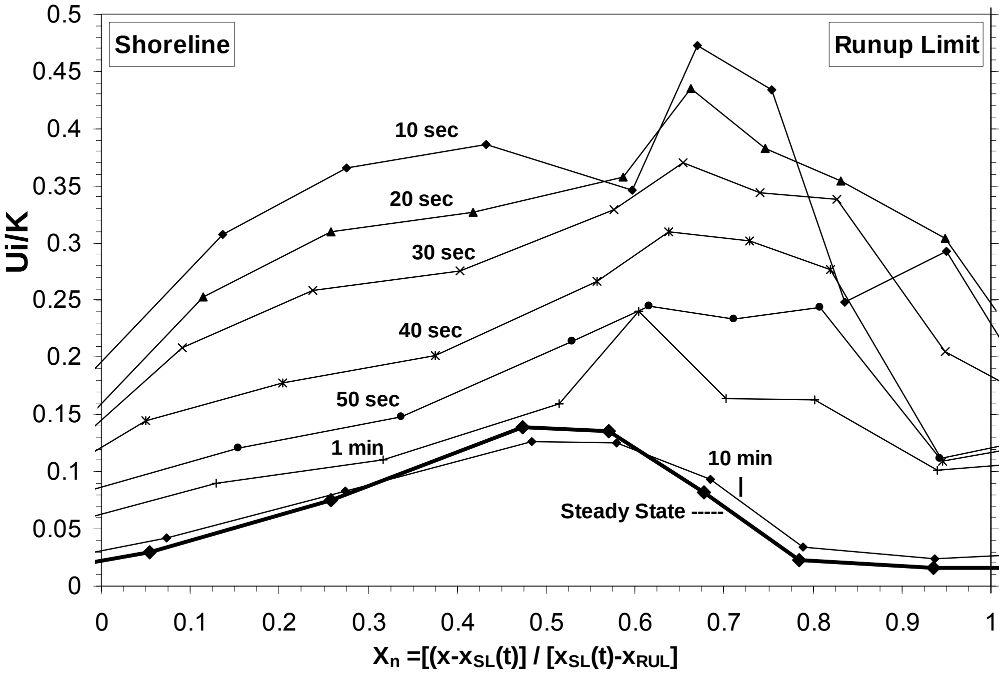

Figure 8.10: Evolution of infiltration distributions in the laboratory.

As there is no runup, and therefore zero supply of water landward of this point it is expected that there is zero infiltration here. This raises the question of what exactly is the physical meaning of the term *Ui* in equation (8.1)?

Figure 8.2 illustrates the conceptual definition of *Ui*. Mathematically, it is an additional flux term accounting for any imbalance between the spatial and time derivatives and that flux is across the water table. So, unless the water table coincides with the sand surface, it is not actually the infiltration rate across the beach face but an aquifer recharge rate. The fact that there is recharge at, and landward of, the runup limit suggests that there is a horizontal flow component in the region between the sand surface and the water table.

If the water table lies below the sand surface then the sub-surface flow will involve a component of partially saturated or tension-saturated flow (see Figure 8.2) that will need to be taken into account when trying to accurately estimate infiltration rates. Knowledge of the flow and pressure distribution in this region will enable us to address the question: How is water in this region transported landward of the runup limit? This issue however, is left for future investigations.

The question still remains though: Is it possible to estimate a flux across a beach face from observed head profiles?

8.5 Numerical experiment

A simple 2D vertical (2DV) numerical model similar to, but not identical to, the laboratory setup was designed to assess the influence of vertical flow on inferred infiltration distributions. The Mike SHE modelling system used here, solves the 3D form of the non-linear Boussinesq equation but is used here in a 2DV application only, i.e. solving,

$$n_e \frac{\partial h^*}{\partial t} = K\left[\frac{\partial}{\partial x}\left(h^* \frac{\partial h^*}{\partial x}\right) + \frac{\partial}{\partial z}\left(h^* \frac{\partial h^*}{\partial z}\right)\right] + P \qquad (8.8)$$

where P is an additional precipitation flux term used in this application as the flux due to infiltration from “wave runup”, *Ui*.

Figure 8.11 illustrates the conceptual model with an “inland” no flow boundary condition and a “seaward” constant head (= initial condition) boundary condition. A constant shape (half cosine curve) “infiltration” distribution was applied as a flux across the free water surface until the head levels reached equilibrium. For comparison, the 1D version [equation (8.1)] of the same model setup was also run.

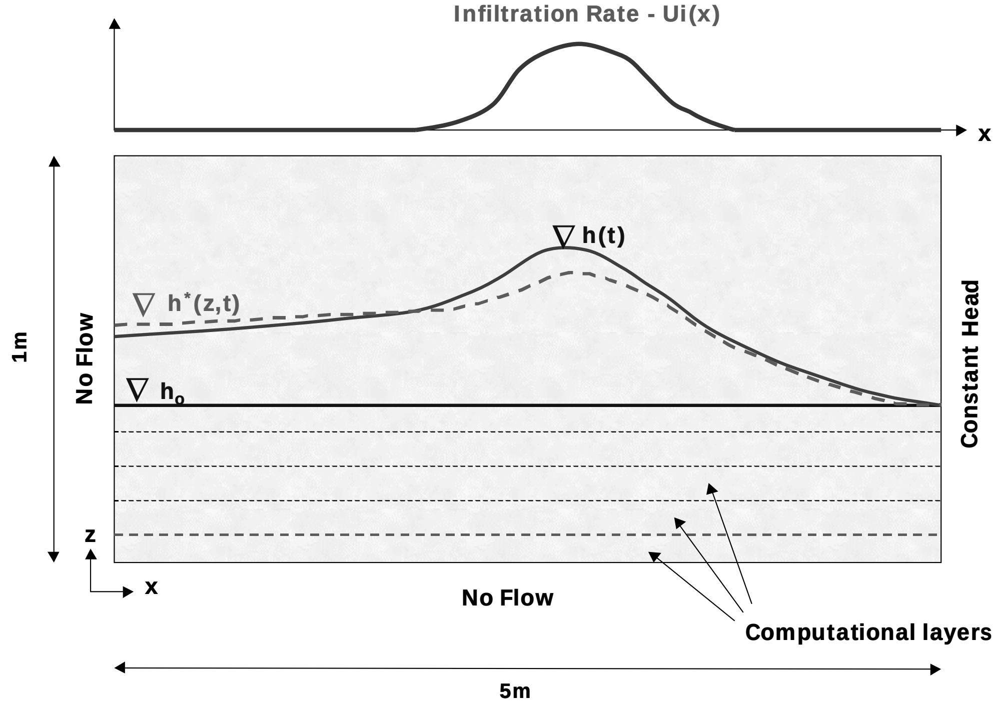

Figure 8.11: Conceptual model for the numerical experiments, h_o = initial head level, h^* = head level from base, h = head level from top layer.

8.5.1 Vertical flow effects

For saturated porous media flows, the vertical flow is described by the Darcy velocity, w,

$$w = -K\frac{\partial h^*}{\partial z} \tag{8.9}$$

Integrating equation (8.9) with respect to z leads to the following correction to piezometric head levels to obtain an expression for the water table level,

$$h = h^* - \int_z^h \frac{w}{K}dz \tag{8.10}$$

Therefore if there is infiltration, i.e. – w, the water table, or head levels measured higher up, is expected to sit above head levels measured at lower levels and vice versa for exfiltration (+ w).

8.5.2 Results and Discussion

Figure 8.12 shows the head level profiles extracted from the bottom and top computational layers of the 2DV model and compares them to the levels obtained from the one layer model. The effect of vertical flow is clearly visible with the downwards directed flow within the "infiltration" zone causing the top layer head levels to sit above those from the bottom layer. The effect of upwardly directed flow is also apparent near the no flow boundary ($x = 0$), with the top layer head levels initially lying underneath the bottom layer levels as the beach fills. As the steady state is approached and vertical flows near the boundary disappear the head levels show the expected hydrostatic pressure distribution, i.e. $h_{TOP} = h_{BASE}$.

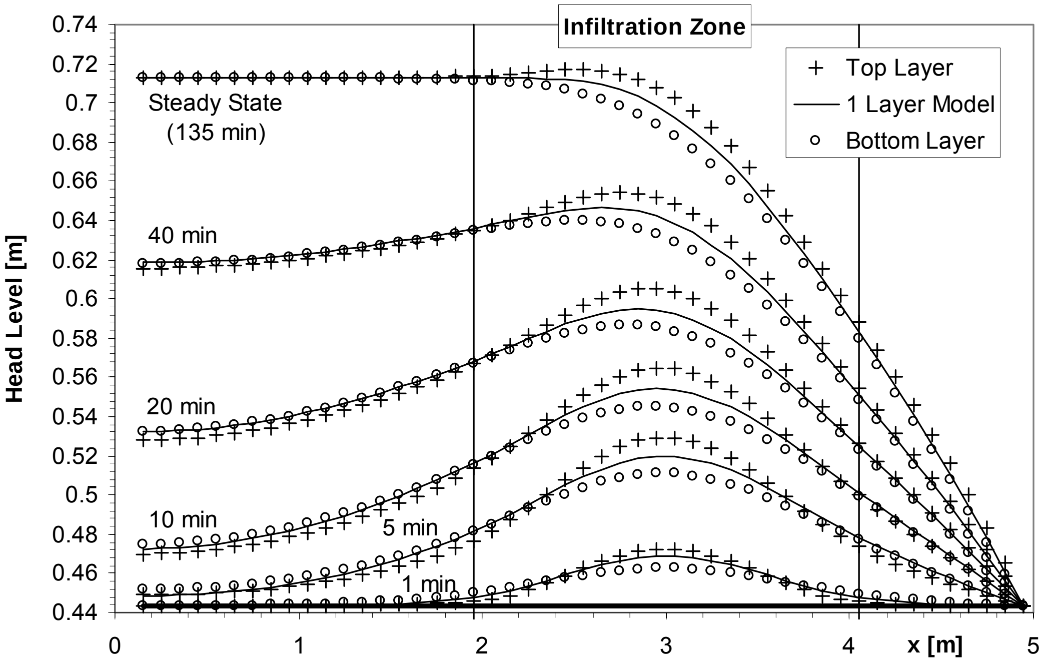

Figure 8.12: Head levels extracted from the top (+) and bottom (o) layers of the 2DV model compared to the head levels from the one layer model (—).

Another point of interest in Figure 8.12 is the difference in curvature of the head profiles when comparing the bottom layer results to that of the top layer. The top layer, closest to the additional flux being added, depicts a much sharper curvature than the bottom layer confirming that the significance of vertical flow effects diminishes with distance from the source of the vertical flow. This difference in the severity of the curvature has implications for computing the spatial derivative in estimating infiltration rates and is discussed later.

Inferred infiltration rates for the time step, *t* = 5min, are shown in Figure 8.13. The curve from the one layer model exactly matches the model input as expected as the equation used to infer the infiltration rate [equation (8.1)] is the equation that the 1D model solves. From the base head levels an infiltration distribution analogous to the laboratory experiments is obtained. At the boundaries of the infiltration zone (i.e. the "runup limit") there is a finite amount of infiltration.

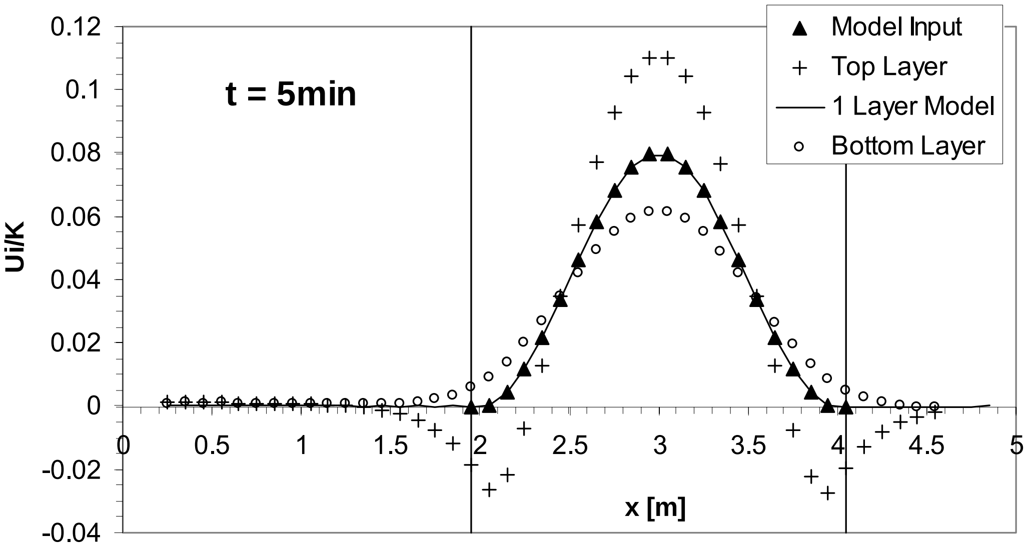

Figure 8.13: Inferred infiltration rates at t = 5min for the top (+) and bottom (o) layers of the 2DV model compared to that from the one layer model (–). The model input is also shown (▲).

A somewhat curious feature of Figure 8.13 is seen in the distribution inferred from the top layer profile which becomes negative within the infiltration zone. This is a consequence of the sharpness of the curvature in the corresponding head profile, leading to the spatial derivative crossing the time derivative as shown in Figure 8.14. A local maximum in the spatial derivative (and hence minimum in *Ui*) is reached when the curvature transitions between upwardly concave to convex and vice versa near, but within, the boundaries of the infiltration zone. This feature however bears no resemblance to anything physical that may be occurring, i.e. it is not possible for exfiltration (upwardly directed flux) to be occurring within an area of active infiltration.

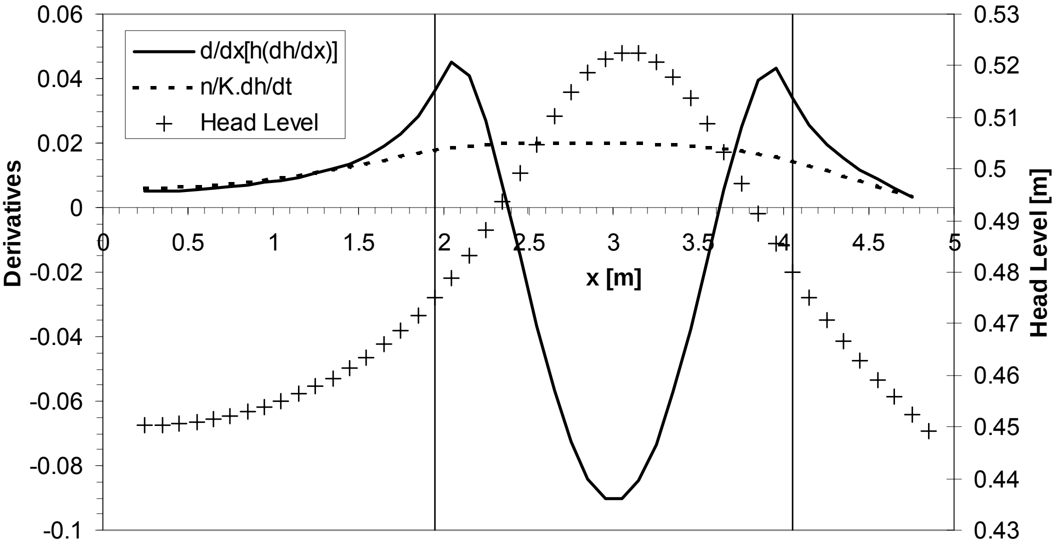

Figure 8.14: Comparison of the top layer head profile (+) with its spatial (–) and temporal (---) derivatives.

8.6 Summary

The use of a modified Boussinesq equation to infer an infiltration distribution due to wave runup on beaches has been critically assessed using field, laboratory and numerical (2DV) experiments. In each of the experiments a finite amount of "infiltration" is observed at the runup limit. This confirms that this model provides us with an estimate of aquifer recharge across the water table. It doesn't provide us with a means of estimating the flux across the sand surface, unless the water table somehow coincides with the sand surface.

Some questions remain for future work. What is the source of the flux across the water table outside the infiltration zone? What happens to the flow in the capillary fringe above the water table? What is the vertical and horizontal pressure distribution in this region?

Chapter 9 – Salinity structure and dynamics in beaches

9.1 Introduction

Coastlines around the world are home to much of the world's population and, as such, water resources in these regions are subject to intensive stresses and demands, one of the big issues is salt water intrusion. Typically, the phenomenon of salt-water intrusion has been studied and modelled at catchment scales, and little consideration has been given to the small scale dynamics near the shore. These dynamics, however, have important implications for interstitial biology and chemistry in the near-shore area [*Li et al.*, 1999a; *Andersen et al.*, 2001] and for local communities who rely upon coastal aquifers directly for their water supply.

Beach groundwater hydrodynamics are the result of combined forcing from the tides and waves at a range of frequencies. Individual and combined contributions of these forcing oscillations to the near-shore groundwater hydrodynamics are not easily resolved [*Nielsen*, 1999a] and their influence on the dynamics of the salt-fresh water interface (SWI) has yet to be addressed in detail.

In this chapter, new field observations of the dynamics of the salinity structure in unconfined beach aquifers are presented adding to the existing database presented by *Nielsen and Voisey* [1998] and *Nielsen* [1999a]. One of the new data sets captures the deposition of a thin salty layer overlying fresh aquifer water due to the infiltration from wave runup.

The second data set captures the response of the salinity structure to a wave-induced pulse in groundwater levels. Such oscillations may affect significantly the fate of chemicals in the aquifer and modify the rates and forms of chemical inputs to adjacent coastal sea and estuary/tidal rivers. *Li et al.* [1999a] showed that the SWI fluctuations can lead to desorption of previously absorbed chemicals from sand particles, producing a local source of contaminants for the aquifer and nearby coastal water bodies. The SWI fluctuations also enhance the mixing of saltwater and freshwater in the aquifer, and hence affect many chemical reactions [*Andersen et al.*, 2001]. Beach rock cementation has also been shown to be dependent upon the mixing of ocean and aquifer water [e.g. *Moore*, 1973]. To examine and quantify the observed SWI fluctuations, a simple, sharp-interface model is developed.

9.2 Field measurements

Sub-surface water samples were obtained using hollow stainless steel “salinity spears” as shown in Figure 9.1. In order to delineate the salinity structure various spears were installed to varying depths at several shore-normal locations as shown in Figure 9.2. The positioning of the sampling cluster was determined by first locating the salt and freshwater limits of the surficial mixing zone and then installing clusters at quasi-regular spacing. The conductivity of each sample were then determined *in situ* along with that of local seawater samples for normalisation of results.

9.3 Effects of infiltration from wave runup

During an experiment at Point Lookout on North Stradbroke Island (cf. Appendix A.1) the surficial SWI was overtopped by the swash zone around high tide, depositing a thin layer of salt water on top the underlying freshwater as shown in Figure 9.3. The resulting unstable, dynamic situation makes for an interesting modelling challenge which is however not taken up here.

The structure was monitored at different times during a 23hour period and is seen to gradually move landward several metres. There was no observable fluctuation of the SWI with the tidal oscillation. This is in agreement with the numerical experiments of *Ataie-Ashtiani et al.* [1999] who found the only influence of the tide was to increase the width of the mixing zone.

Figure 9.1: Hollow, stainless steel sampling “spears”.

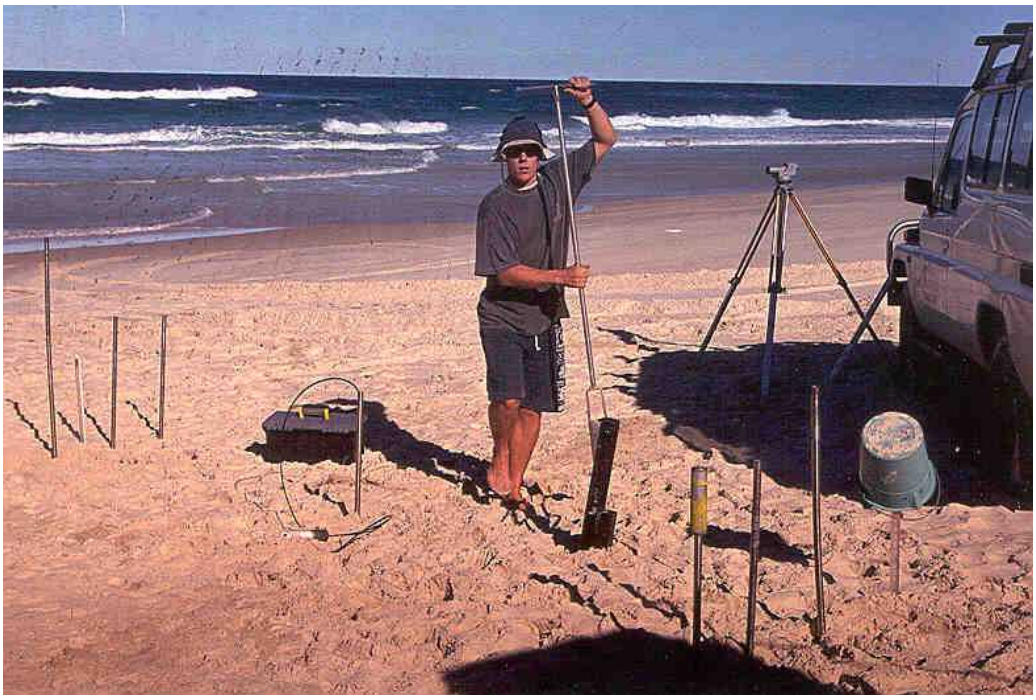

Figure 9.2: Cluster of sampling spears, North Stradbroke Island.

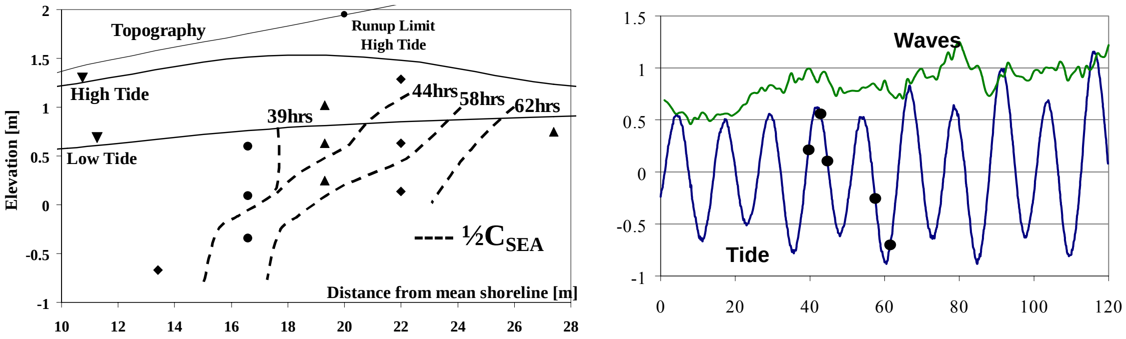

Figure 9.3: (a) Evolution of the 50% of seawater salinity contour in a natural beach. (b) Wave and tide data for the sampling period, sampling times are denoted by (•).

If the SWI doesn't respond directly to the tidal fluctuations then what does it respond to? At this point of the investigation the neap to spring tidal cycle (14days) was suggested as a possible candidate and an experiment was conducted to examine this. Clearly the extent of salt water intrusion will depend on the amount and duration of rainfall, however the data of *Nielsen* [1999a] indicates that the freshwater lens at Bribie Island (cf. Figure 3.1) to respond on the time scale of months.

9.4 Response to an offshore storm

The salinity structure at Brunswick Heads beach was monitored for 15days to examine the influence, if any, of the neap to spring tidal cycle (cf. Appendix A.4).

Figure 9.4 shows the ocean forcing climate leading up to and during the experiment. The tidal range varied from nearly 2m at the spring tide to around 0.5m at the neap tide. The dominant feature in the oceanic forcing during the monitoring period was an increase in the significant wave height (H_{sig}), which began prior to the neap tide (20th of November, event 1 in Figure 9.4 (b)) and lasted for about 3days with two peaks of H_{sig} around 4.5m observed.

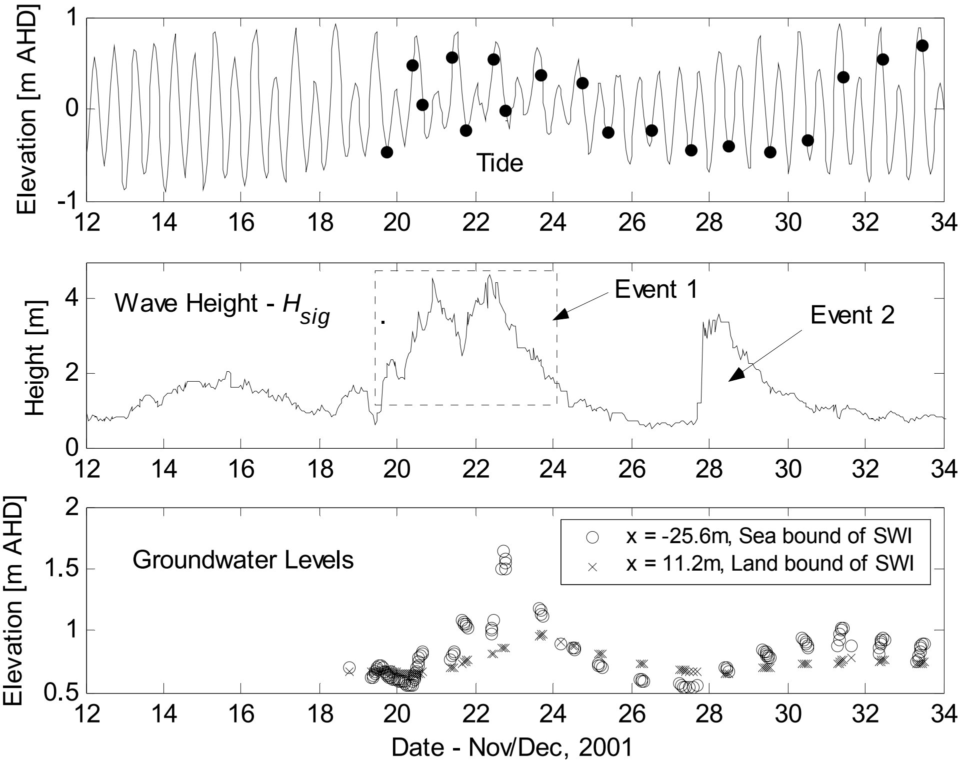

Figure 9.4: (a) and (b) The tide and wave climate prior to and during the two week sampling period, the symbols (•) indicate sampling times. (c) The groundwater levels observed at both the seaward (○) and landward (×) boundaries of the SWI.

9.4.1 Groundwater response

In a direct response to the first, double peaked increase in wave height (event 1 in Figure 9.4 (b)), the most dominant feature in the observed groundwater levels shown in Figure 9.4 (c) is a pulse up to 1m in the vicinity of the seaward boundary of the SWI. This response is due to the corresponding increase in wave setup at the shoreline (cf. section 2.2.2.1). A second, similar in magnitude, single peaked increase in wave height later (event 2 in Figure 9.4 (b)), has relatively little effect on the groundwater levels because of the shorter duration (a day or so). This is despite the approaching spring tide, which can also contribute to an increase in groundwater level [*Raubenheimer et al.*, 1999; *Li et al.*, 2000b]. It is noted that the observed neap-to-spring tidal cycle represented a micro-tidal climate. In a macro-tidal climate (spring tide ranges up to several metres) the neap-spring tidal cycle would have a greater influence on the near shore groundwater dynamics.

Rainfall data from a rain gauge 10km from the site, as shown in Figure 9.5, indicate that no significant (magnitude or duration) rainfall occurred during or in the months prior to the experiment. The response of the very similar Bribie Island coastal-barrier aquifer freshwater lens has been shown to be of the order of several months [*Nielsen*, 1999a]. Observations at shorter time scales (hours to days) show little response of the aquifer to even heavy rainfall events, visual evidence of this can be found by digging away the surface layer of sand which tends to reveal that only the upper few centimetres of sand are wet. *Vigneaux* [2003] found that isolation of rainfall effects from observed beach groundwater dynamics has proven difficult mainly due to the fact that the offshore storm which generated the rainfall also caused marked increases in wave heights and hence shoreline setup (cf. section 3.3.4).

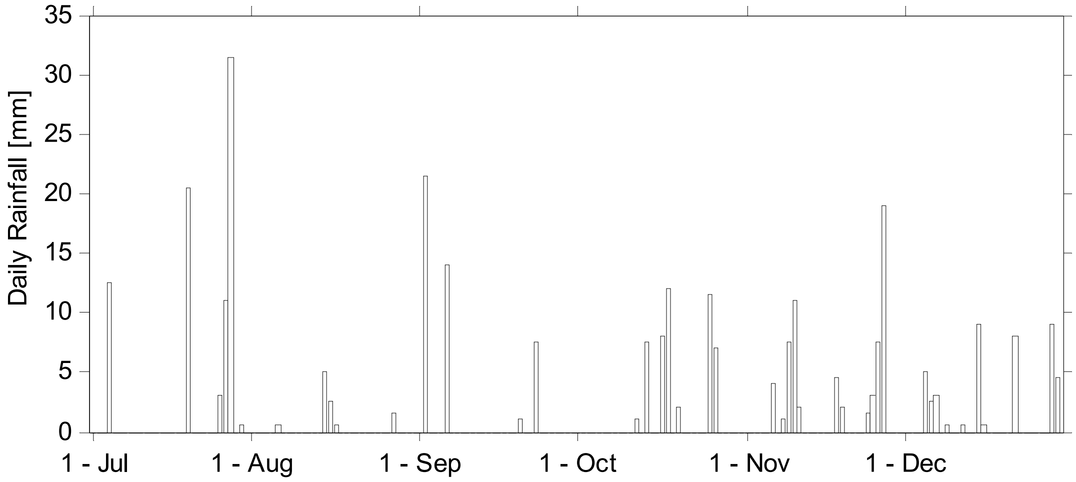

Figure 9.5: Daily rainfall totals, collected from Myocum rain gauge station, 10 km south-west of the field site.

9.4.2 The salinity structure

During the experiment, water samples were collected at least daily [cf. Figure 9.4 (a)] from the sampling locations shown in Figure 9.6 (a). These samples were analysed to determine their salinity. Based on the data, the salinity profile (spatial distribution) was delineated for each day. Figure 9.6 (b) gives a snapshot of the observed salinity structure. A classical "salt-wedge" structure is seen, indicating that infiltration of saltwater at the sand surface had no direct influence on the SWI [cf. section 9.3]. This is supported by the fact that the maximum wave runup limit during the sampling period only just reached the seaward boundary of the SWI [cf. Figure 9.6 (a)].

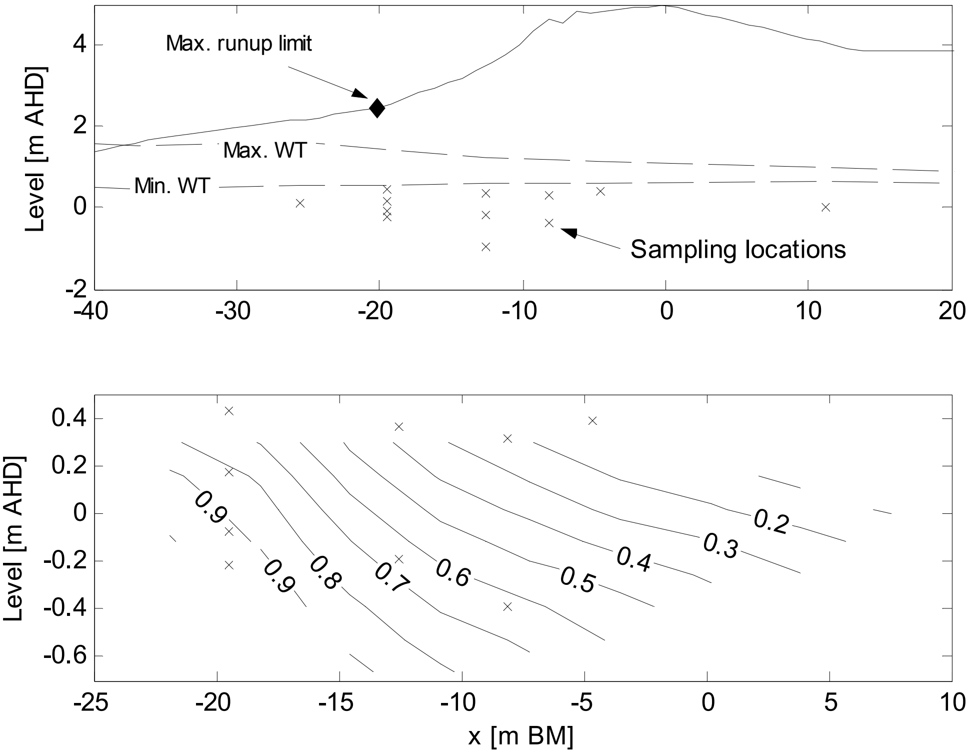

Figure 9.6: (a) Experimental layout and maximum and minimum water table profiles during the sampling period. (b) Snapshot of the observed salinity structure represented as the normalised concentration C/C_{sea}.

The results show (in agreement with *Nielsen and Voisey* [1998]) that the interface is quite diffuse in nature with a horizontal distance of approximately 25m from the almost zero salinity to seawater salinity contours. However, the distribution of the salinity contours is reasonably regular throughout the mixing zone and therefore, for the purposes of investigating the dynamics of the interface, the 50% seawater salinity contour is taken to be representative of the interface's location, i.e., an equivalent sharp interface.

9.4.3 Response of the salt-freshwater interface

The response of the groundwater level and the normalised concentrations, C/C_{sea}, at different elevations at x = -12.6m are shown in Figure 9.7 (b) and (c), respectively. A clear correlation exists between the concentration signal and the 4-day pulse in the forcing shoreline elevation oscillations and the groundwater levels shown in Figure 9.7 (a) and (b), respectively.

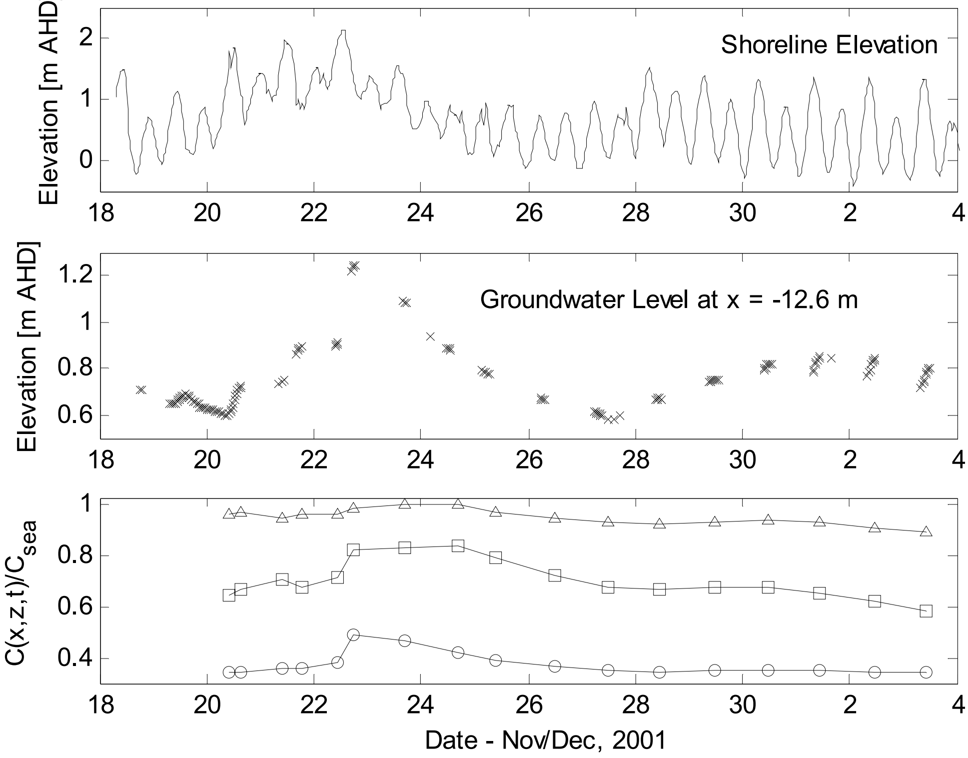

Figure 9.7: (a) Time series of the wave-induced pulse in shoreline elevation calculated using (9.15). (b) Resultant response in groundwater levels and (c) normalised concentrations, C/C_{sea}, at x = -12.6m. The symbols in panel (c) denote data from the different elevations z = 0.39m AHD (○), z = -0.19m AHD (□) and z = -0.74m AHD (Δ).

To examine the overall dynamic response of the interface, the temporal variations of the equivalent SWI (i.e. the 50% seawater salinity contour) are displayed in Figure 9.8. The contours are forced landward up until the 23rd of November as a direct result of the increase in the groundwater levels during the rising phase of the wave-induced groundwater pulse. The most landward coordinates of the wave runup limit were approximately (x,z) = (-20, 2.1) and therefore there was no direct influence from input of saltwater at the sand surface.

Afterwards, the SWI retreated seaward as the groundwater levels decreased (the declining phase of the pulse). Although the second, smaller and shorter wave event together with the approaching spring tide generate a relatively slight increase in the groundwater level, the SWI continued to move seaward, indicating that the tidal effects on the SWI are small relative to the significant (in both magnitude and duration) wave-induced pulse forcing. This observation is in agreement with the observations described in section 9.3 and the numerical experiments of *Ataie-Ashtiani et al.* [1999].

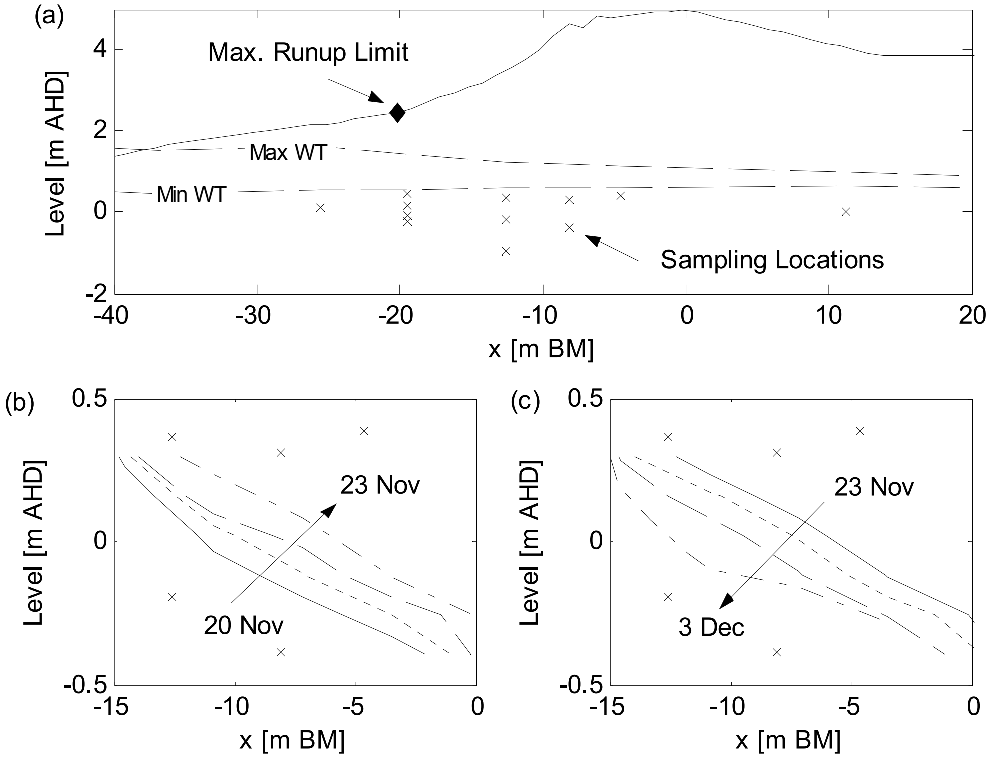

Figure 9.8: (a) Experimental layout and maximum and minimum water table (*WT*) profiles during the sampling period; (b) and (c) evolution of the C/C_{sea}= 0.5 salinity contours. Panel (b) shows contours for the 20/11 (—), 21/11 (---), 22/11 (——) and 23/11 (–-–). Panel (c) shows contours for the 23/11 (—), 24/11 (---), 26/11 (——) and 3/12 (–-–).

9.4.4 Sharp-interface modelling

In this section, the link between the SWI oscillations and the wave/storm event will be established quantitatively. For this purpose, a simple interface fluctuation model (i.e. that based on the sharp interface assumption) is developed to predict the observed fluctuations described above. Note that under this assumption the model is not able to replicate the salinity structure within the observed salt-freshwater mixing zone but it will be demonstrated to reproduce the observed fluctuations of the equivalent SWI, the 50% seawater contour (cf. section 9.4.2). The conceptual framework used in formulating the mathematical model is illustrated in Figure 9.9.

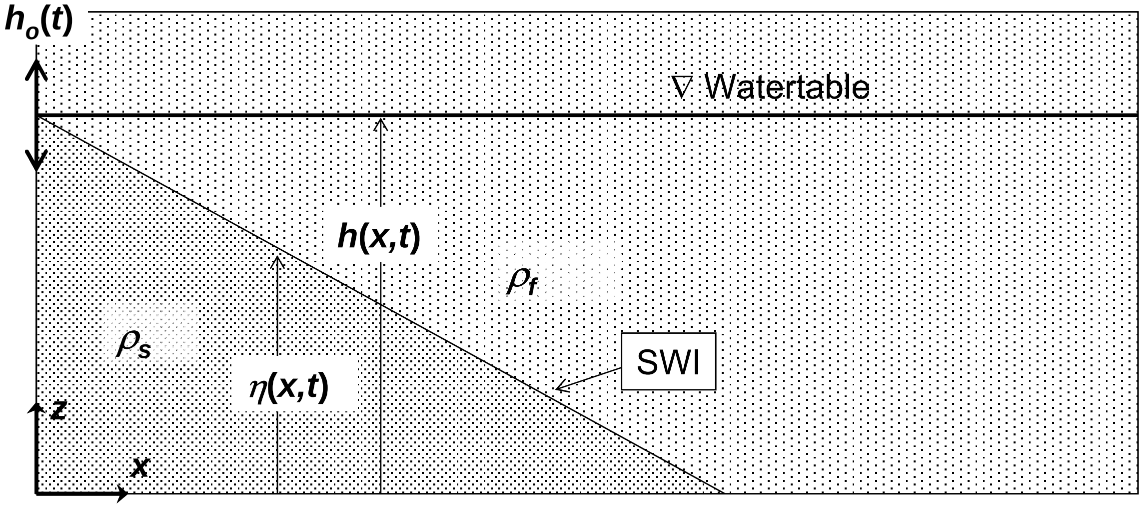

Figure 9.9: Definition of terms and the conceptual model of a sharp salt-freshwater interface subject to a time-varying forcing function, $h_o(t)$.

9.4.4.1 Forcing boundary condition

As the field observations indicate no measurable response of the SWI to either individual tides or the neap-to-spring tidal cycle (cf. Figures 4 and 5), modelling of the SWI response to the storm surge only is attempted here. During storms, the mean shoreline is elevated by the order of $0.4H_{rms}$ (root mean square wave height) above the tide level as a result of wave set-up and runup (Figure 1 of *Hanslow and Nielsen* [1993]). As the storm passes, the wave height decreases and so does the elevation of the mean shoreline. Thus the passing storm produces a pulse in the mean shoreline level. The observed pulse of the forcing shoreline oscillations, $h_o(t)$, follows fairly closely the shape of a Gaussian bell curve and as such a curve of that nature was fit to the data,

$$h_o = A\exp\left[-\left(\frac{t-t_o}{T_p}\right)^2\right] \tag{9.1}$$

where A is the maximum increase of the mean shoreline elevation (representing the magnitude of the oscillation), t_o is the time when the maximum occurs, and T_p is a characteristic time scale of the storm duration. Using a boundary condition of this form enables the use of text book solutions to the linearised groundwater flow equation which takes the form of the diffusion equation as will be outlined in the following.

9.4.4.2 Governing equations

Assuming a shallow aquifer and that $h_o/d << 1$, one can show that with the salinity effects included, the behaviour of the water table can still be described by the linearised Boussinesq equation [*Wang and Tsay*, 2001],

$$\frac{\partial h}{\partial t} = D\frac{\partial^2 h}{\partial x^2} \tag{9.2}$$

where h is the fluctuating groundwater level with respect to the base of the aquifer (Figure 9.9); x is the cross-shore coordinate; and D is the hydraulic diffusivity, $= Kd/n_e$ [d, n_e and K are the mean thickness, effective porosity and hydraulic conductivity (freshwater) of the aquifer, respectively, as shown in Figure 9.9]. Equation (9.1) defines the boundary condition for $x = 0$. Far inland, the oscillation effects are diminished and so, $\lim_{x\to\infty} h(x,t) = 0$. Also, since the focus is on the propagation and effects of the pulse only, it is assumed here that there are zero water table oscillations initially (prior to the pulse/wave event), i.e., $h(x,t=0) = 0$.

As discussed above, although the data showed that the interface is not sharp in nature (cf. Figure 9.6) [*Nielsen and Voisey*, 1998; *Nielsen*, 1999a; *Cartwright and Nielsen*, 2001], the 50% seawater salinity contour is taken here to be representative of an equivalent sharp SWI (section 9.4.2). Since the aim is to model the interface fluctuations in response to the wave-induced pulse and not the observed salinity structure as such, the sharp-interface assumption is made, i.e., immiscible fluids. By conservation of mass for the saline layer, one can show the SWI fluctuations are governed by the following equation,

$$n\frac{\partial \eta}{\partial t} = K_s\frac{\partial}{\partial x}\left(\eta\frac{\partial \phi_s}{\partial x}\right) \tag{9.3}$$

where η is the elevation of the interface with respect to the base of the aquifer; ϕ_s is the hydraulic potential in the saltwater layer; n is the porosity; $K_s = \frac{\nu_f}{\nu_s}K$ is the hydraulic conductivity in the saline layer with ν_f and ν_s the kinematic viscosities of the fresh and sea water, respectively. Under the assumption of a sharp-interface there must be continuous pressure at the interface, i.e. $P_s = P_f = P_\eta$. By definition (with no vertical flow effects),

$$\phi_s = \frac{P_\eta}{\rho_s g} + \eta \tag{9.4}$$

$$\phi_f = h = \frac{P_\eta}{\rho_f g} + \eta \tag{9.5}$$

with g the magnitude of gravitational acceleration and ρ_s and ρ_f the density of seawater and freshwater respectively. Combining (9.4) and (9.5) gives,

$$\phi_s = \frac{\rho_f}{\rho_s} h + \frac{\rho_s - \rho_f}{\rho_s} \eta \tag{9.6}$$

which upon substitution into (9.3) yields,

$$n\frac{\partial \eta}{\partial t} = K_s \frac{\partial}{\partial x}\left[\eta\left(\frac{\rho_f}{\rho_s}\frac{\partial h}{\partial x} + \frac{\rho_s - \rho_f}{\rho_s}\frac{\partial \eta}{\partial x}\right)\right] \tag{9.7}$$

Taking ρ_f = 1000kg/m^3, ρ_s = 1030kg/m^3, the ratio $(\rho_s-\rho_f)/\rho_s \approx 0.03$ and so for small interface slopes ($\partial\eta/\partial x$) the second term is often neglected to simplify the solution of (9.7) [*Wang and Tsay*, 2001]. The appropriateness of this assumption when applied to the present data set is described in detail in the following sections.

Another simplifying assumption is that of small amplitude fluctuations, $|\eta - \overline{\eta}| << \overline{\eta}$ where $\overline{\eta}$ is the mean SWI elevation (i.e., the magnitude of the SWI oscillation is small relative to the local saline layer thickness). Making both of the above simplifying assumptions, equation (9.7) can be reduced to,

$$\frac{\partial \eta}{\partial t} = \frac{0.93K}{n}\frac{\partial}{\partial x}\left(\overline{\eta}\frac{\partial h}{\partial x}\right) \tag{9.8}$$

where the following parameter values have been used: ρ_f = 1000kg/m^3, ρ_s = 1030kg/m^3, ν_f = 1.01m^2/s and ν_s = 1.06m^2/s.

9.4.4.3 Model solution

For the given boundary and initial conditions, the solution to the governing flow equation, (9.2), is [*Carslaw and Jaeger*, 1959],

$$h(x,t)=\int_{-\infty}^{t}\frac{dh_0}{d\tau}erfc\left[\frac{x}{2\sqrt{D(t-\tau)}}\right]d\tau \tag{9.9}$$

Substituting (9.9) into (9.8) leads to the solution of η,

$$\eta(x,t)=\eta_0(x)+\int_{0}^{t}\frac{\partial\eta}{\partial\tau}d\tau \tag{9.10}$$

where,

$$\frac{\partial\eta}{\partial t}=\frac{0.93K}{n}\left(\frac{d\overline{\eta}}{dx}\frac{\partial h}{\partial x}+\overline{\eta}\frac{\partial^2 h}{\partial x^2}\right),\text{ with} \tag{9.11}$$

$$\frac{\partial h}{\partial x}=-\int_{-\infty}^{t}\frac{dh_0}{d\tau}\frac{\exp\left[-\frac{x^2}{4D(t-\tau)}\right]}{\sqrt{\pi D(t-\tau)}}d\tau\text{ and} \tag{9.12}$$

$$\frac{\partial^2 h}{\partial x^2}=-\int_{-\infty}^{t}\frac{dh_0}{d\tau}\frac{x\exp\left[-\frac{x^2}{4D(t-\tau)}\right]}{2\sqrt{\pi D(t-\tau)}D(t-\tau)}d\tau\,. \tag{9.13}$$

Recall that equation (9.11) is only valid for relatively small interface slopes, i.e.

$$\frac{\rho_s-\rho_f}{\rho_f}\frac{\partial\eta}{\partial x}<<\frac{\partial h}{\partial x} \tag{9.14}$$

This criterion may not necessarily be met in other situations, for example, at the sheltered boundary of a coastal barrier where the interface is near vertical [*Nielsen*, 1999a].

9.4.4.4 Results and discussion

The parameters for the model forcing function, $h_o(t)$, were found by fitting (9.1) to the calculated shoreline elevations. The calculation of the shoreline elevation was based on the empirical formulation of *Hanslow and Nielsen* [1993],

$$z_{SL} \approx 0.048\sqrt{H_{rms}L_o} \tag{9.15}$$

where H_{rms} is the offshore root mean square wave height ($\approx H_{sig}/\sqrt{2}$) and $L_o = \frac{gT^2}{2\pi}$ is the deep water wavelength according to linear wave theory. The best-fit parameter values are: A = 0.92m, T_p = 1.92days and t_o = 3.85days with t = 0 corresponding to the date 18.29 in the data shown in Figure 9.4. The comparison of the model boundary condition with equation (9.15) is shown in Figure 9.10 (a). Note that tidal effects have been neglected in the model.

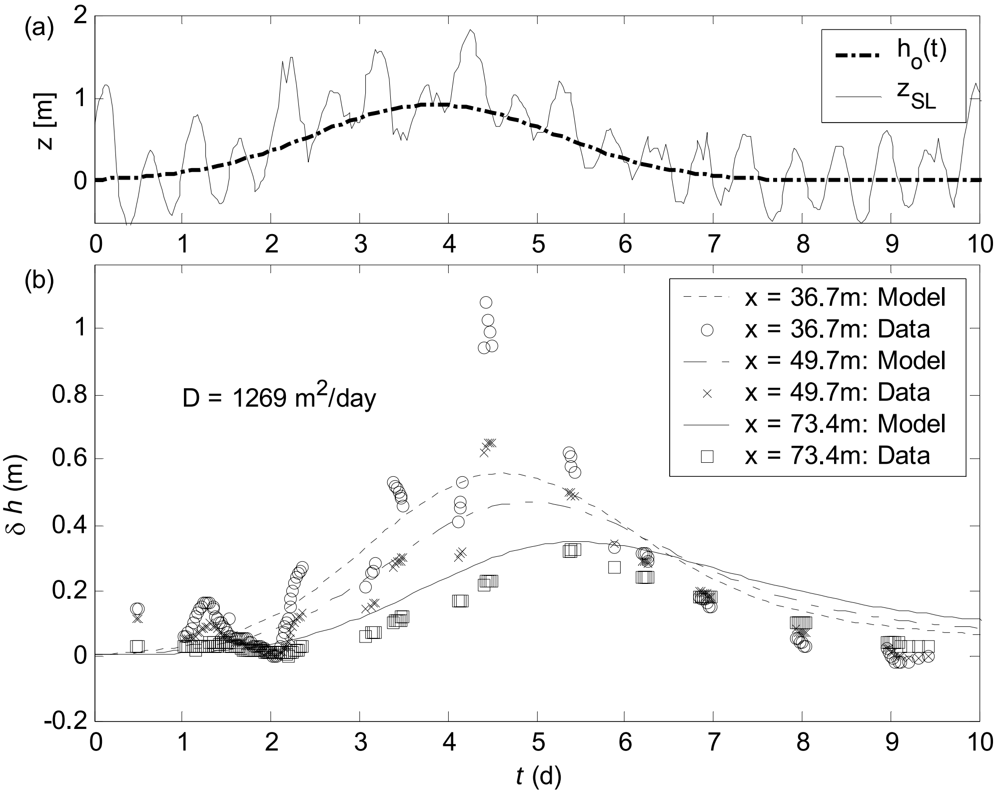

Figure 9.10: (a) Fit of the forcing function $h_o(t)$ to the calculated shoreline, z_{SL}. (b) Comparison of model calibration against field observations with D = 1269m^2/day. Parameters used: n = 0.38; n_e = 0.32; K = 0.00047m/s; d = 10m.

The model was first calibrated against water table fluctuation data from three landward locations by varying the hydraulic diffusivity, D, and was then used to predict the interface fluctuations. To illustrate the model's sensitivity to the input hydraulic parameters, the comparison of the model results with the field observations for two different calibrations are presented.

In each case, the observed mean interface profile was taken to be the initial profile, i.e., $\overline{\eta} = \eta_0 = d - 0.0533x$ where the slope of 0.0533 was derived from the slope of the initial data contour in Figure 9.8. As discussed previously, the 50% seawater salinity contour from the data is assumed to be the representative location of the (sharp) SWI (cf. section 9.4.2).

The aquifer's hydraulic parameters, K, n_e and n, were chosen for this calibration based on values typical for beach aquifers in southeast Queensland and northern New South Wales, Australia [*Kang et al.*, 1994a]. The mean aquifer thickness, d, was estimated based on unpublished numerical simulation of the present dataset.

The result of the first calibration (calibration A) is shown in Figure 9.10 and the agreement is found to be reasonably good. The model tends to under-predict the peaks in the data possibly due to the fact that the model has neglected fluctuations due to the tides and infiltration from wave runup (that are present in the data). Another possible factor in the under-estimation of the data is the choice of the boundary condition. By using the mean shoreline, the influence of seepage face formation (which occurred during the observation period) has been ignored.

Seepage face formation will cause the mean of the water table exit point (the landward boundary of the seepage face) to be greater than the mean shoreline position. *Cartwright and Nielsen* [2001] showed that the use of the exit point rather than the tide for the input boundary condition for *Nielsen's* [1990] analytical model provided much better agreement with the data. *Turner* [1993] provided a predictive model for the exit point based on the tide, beach face and aquifer parameters; but the model neglects the effect of waves, a significant factor in the present data. To the knowledge of the authors, no formulation (even empirical) for the prediction for the exit point including the effect of infiltration from wave runup exists. *Li et al.* [2004] provide a more detailed discussion on the propagation of the groundwater pulse in the aquifer.

Figure 9.11 compares the SWI fluctuation results from the model (calibration A) against the observed fluctuations. The model predicts the interface fluctuation remarkably well considering the underlying, sharp-interface assumption. The most noticeable discrepancies are seen in the transition from the initial profile up to and including the peak profile at 5.4days: the model over-predicting the magnitude of the fluctuations.

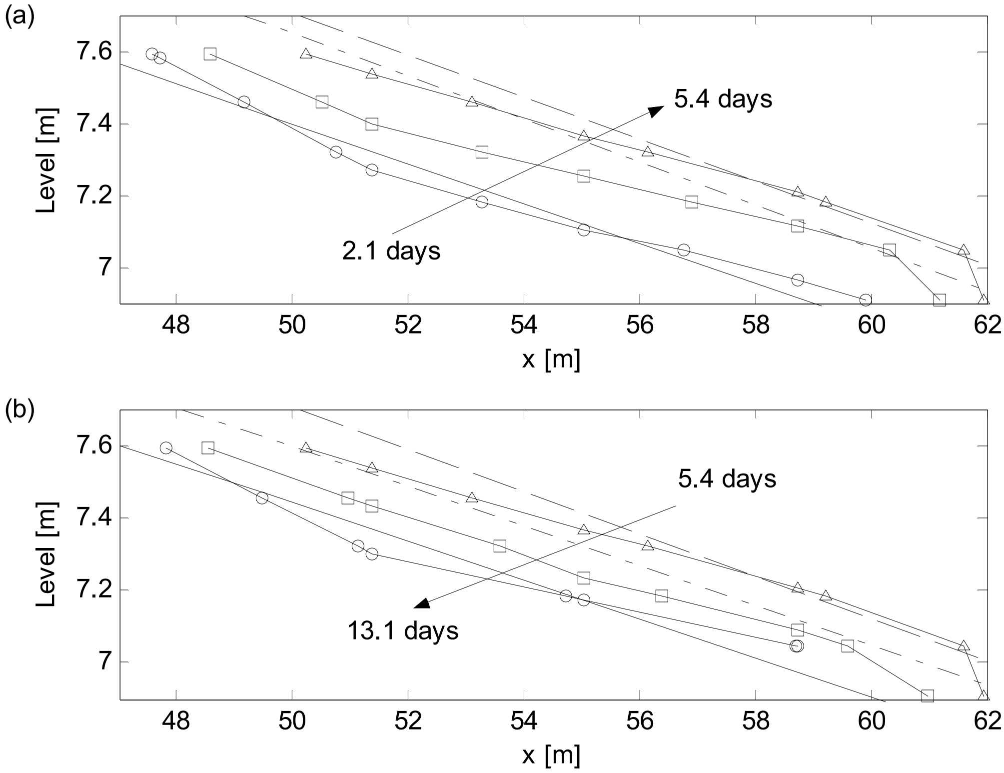

Figure 9.11: Comparison of predicted SWI fluctuations (lines) with observations (symbols). (a) Contours at t = 2.1days (—, ○), 4.1days (–·–, □) and 5.4days (–––, Δ). (b) Contours at t = 5.4days (–––, Δ), 7.1days (–·–, □) and 13.1days (—, ○). Parameters used: n = 0.38; n_e = 0.32; K = 0.00047m/s; d = 10m.

The results with the second model calibration (calibration 2) are shown in Figure 9.12. The effect of the reduced diffusivity leads to the increase in both the damping and phase lag of the pulse as it propagates into the aquifer [*Li et al*., 2004]. The effect, however, is not overly strong.

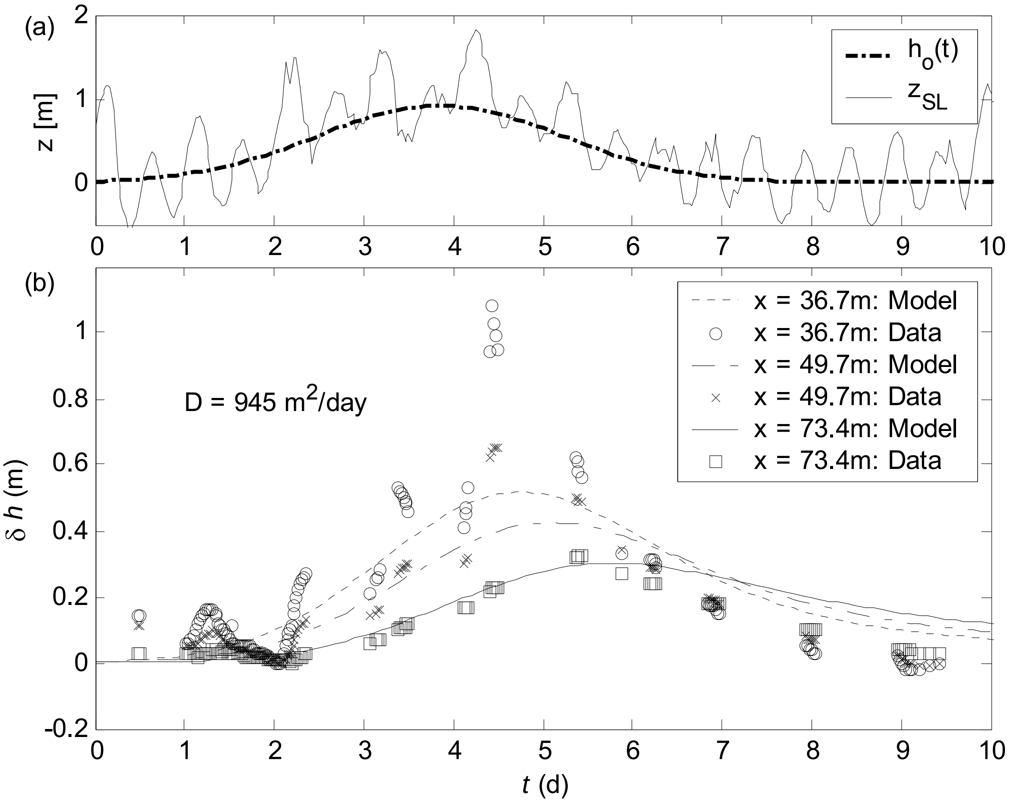

Figure 9.12: (a) Fit of the forcing function $h_o(t)$ to the calculated shoreline, z_{SL}. (b) Comparison of model calibration against field observations with $D = 945\text{m}^2/\text{day}$. Parameters used: $n = 0.38$; $n_e = 0.32$; $K = 0.00035\text{m/s}$; $d = 10\text{m}$.

The reduction in diffusivity gave slightly improved interface predictions as shown in Figure 9.13. The magnitude of the fluctuation is reduced and a better match is seen at the peak of the fluctuation (5.4days). Some discrepancy still existed in the transition from the initial to peak fluctuation with the model over-predicting the landward movement [Figure 9.13 (a)] and conversely under-predicting the recovery [Figure 9.13 (b)]. This is possibly to be due to the underlying sharp-interface assumption excluding any mixing across the interface that would be present in the observed, diffuse mixing zone. In both calibrations, the model tended to generate a steepening of the interface that was not observed in the data. This may be again due to the limiting sharp-interface assumption.

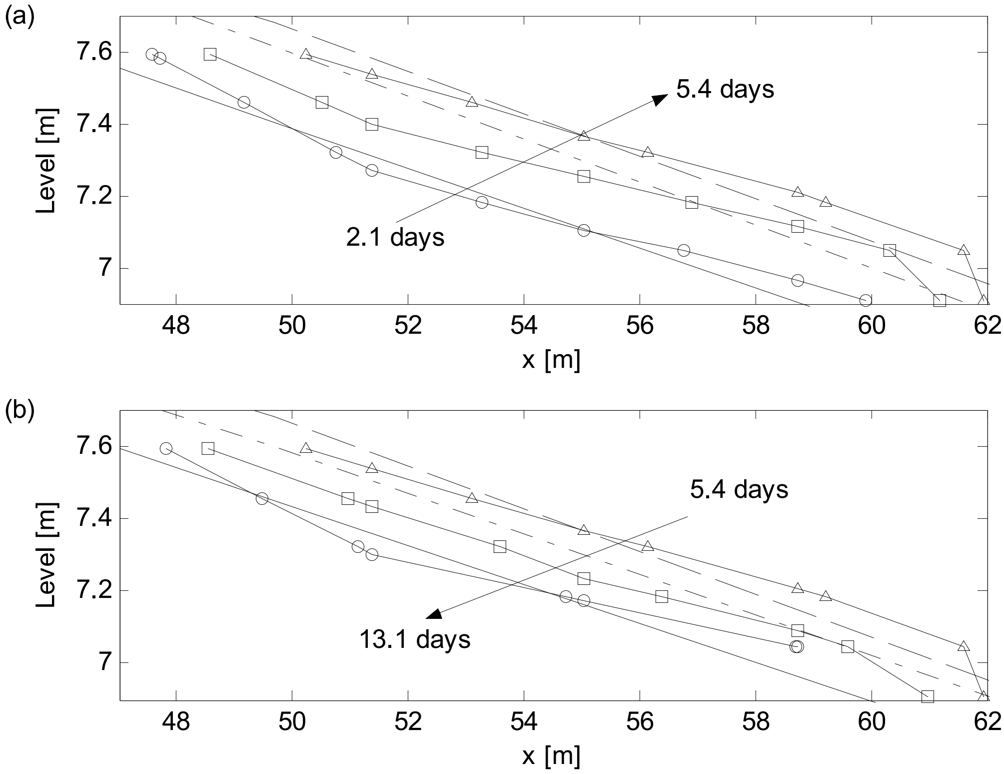

Figure 9.13: Comparison of predicted SWI fluctuations (lines) with observations (symbols). (a) Contours at t = 2.1days (—, ○), 4.1days (–·–, □) and 5.4days (–––, Δ). (b) Contours at t = 5.4days (–––, Δ), 7.1days (–·–, □) and 13.1days (—, ○). Parameters used: n = 0.38; n_e = 0.32; K = 0.00035m/s; d = 10m.

9.5 Summary

New field observations of the dynamics of the salinity structure in beaches have been presented and discussed. In both datasets, there was no measurable response of the salinity structure to the (dominant) semi-diurnal tidal oscillation.

One data set captures the deposition of a thin salty layer overlying fresh aquifer water as a direct result of infiltration from wave runup. Such an unstable situation remains a future challenge for modelling.

The second data set was obtained from an experiment originally designed to capture the response of the SWI to the neap to spring tidal cycle however, the monitoring period was dominated by a significant wave-induced increase in shoreline water levels. The aquifer dynamics were dominated by a corresponding pulse in groundwater levels which induced a fluctuation in the location of the SWI of the order of several metres in the horizontal. A simple sharp-interface model was shown to reasonably reproduce the fluctuations in the observed equivalent sharp-interface, the 50% of seawater salinity contour. It is duly noted however, that the simple model relies on assumptions that may not necessarily applicable to all situations and should be applied with caution. In particular, as a consequence of the sharp-interface assumption the model is unable to replicate the broad mixing zone as observed in the field.

Chapter 10 – Conclusions and recommendations

10.1 Summary of findings

The beach groundwater system has been investigated from a physical perspective via field and laboratory experiments. The observations have been used in process identification and to test and identify limitations in currently available theories.

In Chapter 4, the influence of the capillary fringe on water table oscillations was examined in terms of the complex effective porosity concept of *Nielsen and Perrochet* [2000a,b]. A review of the sand column experiments of *Nielsen and Perrochet* [2000a,b] and *Nielsen and Turner* [2000] highlighted the inadequacy of the non-hysteretic *Green and Ampt* [1911] approximation of the capillary fringe when applied to a simple harmonic oscillating system. Similarly, numerical solution of a non-hysteretic *Richards'* [1931] equation model based on measured first drying curve parameters is unable to reproduce the sand column observations. Interestingly, the sand column observations were reasonably reproduced with a non-hysteretic model (i.e. a single moisture retention curve) with a *van Genuchten* [1980] parameter, $\beta = 3$ [*Perrochet*, 2001 pers. comm.], which corresponds to a less step-like moisture retention curve than the measured first drying curves (cf. Figure 4.15).

New sand column experiments were conducted to examine the influence of a truncated capillary fringe (proximity of the sand surface) subject to simple harmonic periodic forcing. The complex effective porosity, n_ω, [*Nielsen and Perrochet*, 2000a,b] is shown to be significantly reduced with increasing truncation. The reduction in the storage term is in agreement with previous findings under non-periodic forcing conditions [e.g. *Duke*, 1972; *Gillham*, 1984; *Nachabe*, 2002]. The findings have important implications for the dynamic beach groundwater system where the water table can lie close to the sand surface in the inter-tidal zone. For example, the reduced storage will affect the dynamics of the water table exit point.

Field and laboratory data was used to test theoretical predictions of the dispersive properties of water table waves in Chapter 5. The finite aquifer depth theory of *Nielsen et al*. [1997] was shown to predict reasonably well field observations of the dispersion of semi-diurnal, tide-induced water table oscillations. However, shortcomings in available theories accounting for both vertical flow and capillarity effects were highlighted in laboratory experiments conducting at higher oscillation frequencies. The neglect of horizontal flow within the capillary fringe is suggested as one possible contributor that warrants further investigation. In relation to this, the question of the transferability of the complex effective porosity concept from 1D to 2D was also raised.

The influence of vertical flow and capillarity effects on the pressure distribution in an unconfined aquifer was examined in Chapter 6. The oscillations at the base of the aquifer were observed to have larger amplitudes and to also lead those observed near the water table which were reasonably reproduced by the finite aquifer depth theory of *Nielsen et al*. [1997]. The capillary fringe was deemed to be responsible for major differences between the data and capillary-free theory. Firstly, the observed asymptotic water table overheight was seen to be significantly less than that predicted by theoretical consideration of non-linearity in the interior [*Philip*, 1973; *Knight*, 1981]. Secondly, there was no observable generation of higher harmonic terms in the interior as predicted by the theory and observed in the experiments of *Parlange et al*. [1984].

Chapter 7 investigated sloping boundary effects through laboratory experiments supplemented by mathematical and numerical modelling. The generation of higher harmonics in the “intertidal” zone were observed to be strongest near the sand surface. Despite strong evidence of vertical flows in the intertidal zone, perturbation solutions to the one-dimensional Boussinesq equation were shown to reproduce reasonably well the generation of higher harmonics in the intertidal zone using the wave numbers observed in the interior. Small discrepancies between the observed and predicted locations of maxima in the higher harmonic amplitude and phase profiles were shown to be due to the neglect of seepage face formation in all of the solutions. A numerically coupled surface-sub-surface flow model which allows the formation of a seepage face accurately predicted these locations.

In the interior all but the "dual length scale" solution of *Callaghan* [2002 pers. comm.] were unable to match both the amplitude decay and phase profiles. This is due to these solutions relying upon a wave number with equal real and imaginary parts to account for both the decay rate and phase lag. The solution of *Callaghan* [2002, pers. comm.] allows the wave number to have non-equal real and imaginary parts in agreement with the field and laboratory observations presented in Chapter 5.

The numerical model was shown to predict the position of the exit point very well and even predicted the curious observation of the exit point rising prior to being overtopped by the rising shoreline just after low tide [e.g. *Li et al.*, 1997; *Atherton*, 2001].

The use of a modified Boussinesq equation [*Nielsen et al.*, 1988] to estimate an in-exfiltration rate at the sand surface was critically assessed in Chapter 8. The model was applied to field data and was seen to infer a finite amount of "in-exfiltration" at and landward of the runup limit where there is clearly no supply from the surface. Strictly speaking, the additional flux term in the modified Boussinesq equation is a flux across the water table and not the sand surface as assumed in some previous applications [e.g. *Turner and Masselink*, 1998]. The fact that an apparent flux across the water table is seen landward of the runup limit suggests that a horizontal component to flow within the capillary fringe may indeed exist.

The influence of beach groundwater dynamics on the salinity structure is investigated from a field observation perspective in Chapter 9. In one dataset, the deposition of a thin salty layer overlying fresh aquifer water was observed as a direct result of infiltration from wave runup – an interesting modelling challenge. A longer term experiment designed to capture the response of the salinity structure to the neap to spring tidal cycle revealed no such response but did capture a significant response to a wave-induced pulse in groundwater levels. The mixing zone was observed to move several metres landward in response a 1m surge in groundwater levels. The observed fluctuations were reasonably well reproduced by a sharp interface model using the 50% of sea water salinity contours as an equivalent sharp-interface. Clearly though, the model is unable to predict the observed diffuse mixing zone which had a horizontal extent around 25m.

10.2 Recommendations for future research

The findings from the present study have lead to more questions being raised, in turn providing the direction for future research. These can be summarised by the following related topics:

- Periodic (vertical and *horizontal*) flow dynamics within the capillary fringe.
- The transferability of the complex effective porosity concept from 1D to 2D.
- The influence of the sub-surface pressure distribution on dynamic seepage faces.
- Modelling of the true, diffuse and dynamic nature of the salinity structure.

References

Andersen, M. S., V. Nyvang and D. Postma, Geochemical processes at a freshwater/seawater interface in a shallow sandy aquifer, Skansehage Denmark., Proc. 1st Intl. Conf. on Salt Water Intrusion and Coastal Aquifers - Monitoring, Modeling and Management, Essaouira, Morocco, CD-ROM, 2001.

Aseervatham, A. M., Tidal Dynamics of Coastal Water tables, *Ph.D. Thesis*, 253 pp., University of Queensland, Brisbane, Australia, 1994.

Ataie-Ashtiani, B., R. E. Volker and D. A. Lockington, Tidal effects on sea water intrusion in unconfined aquifers, *Journal of Hydrology, 216*, 17-31, 1999.

Atherton, R. J., A. J. Baird and G. F. S. Wiggs, Inter-tidal dynamics of surface moisture content on a meso-tidal beach, *Journal of Coastal Research, 17*(2), 482-489, 2001.

Baldock, T. E. and P. Holmes, Pressure gradients within sediment beds, Proc. 25th Intl. Conf. on Coastal Engineering, ASCE, Orlando, Florida, 4161-4173, 1996.

Barry, D. A., S. J. Barry and J.-Y. Parlange, Capillarity correction to Periodic solutions of the shallow flow approximation, in *Mixing in Estuaries and Coastal Seas, Coastal and Estuarine Studies*, edited by C. B. Pattiaratchi, pp. 496-510, AGU, Washington DC, 1996.

Carslaw, H. S. and J. C. Jaeger, *Conduction of heat in solids*, pp., Clarendon Press, Oxford, 1959.

Cartwright, N. and P. Nielsen, Groundwater Dynamics and Salinity in Beaches., Proc. Coasts and Ports 2001, 15th Australasian Coastal and Ocean Engineering Conference, Gold Coast, Australia., 441-446, September 25-28, 2001.

Childs, E. C., *An introduction to the physical basis of soil water phenomena*, 493 pp., John Wiley and Sons Ltd., London, 1969.

Dagan, G., Second-order theory of shallow free-surface flow in porous media, *Quart. Journ. Mech. and Applied Math., 20*(4), 517-526., 1967.

Dracos, T., Ebene nichtstatinare Grundwasserabflusse mit freier Oberflache., *Rep. 57*, 114 pp., Tech. Hochsch., Zurich, 1963.

Duke, H. R., Capillary properties of soils - Influence upon specific yield, *Transactions of the American Society of Agricultural Engineers, 15*, 688-691, 1972.

Dunn, S. L., P. Nielsen and N. Cartwright, Circulations in coastal aquifers, in preparation, 2003.

Elfrink, B. and T. E. Baldock, Hydrodynamics and sediment transport in the swash zone: a review and perspectives., *Coastal Engineering, 45*(3), 149-167, 2002.

Emery, K. O. and J. F. Foster, Water Tables in Marine Beaches, *Journal of Marine Research, 7*, 644-654, 1948.

Fetter, C. W., *Applied Hydrogeology*, 3rd ed., 691 pp., Prentice Hall, New Jersey, 1994.

Gillham, R. W., The capillary fringe and its effect on water-table response, *Journal of Hydrology, 67*, 307-324, 1984.

Grant, U. S., Influence of the water table on beach aggradation and degradation, *Journal of Marine Research, 7*, 655-660, 1948.

Green, W. H. and G. A. Ampt, Studies on Soil Physics 1. The flow of air and water through soils, *J Agric Sci, IV*(I), 1-24, 1911.

Hanslow, D. J. and P. Nielsen, Shoreline Set-Up on Natural Beaches, *Journal of Coastal Research, SI 15*, 1-10, 1993.

Hegge, B. J. and G. Masselink, Ground water table response to wave runup: An experimental study from Western Australia, *Journal of Coastal Research, 7*(3), 623-634, 1991.

Hillel, D., *Fundamentals of soil physics*, 413 pp., Academic Press, New York, 1980.

Jessen, O. Z., Beach drain tool using the Mike SHE system, *Draft report Unpublished internal report*, 38 pp., DHI Water and Environment, 1998.

Kang, H.-Y., Water table Dynamics Forced by Waves, *PhD Thesis*, 200 pp., University of Queensland, Brisbane, 1995.

Kang, H.-Y., A. M. Aseervatham and P. Nielsen, Field measurements of wave runup and the beach water table, *Research Report CE148*, 44 pp., Dept. of Civil Engineering, University of Queensland, Brisbane, 1994a.

Kang, H.-Y., P. Nielsen and D. J. Hanslow, Water table Overheight due to Wave Runup on a Sandy Beach, Proc. 24th Intl. Conf. on Coastal Engineering, ASCE, Kobe, Japan, 2115-2124, 1994b.

Knight, J. H., Steady Periodic Flow Through a Rectangular Dam, *Water Resources Research, 17*(4), 1222-1224, 1981.

Kool, J. B. and J. C. Parker, Development and evaluation of closed-form expressions for hysteretic soil hydraulic properties, *Water Resources Research, 23*(1), 105-114, 1987.

Kreyszig, E., *Advanced Engineering Mathematics*, 8th ed., 1156 pp., John Wiley& Sons, New York, 1999.

Krumbein, W. C. and G. D. Monk, Permeability as a function of the size parameters of unconsolidated sand., *Am. Inst. Min. Metall. Eng. Tech. Publ. 11*, 11 pp., 1942.

Lanyon, J. A., I. G. Eliot and D. J. Clarke, Groundwater-level Variation during Semidiurnal Spring Tidal Cycles on a Sandy Beach, *Australian Journal of Marine and Freshwater Research, 33*, 377-400, 1982.

Lehman, P., F. Stauffer, C. Hinz, O. Dury and H. Flühler, Effect of hysteresis on water flow in a sand column with a fluctuating capillary fringe, *Journal of Contaminant Hydrology, 33*(1-2), 81-100, 1998.

Li, L., N. Cartwright, P. Nielsen and D. A. Lockington, Response of coastal groundwater table to offshore storms, *China Ocean Engineering*, submitted.

Li, L., D. A. Barry, F. Stagnitti and J.-Y. Parlange, Groundwater wave in a coastal aquifer: A new governing equation including vertical effects and capillarity, *Water Resources Research, 36*(2), 411-420, 2000a.

Li, L., D. A. Barry, F. Stagnitti, J.-Y. Parlange and D.-S. Jeng, Beach water table fluctuations due to spring-neap tides: moving boundary effects, *Advances in Water Resources, 23*, 817-824, 2000b.

Li, L., D. A. Barry, F. Stagnitti and J.-Y. Parlange, Submarine groundwater discharge and associated chemical input to a coastal sea, *Water Resources Research, 35*, 3253-3259, 1999a.

Li, L., D. A. Barry, J.-Y. Parlange and C. B. Pattiaratchi, Reply to Comment on "Beach water table fluctuations due to wave run-up: Capillarity effects by L. Li et al.", by P. Nielsen, *Water Resources Research, 35*(4), 1325-1327, 1999b.

Li, L., D. A. Barry, J.-Y. Parlange and C. B. Pattiaratchi, Beach water table fluctuations due to wave run-up: Capillarity effects, *Water Resources Research, 33*(5), 935-945, 1997.

Longuet-Higgins, M. S. and R. W. Stewart, Radiation stresses in water waves: a physical discussion with applications., *Journal of Deep Sea Research, 11*, 529-562, 1964.

Moore, C. H., Intertidal carbonate cementation Grand Cayman, West Indies, *Journal of Sedimentary Petrology, 43*(3), 591-602, 1973.

Mualem, Y., A modified dependent-domain theory of hysteresis, *Soil Science, 137*(5), 283-291, 1984.

Nachabe, M. H., Analytical expressions for transient specific yield and shallow water table drainage, *Water Resources Research, 38*(10), 1193, 2002.

Nielsen, P. and C. J. Voisey, Water table overheights and salinity in coastal barriers: Field measurements, *Report CH49/98*, 92p pp., Dept. of Civil Engineering, University of Queensland, 1998.

Nielsen, P. and I. Turner, Groundwater Waves and Water Exchange in Beaches, Proc. 27th Intl. Conf. on Coastal Engineering, ASCE, Sydney, Australia, 2356-2363, 2000.

Nielsen, P. and P. Perrochet, Water table dynamics under capillary fringes: experiments and modelling, *Advances in Water Resources, 23*(1), 503-515, 2000a.

Nielsen, P. and P. Perrochet, ERRATA: Water table dynamics under capillary fringes: experiments and modelling [Advances in Water Resources 23 (2000) 503-515], *Advances in Water Resources, 23*, 907-908, 2000b.

Nielsen, P., Groundwater Dynamics and Salinity in Coastal Barriers, *Journal of Coastal Research, 15*(3), 732-740, 1999a.

Nielsen, P., Simple equipment for coastal engineering research and teaching., Coastal field surveys and measurement techniques., Cape Town, South Africa, 1029-1037, 1999b.

Nielsen, P., Comment on "Beach water table fluctuations due to wave run-up: Capillarity effects" by L. Li et al., *Water Resources Research, 35*(4), 1323-1324, 1999c.

Nielsen, P., A. M. Aseervatham, J. D. Fenton and P. Perrochet, Groundwater Waves in Aquifers of Intermediate Depths, *Advances in Water Resources, 20*(1), 37-43, 1997.

Nielsen, P., Tidal Dynamics of the Water Table in Beaches, *Water Resources Research, 26*(9), 2127-2134, 1990.

Nielsen, P., G. A. Davis, J. M. Winterbourne and G. Elias, Wave Setup and the Water Table in Sandy Beaches, *Technical Memorandum, 88/1*, 132 pp., NSW Public Works Dept., Australia, 1988.

Parker, J. C. and R. J. Lenhard, A model for hysteretic constitutive relations governing multiphase flow. 1. Saturation-pressure relations, *Water Resources Research, 23*(12), 2187-2196, 1987.

Parlange, J.-Y. and W. Brutsaert, A Capillarity Correction for Free Surface Flow of Groundwater, *Water Resources Research, 23*(5), 805-808, 1987.

Parlange, J.-Y., F. Stagnitti, J. L. Starr and R. D. Braddock, Free-surface flow in porous media and periodic solution of the shallow-flow approximation, *Journal of Hydrology, 70*, 251-263, 1984.

Philip, J. R., Periodic non-linear diffusion: An integral relation and its physical consequences, *Australian Journal of Physics, 26*, 513-519., 1973.

Raubenheimer, B., R. T. Guza and S. Elgar, Tidal water table fluctuations in a sandy ocean beach, *Water Resources Research, 35*(8), 2313-2320, 1999.

Richards, L. A., Capillary conduction of liquids through porous mediums, *Physics, 1*, 318-333, 1931.

Robinson, C. and L. Li, Laboratory investigations on water exchange and mixing processes in a coastal aquifer, Proc. 6th International Conference on Hydroscience and Engineering, Brisbane, Australia, May 30 - June 3, accepted for presentation 2004.

Silliman, S. E., B. Berkowitz, J. Simunek and M. T. van Genuchten, Fluid flow and solute migration within the capillary fringe, *Ground Water, 40*(1), 76-84, 2002.

Stauffer, F. and W. Kinzelbach, Cyclic hysteretic flow in porous medium column: model, experiment, and simulations, *Journal of Hydrology, 240*(3-4), 264–275, 2001.

Steggenwentz, J. H., The influence of tidal motion of seas and tidal rivers on the height of rise of groundwater (in Dutch), *PhD Thesis*, 138 pp., Delft University of Technology, Delft, Netherlands, 1933.

Teo, H. T., D. S. Jeng, B. R. Seymour, D. A. Barry and L. Li, A new analytical solution for water table fluctuations in coastal aquifers with sloping beaches, *Advances in Water Resources, 26*, 1239–1247, 2003.

Turner, I. and G. Masselink, Swash infiltration-exfiltration and sediment transport., *Journal of Geophysical Research, 103*(C13), 30813-30824, 1998.

Turner, I. and P. Nielsen, Rapid water table fluctuations within the beach face: implications for swash zone sediment mobility?, *Coastal Engineering, 32*, 45-59, 1997.

Turner, I., B. P. Coates and R. I. Acworth, Tides, Waves and the Super-elevation of Groundwater at the Coast, *Journal of Coastal Research, 13*(1), 46-60, 1997.

Turner, I., Water table outcropping on macro-tidal beaches: A simulation model, *Marine Geology, 115*, 227-238, 1993.

Turner, I., The total water content of sandy beaches, *B.Sc. (Honours)*, 143 pp., Univ of Sydney, Sydney, 1989.

van Genuchten, M. T., A closed form equation for predicting the hydraulic conductivity of unsaturated soils, *Soil Science Society of America Journal, 44*, 892-898, 1980.

Vigneaux, P., Analysis and modelling of beach groundwater field data: Brunswick Heads, June 2003, *Traineeship Report Traineeship Report*, 74 pp., Department of Civil Engineering, The University of Queensland, 2003.

Waddell, E., Wave forcing of beach groundwater, Proc. 17th Intl. Conf. on Coastal Engineering, ASCE, Sydney, Australia, 1436-1452, 1980.

Waddell, E., Swash-Groundwater-Beach Profile Interactions, in *Beach and Nearshore Sedimentation*, edited by R. A. Davis and R. L. Ethington, pp. 115-125, Society of Economic Paleontologists and Mineralogists, 1976.

Wang, J. and T.-K. Tsay, Tidal Effects on Groundwater Motions, *Transport in Porous Media, 43*, 159-178, 2001.

Werner, A. D. and D. A. Lockington, Influence of hysteresis on tidal capillary fringe dynamics in a well-sorted sand, *Advances in Water Resources, 26*(11), 1199-1204, 2003.

Appendix A – Field data

In this appendix, the field data collected as part of the present study (five datasets) is compiled for use by the reader.

All water level and topography data have been reduced relative to a local datum and where possible reduced relative to the Australian Height Datum.

Unless otherwise indicated, all times given are in hours from 00:00 on the date given in the header.

The wave and tide data have been reproduced with permission from:

- Coastal Services, Environmental Protection Agency, Queensland.
- New South Wales Department of Public Works and Services', Manly Hydraulics Laboratory for the New South Wales Department of Land and Water Conservation.

Please acknowledge these sources accordingly if using the data.

The data is available in electronic form upon request.

A.1 North Stradbroke Island, 30th May 2000

A.1.1 Water level and topography data

Well #	14	13	12	11	10	9	8	7	6	5	4	3	2	1	SWL	Hrms	Tsig
x [BM]	-50	-25.4	9	17.8	24.1	29.5	34.9	41.3	45.5	50	59	67.4	82.3	104	-	-	-
z sand [m AHD]	7.100	7.009	5.793	3.648	2.592	2.106	1.794	1.418	1.019	0.665	0.159	-0.167	-0.351	-0.921	-	-	-
Time	**WATER LEVELS [m AHD]**														[m AHD]	[m]	[sec]
14	1.21	1.19				0.69	0.582	0.447	0.282	0.334	0.086	0.033	-0.017	-0.062	-0.334	0.98	8.90
14.5	1.21	1.19		0.773	0.753	0.69	0.592	0.467	0.422	0.444	0.216	0.183	0.143	0.078	-0.158	0.99	9.01
15	1.21	1.19		0.803	0.763	0.71	0.632	0.547	0.612	0.624	0.346	0.333	0.273	0.188	0.019	0.99	9.12
15.5	1.21	1.19		0.823	0.813	0.76	0.702	0.697	0.912	0.734	0.546	0.563	0.453	0.368	0.173	0.96	8.97
16	1.21	1.19	0.898	0.863	0.823	0.8	0.752	0.867	0.992	0.744	0.666		0.573	0.518	0.335	0.92	8.81
16.5	1.21	1.19	0.918	0.873	0.873	0.89	0.892	1.207	1.032	0.804	0.726		0.623	0.628	0.477	0.89	8.41
17	1.21	1.19	0.938	0.913	0.913	0.935	1.102	1.217	1.052	0.834	0.796				0.561	0.86	8.00
17.5	1.21	1.19	0.958	0.953	0.963	1.02	1.252	1.257	1.042	0.864	0.81				0.614	0.90	7.55
18	1.21	1.19	0.978	0.973	1.013	1.1	1.342	1.197	1.002	0.864	0.796				0.621	0.94	7.10
18.5	1.21	1.19	1.008	1.003	1.043	1.14	1.292	1.177	0.972	0.834	0.776				0.577	0.95	7.73
19	1.21	1.19	1.018	1.023	1.073	1.16	1.262	1.137	0.932	0.784	0.696				0.525	0.96	8.36
19.5	1.21	1.19	1.028	1.043	1.083	1.15	1.222	1.097	0.912	0.704	0.596				0.438	0.92	8.36
20	1.21	1.19	1.038	1.053	1.083	1.14	1.172	1.027	0.882	0.644	0.476				0.319	0.88	8.35
20.5	1.21	1.19	1.048	1.063	1.073	1.11	1.122	0.977	0.842	0.634	0.336				0.164	0.85	8.00
21	1.21	1.19	1.048	1.053	1.063	1.07	1.062	0.877	0.742	0.584	0.256				0.003	0.81	7.64
21.5	1.21	1.19	1.048	1.043	1.043	1.04	1.002	0.827	0.662	0.504	0.156	0.061			-0.145	0.77	7.51
22	1.21	1.19	1.048	1.033	1.013	1.01	0.952	0.787	0.612	0.444	0.106	-0.07			-0.283	0.73	7.37
22.5	1.21	1.19	1.038	1.023	0.993	0.98	0.912	0.747	0.582	0.414	0.096	-0.15			-0.413	0.77	7.51
23	1.21	1.19	1.038	1.013	0.973	0.95	0.872	0.697	0.552	0.374	0.076	-0.18			-0.51	0.81	7.64
23.5	1.21	1.19	1.028	0.983	0.953	0.92	0.842	0.657	0.522	0.354	0.066	-0.2	-0.129		-0.587	0.79	7.71
24	1.21	1.19	1.018	0.973	0.943	0.9	0.812	0.617	0.502	0.334	0.076	-0.19	-0.119		-0.619	0.76	7.77

24.5	1.21	1.19	0.998	0.943	0.918	0.87	0.772	0.587	0.472	0.324	0.084	-0.18	-0.105		-0.577	0.77	7.53
25	1.21	1.19	0.988	0.953	0.903	0.85	0.752	0.567	0.457	0.314	0.086	-0.14	-0.041		-0.526	0.77	7.29
25.5	1.21	1.19	0.983	0.933	0.883	0.83	0.732	0.547	0.452	0.324	0.098	-0.12	0.015		-0.446	0.78	7.07
26	1.21	1.19	0.973	0.923	0.873	0.82	0.712	0.547	0.467	0.394	0.146	0.001	0.131		-0.321	0.78	6.85
26.5	1.21	1.19	0.968	0.903	0.863	0.805	0.712	0.557	0.512	0.464	0.196	0.121			-0.183	0.78	6.82
27	1.21	1.19	0.958	0.903	0.853	0.8	0.722	0.607	0.622	0.534	0.326	0.291			-0.06	0.78	6.79
27.5	1.21	1.19	0.958	0.903	0.863	0.83	0.757	0.697	0.787	0.644	0.426	0.371			0.08	0.78	6.55
28	1.21	1.19	0.958	0.923	0.888	0.86	0.802	0.837	0.862	0.694	0.536				0.259	0.78	6.30
28.5	1.21	1.19	0.968	0.938	0.913	0.9	0.862	0.967	0.912	0.754	0.606				0.391	0.80	6.98
29	1.21	1.19	0.983	0.963	0.943	0.94	0.922	1.067	0.952	0.774	0.696				0.462	0.81	7.66
29.5	1.21	1.19	0.998	0.973	0.978	0.985	1.002	1.137	0.972	0.814	0.736				0.519	0.81	7.75
30	1.21	1.19	1.018	1.003	0.993	1.02	1.062	1.167	0.972	0.794	0.726				0.521	0.81	7.84
30.5	1.21	1.19	1.038	1.028	1.033	1.055	1.132	1.267	0.957	0.764	0.666	0.631	0.751		0.509	0.82	7.97
31	1.21	1.19	1.043	1.043	1.043	1.07	1.132	1.272	0.952	0.724	0.606	0.591	0.731		0.444	0.83	8.10
31.5	1.21	1.19	1.048	1.053	1.053	1.07	1.102	0.992	0.937	0.674	0.476	0.471	0.611		0.356	0.84	8.11
32	1.21	1.19	1.053	1.053	1.053	1.06	1.062	0.957	0.957	0.654	0.406	0.371	0.531		0.222	0.85	8.11
32.5	1.21	1.19	1.058	1.053	1.033	1.04	1.012	0.877	0.762	0.614	0.316	0.261	0.401		0.089	0.83	8.00
33	1.21	1.19	1.058	1.043	1.013	0.99	0.952	0.807	0.652	0.494	0.166	0.081	0.201		-0.1	0.81	7.88
33.5	1.21	1.19	1.048	1.013	0.983	0.96	0.912	0.757	0.612	0.444	0.146	-0.03	0.071		-0.256	0.80	7.43
34	1.21	1.19	1.038	1.003	0.963	0.94	0.872	0.727	0.572	0.404	0.136	-0.11	-0.039		-0.445	0.79	6.97
34.5	1.21	1.19	1.038	0.983	0.943	0.91	0.842	0.677	0.542	0.374	0.116	-0.16	-0.129		-0.596	0.84	7.03
35	1.21	1.19	1.008	0.973	0.923	0.89	0.802	0.637	0.522	0.354	0.086	-0.17	-0.189		-0.741	0.88	7.09
35.5	1.21	1.19	1.008	0.953	0.913	0.87	0.782	0.607	0.492	0.334	0.076	-0.17	-0.199		-0.804	0.83	6.97
36	1.21	1.19	0.988	0.943	0.903	0.85	0.762	0.577	0.472	0.324	0.066	-0.17	-0.219		-0.87	0.78	6.84
36.5	1.21	1.19	0.983	0.933	0.878	0.83	0.722	0.547	0.442	0.294	0.066	-0.17	-0.179		-0.883	0.76	7.12
37	1.21	1.19	0.978	0.918	0.873	0.81	0.702	0.527	0.427	0.294	0.056	-0.16	-0.139		-0.787	0.74	7.39
37.5	1.21	1.19	0.968	0.913	0.853	0.79	0.682	0.517	0.412	0.284	0.046	-0.15	-0.089		-0.702	0.73	7.32
38	1.21	1.19	0.958	0.903	0.843	0.78	0.672	0.507	0.402	0.294	0.136	-0.09	-0.019		-0.598	0.71	7.24
38.5	1.21	1.19	0.948	0.893	0.833	0.77	0.652	0.497	0.412	0.344	0.166	-0.04	0.061		-0.413	0.73	7.68
39	1.21	1.19	0.938	0.883	0.823	0.76	0.662	0.517	0.462	0.444	0.206	0.141	0.241		-0.247	0.75	8.11
39.5	1.21	1.19	0.938	0.873	0.823	0.78	0.692	0.507	0.652	0.634	0.386	0.361	0.601		-0.058	0.73	8.10
40	1.21	1.19	0.938	0.893	0.863	0.83	0.782	0.867	0.912	0.734	0.516	0.511	0.631		0.154	0.71	8.08
40.5	1.21	1.19	0.958	0.923	0.903	0.89	0.862	1.097	0.992	0.794	0.716	0.711	0.801		0.359	0.80	8.21
41	1.21	1.19	0.988	0.963	0.963	0.97	1.052	1.207	1.052	0.954	0.876	0.901	0.971		0.521	0.89	8.33

41.5	1.21	1.19	1.008	1.003	1.023	1.07	1.372	1.237	1.062	0.974	0.996				0.65	0.87	8.00
42	1.21	1.19	1.028	1.023	1.063	1.19	1.522	1.267	1.122	1.034	1.026				0.75	0.85	7.67
42.5	1.21	1.19	1.058	1.073	1.153	1.33	1.492	1.267	1.132	1.084	1.026				0.813	0.88	7.67
43	1.21	1.19	1.078	1.093	1.183	1.44	1.532	1.257	1.112	1.054	1.046				0.782	0.91	7.66
43.5	1.21	1.19	1.088	1.133	1.233	1.48	1.512	1.227	1.082	0.984	0.966				0.708	0.94	7.64
44	1.21	1.19	1.108	1.153	1.273	1.49	1.442	1.157	0.972	0.894	0.846				0.608	0.97	7.61
44.5	1.21	1.19	1.128	1.173	1.273	1.43	1.362	1.147	0.942	0.814	0.756				0.479	0.98	7.14
45	1.21	1.19	1.138	1.183	1.263	1.37	1.292	1.077	0.892	0.734	0.536	0.521			0.333	0.99	6.66
45.5	1.21	1.19	1.148	1.183	1.233	1.3	1.202	0.987	0.852	0.654	0.416	0.371			0.165	0.95	7.03
46	1.21	1.19	1.148	1.173	1.193	1.25	1.142	0.887	0.742	0.604	0.306	0.201			-0.018	0.91	7.40
57			1.188	1.223	1.233	1.27	1.212	1.147	0.912	0.704	0.466	0.391			0.18	1.07	7.96
57.5			1.188	1.203	1.213	1.24	1.162	0.957	0.812	0.654	0.336	0.241			0.033	1.03	7.49
58			1.178	1.183	1.173	1.18	1.092	0.867	0.712	0.584	0.286	0.101			-0.155	0.99	7.02
58.5								0.827	0.672	0.544	0.276	0.041			-0.369	1.00	7.53
59			1.158	1.143	1.113	1.11	1.002	0.787	0.632	0.484	0.256	-0.02			-0.519	1.00	8.04
59.5			1.148	1.123	1.103	1.08	0.972	0.767	0.612	0.464	0.206	-0.03			-0.665	1.01	8.21
60			1.138	1.103	1.083	1.05	0.932	0.737	0.582	0.434	0.186	-0.04			-0.755	1.02	8.38
60.5			1.128	1.103	1.063	1.03	0.902	0.717	0.562	0.414	0.176	-0.03			-0.842	0.98	8.57
61		1.15	1.118	1.083	1.043	1	0.872	0.687	0.542	0.394	0.166	-0.04			-0.837	0.93	8.76
61.5	1.19		1.108	1.073	1.023	0.98	0.852	0.667	0.532	0.394	0.196	-0.02			-0.788	0.86	8.43
62	1.19	1.16	1.098	1.063	1.013	0.96	0.832	0.637	0.522	0.394	0.186	-0.02			-0.709	0.78	8.10
62.5			1.088	1.043	1.003	0.94	0.812	0.637	0.512	0.404	0.206	-0.01			-0.573	0.76	8.13
63											0.276	0.051			-0.424	0.73	8.16
80.5	1.22	1.21	1.268	1.293	1.313	1.37	1.412	1.057							0.588	0.99	8.04
81	1.22	1.21	1.278	1.293	1.313	1.36	1.352	1.017							0.48	0.98	8.20
81.5		1.21	1.278	1.303	1.303	1.32	1.272	0.977							0.34	1.02	8.19
82		1.21	1.278	1.293	1.283	1.28	1.212	0.907							0.177	1.06	8.17
82.5					1.243	1.22									-0.023	1.04	8.51
83					1.213	1.18									-0.208	1.01	8.85
83.5					1.183										-0.403	0.95	9.34

A.1.2 Salinity data

X [m BM]	C/Csea [ ]	Z [m AHD]	X [m BM]	C/Csea [ ]	Z [m AHD]	X [m BM]	C/Csea [ ]	Z [m AHD]
31/05/2000; 13:30			31/05/2000; 15:30			31/05/2000; 16:30		
24.1	0.077	0.749	24.1	0.098	0.749	24.1	0.141	0.749
29.5	0.085	0.137	29.5	0.141	0.629	29.5	0.154	0.629
32.2	0.514	0.244	29.5	0.071	0.137	29.5	0.092	0.137
34.9	0.874	0.089	32.2	0.412	0.630	32.2	0.326	0.63
			32.2	0.136	0.244	32.2	0.106	0.244
			34.9	0.186	-0.342	34.9	0.092	-0.342
			34.9	0.637	0.089	34.9	0.406	0.089
			34.9	0.831	0.595	34.9	0.745	0.595
			38.1	0.767	-0.672	38.1	0.685	-0.672
31/05/2000; 17:45			31/05/2000; 19:00			31/05/2000; 20:15		
24.1	0.097	0.749	24.1	0.078	0.749	24.1	0.033	0.749
29.5	0.166	0.629	29.5	0.957	1.284	29.5	0.985	1.284
29.5	0.098	0.137	29.5	0.168	0.629	29.5	0.140	0.629
32.2	0.129	0.244	29.5	0.092	0.137	29.5	0.063	0.137
32.2	0.458	0.63	32.2	0.208	0.244	32.2	0.403	0.244
32.2	0.769	1.022	32.2	0.646	0.63	32.2	0.874	0.63
34.9	0.052	-0.342	32.2	0.917	1.022	32.2	0.972	1.022
34.9	0.412	0.089	34.9	0.050	-0.342	34.9	0.071	-0.342
34.9	0.751	0.595	34.9	0.692	0.089	34.9	0.800	0.089
38.1	0.685	-0.672	34.9	0.935	0.595	34.9	1.000	0.595
			38.1	0.715	-0.672	38.1	0.721	-0.672
01/06/2000; 09:30			01/06/2000; 10:30			01/06/2000; 11:45		
24.1	0.086	0.749	24.1	0.100	0.749	24.1	0.111	0.749
29.5	0.888	0.629	29.5	0.924	0.629	29.5	0.985	0.629
29.5	0.363	0.137	29.5	0.564	0.137	29.5	0.591	0.137
32.2	0.697	0.244	32.2	0.955	0.63	32.2	0.870	0.63
32.2	0.967	0.63	32.2	0.779	0.244	32.2	0.985	0.244
32.2	0.997	1.022	34.9	0.742	-0.342	34.9	0.703	-0.342
34.9	0.506	-0.342	34.9	0.945	0.089	34.9	0.976	0.089
34.9	0.739	0.089	34.9	0.964	0.595	34.9	0.976	0.595
34.9	0.879	0.595	38.1	0.906	-0.672	38.1	0.961	-0.672
38.1	0.797	-0.672						
01/06/2000; 13:15			01/06/2000; 15:00			02/06/2000; 08:30		
24.1	0.115	0.749	29.5	0.761	0.137	29.5	0.919	0.629
29.5	0.991	0.629	29.5	0.991	0.629	29.5	0.876	0.137
29.5	0.703	0.137				32.2	0.947	0.63
32.2	0.970	0.63				32.2	0.957	0.244
32.2	0.970	0.244						
34.9	0.876	-0.342						
34.9	0.976	0.089						
34.9	0.976	0.595						
38.1	0.894	-0.672						

A.2 North Stradbroke Island, 1st August 2000

A.2.1 Water level and topography data

Well #	**16**	**15**	**14**	**13**	**12**	**11**	**10**	**9**	**8**	**7**	**6**	**5**	**4**	**3**	**2**	**1**	**Exit**			
x [m BM]	-50.7	-25.7	-15.2	0	6.1	17.1	24.58	34.93	45.38	54.44	64.34	75.84	87.94	99.74	111.08	134	**Point**			
z sand [m AHD]	6.976	7.016	8.536	7.685	5.754	3.764	2.544	2.069	1.492	1.075	0.733	0.388	0.072	-0.152	-0.347	-1.281	**x**	**SWL**	**Hsig**	**Tp**
Time	**WATER LEVELS [m AHD]**																[m BM]	[m AHD]	[m]	[sec]
10	1.29	1.225	1.223	1.214	1.157	1.148	1.127	0.999	0.772	0.71	0.602	0.432	0.336	0.337	0.494		67.64	0.37	0.95	9.25
10.5	1.28	1.225	1.228	1.174	1.157	1.138	1.117	1.004	0.767	0.675	0.542	0.402	0.211	0.227	0.294	0.3	69.69	0.28	0.93	8.895
11	1.295	1.225	1.223	1.169	1.157	1.143	1.107	0.999	0.757	0.65	0.492	0.342	0.136	0.082	0.039	0.2	77.44	0.12	0.91	8.54
11.5	1.29	1.23	1.223	1.164	1.157	1.138	1.107	0.989	0.747	0.64	0.482	0.292	0.096	-0.043	-0.096	0	83.29	-0.07	0.95	9.68
12	1.29	1.23	1.223	1.159	1.157	1.133	1.102	0.984	0.737	0.625	0.457	0.262	0.084	-0.123	-0.231	-0.2	87.94	-0.26	0.99	10.82
12.5	1.29	1.23	1.223	1.154	1.147	1.133	1.097	0.999	0.727	0.62	0.442	0.242	0.061	-0.153	-0.306	-0.4	92.19	-0.46	0.98	10.545
13	1.29	1.23	1.223	1.154	1.147	1.128	1.087	0.979	0.717	0.6	0.432	0.222	0.026	-0.157	-0.348	-0.54	99.74	-0.63	0.97	10.27
13.5	1.29	1.225	1.223	1.154	1.147	1.123	1.087	0.969	0.707	0.59	0.417	0.202	0.006	-0.169	-0.366	-0.63	111.08	-0.79	0.95	9.8
14	1.29	1.225	1.223	1.154	1.147	1.118	1.087	0.959	0.697	0.575	0.407	0.187	-0.004	-0.185	-0.38	-0.696	117.08	-0.88	0.93	9.33
14.5	1.29	1.225	1.223	1.144	1.137	1.118	1.077	0.974	0.682	0.56	0.392	0.182	-0.014	-0.187	-0.38	-0.795	117.5	-0.93	0.965	8.33
15	1.29	1.225	1.223	1.154	1.157	1.108	1.067	0.949	0.667	0.55	0.392	0.162	-0.014	-0.198	-0.406	-0.725	115.48	-0.96	1	7.33
15.5	1.29	1.21	1.213	1.144	1.127	1.103	1.057	0.929	0.662	0.535	0.382	0.172	-0.024	-0.193	-0.38	-0.685	114.08	-0.91	1.01	7.455
16	1.285	1.21	1.208	1.149	1.127	1.098	1.057	0.929	0.647	0.525	0.362	0.172	0.001	-0.183	-0.351	-0.56	104.34	-0.79	1.02	7.58
16.5	1.285	1.21	1.203	1.144	1.122	1.093	1.052	0.919	0.642	0.52	0.362	0.182	0.031	-0.153	-0.306	-0.41	94.79	-0.65	1.015	7.66
17	1.285	1.21	1.203	1.124	1.117	1.088	1.047	0.909	0.642	0.515	0.372	0.212	0.094	-0.115	-0.196	-0.3	79.05	-0.47	1.01	7.74
17.5	1.285	1.21	1.203	1.124	1.117	1.088	1.047	0.919	0.657	0.52	0.392	0.272	0.116	0.017	-0.056	-0.1	74	-0.26	1	7.505
18	1.28	1.21	1.203	1.119	1.107	1.083	1.037	0.899	0.737	0.59	0.492	0.412	0.286	0.217	0.194	0.1	71.34	-0.02	0.99	7.27
18.5	1.28	1.205	1.203	1.129	1.107	1.078	1.032	0.899	0.837	0.72	0.612	0.532	0.506	0.467	0.394	0.3	59.34	0.22	0.975	7.445
19	1.28	1.2	1.193	1.114	1.107	1.118	1.077	0.969	0.917	0.87	0.772	0.712	0.756	0.767	0.694		56.71	0.47	0.96	7.62
19.5	1.28	1.2	1.193	1.144	1.107	1.138	1.087	1.069	1.017	0.97	0.952	0.962	0.956	0.967	0.794		45.13	0.71	0.935	7.725
20	1.28	1.22	1.193	1.154	1.107	1.158	1.097	1.119	1.167	1.07	1.052	1.062	1.056	1.067			43	0.88	0.91	7.83

20.5	1.28	1.2	1.193	1.164	1.127	1.218	1.137	1.189	1.337	1.23	1.192						42.21	1.04	0.935	8.005
21	1.26	1.2	1.193	1.194	1.107	1.238	1.207	1.249	1.407	1.25	1.292						41	1.14	0.96	8.18
21.5	1.26	1.2	1.193	1.194	1.127	1.248	1.217	1.289	1.437	1.25	1.312						42	1.18	0.975	7.62
22	1.26	1.2	1.193	1.184	1.137	1.238	1.187	1.299	1.417	1.21	1.292						43.38	1.14	0.99	7.06
22.5	1.26	1.19	1.183	1.174	1.147	1.218	1.167	1.329	1.317	1.15	1.242	1.062					47.38	1.04	0.955	7.02
23	1.25	1.18	1.193	1.164	1.167	1.178	1.197	1.319	1.207	1.06	1.162	1.012	1.056	1.067			51.44	0.9	0.92	6.98
23.5	1.26	1.18	1.193	1.164	1.177	1.158	1.187	1.289	1.147	0.92	1.042	0.812	0.906	0.767	0.794		54.44	0.72	0.94	8.885
24	1.26	1.19	1.193	1.174	1.187	1.138	1.197	1.269	1.097	0.77	0.892	0.612	0.656	0.467	0.694		62.34	0.54	0.96	10.79
24.5	1.265	1.2	1.213	1.174	1.187	1.128	1.187	1.239	1.037	0.57	0.692	0.397	0.356	0.197	0.394		73.04	0.31	0.98	10.805
25	1.265	1.19	1.203	1.169	1.187	1.128	1.157	1.224	0.987	0.47	0.622	0.362	0.206	0.037	0.094	0.3	74.74	0.08	1	10.82
25.5	1.265	1.2	1.203	1.184	1.187	1.118	1.172	1.184	0.957	0.41	0.572	0.322	0.076	-0.093	-0.106	-0.1	87.94	-0.13	0.99	8.805
26	1.27	1.205	1.213	1.184	1.192	1.098	1.152	1.189	0.927	0.37	0.542	0.302	0.066	-0.123	-0.256	-0.3	89.14	-0.34	0.98	6.79
26.5	1.27	1.205	1.213	1.184	1.192	1.088	1.137	1.149	0.897	0.35	0.522	0.296	0.056	-0.123	-0.326	-0.45	99	-0.52	0.985	6.93
27	1.27	1.205	1.213	1.184	1.187	1.078	1.127	1.154	0.887	0.33	0.502	0.272	0.036	-0.133	-0.351	-0.6	112.48	-0.67	0.99	7.07
27.5	1.27	1.205	1.213	1.184	1.187	1.058	1.107	1.139	0.867	0.31	0.492	0.252	0.031	-0.153	-0.336	-0.68	117.08	-0.76	1.01	7.98
28	1.265	1.21	1.193	1.174	1.157	1.058	1.082	1.129	0.857	0.29	0.482	0.242	0.016	-0.178	-0.325	-0.69	116	-0.77	1.03	8.89
28.5	1.265	1.21	1.193	1.174	1.157	1.048	1.077	1.109	0.837	0.28	0.452	0.237	0.026	-0.168	-0.341	-0.6	115	-0.72	1.03	8.725
29	1.27	1.215	1.218	1.164	1.167	1.058	1.087	1.089	0.817	0.28	0.452	0.252	0.036	-0.138	-0.341	-0.5	113.58	-0.64	1.03	8.56
29.5	1.27	1.215	1.218	1.164	1.167	1.058	1.077	1.069	0.797	0.29	0.457	0.257	0.056	-0.128	-0.316	-0.4	99.74	-0.53	1.02	7.945
30	1.28	1.21	1.223	1.154	1.157	1.068	1.072	1.059	0.787	0.29	0.462	0.262	0.061	-0.083	-0.286	-0.28	94.74	-0.4	1.01	7.33
30.5	1.28	1.21	1.223	1.154	1.157	1.088	1.057	1.059	0.777	0.31	0.462	0.282	0.076	-0.033	-0.186	-0.08	87.94	-0.24	1.01	7.985
31	1.27	1.2	1.203	1.144	1.127	1.1	1.037	1.049	0.757	0.37	0.492	0.342	0.106	0.067	-0.066	0.1	79.39	-0.07	1.01	8.64
31.5	1.27	1.2	1.203	1.134	1.147	1.1	1.037	1.044	0.737	0.42	0.542	0.382	0.186	0.217	0.194	0.3	74.12	0.09	0.985	8.585
32	1.27	1.19	1.183	1.144	1.127	1.1	1.037	1.029	0.757	0.57	0.582	0.422	0.406	0.367	0.494		67.64	0.25	0.96	8.53
32.5	1.27	1.19	1.183	1.134	1.147	1.11	1.037	1.049	0.767	0.67	0.702	0.452	0.506	0.517	0.794		65.69	0.38	0.96	9.145
33	1.29	1.23	1.233	1.174	1.157	1.13	1.107	1.009	0.777	0.71	0.732	0.492	0.556	0.667			62.34	0.48	0.96	9.76
33.5	1.29	1.23	1.233	1.164	1.157	1.15	1.107	0.999	0.787	0.74	0.762	0.542	0.576	0.767			61	0.53	0.955	8.69
34	1.29	1.23	1.223	1.164	1.157	1.15	1.097	1.009	0.787	0.74	0.772	0.552	0.566	0.817			60.34	0.52	0.95	7.62
34.5	1.29	1.23	1.223	1.164	1.157	1.15	1.097	0.999	0.777	0.74	0.742	0.522	0.556	0.717	0.794		66.34	0.46	0.94	7.115
35	1.29	1.23	1.223	1.164	1.157	1.15	1.097	0.999	0.767	0.7	0.642	0.482	0.456	0.487	0.694		71.84	0.36	0.93	6.61
35.5	1.29	1.23	1.223	1.164	1.157	1.15	1.097	0.989	0.747	0.67	0.532	0.392	0.276	0.267	0.394	0.3	76.84	0.22	0.95	7.56
36	1.29	1.22	1.223	1.149	1.147	1.14	1.097	0.979	0.727	0.64	0.497	0.342	0.176	0.167	0.194	0.2	79.84	0.06	0.97	8.51
36.5	1.29	1.22	1.223	1.154	1.147	1.14	1.097	0.974	0.737	0.62	0.467	0.282	0.1	0.067	-0.006	0	86.94	-0.1	0.99	8.13
37	1.29	1.22	1.218	1.149	1.137	1.14	1.077	0.969	0.717	0.615	0.452	0.262	0.078	-0.083	-0.206	-0.2	91.14	-0.27	1.01	7.75

37.5	1.29	1.22	1.218	1.154	1.137	1.13	1.077	0.959	0.707	0.595	0.432	0.242	0.056	-0.103	-0.268	-0.45	97.94	-0.45	0.975	7.675
38	1.29	1.22	1.213	1.154	1.137	1.13	1.077	0.959	0.697	0.58	0.422	0.212	0.026	-0.117	-0.305	-0.54	113.08	-0.62	0.94	7.6
38.5	1.29	1.22	1.213	1.144	1.127	1.12	1.067	0.949	0.687	0.57	0.412	0.197	0.016	-0.168	-0.366	-0.64	116.58	-0.77	0.955	7.9
39	1.29	1.215	1.213	1.134	1.127	1.13	1.067	0.949	0.677	0.56	0.392	0.172	-0.024	-0.193	-0.396	-0.67	116.8	-0.85	0.97	8.2
39.5	1.29	1.215	1.213	1.144	1.127	1.12	1.057	0.969	0.672	0.55	0.392	0.162	-0.044	-0.213	-0.426	-0.7	117.08	-0.87	0.95	8.145
40	1.29	1.21	1.203	1.134	1.122	1.12	1.057	0.939	0.657	0.535	0.372	0.162	-0.034	-0.193	-0.386	-0.65	116	-0.85	0.93	8.09
40.5	1.29	1.21	1.203	1.144	1.117	1.11	1.047	0.929	0.657	0.52	0.362	0.172	-0.014	-0.173	-0.346	-0.59	115.08	-0.8	0.915	7.535
41	1.28	1.21	1.203	1.134	1.117	1.11	1.047	0.919	0.647	0.52	0.362	0.192	0.026	-0.123	-0.266	-0.46	94.74	-0.68	0.9	6.98
41.5	1.28	1.21	1.203	1.124	1.117	1.11	1.037	0.909	0.637	0.51	0.367	0.207	0.056	-0.093	-0.246	-0.3	92.94	-0.54	0.935	9.65
42	1.28	1.21	1.203	1.124	1.112	1.1	1.037	0.904	0.637	0.51	0.367	0.222	0.096	-0.063	-0.146	-0.1	86.94	-0.37	0.97	12.32
42.5	1.28	1.21	1.203	1.124	1.107	1.1	1.027	0.894	0.627	0.51	0.402	0.352	0.166	0.127	0.094	0.2	75.84	-0.15	0.995	10.045
43	1.28	1.2	1.193	1.124	1.107	1.09	1.022	0.899	0.627	0.53	0.542	0.432	0.276	0.267	0.394	0.3	72.84	0.08	1.02	7.77
43.5	1.28	1.2	1.193	1.124	1.097	1.09	1.017	0.904	0.667	0.62	0.692	0.542	0.456	0.467	0.694		60.34	0.31	1.02	7.795
44	1.28	1.2	1.193	1.114	1.097	1.09	1.027	0.919	0.707	0.79	0.812	0.712	0.656	0.667	0.794		55.44	0.52	1.02	7.82
44.5	1.28	1.2	1.193	1.114	1.097	1.1	1.047	0.959	0.817	1.05	0.912	0.962	0.956	0.917			52.44	0.72	1.03	6.22
45	1.28	1.19	1.188	1.114	1.097	1.11	1.067	0.994	0.967	1.105	1.012	1.062	1.056	1.017			48.38	0.89	1.04	4.62
45.5	1.28	1.19	1.193	1.124	1.117	1.13	1.097	1.039	1.187	1.15	1.092			1.067			46	1.01	1.07	4.665
46	1.28	1.19	1.193	1.139	1.122	1.15	1.127	1.089	1.287	1.17	1.142						43.38	1.08	1.1	4.71
46.5	1.275	1.195	1.198	1.144	1.137	1.16	1.147	1.124	1.307	1.15	1.132						45	1.05	1.085	4.605
47	1.27	1.2	1.193	1.154	1.147	1.175	1.157	1.149	1.247	1.12	1.092						47	0.99	1.07	4.5
47.5	1.27	1.2	1.193	1.154	1.147	1.19	1.167	1.149	1.177	1.09	0.972						49	0.88	1.06	5.9
48	1.27	1.2	1.203	1.164	1.167	1.2	1.177	1.164	1.107	1.065	0.872						54.44	0.74	1.05	7.3

A.3 Moreton Island, 11th December 2000

A.3.1 Water level and topography data

Well	**1**	**2**	**3**	**4**	**5**	**6**	**7**	**8**	**9**	**10**	**11**	**12**	**13**	**Exit**	**Runup**	**SWL**	**Hrms**	**Tp**
x [m]	-110.8	-78.4	-68	-58	-46.8	-36.6	-25.8	-13.35	0	15	25.8	42.1	80	**Point**	**Limit**			
z sand [m AHD]	-1.037	-0.165	0.143	0.519	1.04	1.487	1.809	2.57225	3.413	4.9811111	5.068	4.5374	4.634					
Time	Levels [m AHD]																[m]	[sec]
15.5	-0.647	-0.167	0.072	0.321	0.621	0.829	0.936	0.914	0.887	0.88	0.879	0.9	0.95	-0.086	0.206	-0.58	0.625	9.68
16	-0.527	-0.157	0.082	0.311	0.611	0.799	0.916	0.914	0.887	0.88	0.889	0.89	0.95	0.033	0.246	-0.47	0.63	10.06
16.5	-0.307	-0.127	0.142	0.321	0.601	0.789	0.906	0.894	0.887	0.89	0.879	0.89	0.95	0.305	0.364	-0.34	0.63	10.095
17	-0.217	-0.077	0.152	0.341	0.591	0.769	0.896	0.894	0.887	0.89	0.879	0.89	0.95	0.404	0.443	-0.19	0.63	10.13
17.5		0.003	0.182	0.421	0.581	0.759	0.876	0.884	0.887	0.89	0.889	0.9	0.95	0.483	0.767	-0.04	0.655	10.175
18		0.103	0.202	0.451	0.591	0.749	0.876	0.874	0.877	0.89	0.889	0.9	0.95	0.522	0.846	0.13	0.68	10.22
18.5		0.223	0.362	0.531	0.621	0.759	0.876	0.874	0.877	0.88	0.889	0.9	0.95	0.807	1.004	0.25	0.675	9.725
19		0.363	0.372	0.541	0.681	0.739	0.856	0.864	0.867	0.88	0.889	0.9	0.95	0.846	0.965	0.37	0.67	9.23
19.5		0.403	0.382	0.561	0.711	0.749	0.846	0.854	0.877	0.88	0.889	0.9	0.95	0.759	1.083	0.42	0.695	10.085
20		0.413	0.382	0.541	0.721	0.749	0.846	0.854	0.867	0.88	0.889	0.9	0.95	0.886	1.044	0.44	0.72	10.94
20.5		0.403	0.362	0.531	0.711	0.749	0.846	0.854	0.867	0.88	0.889	0.9	0.95	0.799	1.083	0.39	0.715	10.015
21		0.353	0.292	0.521	0.681	0.749	0.856	0.854	0.867	0.88	0.889	0.9	0.95	0.72	1.004	0.31	0.71	9.09
21.5		0.123	0.202	0.471	0.641	0.739	0.826	0.864	0.867	0.88	0.889	0.9	0.95	0.759	1.044	0.21	0.71	9.7
22		0.013	0.152	0.391	0.601	0.719	0.826	0.844	0.867	0.88	0.889	0.9	0.95	0.562	0.601	0.07	0.71	10.31
22.5		-0.137	0.102	0.321	0.581	0.719	0.826	0.844	0.867	0.87	0.889	0.9	0.95	0.285	0.483	-0.09	0.715	10.295
23		-0.207		0.271	0.551	0.709	0.806	0.844	0.857	0.87	0.889	0.9	0.95	0.072	0.246	-0.28	0.72	10.28
23.5	-0.607	-0.217		0.261	0.531	0.689	0.806	0.844	0.857	0.87	0.889	0.9	0.95	-0.126	-0.165	-0.48	0.705	10.18
24	-0.727	-0.217		0.241	0.511	0.669	0.796	0.834	0.857	0.87	0.879	0.9	0.95	-0.007	-0.205	-0.66	0.69	10.08
24.5	-0.847	-0.227		0.231	0.491	0.659	0.786	0.834	0.857	0.87	0.879	0.9	0.95	0.033	-0.363	-0.82	0.69	9.72
25	-0.927	-0.237		0.231	0.481	0.649	0.776	0.824	0.847	0.86	0.879	0.9	0.95	-0.086	-0.481	-0.95	0.69	9.36
25.5	-0.997	-0.237		0.211	0.461	0.629	0.776	0.824	0.847	0.86	0.879	0.9	0.95	-0.442	-0.718	-1.05	0.69	9.79
26	-0.987	-0.237			0.451	0.629	0.766	0.814	0.847	0.86	0.879	0.9	0.95	-0.442	-0.6	-1.06	0.69	10.22

26.5	-0.967	-0.247			0.441	0.609	0.756	0.814	0.837	0.86	0.879	0.9	0.95	-0.402	-0.442	-1.02	0.675	10.27
27	-0.907	-0.237			0.421	0.609	0.746	0.794	0.837	0.86	0.879	0.9	0.95	-0.323	-0.402	-0.92	0.66	10.32
27.5	-0.737	-0.227			0.421	0.589	0.736	0.794	0.827	0.85	0.869	0.9	0.95	-0.244	0.048	-0.8	0.67	9.805
28	-0.597	-0.217			0.411	0.569	0.726	0.784	0.827	0.85	0.869	0.9	0.95	0.171	0.127	-0.63	0.68	9.29
28.5	-0.357	-0.157	0.072		0.401	0.569	0.726	0.794	0.827	0.85	0.869	0.9	0.95	0.325	0.285	-0.43	0.675	9.8
29		-0.037	0.122	0.261	0.401	0.559	0.716	0.784	0.817	0.85	0.869	0.9	0.95	0.384	0.661	-0.21	0.67	10.31
29.5		0.233	0.232	0.461	0.471	0.569	0.706		0.817	0.84	0.859	0.9	0.96	0.68	0.819	0.02	0.655	10.255
30		0.393	0.392	0.551	0.551	0.589	0.716		0.817	0.84	0.859	0.9	0.96	0.945	0.965	0.25	0.64	10.2
30.5		0.583	0.582	0.651	0.871	0.639	0.726		0.817	0.84	0.859	0.9	0.95	1.083	1.202	0.5	0.6	9.53
31		0.803	0.802	0.771	1.021	0.699	0.756	0.784	0.807	0.84	0.859	0.89	0.95	1.123	1.447	0.71	0.56	8.86
31.5				0.891	1.091	0.919	0.806	0.794	0.817	0.84	0.849	0.89	0.95	1.328	1.723	0.86	0.53	9.13
32				0.981	1.141	1.349	0.886	0.844	0.837	0.85	0.859	0.89	0.95	1.486	1.719	0.97	0.5	9.4
32.5				1.031	1.181	1.419	0.956	0.874	0.857	0.86	0.869	0.89	0.95	1.486	1.715	1.03	0.5	9.01
33				0.981	1.171	1.389	1.026	0.904	0.867	0.87	0.869	0.89	0.95	1.486	1.486	1.05	0.5	8.62
33.5				0.951	1.161	1.369	1.056	0.924	0.887	0.89	0.889	0.9	0.95	1.241	1.439	0.96	0.51	9.05
34				0.811	1.081	1.219	1.086	0.944	0.897	0.89	0.899	0.91	0.95	1.182	1.281	0.84	0.52	9.48
34.5			1.766	0.701	1.041	1.139	1.086	0.954	0.907	0.9	0.899	0.91	0.95	1.123	1.123	0.69	0.525	9.2
35			1.686	0.561	0.931	1.099	1.076	0.964	0.917	0.91	0.909	0.92	0.95	0.72	1.083	0.53	0.53	8.92
35.5			1.486	0.521	0.831	1.059	1.066	0.964	0.917	0.91	0.909	0.91	0.95	0.641	0.799	0.34	0.55	9.13
36			1.366	0.491	0.791	1.029	1.046	0.964	0.917	0.91	0.909	0.91	0.95	0.641	0.68	0.13	0.57	9.34
36.5		1.046	1.316	0.421	0.751	0.989	1.026	0.964	0.927	0.91	0.909	0.92	0.97	0.325	0.404	-0.11	0.56	9.325
37	-0.447	0.896	1.316	0.391	0.731	0.959	1.006	0.964	0.927	0.91	0.909	0.92	0.97	0.048	0.048	-0.31	0.55	9.31
37.5	-0.587		1.276	0.371	0.711	0.929	0.996	0.964	0.927	0.92	0.909	0.92	0.97	-0.031	-0.007	-0.47	0.545	8.89
38	-0.687		1.276	0.351	0.691	0.909	0.986	0.954	0.927	0.92	0.919	0.92	0.97	0.072	-0.165	-0.62	0.54	8.47
38.5	-0.757	0.856		0.331	0.671	0.879	0.966	0.954	0.927	0.92	0.919	0.92	0.97	0.072	-0.323	-0.7	0.565	8.55
39	-0.787	0.866		0.321	0.651	0.859	0.956	0.944	0.927	0.92	0.919	0.92	0.97	0.033	-0.442	-0.73	0.59	8.63
39.5	-0.757	0.866		0.311	0.631	0.819	0.936	0.934	0.907	0.92	0.919	0.93	0.97	-0.126	-0.086	-0.69	0.615	9.195
40	-0.727	0.886		0.301	0.621	0.819	0.926	0.924	0.927	0.92	0.919	0.93	0.97	0.072	-0.007	-0.64	0.64	9.76

A.4 Brunswick Heads, 18th November 2001

A.4.1 Water level and topography data

Well #		**1**	**2**	**3**	**4**	**5**	**6**	**6.5**	**7**	**8**	**9**	**10**	**11**	**12**	**13**	**14**	**15**	**16**	**RUL**	**EP**
x [m BM]		-97.62	-83.63	-68.07	-59.07	-49.63	-47.24	-41.1	-36.88	-25.56	-12.56	11.19	45.19	83.59	128.8	171.4	242.3	303		
z sand [m AHD] 18-Nov		-0.997	-0.407	0.148	0.625	1.934	1.932	1.891	1.910	2.125	3.510	4.056	3.825	3.700	2.760	2.354	-0.280	-0.770		
z sand [m AHD] 24-Nov		-1.047	-0.481	-0.071	0.291	0.830	0.976	1.351	1.590	2.181	3.252	4.056	3.825	3.700	2.760	2.354	-0.280	-0.770		
z sand [m AHD] 1-Dec		-0.576	-0.165	0.225	0.468	0.810	0.911	1.284	1.606	2.156	3.510	4.056	3.825	3.700	2.760	2.354	-0.280	-0.770		
Date	**Time**	**Levels [m AHD]**																	**x [m BM]**	
18-Nov	18.5	-0.272	-0.375	0.521	0.313	0.559	0.613		0.681	0.693	0.705	0.667	0.637	0.576	0.538					
	19	-0.162	-0.245	0.551	0.333	0.549	0.593		0.671	0.693	0.705	0.667	0.637	0.576	0.538				-63.07	-68.07
19-Nov	7.5		0.175	0.741	0.553	0.519	0.533		0.571	0.613	0.645	0.667	0.637	0.576	0.538	0.478	0.336			-56
	8		0.325	0.841	0.583	0.579	0.573		0.581	0.613	0.645	0.667	0.637	0.576	0.538	0.478	0.496		-50.63	-54.63
	8.75			0.491	0.653	0.749	0.663		0.621	0.623	0.645	0.667	0.637	0.576	0.538	0.478	0.596		-49.63	-53.63
	9.5			0.701	0.733	0.919	0.763		0.651	0.633	0.645	0.667	0.637	0.576	0.538	0.478	0.746		-49.13	-51.63
	10				0.863	1.059	0.913		0.68	0.653	0.645	0.667	0.637	0.576	0.538	0.478	0.756		-47.24	-49.13
	10.5				0.843	1.069	0.933		0.711	0.673	0.655	0.657	0.637	0.576	0.538	0.478	0.786		-48.63	-49.13
	11				0.893	1.079	0.973		0.731	0.683	0.665	0.667	0.637	0.576	0.538	0.478	0.796		-48.23	-49.13
	11.5				0.853	1.049	0.993		0.751	0.693	0.665	0.667	0.637	0.576	0.538	0.478	0.716		-48.17	-49.13
	12				0.753	1.029	0.993		0.761	0.703	0.675	0.667	0.637	0.576	0.538	0.478	0.676		-47.88	-50.13
	12.5				0.643	0.969	0.943		0.771	0.713	0.675	0.667	0.637	0.576	0.538	0.478	0.636		-48.24	-50.63
	13			0.531	0.553	0.919	0.903		0.781	0.713	0.685	0.667	0.637	0.576	0.538	0.478	0.536		-47.88	-52.13
	13.5			0.401	0.433	0.809	0.833		0.761	0.713	0.685	0.667	0.637	0.576	0.538	0.478	0.416		-47.88	-53.63
	14			0.231	0.353	0.739	0.773		0.751	0.713	0.685	0.667	0.637	0.576	0.538	0.478	0.296		-50.63	-56.55
	14.5		0.025	0.131	0.343	0.679	0.733		0.731	0.713	0.695	0.677	0.627	0.576	0.538	0.498	0.136		-52.63	-57.07

	15		-0.025	0.071	0.343	0.639	0.683		0.711	0.703	0.685	0.677	0.627	0.576	0.538	0.498	0.036		-56.07	-61.07
	15.5	-0.242	-0.195	0.011	0.283	0.589	0.643		0.681	0.693	0.685	0.667	0.627	0.576	0.538	0.498	-0.144			-66.07
	16	-0.302	-0.265	0.021	0.263	0.569	0.623		0.671	0.673	0.685	0.667	0.627	0.576	0.538	0.498	-0.234		-60.57	-64.07
	16.5	-0.392	-0.345	0.001	0.253	0.549	0.603		0.661	0.663	0.675	0.667	0.627	0.576	0.538	0.498	-0.334		-62.07	-71.07
	17	-0.422	-0.375	-0.009	0.243	0.529	0.573		0.641	0.653	0.665	0.672	0.627	0.576	0.538	0.498	-0.374		-66.57	-71.07
	17.5	-0.462	-0.415	-0.019	0.223	0.509	0.553		0.631	0.653	0.665	0.677	0.627	0.576	0.538	0.498	-0.374		-69.07	-71.07
	18	-0.412	-0.335	-0.009	0.223	0.489	0.533		0.621	0.643	0.655	0.677	0.627	0.576	0.538	0.498			-68.07	-70.07
	18.5	-0.392	-0.335	-0.009	0.213	0.469	0.523		0.611	0.633	0.655	0.677	0.627	0.576	0.538	0.498			-66.07	-70.07
	19	-0.322	-0.255	0.021	0.223	0.459	0.503		0.601	0.623	0.655	0.677	0.627	0.576	0.538	0.498			-64.07	-69.07
	19.5	-0.282	-0.235	0.021	0.233	0.449	0.483		0.591	0.663	0.645	0.677	0.627	0.576	0.538	0.498			-62.07	-65.07
	20		-0.145	0.041	0.253	0.439	0.483		0.581	0.613	0.645	0.667	0.627	0.576	0.538	0.498			-56.07	-66.07
	20.5		-0.065	0.051	0.293	0.439	0.473		0.571	0.613	0.645	0.667	0.627	0.576	0.538	0.498			-57.07	-62.07
	21		0.025	0.111	0.353	0.459	0.493		0.571	0.603	0.635	0.667	0.627	0.576	0.538	0.498			-52.63	-59.07
	21.5			0.191	0.373	0.459	0.503		0.561	0.603	0.635	0.667	0.627	0.576	0.538	0.498			-53.63	-56.07
	22			0.221	0.383	0.509	0.523		0.571	0.603	0.635	0.667	0.627	0.576	0.538	0.498			-52.63	-57.07
	22.5			0.231	0.373	0.539	0.543		0.571	0.603	0.635	0.667	0.627	0.576	0.538	0.498			-51.63	-56.07
	23			0.271	0.393	0.559	0.563		0.571	0.603	0.635	0.662	0.627	0.576	0.538	0.498			-50.63	-56.07
	23.5			0.241	0.373	0.549	0.563		0.581	0.603	0.635	0.657	0.627	0.576	0.538	0.498			-50.63	-56.07
20-Nov	0		0.215	0.201	0.373	0.569	0.563		0.581	0.603	0.625	0.657	0.627	0.576	0.538	0.498			-50.63	-58.07
	0.5		0.145	0.161	0.353	0.519	0.533		0.571	0.603	0.625	0.657	0.627	0.576	0.538	0.498			-53.63	-56.63
	1		0.095	0.111	0.353	0.499	0.513		0.561	0.593	0.625	0.657	0.627	0.576	0.538	0.498			-53.63	-58.07
	1.5		0.005	0.021	0.313	0.459	0.483		0.561	0.593	0.625	0.657	0.627	0.576	0.538	0.498			-52.63	-59.27
	2		-0.085	-0.029	0.243	0.439	0.473		0.551	0.583	0.625	0.657	0.627	0.576	0.538	0.498			-56.07	-60.07
	2.5	-0.192	-0.235		0.213	0.419	0.453		0.541	0.583	0.625	0.657	0.627	0.576	0.538	0.498			-59.07	-60.27
	3	-0.202	-0.255		0.173	0.409	0.443		0.541	0.583	0.625	0.657	0.627	0.576	0.538	0.498			-62.07	-67.07
	3.5	-0.362	-0.305		0.163	0.399	0.433		0.531	0.583	0.615	0.657	0.627	0.576	0.538	0.498			-63.07	-68.57
	4	-0.377	-0.335		0.153	0.389	0.433		0.531	0.583	0.615	0.657	0.627	0.576	0.538	0.498			-63.37	-69.07
	4.5	-0.392	-0.355		0.143	0.379	0.413		0.531	0.573	0.615	0.657	0.627	0.576	0.538	0.498			-67.07	-68.07
	5	-0.392	-0.345		0.143	0.369	0.403		0.511	0.573	0.615	0.652	0.627	0.576	0.538	0.498			-65.07	-69.07
	5.5	-0.382	-0.315		0.133	0.359	0.393		0.511	0.563	0.615	0.647	0.627	0.576	0.538	0.498			-64.07	-69.57
	6	-0.272	-0.235		0.153	0.349	0.393		0.501	0.563	0.605	0.647	0.627	0.576	0.538	0.498			-62.07	-65.57
	6.5		-0.145	-0.019	0.193	0.349	0.383		0.491	0.563	0.605	0.647	0.627	0.576	0.538	0.498			-61.07	-63.07
	7		-0.065	0.021	0.273	0.359	0.393		0.491	0.563	0.605	0.647	0.627	0.576	0.538	0.498			-57.87	-59.57
	7.5		0.085	0.121	0.363	0.399	0.423		0.491	0.553	0.605	0.647	0.627	0.576	0.538	0.498			-55.63	-58.07

	8		0.175	0.201	0.403	0.459	0.463		0.501	0.553	0.595	0.647	0.627	0.576	0.538	0.498	0.156		-50.63	-55.63
	8.5		0.335	0.321	0.463	0.569	0.533		0.531	0.553	0.595	0.647	0.627	0.576	0.538	0.498	0.266		-48.63	-54.63
	9			0.471	0.533	0.879	0.683		0.561	0.563	0.595	0.647	0.627	0.576	0.538	0.498	0.376		-47.86	-52.63
	9.5			0.601	0.643	1.019	0.833		0.611	0.583	0.605	0.647	0.627	0.576	0.538	0.498			-47.74	-51.63
	10			0.721	0.733	1.099	0.973		0.641	0.603	0.605	0.647	0.627	0.576	0.538	0.498			-42.77	-51.13
	10.5			0.761	0.793	1.129	1.063		0.671	0.623	0.615	0.647	0.627	0.576	0.538	0.498			-39.88	-49.63
	10.75			0.791	0.813	1.189	1.153		0.701	0.643	0.625	0.647	0.627	0.576	0.538	0.498			-39.88	-49.63
	11			0.791	0.843	1.169	1.183		0.711	0.653	0.625	0.642	0.627	0.576	0.538	0.498			-39.88	-49.13
	11.5			0.811	0.863	1.219	1.253		0.751	0.663	0.635	0.637	0.627	0.576	0.538	0.498	0.776		-39.88	-49.23
	12			0.811	0.903	1.179	1.353		0.861	0.703	0.645	0.647	0.617	0.576	0.538	0.488	0.781		-42	-48.7
	12.5			0.771	0.863	1.169	1.323		0.961	0.723	0.665	0.647	0.617	0.576	0.538	0.488	0.786		-46.37	-48.24
	13			0.721	0.823	1.149	1.303		1.021	0.753	0.685	0.647	0.617	0.576	0.538	0.488	0.701		-42.88	-49.63
	13.5			0.631	0.713	1.139	1.253		1.041	0.773	0.695	0.657	0.617	0.576	0.538	0.488	0.616		-45.88	-50.63
	14			0.531	0.633	1.119	1.223		1.041	0.793	0.705	0.657	0.617	0.576	0.538	0.488	0.526		-46.19	-51.63
	14.5			0.441	0.563	1.039	1.123		1.031	0.803	0.715	0.657	0.617	0.576	0.538	0.488	0.406		-46.19	-52.63
	15	0.218	0.205	0.331	0.483	0.999	1.073		1.021	0.813	0.715	0.667	0.617	0.576	0.538	0.488	0.296		-48.24	-51.63
	15.5		0.165	0.241	0.443	0.899	1.003		1.001	0.823	0.725	0.667	0.617	0.576	0.538	0.488	0.186		-48.63	-57.07
21-Nov	8.5			0.331	0.643	1.009	1.013		0.831	0.763	0.735	0.697	0.617	0.576	0.538	0.478	0.236		-48.24	-56.07
	10			0.661	0.773	1.199	1.213		0.901	0.803	0.745	0.707	0.617	0.576	0.538	0.478	0.566		-45.24	-50.63
	10.5			0.791	0.863	1.239	1.303		0.931	0.813	0.755	0.707	0.617	0.576	0.538	0.478	0.636		-37.88	-49.63
	11			0.831	0.923	1.339	1.353		0.971	0.833	0.755	0.707	0.617	0.576	0.538	0.478	0.706		-41.88	-47.24
	16			0.361	0.503	0.949	1.043		1.291	1.083	0.865	0.737	0.617	0.576	0.538	0.478			-46.24	-47.24
	16.5			0.331	0.483	0.929	1.033		1.261	1.073	0.875	0.747	0.617	0.576	0.538	0.478			-46.24	-61.63
	17			0.221	0.443	0.899	0.993		1.221	1.063	0.885	0.747	0.617	0.576	0.538	0.478			-49.63	-54.07
	17.5			0.141	0.423	0.849	0.943		1.181	1.053	0.885	0.747	0.617	0.576	0.538	0.478			-45.63	-45.63
	18			0.131	0.433	0.829	0.933	1.12	1.151	1.043	0.885	0.747	0.617	0.576	0.538	0.478			-56.07	-57.07
	18.5			0.091	0.433	0.799	0.903	1.08	1.121	1.033	0.895	0.757	0.617	0.576	0.538	0.478			-56.07	-56.07
	19			0.111	0.453	0.799	0.893	1.05	1.091	1.013	0.895	0.757	0.617	0.576	0.538	0.478				
22-Nov	9.5			0.461	0.713	1.159	1.283	1.19	1.091	0.963	0.895	0.807	0.657	0.596	0.538	0.478			-44.24	-48.24
	10			0.591	0.743	1.179	1.303	1.3	1.181	1.003	0.905	0.807	0.657	0.596	0.538	0.478			-32.88	-48.63
	10.5			0.701	0.823	1.219	1.343	1.36	1.261	1.023	0.905	0.807	0.657	0.596	0.538	0.478			-37.88	-47.74

	11			0.811	0.863	1.259	1.413	1.6	1.491	1.083	0.915	0.807	0.667	0.596	0.538	0.478			-41.88	-47.24
	16.5			0.621	0.763	1.029		1.63	1.501	1.493	1.215	0.857	0.667	0.596	0.538	0.478			-28.56	-36.88
	17.5			0.521	0.683	0.929		1.32	1.481	1.633	1.235	0.867	0.667	0.596	0.538	0.478			-24.56	-37.88
	18			0.391	0.643	0.909		1.24	1.391	1.583	1.245	0.867	0.667	0.596	0.538	0.478			-32.88	-46.63
	18.5			0.331	0.583	0.909		1.24	1.441	1.543	1.245	0.867	0.667	0.596	0.538	0.478			-33.88	-45.1
	19			0.291	0.553	0.879		1.15	1.281	1.503	1.245	0.867	0.667	0.596	0.538	0.478			-36.88	-49.63
23-Nov	15.5			0.651	0.703	0.859		1.19	1.251	1.173	1.095	0.957	0.737	0.636	0.558	0.488	0.586		-34.88	-45.1
	16			0.591	0.653	0.859		1.18	1.221	1.163	1.095	0.957	0.737	0.636	0.558	0.488			-36.88	-45.1
	17			0.461	0.543	0.809		1.06	1.131	1.133	1.085	0.967	0.737	0.636	0.558	0.488			-35.88	-48.63
	18			0.381	0.503	0.809		1.01	1.101	1.113	1.085	0.967	0.737	0.636	0.558	0.488			-43.1	-49.63
24-Nov	8.5			0.081	0.393	0.549		0.72	0.781	0.883	0.935	0.907	0.757	0.656	0.578		-0.144		-57.07	-58.07
	16			0.561	0.603	0.829		0.89	0.881	0.863	0.885	0.877	0.637	0.656	0.588				-41.1	-49.63
	16.5			0.541	0.583	0.829		0.88	0.871	0.863	0.885	0.877	0.637	0.656	0.588				-40.1	-48.63
	17			0.481	0.543	0.759		0.86	0.861	0.863	0.885	0.877	0.637	0.656	0.588				-40.1	-48.63
	17.5			0.381	0.473	0.689		0.82	0.831	0.853	0.885	0.877	0.637	0.656	0.588				-51.63	-54.63
	18			0.341	0.453	0.689		0.79	0.811	0.843	0.875	0.877	0.637	0.656	0.588				-51.63	-51.63
25-Nov	7.5			0.071	0.403	0.499		0.63	0.661	0.733	0.795	0.817	0.627	0.656	0.608				-59.07	-59.07
	8			0.051	0.323	0.469		0.61	0.651	0.723	0.795	0.817	0.627	0.656	0.608				-56.07	-56.07
	8.5			0.011	0.273	0.449		0.6	0.641	0.723	0.785	0.817	0.627	0.656	0.608				-59.07	-67.07
	9			0.031	0.283	0.449		0.59	0.641	0.723	0.785	0.817	0.627	0.656	0.608				-63.07	-66.07
	9.5			0.021	0.253	0.429		0.57	0.631	0.713	0.785	0.817	0.627	0.656	0.608				-70.57	-68.07
	10			0.031	0.263	0.419		0.57	0.621	0.713	0.775	0.817	0.627	0.656	0.608				-61.07	-66.07
	10.5			0.031	0.253	0.419		0.56	0.611	0.703	0.775	0.817	0.627	0.656	0.608				-60.07	-68.07
	11			0.031	0.253	0.409		0.56	0.611	0.703	0.775	0.817	0.627	0.656	0.608				-63.07	-64.07
	16																0.396	0.355		
26-Nov	10			-0.019	0.213	0.379			0.521	0.603	0.675	0.737	0.617	0.646	0.598					-71.07
	10.5			-0.009	0.203	0.369			0.521	0.603	0.665	0.737	0.617	0.646	0.598				-65.07	-69.07

	11			-0.049	0.183	0.349			0.511	0.593	0.665	0.737	0.617	0.646	0.598				-69.07	-71.07
	11.5			-0.049	0.193	0.339			0.501	0.593	0.665	0.737	0.617	0.646	0.598					
	12			-0.019	0.193	0.329			0.491	0.583	0.665	0.737	0.617	0.646	0.598				-64.07	-69.57
	12.5			0.011	0.213	0.329			0.491	0.583	0.665	0.737	0.617	0.646	0.598				-60.57	-67.57
27-Nov	10.5				0.223	0.429			0.531	0.573	0.615	0.677	0.617	0.626	0.598					-68.07
	11			-0.049	0.213	0.409			0.521	0.563	0.615	0.677	0.617	0.626	0.598				-68.57	-69.07
	11.5			-0.049	0.203	0.389			0.511	0.553	0.605	0.677	0.617	0.626	0.598				-68.57	-70.07
	12			-0.059	0.193	0.369			0.491	0.543	0.605	0.677	0.617	0.626	0.598				-69.07	-70.57
	12.5			-0.069	0.183	0.349			0.481	0.543	0.605	0.677	0.617	0.626	0.598				-68.07	-70.07
	13			-0.049	0.183	0.339			0.471	0.533	0.595	0.677	0.617	0.626	0.598				-66.07	-67.07
	13.5			-0.029	0.183	0.329			0.461	0.533	0.595	0.677	0.617	0.626	0.598				-66.07	-67.07
	14			-0.019	0.203	0.319			0.461	0.533	0.595	0.667	0.617	0.626	0.598				-60.07	-67.07
	16.5			0.371	0.463	0.499			0.501	0.533	0.585	0.667	0.617	0.626	0.588		0.286	0.255		
	17			0.451	0.513	0.589			0.531	0.543	0.585	0.667	0.617	0.626	0.588				-57.57	-55.07
	17.5			0.461	0.513	0.719			0.551	0.553	0.595	0.667	0.617	0.626	0.588		0.386	0.355	-57.57	-54.07
28-Nov	9.5			0.211	0.373	0.609		0.74	0.741	0.703	0.665	0.657	0.617	0.616	0.598					-56.07
	10			0.121	0.353	0.579		0.72	0.721	0.703	0.665	0.657	0.617	0.616	0.598				-50.13	-56.07
	10.5			0.021	0.323	0.529		0.69	0.701	0.693	0.675	0.657	0.617	0.616	0.598				-56.07	-60.07
	11			-0.109	0.283	0.499		0.67	0.681	0.693	0.675	0.657	0.617	0.616	0.598				-61.07	-65.07
	11.5				0.263	0.479		0.65	0.661	0.683	0.675	0.657	0.617	0.616	0.598				-58.07	-66.07
	12				0.243	0.469		0.63	0.651	0.673	0.665	0.657	0.617	0.616	0.598				-62.57	-68.07
	12.5				0.233	0.449		0.61	0.631	0.663	0.665	0.657	0.617	0.616	0.598				-64.57	-67.07
29-Nov	9.5			0.421	0.533	0.749		0.94	0.971	0.843	0.745	0.697	0.617	0.616	0.588					-59.07
	10			0.361	0.503	0.729		0.92	0.951	0.833	0.745	0.697	0.617	0.616	0.588				-48.63	-52.13
	10.5			0.291	0.483	0.669		0.87	0.911	0.833	0.755	0.697	0.617	0.616	0.588				-47.13	-55.57
	11			0.191	0.473	0.639		0.84	0.881	0.823	0.755	0.697	0.617	0.616	0.588				-50.63	-58.57
	11.5			0.161	0.453	0.609		0.81	0.851	0.813	0.755	0.697	0.617	0.616	0.588				-52.63	-59.07
	12			0.181	0.413	0.579		0.78	0.831	0.803	0.755	0.697	0.617	0.616	0.588				-59.07	-66.07
	12.5			0.181	0.393	0.559		0.76	0.811	0.793	0.755	0.697	0.617	0.616	0.588				-60.57	-71.07
	13			0.171	0.383	0.549		0.74	0.791	0.783	0.755	0.697	0.617	0.616	0.588				-68.07	-71.07

	13.5			0.171	0.373	0.539		0.72	0.771	0.773	0.755	0.697	0.617	0.616	0.588				-66.07	-74.07
	18																0.416	0.385		
30-Nov	10			0.591	0.643	0.829		1.06	1.121	0.933	0.795	0.727	0.617	0.616	0.578				-46.63	-47.63
	10.5			0.411	0.513	0.779		0.99	1.061	0.923	0.805	0.727	0.617	0.616	0.578				-44.1	-52.63
	11			0.391	0.493	0.729		0.95	1.011	0.923	0.805	0.727	0.617	0.616	0.578				-52.13	-54.13
	11.5			0.221	0.473	0.679		0.92	0.981	0.913	0.815	0.727	0.617	0.616	0.578				-51.63	-61.57
	12			0.201	0.453	0.649		0.88	0.941	0.893	0.815	0.727	0.617	0.616	0.578				-51.63	-71.57
	12.5			0.201	0.443	0.629		0.86	0.911	0.883	0.815	0.727	0.617	0.616	0.578				-60.57	-64.07
	13			0.201	0.433	0.609		0.83	0.891	0.873	0.815	0.727	0.617	0.616	0.578				-67.07	-68.07
	13.5			0.201	0.423	0.599		0.81	0.871	0.863	0.815	0.727	0.617	0.616	0.578				-67.07	-68.07
1-Dec	8			1.021	1.073	1.089		1.29	1.361	0.873	0.785	0.737	0.617	0.616	0.578				-31.88	-38.88
	8.5			1.021	1.073	1.049		1.3	1.421	0.923	0.795	0.737	0.617	0.616	0.578				-29.56	-36.88
	9			0.961	1.013	1.059		1.3	1.421	0.973	0.815	0.747	0.617	0.616	0.578				-29.56	-38.88
	9.5			0.891	0.943	0.959		1.26	1.341	1.003	0.825	0.747	0.617	0.616	0.578				-33.88	-41.1
	10			0.751	0.803	0.889		1.21	1.261	1.013	0.835	0.757	0.617	0.616	0.578				-35.38	-45.1
	10.5			0.631	0.683	0.839		1.08	1.171	1.013	0.845	0.757	0.617	0.616	0.578				-34.88	-46.1
	11			0.401	0.563	0.789		1.02	1.121	1.013	0.855	0.757	0.617	0.616	0.578				-41.1	-52.13
	16				0.423	0.589		0.77	0.841	0.873	0.845	0.777	0.617	0.626	0.588				-76.07	-78.07
2-Dec	8.5			0.951	1.003	1.019		1.25	1.151	0.813	0.765	0.747	0.617	0.626	0.578				-32.88	-41.1
	9			0.941	0.993	1.009		1.26	1.241	0.853	0.785	0.747	0.617	0.626	0.578				-29.56	-41.1
	9.5			0.931	0.993	0.999		1.25	1.241	0.893	0.795	0.747	0.617	0.626	0.578				-33.38	-46.63
	10			0.861	0.913	0.959		1.24	1.211	0.913	0.815	0.757	0.617	0.626	0.578				-36.88	-41.1
	10.5			0.751	0.803	0.889		1.19	1.161	0.923	0.825	0.757	0.617	0.626	0.578				-36.88	-43.1
	11			0.591	0.673	0.869		1.11	1.111	0.933	0.835	0.767	0.617	0.626	0.578				-38.38	-44.6
	11.5			0.441	0.573	0.799		0.99	1.051	0.933	0.835	0.767	0.617	0.626	0.578				-40.1	-61.63
	12			0.331	0.543	0.729		0.94	1.001	0.923	0.845	0.767	0.617	0.626	0.578				-47.63	-56.57
3-Dec	8.5			0.901	0.963	0.999		1.11	0.851	0.743	0.715	0.727	0.587	0.626	0.578					-43.1
	9			0.951	1.003	1.029		1.2	0.951	0.763	0.735	0.727	0.587	0.626	0.578				-35.88	-41.1

	9.5			1.011	1.053	1.059		1.27	1.131	0.793	0.745	0.727	0.587	0.626	0.578				-33.88	-40.1
	10			1.001	1.053	1.069		1.25	1.201	0.833	0.755	0.727	0.587	0.626	0.578				-31.88	-40.1
	10.5			0.951	1.003	0.999		1.26	1.231	0.853	0.775	0.727	0.587	0.626	0.578				-34.38	-41.1
	11			0.851	0.903	0.919		1.22	1.181	0.873	0.785	0.727	0.587	0.626	0.578				-35.88	-40.6
	11.5			0.741	0.783	0.849		1.08	1.091	0.883	0.795	0.727	0.587	0.626	0.578				-39.1	-43.6
	12			0.551	0.613	0.809		0.99	1.031	0.893	0.805	0.747	0.587	0.626	0.578				-41.1	-49.63
	12.5			0.441	0.543	0.729		0.94	0.991	0.883	0.805	0.747	0.587	0.626	0.578				-46.13	-55.07

A.4.2 Wave and tide data

Tweed = Tweed offshore tide gauge; BH Riv = Brunswick heads river tide gauge; BBW = Brunswick Heads breakwater tide gauge; Hsig, Hrms and TP1 = wave statistics from Byron Bay.

Date	Time	Tweed	BH Riv	BBW	Hsig	Hrms	TP1
18-Nov	18:00	-0.401	-0.422	-0.28	1.47	1.039	5.66
18-Nov	19:00	-0.191	-0.212	-0.04	1.51	1.068	5.89
18-Nov	20:00	0.069	-0.022	0.1	1.51	1.068	6.35
18-Nov	21:00	0.179	0.098	0.27	1.67	1.181	6.38
18-Nov	22:00	0.289	0.238	0.35	1.52	1.075	7.01
18-Nov	23:00	0.229	0.218	0.33	1.44	1.018	7.08
19-Nov	0:00	0.109	0.108	0.17	1.44	1.018	6.99
19-Nov	1:00	-0.131	-0.122	0	1.47	1.039	7.21
19-Nov	2:00	-0.311	-0.312	-0.25	1.6	1.131	7.31
19-Nov	3:00	-0.441	-0.482	-0.3	1.51	1.068	7.05
19-Nov	4:00	-0.521	-0.522	-0.38	1.51	1.068	7.4
19-Nov	5:00	-0.371	-0.472	-0.27	1.5	1.061	7.33
19-Nov	6:00	-0.191	-0.262	-0.18	0.91	0.643	7.7
19-Nov	7:00	0.089	-0.032	0.17	0.993	0.702	7.7
19-Nov	8:00	0.429	0.258	0.51	0.907	0.641	7.3
19-Nov	9:00	0.619	0.548	0.73	0.861	0.609	6.5
19-Nov	10:00	0.819	0.728	0.89	0.633	0.448	7.3
19-Nov	11:00	0.829	0.788	0.89	0.699	0.494	7.3
19-Nov	12:00	0.669	0.728	0.81	0.916	0.648	7.3
19-Nov	13:00	0.439	0.538	0.63	0.922	0.652	7.3
19-Nov	14:00	0.169	0.248	0.22	0.993	0.702	6.9
19-Nov	15:00	-0.181	-0.042	0.01	1.802	1.274	5.6
19-Nov	16:00	-0.321	-0.302	-0.25	1.889	1.336	6.9
19-Nov	17:00	-0.451	-0.432	-0.3	1.909	1.350	7.7
19-Nov	18:00	-0.491	-0.442	-0.4	2.241	1.585	7.7
19-Nov	19:00	-0.341	-0.352	-0.19	2.203	1.558	7.7
19-Nov	20:00	-0.181	-0.202	-0.04	2.347	1.660	9.4
19-Nov	21:00	0.019	0.008	0.15	2.347	1.660	9.4
19-Nov	22:00	0.189	0.158	0.31	2.192	1.550	8.8
19-Nov	23:00	0.219	0.218	0.36	2.324	1.643	8.3
20-Nov	0:00	0.159	0.188	0.29	1.948	1.377	7.7
20-Nov	1:00	0.029	0.058	0.19	1.857	1.313	7.7
20-Nov	2:00	-0.161	-0.142	-0.03	1.883	1.331	8.2
20-Nov	3:00	-0.301	-0.312	-0.23	1.914	1.353	7.3
20-Nov	4:00	-0.431	-0.382	-0.33	1.834	1.297	11.1
20-Nov	5:00	-0.401	-0.392	-0.29	2.121	1.500	11.1
20-Nov	6:00	-0.241	-0.282	-0.12	2.383	1.685	10.2
20-Nov	7:00	-0.071	-0.082	0.11	2.52	1.782	11.1
20-Nov	8:00	0.149	0.148	0.27	2.599	1.838	11.1
20-Nov	9:00	0.469	0.388	0.46	3.11	2.199	8.8
20-Nov	10:00	0.629	0.598	0.73	2.87	2.029	13.5
20-Nov	11:00	0.769	0.778	0.87	2.85	2.015	8.8
20-Nov	12:00	0.789	0.778	0.93	2.987	2.112	12.2
20-Nov	13:00	0.659	0.698	0.84	3.638	2.572	12.2
20-Nov	14:00	0.469	0.518	0.49	3.355	2.372	11.1
20-Nov	15:00	0.149	0.248	0.28	3.215	2.273	10.2
20-Nov	16:00	-0.071	0.028	0.13	3.188	2.254	12.2
20-Nov	17:00	-0.261	-0.152	-0.15	3.173	2.244	9.4
20-Nov	18:00	-0.331	-0.272	-0.1	3.339	2.361	12.2

20-Nov	19:00	-0.291	-0.322	-0.18	3.667	2.593	12.2
20-Nov	20:00	-0.191	-0.222	-0.1	3.667	2.593	12.2
20-Nov	21:00	-0.041	-0.072	0.12	3.942	2.787	12.2
20-Nov	22:00	0.079	0.078	0.28	4.565	3.228	11.1
20-Nov	23:00	0.149	0.218	0.39	4.383	3.099	12.2
21-Nov	0:00	0.169	0.268	0.48	4.054	2.867	12.2
21-Nov	1:00	0.199	0.218	0.32	3.892	2.752	12.2
21-Nov	2:00	0.029	0.158	0.24	3.953	2.795	13.5
21-Nov	3:00	-0.051	0.028	0.07	3.579	2.531	12.2
21-Nov	4:00	-0.151	-0.102	-0.08	3.744	2.647	13.5
21-Nov	5:00	-0.211	-0.152	0.07	3.759	2.658	12.2
21-Nov	6:00	-0.201	-0.132	-0.1	3.464	2.449	13.5
21-Nov	7:00	-0.081	-0.082	-0.09	3.456	2.444	12.2
21-Nov	8:00	0.049	0.118	0.25	3.44	2.432	12.2
21-Nov	9:00	0.349	0.328	0.42	3.468	2.452	13.5
21-Nov	10:00	0.559	0.528	0.69	3.385	2.394	12.2
21-Nov	11:00	0.799	0.698	1	3.581	2.532	12.2
21-Nov	12:00	0.819	0.798	0.92	3.024	2.138	12.2
21-Nov	13:00	0.829	0.768	0.86	3.089	2.184	12.2
21-Nov	14:00	0.659	0.688	0.72	2.917	2.063	13.5
21-Nov	15:00	0.449	0.468	0.55	2.797	1.978	13.5
21-Nov	16:00	0.169	0.288	0.46	2.48	1.754	9.4
21-Nov	17:00	-0.011	0.128	0.22	2.641	1.867	12.2
21-Nov	18:00	-0.211	-0.092	0.1	2.968	2.099	12.2
21-Nov	19:00	-0.241	-0.202	-0.06	3.623	2.562	12.2
21-Nov	20:00	-0.191	-0.182	0	3.347	2.367	11.1
21-Nov	21:00	-0.131	-0.122	-0.09	3.588	2.537	12.2
21-Nov	22:00	-0.001	-0.002	0.21	3.549	2.510	12.2
21-Nov	23:00	0.119	0.168	0.36	3.754	2.654	12.2
22-Nov	0:00	0.219	0.198	0.36	3.971	2.808	12.2
22-Nov	1:00	0.289	0.248	0.39	3.915	2.768	12.2
22-Nov	2:00	0.149	0.238	0.34	4.03	2.850	13.5
22-Nov	3:00	0.049	0.198	0.38	3.864	2.732	12.2
22-Nov	4:00	0.069	0.148	0.14	3.871	2.737	13.5
22-Nov	5:00	-0.051	0.058	0.08	3.936	2.783	13.5
22-Nov	6:00	-0.121	-0.002	0.02	4.418	3.124	12.2
22-Nov	7:00	-0.081	-0.032	0.27	3.761	2.659	13.5
22-Nov	8:00	0.009	-0.012	0.12	4.565	3.228	12.2
22-Nov	9:00	0.189	0.138	0.22	4.655	3.292	13.5
22-Nov	10:00	0.349	0.248	0.42	4.511	3.190	13.5
22-Nov	11:00	0.599	0.448	0.58	4.118	2.912	13.5
22-Nov	12:00	0.709	0.658	0.61	4.007	2.833	13.5
22-Nov	13:00	0.729	0.658	0.74	4.419	3.125	13.5
22-Nov	14:00	0.699	0.648	0.71	4.419	3.125	13.5
22-Nov	15:00	0.649	0.678	0.71	3.911	2.765	12.2
22-Nov	16:00	0.439	0.538	0.54	3.789	2.679	13.5
22-Nov	17:00	0.169	0.408	0.46	3.695	2.613	13.5
22-Nov	18:00	0.009	0.218	0.14	3.565	2.521	13.5
22-Nov	19:00	-0.131	0.018	0.14	3.4	2.4	
22-Nov	20:00	-0.121	-0.092	-0.07	3.288	2.325	12.2
22-Nov	21:00	-0.211	-0.172	0.09	3.188	2.340	13.5
22-Nov	22:00	-0.001	-0.082	0.11	3.336	2.359	12.2
22-Nov	23:00	0.029	0.008	0	3.28	2.32	
23-Nov	0:00	0.149	0.118	0.24	3.242	2.292	12.2
23-Nov	1:00	0.289	0.238	0.37	3.245	2.295	12.2
23-Nov	2:00	0.349	0.278	0.45	2.711	1.917	12.2
23-Nov	3:00	0.269	0.298	0.44	2.711	1.917	12.2
23-Nov	4:00	0.209	0.268	0.36	2.711	1.917	12.2
23-Nov	5:00	0.079	0.178	0.27	2.711	1.917	12.2
23-Nov	6:00	-0.071	0.068	0.12	2.662	1.882	11.1
23-Nov	7:00	-0.061	-0.042	0.14	2.682	1.896	12.2
23-Nov	8:00	-0.041	-0.032	0.07	2.564	1.813	12.2
23-Nov	9:00	0.039	0.028	0.2	2.608	1.844	11.1
23-Nov	10:00	0.149	0.138	0.24	2.392	1.691	11.1

23-Nov	11:00	0.319	0.268	0.47	2.372	1.677	12.2
23-Nov	12:00	0.429	0.408	0.54	2.685	1.899	11.1
23-Nov	13:00	0.609	0.538	0.7	2.35	1.662	12.2
23-Nov	14:00	0.659	0.618	0.68	2.475	1.750	11.1
23-Nov	15:00	0.629	0.598	0.75	2.291	1.620	10.2
23-Nov	16:00	0.549	0.568	0.61	2.342	1.656	11.1
23-Nov	17:00	0.299	0.358	0.56	2.232	1.578	12.2
23-Nov	18:00	0.069	0.158	0.23	2.141	1.514	11.1
23-Nov	19:00	-0.031	-0.032	0.1	1.827	1.292	11.1
23-Nov	20:00	-0.261	-0.182	-0.14	1.906	1.348	11.1
23-Nov	21:00	-0.271	-0.292	-0.16	1.962	1.387	11.1
23-Nov	22:00	-0.261	-0.302	-0.15	1.912	1.352	11.1
23-Nov	23:00	-0.201	-0.192	-0.02	1.823	1.289	11.1
24-Nov	0:00	-0.091	-0.072	0.05	1.867	1.320	10.2
24-Nov	1:00	0.109	0.068	0.27	1.721	1.217	10.2
24-Nov	2:00	0.219	0.148	0.3	1.721	1.217	11.1
24-Nov	3:00	0.249	0.248	0.42	1.708	1.208	11.1
24-Nov	4:00	0.219	0.238	0.42	1.538	1.088	10.2
24-Nov	5:00	0.149	0.178	0.22	1.538	1.088	10.2
24-Nov	6:00	0.039	0.068	0.18	1.538	1.088	10.2
24-Nov	7:00	-0.061	-0.042	0	1.523	1.077	10.2
24-Nov	8:00	-0.141	-0.122	-0.04	1.541	1.090	11.2
24-Nov	9:00	-0.171	-0.152	-0.06	1.02	0.721	10.43
24-Nov	10:00	-0.121	-0.102	-0.01	1.1	0.778	10.72
24-Nov	11:00	-0.001	0.008	0.1	1.1	0.778	10.43
24-Nov	12:00	0.159	0.138	0.3	1.11	0.785	10.8
24-Nov	13:00	0.339	0.288	0.38	1.18	0.834	10.04
24-Nov	14:00	0.449	0.418	0.56	1.19	0.841	4.6
24-Nov	15:00	0.529	0.498	0.63	1.18	0.834	3.97
24-Nov	16:00	0.489	0.478	0.59	1.27	0.898	4.5
24-Nov	17:00	0.349	0.398	0.43	1.31	0.926	4.48
24-Nov	18:00	0.209	0.228	0.36	1.27	0.898	10.31
24-Nov	19:00	-0.041	0.028	0.11	1.29	0.912	10.88
24-Nov	20:00	-0.201	-0.202	-0.07	1.15	0.813	10.89
24-Nov	21:00	-0.411	-0.382	-0.31	1.11	0.785	9.73
24-Nov	22:00	-0.501	-0.492	-0.39	1.12	0.792	11.56
24-Nov	23:00	-0.471	-0.462	-0.32	1.12	0.792	10.36
25-Nov	0:00	-0.331	-0.342	-0.18	1	0.707	10.32
25-Nov	1:00	-0.111	-0.182	-0.02	1.02	0.721	12.88
25-Nov	2:00	0.049	-0.012	0.16	0.99	0.700	12.19
25-Nov	3:00	0.189	0.148	0.3	1.05	0.742	12.35
25-Nov	4:00	0.289	0.228	0.38	1.07	0.757	5.8
25-Nov	5:00	0.279	0.248	0.34	1.11	0.785	12.29
25-Nov	6:00	0.129	0.168	0.26	1.04	0.735	11.43
25-Nov	7:00	0.009	0.038	0.15	0.97	0.686	5.58
25-Nov	8:00	-0.141	-0.122	-0.01	0.97	0.686	5.81
25-Nov	9:00	-0.231	-0.222	-0.08	1.02	0.721	5.8
25-Nov	10:00	-0.271	-0.272	-0.14	0.921	0.651	11.1
25-Nov	11:00	-0.251	-0.272	-0.14	0.734	0.519	11.1
25-Nov	12:00	-0.141	-0.142	0.04	0.948	0.670	10.2
25-Nov	13:00	0.059	-0.022	0.15	0.948	0.670	11.48
25-Nov	14:00	0.209	0.138	0.37	0.948	0.670	11.09
25-Nov	15:00	0.359	0.298	0.4	0.948	0.670	11.39
25-Nov	16:00	0.349	0.388	0.51	0.948	0.670	10.85
25-Nov	17:00	0.359	0.368	0.52	0.948	0.670	10.86
25-Nov	18:00	0.199	0.238	0.28	0.948	0.670	6.27
25-Nov	19:00	-0.001	0.018	0.1	0.823	0.582	10.2
25-Nov	20:00	-0.241	-0.202	-0.16	0.893	0.631	11.1
25-Nov	21:00	-0.441	-0.412	-0.33	0.795	0.562	11.1
25-Nov	22:00	-0.561	-0.552	-0.43	0.738	0.522	11.1
25-Nov	23:00	-0.611	-0.572	-0.51	0.738	0.522	10.87
26-Nov	0:00	-0.511	-0.512	-0.39	0.738	0.522	10.83
26-Nov	1:00	-0.311	-0.372	-0.16	0.738	0.522	6.99
26-Nov	2:00	-0.111	-0.182	-0.02	0.738	0.522	6.67

26-Nov	3:00	0.129	0.038	0.15	0.738	0.522	7.28
26-Nov	4:00	0.279	0.208	0.4	0.738	0.522	7.31
26-Nov	5:00	0.339	0.298	0.39	0.599	0.424	10.2
26-Nov	6:00	0.299	0.298	0.4	0.649	0.459	9.4
26-Nov	7:00	0.129	0.138	0.25	0.606	0.429	11.1
26-Nov	8:00	-0.081	-0.052	0.01	0.633	0.448	11.1
26-Nov	9:00	-0.241	-0.242	-0.14	0.576	0.407	10.2
26-Nov	10:00	-0.361	-0.382	-0.21	0.588	0.416	10.2
26-Nov	11:00	-0.411	-0.442	-0.28	0.639	0.452	10.2
26-Nov	12:00	-0.351	-0.392	-0.26	0.56	0.396	9.4
26-Nov	13:00	-0.211	-0.242	-0.13	0.516	0.365	10.2
26-Nov	14:00	0.009	-0.062	0.04	0.583	0.412	10.2
26-Nov	15:00	0.189	0.108	0.28	0.588	0.416	10.2
26-Nov	16:00	0.359	0.278	0.42	0.639	0.452	10.2
26-Nov	17:00	0.399	0.368	0.5	0.64	0.453	9.4
26-Nov	18:00	0.339	0.348	0.52	0.633	0.448	10.2
26-Nov	19:00	0.179	0.178	0.23	0.667	0.472	10.2
26-Nov	20:00	-0.081	-0.042	0.1	0.67	0.474	11.1
26-Nov	21:00	-0.341	-0.302	-0.2	0.659	0.466	10.2
26-Nov	22:00	-0.551	-0.532	-0.42	0.604	0.427	11.1
26-Nov	23:00	-0.631	-0.662	-0.48	0.585	0.414	12.2
27-Nov	0:00	-0.611	-0.652	-0.5	0.632	0.447	12.2
27-Nov	1:00	-0.471	-0.532	-0.39	0.568	0.402	12.2
27-Nov	2:00	-0.241	-0.302	-0.17	0.593	0.419	12.2
27-Nov	3:00	0.059	-0.042	0.14	0.667	0.472	10.2
27-Nov	4:00	0.309	0.178	0.32	0.688	0.486	11.1
27-Nov	5:00	0.459	0.368	0.56	0.618	0.437	11.1
27-Nov	6:00	0.459	0.428	0.54	0.644	0.455	12.2
27-Nov	7:00	0.359	0.348	0.48	0.723	0.511	12.2
27-Nov	8:00	0.159	0.178	0.28	0.706	0.499	11.1
27-Nov	9:00	-0.081	-0.042	0.1	0.658	0.465	12.2
27-Nov	10:00	-0.281	-0.252	-0.14	0.65	0.460	11.1
27-Nov	11:00	-0.431	-0.422	-0.29	0.637	0.450	12.2
27-Nov	12:00	-0.481	-0.482	-0.33	0.688	0.486	12.2
27-Nov	13:00	-0.401	-0.392	-0.31	0.694	0.491	11.1
27-Nov	14:00	-0.181	-0.232	-0.09	0.62	0.438	11.1
27-Nov	15:00	0.039	-0.022	0.14	0.669	0.473	11.1
27-Nov	16:00	0.239	0.178	0.24	0.767	0.542	11.1
27-Nov	17:00	0.389	0.338	0.5	1.217	0.861	5
27-Nov	18:00	0.399	0.408	0.51	1.217	0.861	5.06
27-Nov	19:00	0.249	0.258	0.39	1.217	0.861	5.94
27-Nov	20:00	0.039	0.098	0.14	3.382	2.391	8.8
27-Nov	21:00	-0.231	-0.152	-0.08	3.022	2.137	9.4
27-Nov	22:00	-0.451	-0.422	-0.31	3.226	2.281	10.2
27-Nov	23:00	-0.651	-0.602	-0.51	2.957	2.091	9.5
28-Nov	0:00	-0.681	-0.702	-0.54	3.445	2.436	7.7
28-Nov	1:00	-0.591	-0.612	-0.48	3.059	2.163	8.8
28-Nov	2:00	-0.341	-0.402	-0.28	3.453	2.442	8.8
28-Nov	3:00	-0.021	-0.132	0.01	3.438	2.431	9.4
28-Nov	4:00	0.269	0.158	0.32	3.118	2.205	9.4
28-Nov	5:00	0.499	0.408	0.57	3.411	2.412	9.4
28-Nov	6:00	0.629	0.578	0.7	3.598	2.544	9.4
28-Nov	7:00	0.599	0.628	0.74	3.355	2.372	8.8
28-Nov	8:00	0.419	0.498	0.56	3.355	2.372	8.8
28-Nov	9:00	0.209	0.288	0.4	3.384	2.393	9.5
28-Nov	10:00	-0.081	0.018	0.05	3.365	2.379	9.5
28-Nov	11:00	-0.321	-0.222	-0.16	3.365	2.379	9.5
28-Nov	12:00	-0.441	-0.382	-0.34	3.365	2.379	9.5
28-Nov	13:00	-0.441	-0.402	-0.3	3.019	2.135	7.7
28-Nov	14:00	-0.281	-0.282	-0.13	2.861	2.023	8.2
28-Nov	15:00	-0.061	-0.092	0.06	2.696	1.906	9.5
28-Nov	16:00	0.179	0.138	0.32	2.69	1.902	9.4
28-Nov	17:00	0.409	0.338	0.47	2.734	1.933	8.8
28-Nov	18:00	0.479	0.468	0.59	2.527	1.787	8.2

28-Nov	19:00	0.459	0.468	0.64	2.347	1.660	8.8
28-Nov	20:00	0.309	0.338	0.41	2.518	1.780	8.8
28-Nov	21:00	0.039	0.138	0.15	2.619	1.852	8.2
28-Nov	22:00	-0.261	-0.142	-0.1	2.452	1.734	8.2
28-Nov	23:00	-0.481	-0.372	-0.33	2.562	1.812	8.8
29-Nov	0:00	-0.651	-0.562	-0.41	2.281	1.613	8.2
29-Nov	1:00	-0.641	-0.582	-0.49	2.282	1.614	7.7
29-Nov	2:00	-0.431	-0.462	-0.29	2.217	1.568	8.2
29-Nov	3:00	-0.141	-0.212	-0.03	2.267	1.603	8.2
29-Nov	4:00	0.199	0.088	0.27	2.164	1.530	8.8
29-Nov	5:00	0.539	0.378	0.55	2.095	1.481	8.2
29-Nov	6:00	0.759	0.628	0.8	2.118	1.498	7.7
29-Nov	7:00	0.789	0.758	0.89	2.037	1.440	8.2
29-Nov	8:00	0.679	0.718	0.81	2.037	1.440	8.2
29-Nov	9:00	0.419	0.538	0.68	1.764	1.247	8.2
29-Nov	10:00	0.119	0.228	0.28	1.726	1.220	7.3
29-Nov	11:00	-0.161	-0.032	0.03	1.794	1.269	8.2
29-Nov	12:00	-0.401	-0.292	-0.25	1.684	1.191	8.2
29-Nov	13:00	-0.491	-0.402	-0.28	1.645	1.163	7.3
29-Nov	14:00	-0.431	-0.412	-0.33	1.463	1.034	8.2
29-Nov	15:00	-0.271	-0.272	-0.13	1.604	1.134	7.7
29-Nov	16:00	-0.021	-0.042	0.02	1.533	1.084	8.2
29-Nov	17:00	0.259	0.198	0.33	1.487	1.051	8.2
29-Nov	18:00	0.449	0.378	0.6	1.569	1.109	7.7
29-Nov	19:00	0.489	0.508	0.56	1.501	1.061	8.2
29-Nov	20:00	0.399	0.438	0.48	1.52	1.075	7.7
29-Nov	21:00	0.169	0.228	0.29	1.413	0.999	8.8
29-Nov	22:00	-0.121	-0.012	0.09	1.416	1.001	8.8
29-Nov	23:00	-0.401	-0.292	-0.26	1.439	1.018	7.7
30-Nov	0:00	-0.631	-0.532	-0.4	1.369	0.968	7.7
30-Nov	1:00	-0.711	-0.632	-0.49	1.387	0.981	7.3
30-Nov	2:00	-0.611	-0.602	-0.43	1.453	1.027	7.7
30-Nov	3:00	-0.321	-0.342	-0.29	1.446	1.022	8.2
30-Nov	4:00	0.019	-0.052	0.14	1.465	1.036	8.2
30-Nov	5:00	0.399	0.278	0.45	1.357	0.960	8.2
30-Nov	6:00	0.709	0.548	0.77	1.328	0.939	8.2
30-Nov	7:00	0.849	0.788	0.98	1.277	0.903	8.2
30-Nov	8:00	0.839	0.868	0.97	1.256	0.888	8.2
30-Nov	9:00	0.679	0.738	0.81	1.226	0.867	8.2
30-Nov	10:00	0.369	0.498	0.62	1.2	0.849	8.2
30-Nov	11:00	0.019	0.188	0.26	1.172	0.829	8.2
30-Nov	12:00	-0.311	-0.112	-0.12	1.1	0.778	7.7
30-Nov	13:00	-0.481	-0.372	-0.33	1.073	0.759	7.7
30-Nov	14:00	-0.551	-0.462	-0.34	1.025	0.725	8.2
30-Nov	15:00	-0.451	-0.412	-0.33	1.025	0.725	8.2
30-Nov	16:00	-0.251	-0.242	-0.1	0.949	0.671	7.7
30-Nov	17:00	0.039	-0.012	0.12	0.975	0.689	7.3
30-Nov	18:00	0.289	0.228	0.34	1.13	0.799	7.74
30-Nov	19:00	0.419	0.398	0.51	1.04	0.735	8.66
30-Nov	20:00	0.429	0.458	0.58	1.01	0.714	8.99
30-Nov	21:00	0.289	0.358	0.48	1.08	0.764	8.24
30-Nov	22:00	0.039	0.148	0.2	1.09	0.771	7.94
30-Nov	23:00	-0.271	-0.152	-0.16	1.04	0.735	9.87
1-Dec	0:00	-0.561	-0.442	-0.44	1.11	0.785	10.12
1-Dec	1:00	-0.681	-0.602	-0.41	1.03	0.728	8.47
1-Dec	2:00	-0.701	-0.632	-0.5	1.06	0.750	8.82
1-Dec	3:00	-0.511	-0.492	-0.35	1.09	0.771	7.28
1-Dec	4:00	-0.241	-0.252	-0.07	1.13	0.799	8.35
1-Dec	5:00	0.189	0.078	0.31	1.01	0.714	7.36
1-Dec	6:00	0.559	0.408	0.59	1.14	0.806	8.16
1-Dec	7:00	0.829	0.688	0.88	0.814	0.576	7.3
1-Dec	8:00	0.929	0.858	1.01	0.791	0.559	9.5
1-Dec	9:00	0.829	0.868	1.02	0.98	0.693	8.5
1-Dec	10:00	0.589	0.678	0.78	1.01	0.714	8.22

1-Dec	11:00	0.259	0.388	0.37	1.02	0.721	8.49
1-Dec	12:00	-0.101	0.048	0.17	1.02	0.721	7.66
1-Dec	13:00	-0.401	-0.252	-0.25	1.14	0.806	8.14
1-Dec	14:00	-0.611	-0.492	-0.39	1.05	0.742	8.25
1-Dec	15:00	-0.601	-0.542	-0.4	1.04	0.735	7.86
1-Dec	16:00	-0.481	-0.432	-0.34	1.06	0.750	8.85
1-Dec	17:00	-0.241	-0.252	-0.08	1.04	0.735	8.08
1-Dec	18:00	0.039	-0.032	0.16	1.05	0.742	9.87
1-Dec	19:00	0.249	0.178	0.33	1.01	0.714	9.3
1-Dec	20:00	0.349	0.328	0.48	0.99	0.700	9.83
1-Dec	21:00	0.319	0.318	0.39	0.99	0.700	10.28
1-Dec	22:00	0.139	0.178	0.29	0.93	0.658	10.14
1-Dec	23:00	-0.151	-0.072	-0.03	0.9	0.636	8.93
2-Dec	0:00	-0.431	-0.372	-0.37	0.94	0.665	9.27
2-Dec	1:00	-0.681	-0.622	-0.51	0.9	0.636	8.69
2-Dec	2:00	-0.801	-0.782	-0.59	0.785	0.555	8.8
2-Dec	3:00	-0.731	-0.712	-0.54	0.716	0.506	10.2
2-Dec	4:00	-0.481	-0.502	-0.39	0.777	0.549	8.8
2-Dec	5:00	-0.151	-0.202	-0.07	0.748	0.529	8.2
2-Dec	6:00	0.239	0.108	0.31	0.726	0.513	9.5
2-Dec	7:00	0.589	0.428	0.63	0.748	0.529	10.2
2-Dec	8:00	0.809	0.688	0.88	0.704	0.498	8.8
2-Dec	9:00	0.879	0.828	0.99	0.812	0.574	10.2
2-Dec	10:00	0.759	0.778	0.9	0.789	0.558	9.4
2-Dec	11:00	0.459	0.538	0.57	0.846	0.598	10.2
2-Dec	12:00	0.089	0.198	0.23	0.795	0.562	9.4
2-Dec	13:00	-0.291	-0.132	-0.1	0.857	0.606	7.7
2-Dec	14:00	-0.571	-0.432	-0.4	0.856	0.605	10.2
2-Dec	15:00	-0.711	-0.612	-0.52	0.92	0.651	9.93
2-Dec	16:00	-0.671	-0.642	-0.44	1	0.707	10.26
2-Dec	17:00	-0.521	-0.512	-0.36	0.94	0.665	9.91
2-Dec	18:00	-0.271	-0.312	-0.12	0.94	0.665	10
2-Dec	19:00	-0.021	-0.072	0.06	0.89	0.629	9.8
2-Dec	20:00	0.189	0.138	0.28	0.9	0.636	9.77
2-Dec	21:00	0.249	0.238	0.35	0.88	0.622	9.93
2-Dec	22:00	0.189	0.198	0.24	0.82	0.580	9.98
2-Dec	23:00	-0.011	0.038	0.1	0.82	0.580	9.41
3-Dec	0:00	-0.281	-0.222	-0.17	0.74	0.523	9.38
3-Dec	1:00	-0.561	-0.502	-0.4	0.77	0.544	9.8
3-Dec	2:00	-0.741	-0.692	-0.54	0.74	0.523	9.96
3-Dec	3:00	-0.781	-0.762	-0.59	0.69	0.488	10.8
3-Dec	4:00	-0.681	-0.672	-0.54	0.77	0.544	10.34
3-Dec	5:00	-0.401	-0.432	-0.27	0.78	0.552	10.11
3-Dec	6:00	-0.031	-0.102	0.07	0.71	0.502	10.14
3-Dec	7:00	0.379	0.218	0.39	0.8	0.566	9.79
3-Dec	8:00	0.709	0.538	0.79	0.8	0.566	10.28
3-Dec	9:00	0.879	0.748	0.93	0.78	0.552	10.28
3-Dec	10:00	0.879	0.868	1.03	0.79	0.559	10.11
3-Dec	11:00	0.689	0.768	0.86	0.82	0.580	9.5
3-Dec	12:00	0.379	0.498	0.46	0.85	0.601	9.9
3-Dec	13:00	-0.001	0.168	0.16	0.9	0.636	10.2

A.4.3 Salinity data

X [m BM]	Z sample [m AHD]	C(z)/Cs [ ]	X [m BM]	Z sample [m AHD]	C(z)/Cs [ ]	X [m BM]	Z sample [m AHD]	C(z)/Cs [ ]	X [m BM]	Z sample [m AHD]	C(z)/Cs [ ]
20/11/2001, 15:00:00			**21/11/2001, 10:00:00**			**21/11/2001, 18:00:00**			**22/11/01, 18:00**		
-25.56	0.117	0.971	-25.56	0.117	1.010	-25.56	0.117	0.984	-25.56	0.117	1.006
-19.46	0.431	0.676	-19.46	0.431	0.721	-19.46	0.431	0.747	-19.46	0.431	0.763
-19.46	0.173	0.841	-19.46	0.173	0.897	-19.46	0.173	0.849	-19.46	0.173	0.908
-19.46	-0.075	0.951	-19.46	-0.075	0.968	-19.46	-0.075	0.936	-19.46	-0.075	0.949
-19.46	-0.219	0.974	-19.46	-0.219	0.984	-19.46	-0.219	0.942	-19.46	-0.219	0.965
-12.56	0.364	0.340	-12.56	0.364	0.356	-12.56	0.364	0.359	-12.56	0.364	0.491
-12.56	-0.19	0.667	-12.56	-0.19	0.712	-12.56	-0.19	0.679	-12.56	-0.19	0.826
-12.56	-0.939	0.974	-12.56	-0.939	0.949	-12.56	-0.939	0.962	-12.56	-0.939	0.991
-8.09	0.31	0.230	-8.09	0.31	0.235	-8.09	0.31	0.270	-8.09	0.31	0.353
-8.09	-0.387	0.654	-8.09	-0.387	0.683	-8.09	-0.387	0.708	-8.09	-0.387	0.801
-4.6	0.385	0.104	-4.6	0.385	0.110	-4.6	0.385	0.128	-4.6	0.385	0.202
23/11/01, 17:00			**24/11/01, 17:00**			**25/11/01, 09:00**			**26/11/01, 10:00**		
-25.56	0.117	0.987	-25.56	0.117	0.903	-25.56	0.117	0.905	-25.56	0.117	0.890
-19.46	0.431	0.766	-19.46	0.431	0.893	-19.46	0.431	0.950	-19.46	0.431	0.893
-19.46	0.173	0.845	-19.46	0.173	0.764	-19.46	0.173	0.858	-19.46	0.173	0.827
-19.46	-0.075	0.930	-19.46	-0.075	0.858	-19.46	-0.075	0.845	-19.46	-0.075	0.865
-19.46	-0.219	0.946	-19.46	-0.219	0.896	-19.46	-0.219	0.871	-19.46	-0.219	0.846
-12.56	0.364	0.468	-12.56	0.364	0.417	-12.56	0.364	0.389	-12.56	0.364	0.366
-12.56	-0.19	0.832	-12.56	-0.19	0.836	-12.56	-0.19	0.795	-12.56	-0.19	0.726
-12.56	-0.939	1.006				-8.09	0.31	0.277	-8.09	0.31	0.255
-8.09	0.31	0.364				-8.09	-0.387	0.707	-8.09	-0.387	0.676
-8.09	-0.387	0.801				-4.6	0.385	0.192	-4.6	0.385	0.153
-4.6	0.385	0.248							11.19	0.007	0.032
11.19	0.007	0.033									

X [m BM]	Z sample [m AHD]	C(z)/Cs [ ]	X [m BM]	Z sample [m AHD]	C(z)/Cs [ ]	X [m BM]	Z sample [m AHD]	C(z)/Cs [ ]	X [m BM]	Z sample [m AHD]	C(z)/Cs [ ]
27/11/01, 11:00			**28/11/01, 10:00**			**29/11/01, 10:00**			**30/11/01, 11:00**		
-25.56	0.117	0.871	-25.56	0.117	0.876	-25.56	0.117	0.870	-25.56	0.117	0.908
-19.46	0.431	0.862	-19.46	0.431	0.847	-19.46	0.431	0.899	-19.46	0.431	0.927
-19.46	0.173	0.931	-19.46	0.173	0.997	-19.46	0.173	0.953	-19.46	0.173	0.870
-19.46	-0.075	0.884	-19.46	-0.075	0.917	-19.46	-0.075	0.883	-19.46	-0.075	0.908
-19.46	-0.219	0.875	-19.46	-0.219	0.917	-19.46	-0.219	0.889	-19.46	-0.219	0.899
-12.56	0.364	0.354	-12.56	0.364	0.342	-12.56	0.364	0.351	-12.56	0.364	0.350
-12.56	-0.19	0.677	-12.56	-0.19	0.669	-12.56	-0.19	0.677	-12.56	-0.19	0.677
-12.56	-0.743	0.931	-12.56	-0.743	0.927	-12.56	-0.743	0.930	-12.56	-0.743	0.940
-8.09	0.31	0.239	-8.09	0.31	0.233	-8.09	0.31	0.241	-8.09	0.31	0.242
-8.09	-0.387	0.652	-8.09	-0.387	0.653	-8.09	-0.387	0.668	-8.09	-0.387	0.684
-4.6	0.385	0.122	-4.6	0.385	0.109	-4.6	0.385	0.121	-4.6	0.385	0.127
11.19	0.007	0.028	11.19	0.007	0.030	11.19	0.007	0.031	11.19	0.007	0.032
01/12/01, 10:00			**02/12/01, 11:00**			**03/12/01, 11:00**					
-25.56	0.117	0.921	-25.56	0.117	0.931	-25.56	0.117	0.938			
-19.46	0.431	0.917	-19.46	0.431	0.866	-19.46	0.431	0.776			
-19.46	0.173	0.854	-19.46	0.173	0.838	-19.46	0.173	0.810			
-19.46	-0.075	0.911	-19.46	-0.075	0.891	-19.46	-0.075	0.879			
-19.46	-0.219	0.949	-19.46	-0.219	0.947	-19.46	-0.219	0.935			
-12.56	0.364	0.354	-12.56	0.364	0.346	-12.56	0.364	0.341			
-12.56	-0.19	0.654	-12.56	-0.19	0.622	-12.56	-0.19	0.583			
-12.56	-0.743	0.930	-12.56	-0.743	0.909	-12.56	-0.743	0.894			
-8.09	0.31	0.250	-8.09	0.31	0.255	-8.09	0.31	0.248			
-8.09	-0.387	0.676	-8.09	-0.387	0.672	-8.09	-0.387	0.651			
-4.6	0.385	0.136	-4.6	0.385	0.159	-4.6	0.385	0.135			
11.19	0.007	0.033	11.19	0.007	0.034	11.19	0.007	0.028			

X [m BM]	Z sample [m AHD]	C(z)/Cs [ ]	X [m BM]	Z sample [m AHD]	C(z)/Cs [ ]	X [m BM]	Z sample [m AHD]	C(z)/Cs [ ]	X [m BM]	Z sample [m AHD]	C(z)/Cs [ ]
20/11/2001, 15:00:00			**21/11/2001, 10:00:00**			**21/11/2001, 18:00:00**			**22/11/01, 18:00**		
-25.56	0.117	0.971	-25.56	0.117	1.010	-25.56	0.117	0.984	-25.56	0.117	1.006
-19.46	0.431	0.676	-19.46	0.431	0.721	-19.46	0.431	0.747	-19.46	0.431	0.763
-19.46	0.173	0.841	-19.46	0.173	0.897	-19.46	0.173	0.849	-19.46	0.173	0.908
-19.46	-0.075	0.951	-19.46	-0.075	0.968	-19.46	-0.075	0.936	-19.46	-0.075	0.949
-19.46	-0.219	0.974	-19.46	-0.219	0.984	-19.46	-0.219	0.942	-19.46	-0.219	0.965
-12.56	0.364	0.340	-12.56	0.364	0.356	-12.56	0.364	0.359	-12.56	0.364	0.491
-12.56	-0.19	0.667	-12.56	-0.19	0.712	-12.56	-0.19	0.679	-12.56	-0.19	0.826
-12.56	-0.939	0.974	-12.56	-0.939	0.949	-12.56	-0.939	0.962	-12.56	-0.939	0.991
-8.09	0.31	0.230	-8.09	0.31	0.235	-8.09	0.31	0.270	-8.09	0.31	0.353
-8.09	-0.387	0.654	-8.09	-0.387	0.683	-8.09	-0.387	0.708	-8.09	-0.387	0.801
-4.6	0.385	0.104	-4.6	0.385	0.110	-4.6	0.385	0.128	-4.6	0.385	0.202
23/11/01, 17:00			**24/11/01, 17:00**			**25/11/01, 09:00**			**26/11/01, 10:00**		
-25.56	0.117	0.987	-25.56	0.117	0.903	-25.56	0.117	0.905	-25.56	0.117	0.890
-19.46	0.431	0.766	-19.46	0.431	0.893	-19.46	0.431	0.950	-19.46	0.431	0.893
-19.46	0.173	0.845	-19.46	0.173	0.764	-19.46	0.173	0.858	-19.46	0.173	0.827
-19.46	-0.075	0.930	-19.46	-0.075	0.858	-19.46	-0.075	0.845	-19.46	-0.075	0.865
-19.46	-0.219	0.946	-19.46	-0.219	0.896	-19.46	-0.219	0.871	-19.46	-0.219	0.846
-12.56	0.364	0.468	-12.56	0.364	0.417	-12.56	0.364	0.389	-12.56	0.364	0.366
-12.56	-0.19	0.832	-12.56	-0.19	0.836	-12.56	-0.19	0.795	-12.56	-0.19	0.726
-12.56	-0.939	1.006				-8.09	0.31	0.277	-8.09	0.31	0.255
-8.09	0.31	0.364				-8.09	-0.387	0.707	-8.09	-0.387	0.676
-8.09	-0.387	0.801				-4.6	0.385	0.192	-4.6	0.385	0.153
-4.6	0.385	0.248							11.19	0.007	0.032
11.19	0.007	0.033									

X [m BM]	Z sample [m AHD]	C(z)/Cs [ ]	X [m BM]	Z sample [m AHD]	C(z)/Cs [ ]	X [m BM]	Z sample [m AHD]	C(z)/Cs [ ]	X [m BM]	Z sample [m AHD]	C(z)/Cs [ ]
27/11/01, 11:00			**28/11/01, 10:00**			**29/11/01, 10:00**			**30/11/01, 11:00**		
-25.56	0.117	0.871	-25.56	0.117	0.876	-25.56	0.117	0.870	-25.56	0.117	0.908
-19.46	0.431	0.862	-19.46	0.431	0.847	-19.46	0.431	0.899	-19.46	0.431	0.927
-19.46	0.173	0.931	-19.46	0.173	0.997	-19.46	0.173	0.953	-19.46	0.173	0.870
-19.46	-0.075	0.884	-19.46	-0.075	0.917	-19.46	-0.075	0.883	-19.46	-0.075	0.908
-19.46	-0.219	0.875	-19.46	-0.219	0.917	-19.46	-0.219	0.889	-19.46	-0.219	0.899
-12.56	0.364	0.354	-12.56	0.364	0.342	-12.56	0.364	0.351	-12.56	0.364	0.350
-12.56	-0.19	0.677	-12.56	-0.19	0.669	-12.56	-0.19	0.677	-12.56	-0.19	0.677
-12.56	-0.743	0.931	-12.56	-0.743	0.927	-12.56	-0.743	0.930	-12.56	-0.743	0.940
-8.09	0.31	0.239	-8.09	0.31	0.233	-8.09	0.31	0.241	-8.09	0.31	0.242
-8.09	-0.387	0.652	-8.09	-0.387	0.653	-8.09	-0.387	0.668	-8.09	-0.387	0.684
-4.6	0.385	0.122	-4.6	0.385	0.109	-4.6	0.385	0.121	-4.6	0.385	0.127
11.19	0.007	0.028	11.19	0.007	0.030	11.19	0.007	0.031	11.19	0.007	0.032
01/12/01, 10:00			**02/12/01, 11:00**			**03/12/01, 11:00**					
-25.56	0.117	0.921	-25.56	0.117	0.931	-25.56	0.117	0.938			
-19.46	0.431	0.917	-19.46	0.431	0.866	-19.46	0.431	0.776			
-19.46	0.173	0.854	-19.46	0.173	0.838	-19.46	0.173	0.810			
-19.46	-0.075	0.911	-19.46	-0.075	0.891	-19.46	-0.075	0.879			
-19.46	-0.219	0.949	-19.46	-0.219	0.947	-19.46	-0.219	0.935			
-12.56	0.364	0.354	-12.56	0.364	0.346	-12.56	0.364	0.341			
-12.56	-0.19	0.654	-12.56	-0.19	0.622	-12.56	-0.19	0.583			
-12.56	-0.743	0.930	-12.56	-0.743	0.909	-12.56	-0.743	0.894			
-8.09	0.31	0.250	-8.09	0.31	0.255	-8.09	0.31	0.248			
-8.09	-0.387	0.676	-8.09	-0.387	0.672	-8.09	-0.387	0.651			
-4.6	0.385	0.136	-4.6	0.385	0.159	-4.6	0.385	0.135			
11.19	0.007	0.033	11.19	0.007	0.034	11.19	0.007	0.028			

A.5 Brunswick Heads, 18th February 2002

A.5.1 Water level and topography data

Well	**2**	**2.5**	**3**	**3.3**	**3.6**	**4**	**5**	**6**	**7**	**8**	**9**	**10**	**11**	**EP**	**RUL**	**SWL**	**H**	**T**
x [m]	95.25	88.97	83.37	78.98	75.5	71.38	67.56	63.69	60.37	57.16	53.97	50.9	47.72					
z sand [m AHD]	-0.004	0.206	0.375	0.512	0.615	0.712	0.808	0.875	0.931	0.980	1.041	1.110	1.170					
Time	**Levels [m AHD]**																[m]	[sec]
6	0.043	0.204	0.286	0.333	0.366	0.428	0.459	0.513	0.557	0.59	0.634	0.664	0.687	0.112		-0.28	0.884	8.12
6.17	0.053	0.204	0.306	0.373	0.406	0.438	0.489	0.523	0.557	0.59	0.634	0.664	0.687	0.254	0.47	-0.2562	0.883	8.20
6.33	0.073	0.224	0.326	0.373	0.396	0.428	0.469	0.513	0.557	0.58	0.634	0.654	0.677	0.4	0.519	-0.2338	0.883	8.27
6.5	0.073	0.224	0.336	0.363	0.386	0.428	0.479	0.513	0.547	0.58	0.634	0.654	0.677	0.352	0.483	-0.21	0.882	8.34
6.67	0.083	0.224	0.326	0.353	0.376	0.428	0.469	0.513	0.547	0.58	0.624	0.654	0.677	0.327	0.434	-0.1862	0.881	8.41
6.83	0.083	0.234	0.346	0.423	0.466	0.478	0.499	0.523	0.547	0.58	0.624	0.654	0.677	0.376	0.606	-0.1638	0.880	8.48
7	0.093	0.234	0.346	0.403	0.426	0.458	0.489	0.523	0.547	0.58	0.624	0.644	0.677	0.4	0.446	-0.14	0.880	8.55
7.17	0.103	0.244	0.356	0.443	0.496	0.498	0.529	0.543	0.547	0.58	0.614	0.644	0.677	0.446	0.631	-0.1026	0.879	8.62
7.33	0.113	0.244	0.356	0.433	0.526	0.478	0.509	0.533	0.547	0.58	0.614	0.644	0.677	0.303	0.561	-0.0674	0.878	8.69
7.5	0.123	0.254	0.366	0.453	0.496	0.508	0.529	0.553	0.547	0.58	0.614	0.644	0.677	0.434	0.699	-0.03	0.877	8.76
7.67	0.128	0.254	0.366	0.453	0.476	0.508	0.529	0.553	0.577	0.59	0.624	0.644	0.677	0.446	0.699	0.0074	0.877	8.83
7.83	0.133	0.259	0.376	0.473	0.506	0.478	0.549	0.563	0.577	0.6	0.624	0.644	0.677	0.446	0.519	0.0426	0.876	8.90
8	0.133	0.264	0.386	0.453	0.476	0.508	0.529	0.553	0.577	0.59	0.624	0.644	0.677	0.458	0.637	0.08	0.875	8.97
8.17	0.178	0.274	0.396	0.473	0.526	0.558	0.569	0.583	0.587	0.61	0.624	0.654	0.677	0.47	0.711	0.114	0.874	9.05
8.33	0.203	0.294	0.396	0.483	0.526	0.568	0.579	0.583	0.597	0.62	0.634	0.654	0.677	0.483	0.711	0.146	0.874	9.12
8.5	0.223	0.304	0.406	0.483	0.546	0.588	0.629	0.613	0.607	0.63	0.634	0.654	0.677	0.543	0.76	0.18	0.873	9.19
8.67	0.243	0.314	0.416	0.493	0.556	0.598	0.599	0.613	0.617	0.63	0.644	0.654	0.677	0.619	0.805	0.214	0.872	9.26

8.83	0.273	0.334	0.416	0.503	0.566	0.628	0.649	0.643	0.637	0.65	0.654	0.664	0.687	0.643	0.842	0.246	0.871	9.33
9	0.293	0.354	0.441	0.523	0.596	0.648	0.729	0.823	0.687	0.74	0.674	0.684	0.687	0.667	1.013	0.28	0.870	9.40
9.17	0.313	0.374	0.441	0.513	0.576	0.648	0.729	0.683	0.697	0.69	0.694	0.694	0.687	0.667	0.83	0.3055	0.863	9.40
9.33	0.333	0.394	0.456	0.533	0.586	0.648	0.749	0.693	0.697	0.76	0.699	0.704	0.707	0.711	0.988	0.3295	0.857	9.40
9.5	0.373	0.424	0.476	0.543	0.596	0.668	0.719	0.733	0.737	0.72	0.714	0.704	0.717	0.711	0.805	0.355	0.850	9.40
9.67	0.383	0.434	0.486	0.563	0.616	0.678	0.749	0.823	0.757	0.73	0.724	0.714	0.717	0.736	0.988	0.3805	0.843	9.40
9.83	0.403	0.454	0.476	0.533	0.596	0.668	0.719	0.733	0.737	0.8	0.724	0.724	0.717	0.679	0.805	0.4045	0.836	9.40
10	0.423	0.464	0.506	0.573	0.616	0.688	0.759	0.803	0.827	0.8	0.744	0.734	0.727	0.736	1.001	0.43	0.829	9.40
10.17	0.453	0.494	0.536	0.583	0.636	0.698	0.769	0.833	0.857	0.81	0.784	0.774	0.757	0.748	0.83	0.4555	0.828	9.40
10.33	0.453	0.494	0.536	0.593	0.636	0.688	0.769	0.833	0.807	0.92	0.824	0.774	0.757	0.748	1.054	0.4795	0.827	9.40
10.5	0.483	0.514	0.566	0.623	0.676	0.708	0.789	0.843	0.877	0.95	0.824	0.804	0.797	0.83	1.09	0.505	0.826	9.40
10.67	0.503	0.544	0.586	0.633	0.656	0.718	0.789	0.853	0.877	0.92	0.874	0.844	0.827	0.83	1.013	0.5305	0.825	9.40
10.83	0.523	0.564	0.596	0.643	0.676	0.718	0.789	0.863	0.917	0.9	0.944	0.944	0.857	0.923	1.116	0.5545	0.824	9.40
11	0.523	0.574	0.606	0.633	0.656	0.708	0.779	0.863	0.907	0.92	0.914	0.874	0.847	0.971	1.066	0.58	0.823	9.40
11.17	0.533	0.564	0.596	0.643	0.666	0.718	0.789	0.863	0.917	0.93	0.934	0.894	0.877	0.988	1.193	0.5732	0.828	9.30
11.33	0.523	0.564	0.596	0.623	0.656	0.718	0.799	0.873	0.917	0.96	0.954	1.014	0.947	0.988	1.312	0.5668	0.833	9.20
11.5	0.523	0.564	0.576	0.623	0.656	0.718	0.789	0.873	0.927	0.97	1.004	0.964	0.937	1.013	1.23	0.56	0.838	9.10
11.67	0.543	0.584	0.616	0.653	0.676	0.728	0.799	0.873	0.917	0.97	0.994	0.964	0.937	0.964	1.218	0.5532	0.842	9.00
11.83	0.533	0.574	0.606	0.633	0.666	0.708	0.789	0.863	0.907	0.9	0.904	0.884	0.877	0.91	1.218	0.5468	0.847	8.90
12	0.523	0.554	0.576	0.613	0.646	0.708	0.789	0.873	0.917	0.96	0.974	0.934	0.907	0.83	1.054	0.54	0.852	8.80
12.17	0.513	0.544	0.576	0.623	0.656	0.708	0.789	0.873	0.907	0.97	0.934	0.934	0.897	0.805	1.066	0.5162	0.858	8.80
12.33	0.503	0.544	0.566	0.593	0.636	0.698	0.779	0.863	0.917	0.9	0.934	0.904	0.897	0.76	1.14	0.4938	0.863	8.80
12.5	0.463	0.504	0.526	0.573	0.626	0.698	0.759	0.873	0.917	0.96	0.934	0.904	0.887	0.725	1.066	0.47	0.869	8.80
12.67	0.463	0.494	0.526	0.573	0.616	0.688	0.779	0.853	0.857	0.96	0.864	0.874	0.867	0.83	1.042	0.4462	0.875	8.80
12.83	0.453	0.484	0.516	0.583	0.626	0.698	0.789	0.863	0.887	0.9	0.884	0.874	0.867	0.711	1.001	0.4238	0.880	8.80
13	0.433	0.464	0.496	0.553	0.606	0.688	0.779	0.823	0.837	0.82	0.834	0.834	0.847	0.736	0.935	0.4	0.886	8.80
13.17	0.393	0.434	0.476	0.543	0.606	0.698	0.789	0.863	0.877	0.91	0.894	0.864	0.857	0.781	1.066	0.3626	0.884	8.77
13.33	0.373	0.404	0.446	0.513	0.586	0.688	0.749	0.763	0.827	0.77	0.824	0.824	0.837	0.748	1.066	0.3274	0.882	8.73
13.5	0.343	0.374	0.426	0.503	0.586	0.678	0.759	0.783	0.787	0.78	0.804	0.814	0.827	0.772	0.886	0.29	0.880	8.70
13.67	0.313	0.344	0.416	0.513	0.596	0.688	0.739	0.763	0.777	0.76	0.794	0.804	0.827	0.619	0.964	0.2526	0.878	8.67
13.83	0.273	0.334	0.396	0.503	0.596	0.678	0.769	0.813	0.777	0.81	0.794	0.804	0.817	0.667	0.898	0.2174	0.876	8.63
14	0.263	0.304	0.386	0.483	0.586	0.668	0.749	0.773	0.747	0.76	0.774	0.794	0.807	0.619	0.91	0.18	0.874	8.60
14.17	0.243	0.294	0.376	0.493	0.576	0.658	0.709	0.723	0.737	0.73	0.764	0.784	0.807	0.567	0.724	0.1545	0.872	8.57
14.33	0.203	0.274	0.376	0.493	0.586	0.688	0.739	0.723	0.737	0.76	0.764	0.784	0.797	0.543	0.818	0.1305	0.870	8.53

14.5	0.193	0.244	0.366	0.493	0.586	0.678	0.749	0.773	0.757	0.76	0.774	0.784	0.797	0.543	0.886	0.105	0.868	8.50
14.67	0.133	0.224	0.356	0.483	0.566	0.648	0.689	0.723	0.717	0.71	0.754	0.774	0.787	0.567	0.83	0.0795	0.866	8.47
14.83	0.103	0.204	0.346	0.463	0.496	0.568	0.589	0.633	0.687	0.68	0.734	0.764	0.777	0.388	0.631	0.0555	0.864	8.43
15	0.093	0.194	0.346	0.463	0.526	0.558	0.599	0.623	0.657	0.67	0.764	0.764	0.777	0.376	0.711	0.03	0.861	8.40
15.17	0.083	0.204	0.346	0.443	0.556	0.618	0.629	0.653	0.657	0.69	0.724	0.754	0.777	0.352	0.519	-0.0074	0.859	8.37
15.33	0.053	0.184	0.326	0.423	0.446	0.488	0.539	0.583	0.637	0.67	0.724	0.734	0.767	0.352	0.531	-0.0426	0.857	8.33
15.5	0.043	0.174	0.316	0.383	0.426	0.478	0.529	0.573	0.617	0.66	0.704	0.734	0.767	0.352	0.619	-0.08	0.855	8.30
15.67	0.033	0.174	0.316	0.383	0.416	0.468	0.519	0.563	0.617	0.65	0.704	0.734	0.757	0.352	0.483	-0.1174	0.853	8.27
15.83	0.033	0.184	0.326	0.423	0.436	0.478	0.529	0.573	0.617	0.65	0.704	0.764	0.757	0.352	0.543	-0.1526	0.851	8.23
16	0.023	0.184	0.316	0.413	0.446	0.478	0.529	0.573	0.617	0.65	0.694	0.724	0.747	0.24	0.376	-0.19	0.849	8.20
16.17	0.013	0.174	0.286	0.343	0.386	0.438	0.499	0.553	0.597	0.64	0.684	0.714	0.737	0.216	0.434	-0.2172	0.859	8.40
16.33	-0.007	0.184	0.296	0.343	0.386	0.478	0.499	0.553	0.597	0.64	0.674	0.704	0.727	0.216	0.315	-0.2428	0.869	8.60
16.5	0.003	0.184	0.296	0.383	0.456	0.458	0.519	0.543	0.587	0.63	0.684	0.694	0.727	0.216	0.543	-0.27	0.879	8.80
16.67	0.013	0.184	0.286	0.333	0.376	0.428	0.489	0.543	0.587	0.62	0.674	0.704	0.717	0.191	0.376	-0.2972	0.889	9.00
16.83	0.003	0.174	0.266	0.323	0.366	0.418	0.479	0.533	0.577	0.61	0.664	0.694	0.717	0.191	0.352	-0.3228	0.899	9.20
17	0.003	0.164	0.236	0.293	0.356	0.418	0.469	0.533	0.577	0.61	0.664	0.694	0.717	0.112	0.203	-0.35	0.909	9.40
17.17	0.013	0.154	0.206	0.283	0.346	0.408	0.469	0.523	0.567	0.61	0.654	0.684	0.707	0.112	0.446	-0.3568	0.906	9.30
17.33	0.013	0.164	0.236	0.303	0.336	0.408	0.469	0.523	0.567	0.61	0.654	0.684	0.707	0.112	0.364	-0.3632	0.903	9.20
17.5	0.033	0.184	0.316	0.323	0.356	0.428	0.469	0.523	0.567	0.6	0.644	0.684	0.697	0.112	0.495	-0.37	0.900	9.10
17.67	0.033	0.184	0.286	0.333	0.366	0.418	0.459	0.523	0.557	0.6	0.644	0.674	0.697	0.087	0.315	-0.3768	0.897	9.00
17.83	0.033	0.184	0.276	0.323	0.366	0.418	0.459	0.523	0.557	0.59	0.644	0.674	0.697	0.087	0.458	-0.3832	0.894	8.90
18	0.033	0.174	0.256	0.303	0.346	0.408	0.459	0.513	0.557	0.59	0.634	0.674	0.697	0.087	0.376	-0.39	0.891	8.80
18.17	0.043	0.174	0.266	0.323	0.366	0.408	0.459	0.513	0.547	0.58	0.634	0.664	0.687	0.112	0.483	-0.3628	0.883	8.70
18.33	0.043	0.204	0.306	0.333	0.376	0.418	0.449	0.513	0.547	0.58	0.634	0.664	0.687	0.191	0.422	-0.3372	0.875	8.59

Well	**12**	**13**	**14**	**15**	**16**	**17**	**18**	**19**
x [m]	44.34	40.71	32.57	23.85	14.3	-11.19	-45.2	-83.59
z sand [m AHD]	1.281	1.435	1.832	2.452	3.667	4.056	3.825	3.700
Time								
6	0.703	0.721	0.748	0.753	0.763	0.777	0.728	0.7
6.5	0.703	0.721	0.748	0.753	0.763	0.777	0.728	0.7

7	0.703	0.721	0.748	0.753	0.763	0.777	0.728	0.7
7.5	0.693	0.711	0.748	0.753	0.763	0.777	0.728	0.7
8	0.693	0.711	0.738	0.753	0.763	0.777	0.728	0.7
8.5	0.693	0.711	0.738	0.753	0.763	0.777	0.728	0.7
9	0.703	0.711	0.738	0.753	0.763	0.777	0.728	0.7
9.5	0.723	0.721	0.738	0.743	0.753	0.777	0.728	0.7
10	0.713	0.731	0.748	0.753	0.753	0.777	0.728	0.7
10.5	0.763	0.761	0.758	0.773	0.763	0.777	0.728	0.7
11	0.813	0.781	0.758	0.763	0.763	0.777	0.728	0.7
11.5	0.863	0.821	0.788	0.773	0.763	0.777	0.728	0.7
12	0.873	0.831	0.798	0.783	0.763	0.777	0.728	0.7
12.5	0.863	0.831	0.808	0.783	0.763	0.777	0.728	0.7
13	0.843	0.831	0.808	0.793	0.773	0.777	0.728	0.7
13.5	0.833	0.831	0.808	0.793	0.773	0.777	0.728	0.7
14	0.813	0.811	0.808	0.793	0.773	0.777	0.728	0.7
14.5	0.803	0.801	0.798	0.783	0.773	0.777	0.728	0.7
15	0.783	0.791	0.788	0.783	0.773	0.777	0.728	0.7
15.5	0.763	0.771	0.788	0.783	0.763	0.777	0.728	0.7
16	0.763	0.771	0.778	0.783	0.783	0.777	0.728	0.7
16.5	0.743	0.751	0.768	0.773	0.773	0.777	0.728	0.7
17	0.723	0.741	0.748	0.763	0.773	0.767	0.728	0.7
17.5	0.713	0.721	0.748	0.753	0.763	0.767	0.728	0.7
18	0.703	0.721	0.748	0.753	0.763	0.767	0.728	0.7
18.5	0.698	0.716	0.743	0.748	0.758	0.767	0.728	0.7

A.5.2 Wave runup statistics

The transgression statistics presented below were extracted from video footage. The time indicated represents the start time, the monitoring interval was 30 minutes.

N represents the total number of runup events entering the monitoring region during the 30 minute period.

n_i denotes the number of swash fronts transgressing a given shore-normal beach face coordinate (x_i, z_i).

The reader is referred to *Hanslow and Nielsen* [1993] for analysis techniques for interpreting wave runup distributions.

Well ID	**1**	**2**	**2.5**	**3**	**3.3**	**3.6**	**4**	**5**	**6**	**7**	**8**	**9**	**10**
x [m BM]	112.38	95.25	88.97	83.37	78.98	75.5	71.38	67.56	63.69	60.37	57.16	53.97	50.9
z sand [m AHD]	0.497	0.06	0.21	0.36	0.45	0.54	0.66	0.73	0.83	0.91	0.96	1.03	1.07

Time	**N**	**n_i ------------------------------->**											
7	232	102	44	20	6	1							
8	135	135	95	57	30	14	7						
9	198	198	165	108	67	54	31	14	5	1			
10	190	190	190	155	117	93	68	44	23	12	7		
11	197	197	197	187	162	108	99	72	41	23	10	1	
12	177	177	177	177	167	141	106	60	39	26	15	3	1
13	155	155	155	155	124	95	66	38	26	19	7	1	
14	184	184	150	114	73	47	28	16	5	3			
15	168	157	103	55	15	8							
16	175	104	43	11	3	1							
17	146	47	12	2									
18	161	64	26	5									

Appendix B – Sand column data

Here the existing sand column data from *Nielsen and Perrochet* [2000a,b] and *Nielsen and Turner* [2000] is reproduced in Appendix B.1 followed by the present sand column data collected to investigate the influence of a truncated capillary fringe on an oscillating water table in Appendix B.2.

B.1 Sand column data from *Nielsen and Turner* [2000] and *Nielsen and Perrochet* [2000a,b]

Nielsen and Turner [2000]

d_{50} [mm]	n [-]	K [m/s]	H_ψ [m]	T [s]	d [m]	$\lvert\eta_o\rvert$ [m]	$\lvert\eta\rvert$ [m]	ϕ_{wt} [rad]	$\Re\{n_\omega\}$ [-]	$\Im\{n_\omega\}$ [-]
.082	.5	$2.8x10^{-5}$	1.5	1785	.554	.174	.142	.151	.0027	-.0031
.082	.5	$2.8x10^{-5}$	1.5	1785	.552	.169	.150	.192	.0031	-.0015
.082	.5	$2.8x10^{-5}$	1.5	2460	.549	.173	.150	.230	.0052	-.0024
.082	.5	$2.8x10^{-5}$	1.5	1230	.549	.174	.126	.303	.0041	-.0031
.082	.5	$2.8x10^{-5}$	1.5	870	.569	.174	.116	.318	.0032	-.0029
.082	.5	$2.8x10^{-5}$	1.5	3780	.569	.171	.147	.234	.0080	-.0040
.082	.5	$2.8x10^{-5}$	1.5	7380	.569	.169	.160	.124	.0075	-.0026
.082	.5	$2.8x10^{-5}$	1.5	1050	.570	.174	.121	.321	.0037	-.0030
.082	.5	$2.8x10^{-5}$	1.5	6150	.569	.166	.151	.187	.0099	-.0040
.082	.5	$2.8x10^{-5}$	1.5	25200	.572	.168	.163	.058	.0117	-.0051
.082	.5	$2.8x10^{-5}$	1.5	12600	.570	.166	.157	.107	.0111	-.0050
.082	.5	$2.8x10^{-5}$	1.5	390	.510	.172	.107	.237	.0013	-.0019
.082	.5	$2.8x10^{-5}$	1.5	283	.516	.169	.102	.283	.0011	-.0014
.082	.5	$2.8x10^{-5}$	1.5	900	.515	.173	.117	.196	.0022	-.0035
.082	.5	$2.8x10^{-5}$	1.5	170	.514	.175	.099	.339	.0009	-.0010
.082	.5	$2.8x10^{-5}$	1.5	210	.516	.175	.101	.424	.0013	-.0010
.082	.5	$2.8x10^{-5}$	1.5	140	.515	.175	.094	.521	.0011	-.0007
.082	.5	$2.8x10^{-5}$	1.5	385	.510	.171	.113	.298	.0015	-.0015
.082	.5	$2.8x10^{-5}$	1.5	210	.511	.169	.101	.341	.0010	-.0010
.082	.5	$2.8x10^{-5}$	1.5	360	.511	.174	.117	.365	.0017	-.0012
.082	.5	$2.8x10^{-5}$	1.5	3300	.508	.173	.153	.137	.0045	-.0034
.78	.41	$2.5x10^{-3}$	.085	1320	.589	.173	.163	.158	.1482	-.0380
.78	.41	$2.5x10^{-3}$	.085	2370	.587	.172	.164	.105	.1765	-.0699
.78	.41	$2.5x10^{-3}$	.085	386.3	.589	.163	.123	.423	.1420	-.0546
.78	.41	$2.5x10^{-3}$	.085	163	.599	.155	.088	.485	.0888	-.0603
.78	.41	$2.5x10^{-3}$	.085	137	.600	.151	.077	.508	.0867	-.0648
.78	.41	$2.5x10^{-3}$	.085	573	.601	.168	.141	.321	.1425	-.0494
.78	.41	$2.5x10^{-3}$	.085	278	.601	.159	.109	.463	.1198	-.0558
.78	.41	$2.5x10^{-3}$	.085	234	.597	.158	.104	.479	.1093	-.0546

.2	.4	1.47×10^{-4}	.6	137	.602	.175	.088	.384	.0040	-.0045
.2	.4	1.47×10^{-4}	.6	524	.599	.171	.103	.317	.0106	-.0118
.2	.4	1.47×10^{-4}	.6	890	.594	.172	.115	.275	.0143	-.0155
.2	.4	1.47×10^{-4}	.6	547	.621	.173	.086	.366	.0148	-.0181
.2	.4	1.47×10^{-4}	.6	547	.745	.173	.081	.414	.0148	-.0164
.2	.4	1.47×10^{-4}	.6	552	.495	.171	.104	.276	.0117	-.0152
.2	.4	1.0×10^{-4}	.6	1.3	.530	.151	.045	1.918	.0010	.0007
.2	.4	1.0×10^{-4}	.6	14.4	.553	.153	.042	1.611	.0015	.0005
.2	.4	1.0×10^{-4}	.6	27	.534	.148	.053	1.051	.0020	-.0003
.2	.4	1.0×10^{-4}	.6	6.5	.557	.146	.055	.473	.0021	-.0024
.2	.4	1.0×10^{-4}	.6	12.6	.551	.154	.046	1.809	.0012	.0007
.2	.4	1.0×10^{-4}	.6	61	.538	.145	.054	.485	.0023	-.0025
.2	.4	1.0×10^{-4}	.6	2.1	.551	.152	.048	1.322	.0018	.0001
.2	.4	1.0×10^{-4}	.6	87.9	.536	.144	.056	.269	.0018	-.0039
.2	.4	1.0×10^{-4}	.6	269.8	.542	.144	.047	.065	.0016	-.0163
.2	.4	1.0×10^{-4}	.6	121.3	.561	.145	.050	.179	.0018	-.0064
.2	.4	1.0×10^{-4}	.6	309.3	.551	.146	.080	.033	.0005	-.0074
.2	.4	1.0×10^{-4}	.6	195.5	.543	.148	.087	.032	.0003	-.0040
.2	.4	1.0×10^{-4}	.6	178.9	.530	.145	.062	.079	.0010	-.0072
.2	.4	1.0×10^{-4}	.6	468.5	.533	.142	.043	.149	.0069	-.0317
.2	.4	1.0×10^{-4}	.6	24.1	.541	.142	.082	.024	.0003	-.0052
.2	.4	1.0×10^{-4}	.6	1.4	.539	.152	.041	1.773	.0011	.0005
.2	.4	1.0×10^{-4}	.6	530	.543	.142	.041	.146	.0078	-.0377
.2	.4	1.0×10^{-4}	.6	359.4	.542	.143	.042	.061	.0022	-.0253
.2	.4	1.0×10^{-4}	.6	3120	.756	.169	.128	.215	.0185	-.0190
.2	.4	1.0×10^{-4}	.6	1935	.753	.168	.116	.242	.0142	-.0166
.2	.4	1.0×10^{-4}	.6	840	.759	.169	.103	.271	.0077	-.0102
.2	.4	1.0×10^{-4}	.6	1410	.754	.168	.111	.251	.0112	-.0139
.2	.4	1.0×10^{-4}	.6	2610	.760	.169	.121	.025	.0019	-.0217
.2	.4	1.0×10^{-4}	.6	5160	.756	.168	.134	.234	.0316	-.0238
.2	.4	1.0×10^{-4}	.6	6120	.759	.169	.137	.216	.0340	-.0263
.2	.4	1.0×10^{-4}	.6	380	.749	.163	.069	.479	.0088	-.0088
.2	.4	1.0×10^{-4}	.6	466	.749	.165	.069	.435	.0100	-.0116
.2	.4	1.0×10^{-4}	.6	600	.754	.164	.074	.416	.0113	-.0130

Nielsen and Perrochet [2000a,b] data

.78	.41	2.5×10^{-3}	.085	877.5	.588	.171	.152	.252	.1660	-.0512
.2	.3	4.7×10^{-4}	.55	4008	.527	.143	.140	.070	.0405	-.0108
.2	.3	4.7×10^{-4}	.55	4200	.524	.141	.138	.064	.0393	-.0131
.2	.3	4.7×10^{-4}	.55	4140	.527	.146	.136	.168	.1055	-.0343
.2	.3	4.7×10^{-4}	.55	1440	.525	.141	.132	.153	.0335	-.0119
.2	.3	4.7×10^{-4}	.55	9000	.524	.141	.137	.035	.0461	-.0320
.2	.3	4.7×10^{-4}	.55	14700	.527	.139	.137	.026	.0550	-.0297
.2	.3	4.7×10^{-4}	.55	23500	.525	.139	.136	.014	.0480	-.0809
.2	.3	4.7×10^{-4}	.55	888	.527	.143	.116	.192	.0297	-.0265
.2	.3	4.7×10^{-4}	.55	1050	.524	.140	.122	.189	.0322	-.0184
.2	.3	4.7×10^{-4}	.55	1740	.528	.142	.134	.143	.0371	-.0109

B.2 Truncated fringe sand column data

z_{sand}	T	K	$\overline{h_o}$	$\lvert\eta_o\rvert$	$\overline{h}$	$\lvert\eta\rvert$	ϕ	$\Re\{n_\omega\}$	$\Im\{n_\omega\}$	$\lvert n_\omega\rvert$	-Arg$\{n_\omega\}$
[m]	[s]	[m/s]	[m]	[m]	[m]	[m]	[rad]	[ ]	[ ]	[ ]	[ ]
1.40	350	0.00014	0.731	0.169	0.722	0.101	0.290	0.0051	-0.0064	0.0082	0.9004
1.37	352	0.00014	0.722	0.168	0.720	0.098	0.219	0.0040	-0.0073	0.0084	1.0656
1.34	351	0.00014	0.708	0.167	0.708	0.100	0.296	0.0054	-0.0066	0.0085	0.8867
1.30	351	0.00014	0.679	0.167	0.676	0.103	0.275	0.0051	-0.0065	0.0082	0.9049
1.27	351	0.00014	0.733	0.171	0.737	0.098	0.310	0.0057	-0.0071	0.0091	0.8934
1.27	351	0.00014	0.733	0.170	0.732	0.097	0.311	0.0057	-0.0071	0.0091	0.8947
1.24	351	0.00014	0.732	0.170	0.735	0.097	0.345	0.0063	-0.0069	0.0094	0.8309
1.24	351	0.00014	0.733	0.169	0.736	0.097	0.310	0.0057	-0.0070	0.0090	0.8923
1.21	351	0.00014	0.729	0.170	0.737	0.103	0.327	0.0057	-0.0060	0.0083	0.8155
1.21	351	0.00014	0.731	0.170	0.736	0.103	0.314	0.0055	-0.0061	0.0082	0.8409
1.19	351	0.00014	0.730	0.169	0.736	0.103	0.329	0.0057	-0.0059	0.0082	0.8063
1.19	351	0.00014	0.729	0.170	0.737	0.103	0.327	0.0057	-0.0060	0.0083	0.8155
1.17	351	0.00014	0.734	0.171	0.739	0.103	0.269	0.0047	-0.0064	0.0079	0.9371
1.17	351	0.00014	0.734	0.172	0.736	0.105	0.238	0.0041	-0.0063	0.0075	0.9927
1.15	351	0.00014	0.735	0.170	0.728	0.104	0.315	0.0054	-0.0059	0.0080	0.8304
1.15	351	0.00014	0.734	0.172	0.750	0.105	0.325	0.0056	-0.0059	0.0081	0.8126
1.14	351	0.00014	0.733	0.171	0.729	0.104	0.313	0.0054	-0.0060	0.0081	0.8396
1.14	351	0.00014	0.734	0.170	0.726	0.104	0.300	0.0051	-0.0060	0.0079	0.8604
1.12	351	0.00014	0.734	0.172	0.750	0.105	0.325	0.0056	-0.0059	0.0081	0.8126
1.12	351	0.00014	0.730	0.170	0.727	0.104	0.311	0.0054	-0.0060	0.0080	0.8383
1.08	351	0.00014	0.734	0.170	0.728	0.104	0.295	0.0051	-0.0060	0.0079	0.8706
1.08	351	0.00014	0.733	0.169	0.730	0.104	0.286	0.0049	-0.0060	0.0077	0.8839
1.06	351	0.00014	0.733	0.171	0.733	0.108	0.351	0.0058	-0.0052	0.0078	0.7296
1.06	351	0.00014	0.733	0.171	0.732	0.108	0.355	0.0059	-0.0052	0.0078	0.7220
1.04	351	0.00014	0.734	0.171	0.746	0.110	0.301	0.0049	-0.0052	0.0071	0.8105
1.04	351	0.00014	0.732	0.172	0.735	0.107	0.309	0.0052	-0.0057	0.0077	0.8270
1.02	351	0.00014	0.733	0.171	0.745	0.118	0.305	0.0046	-0.0041	0.0062	0.7208
1.02	351	0.00014	0.735	0.173	0.745	0.119	0.378	0.0057	-0.0037	0.0068	0.5795
1.00	351	0.00014	0.733	0.172	0.746	0.139	0.331	0.0043	-0.0018	0.0047	0.4005
1.00	351	0.00014	0.735	0.171	0.745	0.139	0.320	0.0041	-0.0018	0.0045	0.4091
0.98	351	0.00014	0.731	0.171	0.742	0.130	0.329	0.0045	-0.0026	0.0052	0.5227
0.98	351	0.00014	0.733	0.171	0.747	0.148	0.315	0.0038	-0.0011	0.0040	0.2687
0.96	351	0.00014	0.733	0.171	0.746	0.150	0.309	0.0037	-0.0009	0.0038	0.2432
0.96	351	0.00014	0.723	0.169	0.736	0.145	0.320	0.0040	-0.0012	0.0041	0.2823
0.93	351	0.00014	0.731	0.170	0.745	0.157	0.268	0.0031	-0.0005	0.0031	0.1593
0.93	351	0.00014	0.730	0.171	0.746	0.159	0.275	0.0031	-0.0004	0.0032	0.1195
0.90	351	0.00014	0.732	0.172	0.747	0.163	0.248	0.0028	-0.0002	0.0028	0.0883
0.90	351	0.00014	0.729	0.170	0.741	0.160	0.257	0.0029	-0.0003	0.0029	0.1019
0.88	351	0.00014	0.732	0.173	0.747	0.166	0.182	0.0020	-0.0003	0.0020	0.1315
0.83	351	0.00014	0.729	0.170	0.733	0.148	0.242	0.0030	-0.0012	0.0032	0.3963
0.83	351	0.00014	0.733	0.173	0.730	0.147	0.120	0.0015	-0.0018	0.0023	0.8741